PhD Thesis

Single ionization of the hydrogen molecule induced by pump - probe techniques with ultrashort laser pulses

Universidad Autónoma de Madrid
Departamento de Química

Alberto González Castrillo

Supervised by:
Fernando Martín García
Alicia Palacios Cañas

Madrid, March 2014

Dedicated to my parents, Adolfo and Paloma,

and my baby, Kinga.

Acknowledgments

I would like to thanks:

My PhD. supervisor, Alicia Palacios Cañas, who has always been there to help me, to guide me and even to cheer me up in the moments of frustration. Without her, her confidence in my capacities and her support, this PhD thesis would not exit.

My PhD. supervisor, Fernando Martín, the “Boss”, for giving me the opportunity to made my doctorate in his group, for guiding me in the best direction and for making the effort to understand my cofusing explanations.

My "boss" in Bordeaux, Henri Bachau, for hosting in “galas” lands, for his fruitful collaboration and because chat with him is a real pleasure.

José Luis Sanz Vicario, for the fruitful discussion during the PhD writing and for our long talks about many common hobbies.

Manuel Alcamí, Manuel Yáñez, and Otilia Mó, for their selfless support and always take care of children in the department.

The different members of the Chemistry Department, the Professors, post-doctorate investigators as well as my PhD and Master colleagues, who have made this arduos journey easier and more entertaining.

My parents, Adolfo and Paloma, who have always had faith in me, have been supporting me, helping me and giving me everything possible to make me happy and achieve my life goals.

And my Baby, Kinga, for giving a meaning to my life and deciding to join our paths to be happy together.

Contents

Abstract

This PhD thesis reports *ab initio* calculations to describe the interaction of laser pulses with the hydrogen molecule using different schemes, from isolated attosecond pulses to one and two-color pump - probe schemes. The main goal of the present work is to obtain time-resolved images of a manifold of laser-induced processes that are general to any molecule, with special focusing on the autoionization processes. The theoretical description here presented aims to unravel the natural time and spatial evolution of electronic motion in diatomic molecules, therefore including the coupled motion of electrons and nuclei in time.

Our *ab initio* calculations are based on the solution of the time-dependent Schrödinger equation (TDSE) using a semiclassical approximation, in which the molecular system is treated by quantum mechanics and the laser field by classical electrodynamics within the dipole approximation. We employ a spectral method, which uses the eigenfunctions of the isolated system (without the external perturbation) to expand the time dependent wavefunction of the system. These eigenstates are calculated for the bound and scattering states within the Born-Oppenheimer approximation and the Feshbach formalism. This method, previously developed in our group, allows a straightforward access to the excitation and ionization observables.

In this context, we will first explore the dynamics followed by an electronic wave packet created upon one-photon absorption after the interaction of H_2 with a single attosecond pulse. In particular, we look into the single photoionization process induced by sub-femtosecond XUV pulses to obtain an image in time of the autoionization events. The photon energies carried by these ultrashort pulses in the XUV region reach the doubly excited states, molecular states lying above the ionization limit where both electrons of the molecule are simultaneously excited. Its decay in time is captured and the build-up of its interference with the background ionization continua. We analyze energy-differential distributions, i.e. densities of ionization probability as a function of both nuclear and electronic energies, or integrated over one of them. For one-photon transitions, the dependence of the observed spectra with the laser parameters can only be formally factored out as long as all ejected particles are measured in coincidence, as we shortly discuss. These energy-differential distributions present patterns resulting from the coherent contribution of direct photoionization and autoionization. These patterns can be easily explained through a simple semiclassical model developed in our group [128], following the formalism used for Penning ionization by W. Miller. This model can predict not only the energy-differential ionization signal, but also the

angular dependencies of the ejected electrons. Using both, *ab initio* calculations and this semiclassical model, we will obtain a time-resolved image of the doubly excited states decay into the electronic continua. It will be discussed in detail the time evolution of the different observables: ionization probabilities integrated and/or differential in both energies and angles of the ejected fragments.

Once this dynamics is understood from a theoretical point of view, a second pulse is introduced, a probe pulse, to simulate those experiments using a XUV pump - XUV pump or XUV pump - IR probe schemes and explore the dependence of the ionization probabilities with the time delay between the XUV pump and the probe pulse. The second pulse will strongly modify the process under observation.

We first will explore the widely used XUV pump - IR probe schemes, in which the pump launches the dynamics into the ionic states on the energetic region where the autoionization process takes place, and the probe traces this dynamics as a function of the time delay between them. We specially analyze the effects over the proton and fully energy-differential distributions, focusing on the time delays when the pump and probe fields are overlapped, producing the laser-assisted photoionization where the system is simultaneously pumped and probed. In addition, we analyze the streaking patterns observed in the electron distributions resolved in the space as well as integrated over all the possible electron ejection angles. As it is observed, the presence of the resonant states induces several modifications over all these spectra with respect to the obtained for isolated pulses. In addition, the electron angular distributions where the doubly excited states decay, present more complex features than the obtained from the simple classical pictures used to explain the electron streaking by IR fields.

On the other hand, using a similar XUV pump - IR probe scheme, but with a more complex pump constituted by a XUV APT phase locked with an IR pulse, is used to explore and even control the vibronic (electronic and nuclear) dynamics into the single excited states of the hydrogen molecule. In this way, the final interferometric spectra obtained can be used to extract the relevant information about the dynamics into the intermediate states.

Finally, due to the distortion of the potential energy curves by the IR, the natural electronic and fast nuclear motion on single excited and ionic states can be only traced with a XUV pump - XUV probe scheme. We propose a scheme constituted by two identical sub-fs XUV pulses, which populate by one-photon absorption the single excited states and by two-photon absorption the final observed ionic states. One creates a molecular interferometer when the molecule is irradiated with time-delayed attosecond XUV pulses, where the two-photon "direct" absorption paths interferes with the two-photon "sequential" path. From the interferometric signal appearing in the ionization channel, one can reconstruct the evolution of the electronic and nuclear wavepacket created in the single excited states of the molecule. The application of the different analysis tools, as the short term Fourier transform (STFT), allows us to extract from the final interferometric signals observed in the different observables studied, the relevant dynamical information of the coupled motion among electrons and nuclei.

Resumen

Esta tesis de doctorado reporta cálculos *ab initio* para describir la interacción de pulsos láser con la molécula de hidrógeno usando diferentes esquemas, desde pulsos independientes de attosegundos a esquemas pump - probe de uno y dos colores. El principal objetivos del presente trabajo es obtener las imágenes resueltas en el tiempo de múltiples procesos inducidos por láser, que son generales para cualquier molécula, con especial atención a los procesos de autoionización. La descripción teórica aquí presentada pretende aclarar la evolución espacial y temporal del movimiento electrónico en moléculas diatómicas, y por lo tanto, incluye el movimiento acoplado de electrones y núcleos en el tiempo.

Nuestros cálculos *ab initio* están basados en solución de la Equación de Schrödinger Dependiente del Tiempo (TDSE) usando una aproximación semiclásica, en la cuál el sistema molecular es tratado mediante mecánica cuántica y el campo láser por la electrodinámica clásica dentro de la aproximación dipolar. Nosotros empleamos el método espectral, que usa las funciones propias del sistema (sin la perturbación externa) para expandir la función de onda dependiente del tiempo del sistema. Estas funciones propias son calculadas para los estados ligados y de dispersión dentro de la aproximación de Born-Oppenehimer y el formalismo de Feshbach. Este método, desarrollado previamente in nuestro grupo, permite un acceso directo a los observables obtenidos para la excitación y la ionización.

En este contexto, primero exploraremos la dinámica seguida por un paquete de ondas creado tras la absorción de un fotón después de la interacción del H_2 con un pulso de attosegundos. En particular, nosotros investigamos el proceso de ionización simple, inducido por pulsos XUV de sub-femtosegundo, para obtener una imagen temporal del evento de autoionización. Las energías de fotón de estos pulsos ultracortos en la región XUV alcanza los estados doblemente excitados, estados moleculares por encima de los límites de ionización donde ambos electrones de la molécula están simultáneamente excitados. Nosotros analizamos las distribuciones diferenciales en energía, es decir, las densidades de probabilidad de ionización en función de las energías cinéticas de núcleos y electrones, o integradas sobre una de ellas. Para las transiciones a un fotón, la dependencia de los espectros observados con los parámetros del láser pueden ser solo formalmente factorizados en tanto que todas las partículas eyectadas son medidas en coincidencia, como nosotros discutiremos. Estas distribuciones diferenciales en energía presentan patrones resultantes de la combinación coherente of la fotoionización directa y la autoionización. Estos patrones pueden ser fácilmente explicados a través de un modelo semiclásico desarrollado en nuestro grupo [128], el cuál sigue

el formalismo usado por W. Miller para la ionización de Penning. Este modelo puede no solo predecir la señal de la distribuciones diferenciales en energía, sino también la dependencias angulares del electrón eyectado. Usando ambos, los cálculos *ab initio* y este modelo semiclásico, nosotros obtendremos la imagen temporal del decaimiento de los estados doblemente excitados en los continuos electrónicos. Será discutido en detalle la evolución temporal de los diferentes observables: Las probabilidades de ionización integradas y/o diferenciales en ambas energías y ángulos del electrón eyectado.

Una vez esta dinámica es comprendida desde un punto de vista teórico, un segundo pulso es introducido, conocido pulso probe, para simular estos experimentos usando esquemas XUV pump - XUV pump o XUV pump - IR probe y explorando la dependencia de las probabilidades de ionización con el retraso temporal entre el XUV pump y el pulso probe. Según el tipo de pulso usado como probe los procesos bajo observación serán fuertemente modificados.

Primero nosotros exploraremos los ampliamente usados esquemas XUV pump - IR probe, en los cuales el pump lanza la dinámica en los estados iónicos en la región energética donde el procesos de autoionización tiene lugar, y el probe traza esta dinámica como función del retraso temporal entre ellos. Especialmente nosotros analizamos el efecto sobre las distribuciones diferenciales energéticas completa y de protón, centrándose en la separación temporal cuando los campos pump y probe están superpuestos, produciendo la conocida fotoionización asistida por láser donde el sistema es simultáneamente bombeado y probado. Además, nosotros analizamos los patrones de streaking observados en las distribuciones electrónicas resueltas en el espacio así como integradas sobre todos los posibles ángulos del electrón eyectado. Como puede ser observado, la presencia de los estados doblemente excitados induce varias modificaciones sobre todos estos espectros con respecto a los obtenidos para pulsos aislados. Además, las distribuciones angulares del electrón donde los estados resonantes decaen presentan características más complejas que las obtenidas desde la imagen clásica simple usada para explicar el streaking del electron por el campo IR.

Por otro lado, usando un esquema similar XUV pump - IR probe, pero con un pump más complejo, constituido por un XUV APT con la fase fijada con respecto a un pulso IR, es usado para explorar e incluso controlar la dinámica vibrónica (electrónica y nuclear) en los estados simplemente excitados de la molécula de hidrógeno. En este sentido, los espectros interferométricos finales obtenidos pueden ser usados para extraer la información relevante sobre la dinámica en estos estados intermedios.

Finalmente, debido a la distrosión de las curvas de energía potencial por el IR, el movimiento natural electrónico y nuclear en los estados simplemente excitados e iónicos pueden ser solo trazados con un esquema XUV pump - XUV probe. Nosotros proponemos un esquema constituido por dos pulsos XUV idénticos con duraciones de sub-fs, los cuales pueblan por absorción de un fotón los estados simplemente excitados y por absorción de dos fotones los estados finales iónicos observados. Así, se crea un interferómetro molecular cuando la molécula es irradiada con los pulsos de attosegundos XUV separados temporalmente, donde el camino de absorción "directa" de dos fotones interfiere con el camino "secuencial"

de dos fotones. Desde la señal interferométrica en el canal de ionización, uno puede reconstruir la evolución del paquete de ondas electrónico y nuclear creado en los estados simplemente excitados de la molécula. La aplicación de las diferentes herramientas de análisis, como la Trasformada de Fourier de corto tiempo (STFT), nos permite extraer de las señales interferométricas finales observadas en los diferentes observables estudiados, la información dinámica relevante del movimiento acoplado entre electrones y núcleos.

Introduction

The fast development of laser sources to produce shorter pulses makes attophysics a reality, the new frontier of the atomic and molecular science to explore the electronic and fast nuclear dynamics. The typical attosecond ($1\,\mathrm{as} = 10^{-18}\,\mathrm{s}$) timescales of the electronic motion can be inferred by classical mechanics, using the Borh model for the hydrogen atom. However, the intrinsic behavior of the electron dynamics follows the quantum mechanics, where the analog of the classical motion is given by a wavepacket. The evolution of an electronic wavepacket constituted by the two first states of the hydrogen atom is given by $\phi = \exp\left[-i\left(E_1 - E_0\right)t/\hbar\right]$, whose period is $T = 2\pi\hbar/\left(E_1 - E_0\right)$. Using the well-known energies for this atomic system [141], the typical timescale for this oscillation is around 150 as. Consequently, the capability of observing in time the electronic dynamics requires interaction times shorter than their natural timescales of motion, i.e. interaction in the sub-femtosecond ($1\,\mathrm{fs} = 10^{-15}\,\mathrm{s}$) and attosecond ($1\,\mathrm{as} = 10^{-18}\,\mathrm{s}$) regime. Because the number of oscillations inside the pulse is limited by its duration, these timescales force to use pulses in the energetic region of the extreme ultraviolet (XUV) [80]. Two main techniques allow to obtain pulses with these *as* durations and XUV energies: The high harmonic generation (HHG) techniques and the free electron laser (FEL and XFEL).

The HHG sources are based on a non-perturbative non-linear optical process in an atomic, molecular or plasma system. Firstly studied by McPherson et. al. [109], the theoretical background of the HHG is described by the well-known three step model developed by Corkum and Kulander in 1993 [32], based on the work of Keldysh [81] as well as Ammosov, Delone and Krainov [3]. This semi-classical model uses the SAE (single active electron) approximation, where all the electrons of the system are frozen except one. In the first step, a strong driving field, usually near infrared (IR) or visible pulsed laser, deforms the atomic (or molecular) potential, allowing the emission of one electron by tunneling ionization. This ionization process is more probable in a narrow window of time, every half cycle of the IR generating laser field, typically around several hundreds of attoseconds, generating an electronic wavepacket which is accelerated by the driving field in the second step. Within the SFA (strong field approximation), the trajectory of the ejected electron follows the vector potential of the driving field. Consequently, at the half oscillation after the electron emission, the electronic wavepacket generated is driven back to the parent ion. This results in the third step, where the ejected electron recollides with the parent ion. From a quantum mechanical point of view, this recombination is described by the dipole transition

from the continium state of the ejected electron to a bound state, which induces the stimulated emission of a photon whose frequency is determined by the kinetic energy, E_k, gained by the electron during its trajectory, $\hbar\omega = E_k + I_p$ (where ω is the photon frequency and I_p is the ionization potential of the system) in the second step. This kinetic energy is determined by the amplitude and wavelength of the driving field, and the allowed maximum photon energy, $\hbar\omega_{max} = I_p + 3.17U_p$, is determined by ionization potential and the ponderomotive energy, U_p. Since the three steps are repeated every half optical cycle of the driving laser, the final emitted light is constituted by a coherent combination of a burst of attosecond pulses, giving an attosecond pulse train (APT), whose time separation is equal to half period of the driving field, $T_{IR}/2$, and whose energy spectrum is distributed by peaks (harmonics) separated by the photon energy of the driving pulse. If coherent interferences of N harmonics are perfect, the APT are constituted by pulses with durations equal to $T_{IR}/2N$.

However, many applications need the reduction of the APT generated by the HHG techniques to a single attosecond pulse (SAP). To this purpose, the most straightforward approach consists in the use of a few-cycle driving field obtained with techniques as the hollow fiber filled with noble gases compression. In this technique, developed in 90s, a femtosecond carrier envelope phase-stabilized pulses generated by the Ti:Sapphire laser is compressed by a non-linear effect during its propagation in a dielectric capillaries filled with noble gases [122, 152]. Other approaches, which also used Ti:Sapphire lasers as the driving pulses, are the polarization gating (PG) techniques. Contrary to the above hollow fiber filled technique, the PG consists in reducing the active optical driving field by a temporal window, with timescales similar to the half optical cycle of the driving pulse. Several PG techniques generates this temporal window by the use of elliptic (or even circular) driving laser fields, which decrease the conversion efficiency of the HHG process in noble gases [21, 38]. This conversion efficiency decrease can be explained using the three step model. With linearly polarized driving fields, the emitted electron is accelerated out of the atom through the same trajectory than the used for driving back to its parent ion. However, when the driving field has an elliptic or circular polarization, the ejected electron follows different trajectories to go out and coming back to the parent ion. Thus, the electron never passes from the position of the parent ion and the HHG cannot take place. To reproduce an elliptic driving field, the PG technique combines two pulses with different linearly polarized directions and phases, reducing the HHG process to only one half of the optical cycle, emitting a SAP.

The shortest SAP up to date, 67 as [190] and 80 as [66, 149, 60], have been generated by HHG. However, the HHG technique generates APT and SAP with too low energies and intensities. Significant efforts are realized to overcome the main limitations: the reduction of the conversion efficiency up to the 100 eV due to a limited reabsorption of the HHG light by the medium [50, 60], the dephasing between the driving pulse and the HHG light or the destruction of the driving field due to the dispersion processes generated by the free electron [188, 189, 131, 186]. Despite these promising progresses, achieving higher intensities and photon energies nowadays still constitutes a technological challenge with the HHG techniques.

These limitations are absent in the FEL (free electron laser), where specially the XFEL (x-ray free electron laser) constitutes the most adequate technique to produce photons with high energy, in the region of the XUV and even the X-ray, and high intensity. The FEL technique was presented in 80s by Madey [100] as an extension of the the synchrotron sources, where the electrons are accelerated by a perpendicular strong magnetic field, which forces them to move in a circular motion at velocities close to the light speed, inducing the emission of photons with low intensity and high frequency. As the synchrotron sources, the FEL technique uses unbound electrons, different from the traditional laser, whose photon emission are due to transitions between bound states. The FEL concept is relatively simple, the free electrons beam, previously accelerated, is introduced in a linear undulator, also called wiggler magnetic array, which presents an alternative transverse magnetic field. This magnetic field induces an sinusoidal motion of the free electrons along the undulator, which accelerates these electrons in a perpendicular direction with respect to their propagation direction, increasing their kinetic energy. At certain point, by a SASE (self-amplied spontaneous emission) process, the gained kinetic energy by the electrons is emitted spontaneously as a photon [175, 113]. This SASE process produces high coherently laser pulses [183] with high photon energies, up to 700 eV [13], high intensities peaks, up to $10^{15}\,\mathrm{W}\cdot\mathrm{cm}^{-2}$, and narrow bandwidths around the central frequency [9]. In addition, one advantage of this technique is that the photon energy can be easily modified increasing/decreasing the initial velocity of the electrons or the magnitude of the perpendicular magnetic field [143]. However, although the deep development of the XFEL source as in the facilities FLASH in Hamburg or LCLS in Standford, this technique is not capable nowadays of producing laser shorter than several femtoseconds [11].

A full characterization of the ultrashort pulses generated by the different HHG and XFEL sources, is often needed for their applications. However, traditional optical characterization techniques cannot be applied to ultrashort pulses because their typical XUV photon energy decreases the efficiency of the induced nonlinear processes into different media. In this way, several techniques have been proposed to obtain the amplitude and phase which define the time evolution of the attosecond pulse as a function of the structures obtained from the electronic wavepackets generated after the ionization processes with these pulses. Some of these techniques, as the attosecond streaking camera [66, 69] and FROG CRAB (frequency-resolved optical gating for complete reconstruction of attosecond bursts) [66, 61, 102, 137, 78] methods, the attosecond pulse induces the single ionization of an atomic system, generating an electronic wavepacket, whose momentum changes by the presence of the strong IR field. The photoelectron spectrum, obtained as a function of the momentum and time delay between both pulses, contains the amplitude and phase of both XUV and strong IR pulses and can be extracted using different analysis algorithms as the PCGPA (Principal Component Generalized Projections Algorithm) [79]. In addtion, the well-known the RABBIT (reconstruction of attosecond beating by interference of two-photon transitions) [174, 132, 116] technique is used to characterize the APT. On the other hand, the SPIDER (spectral interferometric for direct electric-field recon-

struction of ultrashort optical pulses) technique is based on the spectral sharing interferometry. This technique splits the attosecond XUV pulse into two delayed pulses, which interact with an atomic system, whose ionization spectra are knowledge and soft [68, 136, 34, 164]. The first XUV pulse induces the ionization of the system, generating a first electronic wavepacket, which propagates in time and space. The second XUV pulse generates a identical wavepacket into the same continuum states, but delayed with respect to the first. Due to the different phases, both electronic wavepackets coherently interfere. Since the intensity of the spectral distribution is associated with the amplitude of the original XUV pulse and the phase interference between both split pulses imprint into this distribution the phase of the pulse, the characterization of the attosecond XUV pulse can be obtained. The above techniques thus lead to well characterized attosecond pulses that can be now used to pump matter into excited or ionized states to be later probed by a second pulse. These are the well-known pump - probe schemes.

The pump - probe schemes can be used to give access to the information of the dynamical processes induced by the laser-matter interaction. The present PhD thesis is oriented in the exploration of the electrons and fast nuclei dynamics induced by different pump - probe schemes. The pump - probe techniques were used previously in femtochemistry to follow the nuclear motion in chemical reactions [187]. In this area of the chemistry, the hundreds of fs timescales in which the formation and rupture of the chemical bounds take place, make that the pulse duration, needed for time resolution enough to obtain the real time imagine of the chemical reaction, is in the order of tens of fs. In these experiments, both pump and probe pulses have frequencies in the IR regime, due to the closer energy difference between the nuclear states, where the pump excites the system and launches the nuclear dynamics by the creation of an excited vibrational wavepacket, while the probe pulse follows this dynamics taking "snapshots" of the motion, as a function of the time delay between both pulses. Although limited to pulse durations of a few tens of fs, these femtochemistry pump - probe techniques were applied to attophysics, analyzing the fingerprint of the coupled electron dynamics into the nuclear motion. These experiments use as pump and probe the same IR pulses, with durations from tens to several fs, which interact with the hydrogen molecule and its isotopes, producing its ionization. Different protocols have been proposed, as use the recolission of the ejected electron [120, 85], as in the HHG technique, or a second photon absorption to populate a different ionic states of the residual ion [88], to give information about the electron localization, through the changes in the nuclear motion.

More recently, the pump - probe schemes that become more widely used in attophysics, use XUV APT and SAP sources combined with and IR field. These XUV pump - IR probe schemes were applied to atoms [97, 164, 98, 52] and starts to molecules [82, 51] to explore the electronic dynamics in its timescales. In all these experiments, the sub-fs or as XUV pulse triggers the electron dynamics by one or more photon absorption processes, ionizing the system. The strong IR field used as a probe pulse drives the ejected electron, and similarly as performed in the attosecond streaking camera [66], gives access to the electron dynamics information. Although in a pump - probe scheme would aim for both pump and

probe being separated in time, most of the available experiments come out using overlapping in time. This is particular important for the use of XUV SAP as a pump, where in the so-called laser-assisted photoionization, the system is simultaneously pumped and probed.

These XUV pump - IR probe experiments in molecules require theoretical simulations which give a complete theoretical background. The hydrogen molecule constitutes a prototypical system for the theoretical exploration of the laser-molecule interaction. It is the simplest molecular system with all the possible interactions presented in any other molecules, as the electron correlation and the coupled motion among electrons and nuclei. However, even in this simply molecular system, a full dimensional treatment including all electronic and nuclear degrees of freedom is a challenge for theory. Therefore, several works have used approximations to solve the laser-molecule interaction problems within the numerical or spectral approaches. Pure numerical methods were used in several works to study the single and double ionization in atoms [72, 126, 127, 182, 45]. Applications to molecular systems are more limited [24, 173, 172], and spectral methods are more common approach used to solve the problem of the interaction with pulse radiation. Several of these works, even in diatomic molecules, have reported electronic correlated calculations within the FNA (fixed nuclei approximation) [63, 31, 4, 8] or assuming that the dipole transition moments are independent of the internuclear distance [110, 162]. However, these methods neglect the coupled motion among electrons and nuclei. In this way, the first fully correlated calculation which takes all the electronic and nuclear degrees of freedom, for the light-matter interaction in H_2 and D_2 molecules was performed within the time-independent perturbation theory by our group [145, 144, 146, 147, 148]. Although limited to the photoionization processes by monochromatic radiation within the Born-Oppenheimer approximation, the description of the scattering states within the Fesbach formalism includes the correct and accurate treatment of the autoionization processes, allowing the access to the resonant state lifetimes, dissociative and photoionization cross sections, even resolved in the ejected electron angles, etc.. The correct description of the continuum states permits to this theory to give a theoretical background for a large variety of experiments performed with synchrotron radiation [104, 42, 140]. However, a deep and complete analysis of the pump - probe schemes requires a full dimensional treatment of the hydrogen molecule, which includes the time-dependent solution of the multiphoton absorption processes. This implementation is at the core of the methodology employed for the simulations presented in this PhD thesis.

The present PhD thesis is devoted to the theoretical analysis of the laser-matter interaction between the hydrogen molecule with pump - probe schemes using sub-fs XUV pulses. Our description of the hydrogen molecule includes all the electronic degrees of freedom, within the Born-Oppenheimer approximation. The spectral method used, based on the above first order time-independent perturbation theory using the Feshbach formalism, includes a complete description of the bound states (ground and single excited states) as well as the scattering states, constituted by the ejected electron (continuum states) and resonant states (doubly excited states). This assures a correct description of the different ionization

processes, including the direct ionization in the continuum states and the autoionization processes of the resonant states decaying into the continua. For a comprehensive picture of the laser-induced processes that will be explored in the context of pump - probe schemes, we first perform a theoretical description giving a complete overview of the main signatures obtained when an isolated attosecond XUV pulse interacts with this molecular system. We analyze the ionization probabilities, specially those measure in coincidence as a function of the ejected particle energies. As a difference with the well-known Fano-lineshapes [44], observed around the decay energies into the continua in atoms [44] and in hydrogen within the FNA [146], when the nuclear motion in light molecules is taking into account, they are not presented. However, the complex interferometric structure obtained in the final observables remains the coherent superposition between both direct ionization and autoionization processes. Consequently, the dynamical information of the decay can be extracted using a model, similarly to the Fano formalism in atoms [44]. Based on the previous studies of the Penning ionization by W. Miller [112] and using the WKB model and reflexion approximation, in this PhD thesis we present a theoretical model developed by A. Palacios et al [128]. This model predicts the structures observed in the energy-differential distributions as well as in the angular distributions of the ejected electrons and allows to retrieve the dynamical information about the decay process, as the lifetimes and widths of the resonances.

Once the above analysis allows us to understand the autoionization processes, we use the pump - probe schemes, as in previous presented experiments, to obtain the time-resolved image of the ionization processes, in the energy region where the resonant states decay. In this way, we analyze the induced processes due to the interaction of the hydrogen molecule with a similar XUV pump - IR probe schemes than the used in [150]. As in the atoms experiments, the sub-fs XUV pump launches the electronic dynamics by generation of electronic and nuclear (vibronic) wavepackets in the ionic continuum, whose motion is driven by the strong IR field used as a probe pulse. We take into account from negative time delays, when the IR field arrives before than the XUV, to positive time delays, including the time delay region where is produced the laser-assisted photoionization. Although in atoms [52, 27, 134, 123], the presence of the resonant states is well-defined and explored, there are a few works for molecules, so the play role of the resonant states in this laser-assisted photoionization scenario is not well established. In addition, the inclusion of the nuclear dynamics of the light hydrogen, with similar motion timescales to the autoionization process, introduces an extra complexity in the analysis. As in atoms [52], during the laser-assisted photoionization region, the IR field can produce interchange in the populations of the resonant and continuum states of the hydrogen molecule, following the oscillation of the IR field. However, the inclusion of the nuclear motion in molecules, induces important changes in the final ionization probabilities studied. In addition, similar to the attosecond streaking camera, the IR drives the ejected electron motion. Although the classical models which determine the variation of the electric momentum as a function of the IR vector potential are valid [69, 161], the higher contribution of the autoionization in the dissociative ionization, when the

residual molecular ion is broken in one proton and one hydrogen atom, gives more complicated features, burring the simple classical picture of the streaking patterns.

As a step-forward, we will present a work in collaboration with the experimental group of Prof. M. Murname and H. Kapteyn, using a phase-locked XUV APT with and IR as the pump, followed by an IR as the probe in the laser-assisted photoionization region. This complex pump allows the population of gerade and ungerade symmetries, whose evolution is traced in the final ionic channels reached by the multiphoton absorption of the probe IR pulse. The interferometry is well-known in optics to obtain information about the spatial and time propagation of the light [12, 68]. In the case of atoms and molecules, the interferometry is based on the contribution into the same final channels of different quantum paths, where the contribution of each path coherently combines with the other path contributions, generating interferometric features. These paths carry the information of the dynamical processes of the intermediate state, which is imprinted over the final interferometric signatures. This atomic interferometry was used in previous works [164, 108, 45] to study the electron dynamics with XUV pump - IR probe schemes. However, in the case of molecules, the electronic dynamics is coupled with the nuclear motion, so the molecular interferometer has to take into account the motion of both.

The strong IR used in the XUV pump - IR probe schemes disturbs the atomic or molecular potential felt by the ejected electron, which mainly follows the IR field given streaking patterns. To obtain the natural evolution of the system after the interaction with the sub-fs XUV pulse, it is necessary as a probe a laser field weak enough to avoid the distortion of the atomic and molecular potential. The state-of-art to this purpose is the combination of two XUV pulses, given XUV pump - XUV probe schemes. These proposed schemes are closer to the traditional pump - probe schemes used in femtochemistry and have been implemented in several experiments nowadays [169, 23]. However, the generation of two sub-fs XUV pulses with a control of the time delay between them constitutes nowadays a challenge for the experimentalists. As with the XUV pump - IR probe schemes, the dynamics can be followed by the molecular interferometer generated by two or more paths which populate the same final states. This interferometry is more similar to the previous used in the femtochemistry, as in the works of [43, 16, 15], where the nuclear motion into a concrete electronic states is traced in its natural timescales with the use of a IR pump - IR probe schemes. Specially the work [43] where the nuclear motion of the Na_2 molecule is followed using two identical femtosecond IR pulses, where the possible paths followed by the system in the excitation processes are very close to the present in our XUV pump - XUV probe scheme. This proposed scheme reaches the final ionic states by three main paths: a) the "direct" ionization from the ground states by the two-photon absorption of the pump pulse, b) the same two-photon absorption from the ground state but induced by the probe pulse and c) "sequential" path, in which the the pump excited the system to a bunch of vibrational states of different bound electronic states and the probe ionizes from these intermediate states to the final states. As a function of the time delay, the two different "direct" and the "sequential"

paths interfere due to their different phases. These phases are associated with the energies (wavepacket phases) of the states involved during the transition process. As the interference contains the relative phase differences between the paths, the information of the dynamics is imprinted in the interferometric signal. To extract this information from the observables analyzed, we use different tools as the Fourier transform analysis or the short term Fourier transform, which can unravel from the final interferometric signal the electronic and nuclear dynamics of the intermediate and even final states.

The present PhD thesis is divided in two main parts. The first four chapters give a general overview of the theoretical background used in our simulations and the last three chapters analyze the results obtained in the different explored ionization schemes. The first chapter is devoted to present the light-matter interaction within the semiclassical approximation used, where the system is treated by quantum mechanics and the electromagnetic field classically. In this chapter we treat a general case of the interaction between a system constituted by any number of charge particles with an external electromagnetic field, specifically the continuous electromagnetic wave, through a spectral method. In addiction, we introduce the dipole approximation to simplify its description. In the second chapter we give a general overview of the mathematical description of the laser fields, focusing on the sine squared envelope laser. The ultrashort pulses are described in both time and frequency (energy) domains, which give *a priori*, important information for the application of spectral method, as the selected basis set of eigenstates need in our expansion to describe properly all the possible transition processes. Following with the description of the ingredients needed in our theoretical treatment, in the third chapter we present the main points to obtain the eigenstates of the isolated hydrogen system. We introduce the Born-Oppenheimer approximation used to reduce the complexity of the multiparticle problem, separating as to independent problems the calculation of the nuclear and electronic states. In this chapter, our first step is to obtain the one-electron hydrogen molecular ionic states which will be used as a basis set to obtain the two-electron eigenstates for the hydrogen molecule. These two-electron wavefunctions for the bound states are calculated by the well-known interaction configuration method (IC), while the Feshbach formalism used to treat the scattering states divides the Hilbert space in two subspaces: one for the continuum states constituted by the ejection of one electron, and the other for the resonant states (doubly excited states, DES). Using the above electronic energies as the potential energy curves (PEC), which the nuclei feel in their motion, the nuclear wavefunctions are calculated within the Born-Oppenheimer approximation. Finally, in the fourth chapter, we briefly present the Runge-Kutta integration method used to solve the time-dependent Schrödinger equation (TDSE). The time dependent wavefunction solution of this TDSE is calculated using the spectral method introduced in the first chapter, where it is expanded as a linear combinations of the eigenfunctions of the field-free molecular system, calculated in the third chapter. With the amplitudes obtained, we give the expression for the different observables, probabilities and densities of probability, that we use in the next chapters to study the excitation and ionization processes.

In the last three chapter, we focus on three different excitation and ionization schemes. In chapter five, we explore the ionization process due to the interaction of the molecular system with an isolated sub-fs XUV pulse. Our analysis of different observables, as the density of ionization probability measured in coincidence for both emitted charge particles, indicates that the decay of the resonant states into the ejected electron continua leaves a coherent interferometry which is reflected in the final channels observed. To extract the relevant information about the resonant states from this interferometry, we present a semiclassical model developed by A. Palacio et al [128], based on the works of Miller [112], to explain the autoionization processes in molecules, similar to the Fano studies in atoms [44]. Finally, we apply this model to the study of the resonant state fingerprint into the electron angular distributions. In chapter six, we study the ionization processes in the energetic region where the resonant states decay, by a XUV pump - IR probe scheme. We analyze the different observables, with special attention on the driving effect of the IR probe. In the second part of this chapter, we analyze the vibronic (electronic and nuclear) wavepacket control induced by a complex pump - probe scheme, consisted in a XUV APT phase locked with an IR pulse as the pump, following by and IR field as the probe. Although these schemes, are capable of study the vibronic dynamics, the strong IR perturbs the electronic motion, and consequently, to study the natural time and spatial evolution of electrons and nuclei, is needed a different pump - probe scheme. In chapter seven, we analyze the dynamics of the single excited state using an XUV pump - XUV probe protocols. The interferometric signal into the final ionic channels allows us to extract the fingerprint of the intermediate bound states and unravel their natural dynamics without the perturbation introduced by an IR probe.

Chapter 1

Light-matter interaction

Our goal is to study theoretically the dynamical processes induced in the molecular hydrogen by interaction with ultrashort laser pulses. The spatial scale of the molecular system implies that a correct description of its physical evolution requires of quantum mechanics. In quantum mechanics, the time evolution of the system is determined by the well-known time dependent Schrödinger equation (TDSE), whose solutions (time dependent wavefunctions) contain all the possible information about the system. The solution of this equation implies an enormous complexity. To solve the light-matter interaction problem, several works [145, 144, 147, 148] used the first order time dependent perturbation theory (TDPT). However, this description of the light-matter interaction is restricted to the one-photon processes. Consequently, a full theoretical description of the multiphoton processes is only achieved by the full dimensional solution of the TDSE. To resolve this problem, we use a spectral method, in which the time dependent wavefunction is expanded as a linear combination of the eigenfunctions obtained for the system without the interaction of the external electromagnetic field. As we present in this chapter, this spectral method can be extrapolated to any system constituted by any number of different charged particles.

On the other hand, a rigorous and complete description of the electromagnetic field is provided by quantum electrodynamics. This theory describes the electromagnetic field as built of light quanta, called photons. However, the use of an intense electromagnetic field gives a density of photons high enough to consider that the number of photons is a continuous variable. Therefore, the electromagnetic field can be described by the classical electrodynamics. Consequently, we use a semiclassical approach to treat the light-matter interaction, in which the molecular system is described by quantum mechanics and the radiation by classical electrodynamics.

1.1 Time dependent Schrödinger equation

The quantum treatment of the molecular system implies that its time evolution is dictated by the time dependent Schrödinger equation, TDSE:

$$i\hbar\frac{\partial}{\partial t}\Psi\left(\mathbf{r},t\right)=\widehat{H}\left(t\right)\Psi\left(\mathbf{r},t\right) \tag{1.1.1}$$

where $\widehat{H}\left(t\right)$ is the time dependent Hamiltonian operator in the position representation, which contains the operators of the kinetic and potential energies of the system as well as the interaction with the electromagnetic field. Using the principle of correspondence, the quantum expression of the Hamiltonian operator can be obtained from the classical expression of the interaction of a system with an external time varying electromagnetic field. The representation of the classical Hamiltonian for interaction of n charge particles among them and with an external electromagnetic field is [28]:

$$\mathcal{H}=\sum_{i=1}^{n}\frac{1}{2m_i}\left[\mathbf{p}_i-q_i\mathbf{A}\left(\mathbf{r}_i,t\right)\right]^2+\sum_{i=1}^{n}\sum_{j>i}^{n}\frac{1}{4\pi\varepsilon_0}\frac{q_iq_j}{\left|\mathbf{r}_i-\mathbf{r}_j\right|}+\sum_{i=1}^{n}q_i\phi\left(\mathbf{r}_i,t\right) \tag{1.1.2}$$

where $\mathbf{p}_i$ and $\mathbf{r}_i$ are the momentum and position vectors of the particle i, m_i and q_i are the mass and the electric charge of the particle i. $\mathbf{A}\left(\mathbf{r}_i,t\right)$ and $\phi\left(\mathbf{r}_i,t\right)$ are the vector and scalar potentials of the electromagnetic field, as defined in appendix A. In equation 1.1.2, the first term corresponds to the kinetic energies of the particles in presence of the electromagnetic field, the second term is the Coulomb interaction between the particles and the third term is the interaction potential with the electromagnetic field.

The quantum Hamiltonian operator, $\widehat{H}\left(t\right)$, for the interaction between any system of charge particles with an external electromagnetic field, can be obtained by substituting the definition of the position vector, $\mathbf{r}_i$, and momentum vector, $\mathbf{p}_i$, with their corresponding operators in the position representation:

$$\widehat{H}\left(t\right)=\sum_{i=1}^{n}\frac{1}{2m_i}\left[i\hbar\nabla_i-q_i\mathbf{A}\left(\mathbf{r}_i,t\right)\right]^2+\sum_{i=1}^{n}\sum_{j>i}^{n}\frac{1}{4\pi\varepsilon_0}\frac{q_iq_j}{\left|\mathbf{r}_i-\mathbf{r}_j\right|}+\sum_{i=1}^{n}q_i\phi\left(\mathbf{r}_i,t\right) \tag{1.1.3}$$

where ∇_i is the gradient of the particle i and $\hbar$ is the reduced Planck constant. Expanding the square of the kinetic energy term in equation 1.1.3, the Hamiltonian operator, $\widehat{H}\left(t\right)$, becomes:

$$\begin{aligned}\widehat{H}\left(t\right)=&-\sum_{i=1}^{n}\frac{\hbar^2}{2m_i}\nabla_i^2+\sum_{i=1}^{n}\frac{q_i^2}{2m_i}\mathbf{A}\left(\mathbf{r}_i,t\right)^2-i\sum_{i=1}^{n}\frac{q_i\hbar}{2m_i}\left[\nabla_i\cdot\mathbf{A}\left(\mathbf{r}_i,t\right)\right]-\\&-2i\sum_{i=1}^{n}\frac{q_i\hbar}{2m_i}\mathbf{A}\left(\mathbf{r}_i,t\right)\cdot\nabla_i+\sum_{i=1}^{n}\sum_{j>i}^{n}\frac{1}{4\pi\varepsilon_0}\frac{q_iq_j}{\left|\mathbf{r}_i-\mathbf{r}_j\right|}+\sum_{i=1}^{n}q_i\phi\left(\mathbf{r}_i,t\right)\end{aligned} \tag{1.1.4}$$

The first and fifth terms, in the above expression, are the kinetic energy and the Coulomb interaction potential of the charge particles. Both terms contain only information of the isolated system and constitute the Hamiltonian operator

of the field-free system, $\widehat{H}_0$. On the other hand, the other terms describe the interaction potential between the charge particles and the electromagnetic field, and can be represented by an external interaction potential, $\widehat{V}(t)$, which varies in time. The Hamiltonian operator, $\widehat{H}(t)$, can be written as the sum of the field-free Hamiltonian operator, $\widehat{H}_0$, plus the external interaction potential, $\widehat{V}(t)$:

$$\widehat{H}(t) = \widehat{H}_0 + \widehat{V}(t) \tag{1.1.5}$$

where, $\widehat{H}_0$ is:

$$\widehat{H}_0 = -\sum_{i=1}^{n} \frac{\hbar^2}{2m_i}\nabla_i^2 + \sum_{i=1}^{n}\sum_{j>i}^{n} \frac{1}{4\pi\varepsilon_0}\frac{q_i q_j}{|\mathbf{r}_i - \mathbf{r}_j|} \tag{1.1.6}$$

and $\widehat{V}(t)$ is:

$$\widehat{V}(t) = \sum_{i=1}^{n} \frac{q_i^2}{2m_i}\mathbf{A}(\mathbf{r}_i,t)^2 - i\sum_{i=1}^{n}\frac{q_i\hbar}{2m_i}\left[\nabla_i \cdot \mathbf{A}(\mathbf{r}_i,t)\right] - 2i\sum_{i=1}^{n}\frac{q_i\hbar}{2m_i}\mathbf{A}(\mathbf{r}_i,t)\cdot\nabla_i + \\ + \sum_{i=1}^{n} q_i\phi(\mathbf{r}_i,t) \tag{1.1.7}$$

The first step in a general spectral method is the solution of the TDSE for the system without the interaction with the external electromagnetic field:

$$i\hbar\frac{\partial}{\partial t}\Psi_n^0(\mathbf{r},t;\varepsilon) = \widehat{H}_0\Psi_n^0(\mathbf{r},t;\varepsilon) \tag{1.1.8}$$

where $\Psi_n^0(\mathbf{r},t;\varepsilon)$ are the time dependent wavefunctions of the field-free system. $\Psi_n^0(\mathbf{r},t;\varepsilon)$ depends on two quantum numbers, the discrete quantum number n and the continuous ε. Because, the field-free Hamiltonian operator, $\widehat{H}_0$, is time independent, the time dependent wavefunctions of the field-free system, $\Psi_n^0(\mathbf{r},t;\varepsilon)$, can be expressed as:

$$\Psi_n^0(\mathbf{r},t;\varepsilon) = \psi_n(\mathbf{r};\varepsilon)\,\Phi_n(t;\varepsilon) \tag{1.1.9}$$

The substitution of the above expression for $\Psi_n^0(\mathbf{r},t;\varepsilon)$ in equation 1.1.8, gives that $\Phi_n(t;\varepsilon)$ is a stationary phase, which depends on the energy of the field-free system, $E_n(\varepsilon)$, and the time:

$$\Phi_n(t;\varepsilon) = e^{\left(-i\frac{E_n(\varepsilon)}{\hbar}t\right)} \tag{1.1.10}$$

and the time independent (stationary) wavefunctions, $\psi_n(\mathbf{r};\varepsilon)$, are the eigenfunctions of the time independent Schrödinger equation:

$$\widehat{H}_0\psi_n(\mathbf{r};\varepsilon) = E_n(\varepsilon)\,\psi_n(\mathbf{r};\varepsilon) \tag{1.1.11}$$

These wavefunctions and energies depend on quantum parameters which determine a state of the system. These quantum number can be discrete or continuum. For a more complete description of the TDSE solution, we consider that our field-free system is described by wavefunctions and energies, $\psi_n(\mathbf{r};\varepsilon)$ and $E_n(\varepsilon)$, which depend on both discrete and continuum quantum parameters, symbolized by n and ε, respectively.

The total time dependent wavefunction solution of equation 1.1.1, $\Psi(\mathbf{r},t)$, is expanded as a linear combination of the stationary wavefunctions, $\psi_n(\mathbf{r};\varepsilon)$, with their respective stationary phases, $\exp[-iE_n(\varepsilon)t/\hbar]$:

$$\Psi(\mathbf{r},t) = \sum_n \int_\varepsilon c_n(t;\varepsilon)\,\psi_n(\mathbf{r};\varepsilon)\,e^{\left[-i\frac{E_n(\varepsilon)}{\hbar}t\right]}d\varepsilon \tag{1.1.12}$$

where $c_n(t;\varepsilon)$ are the time dependent coefficients which determine the contribution of each stationary state to the total time dependent wavefunction, $\Psi(\mathbf{r},t)$.

Substitution the above equation in equation 1.1.1, the TDSE is given by:

$$\begin{aligned} i\hbar\frac{\partial}{\partial t}\sum_n \int_\varepsilon c_n(t;\varepsilon)\,\psi_n(\mathbf{r};\varepsilon)\,e^{\left[-i\frac{E_n(\varepsilon)}{\hbar}t\right]}d\varepsilon = \\ = \left[\widehat{H}_0 + \widehat{V}(t)\right]\sum_n \int_\varepsilon c_n(t;\varepsilon)\,\psi_n(\mathbf{r};\varepsilon)\,e^{\left[-i\frac{E_n(\varepsilon)}{\hbar}t\right]}d\varepsilon \end{aligned} \tag{1.1.13}$$

where $\widehat{H}(t)$ is substituted by the sum of $\widehat{H}_0$ and $\widehat{V}(t)$. Using the identity in equation 1.1.8, the TDSE can be written as:

$$\begin{aligned} i\hbar\sum_n \int_\varepsilon \frac{\partial c_n(t;\varepsilon)}{\partial t}\psi_n(\mathbf{r};\varepsilon)\,e^{\left[-i\frac{E_n(\varepsilon)}{\hbar}t\right]}d\varepsilon = \\ = \sum_n \int_\varepsilon c_n(t;\varepsilon)\,\widehat{V}(t)\,\psi_n(\mathbf{r};\varepsilon)\,e^{\left[-i\frac{E_n(\varepsilon)}{\hbar}t\right]}d\varepsilon \end{aligned} \tag{1.1.14}$$

where the unknown variables are the coefficients $c_n(t;\varepsilon)$. To obtain these coefficients, we project into both sides of the above equation the complex conjugate wavefunction, $\overline{\psi}_{n'}(\mathbf{r};\varepsilon')\exp[-iE_{n'}(\varepsilon')t/\hbar]$:

$$\begin{aligned} i\hbar\sum_n \int_\varepsilon \frac{\partial c_n(t;\varepsilon)}{\partial t}\int_{S(\mathbf{r})} \overline{\psi}_{n'}(\mathbf{r};\varepsilon')\,\psi_n(\mathbf{r};\varepsilon)\,d^3\mathbf{r}e^{\left[i\frac{E_{n'}(\varepsilon')-E_n(\varepsilon)}{\hbar}t\right]}d\varepsilon = \\ = \sum_n \int_\varepsilon c_n(t;\varepsilon)\int_{S(\mathbf{r})} \overline{\psi}_{n'}(\mathbf{r};\varepsilon')\,\widehat{V}(t)\,\psi_n(\mathbf{r};\varepsilon)\,d^3\mathbf{r}e^{\left[i\frac{E_{n'}(\varepsilon')-E_n(\varepsilon)}{\hbar}t\right]}d\varepsilon \end{aligned} \tag{1.1.15}$$

where $S(\mathbf{r})$ indicates that integral is over the three components of the position vector, each of them from $-\infty$ to ∞.

On the other hand, we know that the normalized eigenfunctions of any hermitician operator are orthonormal. As the $\widehat{H}_0$ satisfies the hermitician properties,

its wavefunctions are orthonormal between them and therefore they satisfy the relations:

$$\int_{S(\mathbf{r})} \overline{\psi}_{n'}\left(\mathbf{r};\varepsilon'\right)\psi_n\left(\mathbf{r};\varepsilon\right)d^3\mathbf{r} = \delta_{n,n'}\delta\left(\varepsilon-\varepsilon'\right) \tag{1.1.16}$$

where $\delta_{n,n'}$ is the Kronecker's delta and $\delta\left(\varepsilon-\varepsilon'\right)$ is the Dirac's delta [117]. Consequently, introducing this orthonormal relation in equation 1.1.15, it can be rewritten as a linear set of first order differential equations:

$$\frac{\partial c_{n'}\left(t;\varepsilon'\right)}{\partial t} = -\frac{i}{\hbar}\sum_n \int_\varepsilon c_n\left(t;\varepsilon\right)\int_{S(\mathbf{r})} \overline{\psi}_{n'}\left(\mathbf{r};\varepsilon'\right)\widehat{V}\left(t\right)\psi_n\left(\mathbf{r};\varepsilon\right)d^3\mathbf{r}e^{\left[i\frac{E_{n'}(\varepsilon')-E_n(\varepsilon)}{\hbar}t\right]}d\varepsilon \tag{1.1.17}$$

The solutions of this set of differential linear equations give the time dependent coefficients, $c_n\left(t;\varepsilon\right)$, which determine the time evolution of the system.

The interaction potential, $\widehat{V}\left(t\right)$, given in equation 1.1.7, depends on two physical magnitudes, the vector potential, $\mathbf{A}\left(\mathbf{r}_i,t\right)$, and the scalar potential, $\phi\left(\mathbf{r}_i,t\right)$, which describe the time and spatial evolution of the electromagnetic field. They are the solutions of the Maxwell's equations presented in appendix A and are associated with the electric field vector, $\mathbf{E}\left(\mathbf{r},t\right)$, and magnetic field vector, $\mathbf{B}\left(\mathbf{r},t\right)$, by the equations:

$$\mathbf{E}\left(\mathbf{r},t\right) = -\nabla\phi\left(\mathbf{r},t\right) - \frac{\partial\mathbf{A}\left(\mathbf{r},t\right)}{\partial t} \tag{1.1.18}$$

$$\mathbf{B}\left(\mathbf{r},t\right) = -\nabla\times\mathbf{A}\left(\mathbf{r},t\right) \tag{1.1.19}$$

The continuous radiation and the pulses can be described as electromagnetic waves, electromagnetic fields which freely propagate in the space. This free propagation indicates that the electromagnetic waves do not have internal charges, and consequently, the electric density, $\rho\left(\mathbf{r},t\right)$, and the current density vector, $\mathbf{J}\left(\mathbf{r},t\right)$, are zero. These properties of the electromagnetic waves simplify Maxwell's equations in terms of the vector potential, $\mathbf{A}\left(\mathbf{r}_i,t\right)$, and the scalar potential, $\phi\left(\mathbf{r}_i,t\right)$. The absence of any electric density, $\rho\left(\mathbf{r},t\right)$, and current density vector, $\mathbf{J}\left(\mathbf{r},t\right)$, simplify the Maxwell's equations A.0.13 and A.0.14 in:

$$-\nabla^2\phi\left(\mathbf{r},t\right) = \nabla\cdot\frac{\partial\mathbf{A}\left(\mathbf{r},t\right)}{\partial t} \tag{1.1.20}$$

$$\nabla^2\mathbf{A}\left(\mathbf{r},t\right) - \nabla\cdot\left[\nabla\cdot\mathbf{A}\left(\mathbf{r},t\right)\right] = \mu_0\varepsilon_0\left[\frac{\partial\nabla\phi\left(\mathbf{r},t\right)}{\partial t} + \frac{\partial^2\mathbf{A}\left(\mathbf{r},t\right)}{\partial t^2}\right] \tag{1.1.21}$$

On the other hand, the vector potential, $\mathbf{A}\left(\mathbf{r}_i,t\right)$, and the scalar potential, $\phi\left(\mathbf{r}_i,t\right)$, introduce an indeterminacy in the description of the electromagnetic field, which does not appear when the electromagnetic fields are described by the electric field vector, $\mathbf{E}\left(\mathbf{r},t\right)$, and the magnetic field vector, $\mathbf{B}\left(\mathbf{r},t\right)$. To fix this

indeterminacy, it is necessary to introduce a boundary condition, called gauge, which transforms the vector potential, $\mathbf{A}(\mathbf{r}_i, t)$, and the scalar potential, $\phi(\mathbf{r}_i, t)$, into a new vector potential, $\mathbf{A}'(\mathbf{r}_i, t)$, and a new scalar potential, $\phi'(\mathbf{r}_i, t)$:

$$\mathbf{A}'(\mathbf{r}, t) = \mathbf{A}(\mathbf{r}, t) + \nabla\lambda(\mathbf{r}, t) \tag{1.1.22}$$

$$\phi'(\mathbf{r}, t) = \phi(\mathbf{r}, t) - \frac{\partial\lambda(\mathbf{r}, t)}{\partial t} \tag{1.1.23}$$

There are several gauge transformations of the vector and scalar potentials, $\mathbf{A}(\mathbf{r}, t)$ and $\phi(\mathbf{r}, t)$, which simplify equations 1.1.20 and 1.1.21 and their solutions. One of them is the Coulomb gauge, whose definition is that the divergence of the vector potential, $\mathbf{A}(\mathbf{r}, t)$, is equal to zero:

$$\nabla \cdot \mathbf{A}(\mathbf{r}, t) = 0 \tag{1.1.24}$$

Consequently, introducing the Coulomb gauge definition in equations 1.1.20 and 1.1.21, the modified Maxwell's equations are:

$$\nabla^2\phi(\mathbf{r}, t) = 0 \tag{1.1.25}$$

$$\nabla^2\mathbf{A}(\mathbf{r}, t) = \mu_0\varepsilon_0\left[\frac{\partial\nabla\phi(\mathbf{r}, t)}{\partial t} + \frac{\partial^2\mathbf{A}(\mathbf{r}, t)}{\partial t^2}\right] \tag{1.1.26}$$

Equation 1.1.25 is the well-known Laplace equation [17]. The unique solution of the Laplace equation, which is regular in all space, is a function equal to zero for every point of the spatial and time domains. Therefore, as the scalar potential, $\phi(\mathbf{r}, t)$, has to be a regular function in all space and satisfies the Laplacian equation, the scalar potential, $\phi(\mathbf{r}, t)$, has to be equal to zero:

$$\phi(\mathbf{r}, t) = 0 \tag{1.1.27}$$

And from equation 1.1.26, it is obtained that the Maxwell's equation, whose solutions determine the evolution of any electromagnetic wave, is:

$$\nabla^2\mathbf{A}(\mathbf{r}, t) = \mu_0\varepsilon_0\frac{\partial^2\mathbf{A}(\mathbf{r}, t)}{\partial t^2} \tag{1.1.28}$$

Equation 1.1.28 is called the wave equation and its solutions give the vector potential, $\mathbf{A}(\mathbf{r}, t)$. In the present work, we restrict our description to linearly polarized electromagnetic fields, so the vector potential, $\mathbf{A}(\mathbf{r}, t)$, can be expressed as a combination of a scalar function, which is the vector potential in the polarization direction, $A(\mathbf{r}, t)$, multiplied by the polarization vector, $\mathbf{u}_A$:

$$\mathbf{A}(\mathbf{r}, t) = A(\mathbf{r}, t)\,\mathbf{u}_A \tag{1.1.29}$$

Because the polarization vector, $\mathbf{u}_A$, does not depend on the position vector, $\mathbf{r}$, nor on time, t, the wave equation 1.1.28, can be written only in terms of the vector potential in the polarization direction, $A(\mathbf{r},t)$:

$$\nabla^2 A(\mathbf{r},t) = \mu_0\varepsilon_0 \frac{\partial^2 A(\mathbf{r},t)}{\partial t^2} \tag{1.1.30}$$

To solve the wave equation, the vector potential in the polarization direction can be expressed as the inverse Fourier-Laplace transform of a function, $A(\mathbf{k},\omega)$, where $\mathbf{k}$ is the wavevector and the ω is the frequency of the electromagnetic field [124]:

$$\begin{aligned} A(\mathbf{r},t) = \frac{1}{(2\pi)^2}\Bigg[\int_{-\infty}^{\infty}\int_{S(\mathbf{k})} A(\mathbf{k},\omega)\, e^{[i(\mathbf{k}\cdot\mathbf{r}+\omega t)]} d^3\mathbf{k}d\omega + \\ + \int_{-\infty}^{\infty}\int_{S(\mathbf{k})} \overline{A}(\mathbf{k},\omega)\, e^{[-i(\mathbf{k}\cdot\mathbf{r}+\omega t)]} d^3\mathbf{k}d\omega\Bigg] \end{aligned} \tag{1.1.31}$$

The normalization factor $1/(2\pi)^2$ comes from the definition of the Fourier-Laplace transform. Because the vector potential is a physical magnitude whose values have to be real and the inverse Fourier-Laplace transform gives complex functions, the vector potential is equal to the inverse Fourier transform of the function $A(\mathbf{k},\omega)$ plus its complex conjugate. The above expression satisfies the wave equation when $\mathbf{k}$ and the ω are associated through the velocity propagation of the field, which is the speed of light in vacuum, $c = 1/\sqrt{\mu_0\varepsilon_0}$:

$$|\mathbf{k}| = \sqrt{\mu_0\varepsilon_0}\omega = \frac{\omega}{c} \tag{1.1.32}$$

The function $A(\mathbf{k},\omega)$ can be centered in the wavevector $\mathbf{k}_0$ and frequency ω_0, expressing as $A(\mathbf{k}-\mathbf{k}_0, \omega-\omega_0)$. Making the transformation of integration variables, equation 1.1.31 becomes:

$$\begin{aligned} A(\mathbf{r},t) = \frac{1}{(2\pi)^2}\Bigg[e^{[i(\mathbf{k}_0\cdot\mathbf{r}+\omega_0 t)]}\int_{-\infty}^{\infty}\int_{S(\mathbf{k})} A(\mathbf{k},\omega)\, e^{[i(\mathbf{k}\cdot\mathbf{r}+\omega t)]} d^3\mathbf{k}d\omega + \\ + e^{[-i(\mathbf{k}_0\cdot\mathbf{r}+\omega_0 t)]}\int_{-\infty}^{\infty}\int_{S(\mathbf{k})} \overline{A}(\mathbf{k},\omega)\, e^{[-i(\mathbf{k}\cdot\mathbf{r}+\omega t)]} d^3\mathbf{k}d\omega\Bigg] \end{aligned} \tag{1.1.33}$$

where the plane waves $\exp[\pm i(\mathbf{k}_0\cdot\mathbf{r}+\omega_0 t)]$ are traveling waves, which oscillate in the spatial and time dimensions, and can be converted into trigonometric functions using the Euler's formula [117]. In addition, the $A(\mathbf{k},\omega)$ function can be expressed as $A(\mathbf{k},\omega) = A_0 F(\mathbf{k},\omega)\exp(i\varphi)/2i$, where A_0 is a real factor, $\exp(i\varphi)$ is an arbitrary phase and $F(\mathbf{k},\omega)$ is a real and symmetric distribution function, valid for the electromagnetic waves treated. Applying these expressions, the above expression is written as:

$$A(\mathbf{r},t) = A_0\frac{1}{(2\pi)^2}\int_{-\infty}^{\infty}\int_{S(\mathbf{k})} F(\mathbf{k},\omega)\, e^{[i(\mathbf{k}\cdot\mathbf{r}+\omega t)]} d^3\mathbf{k}d\omega \sin(\mathbf{k}_0\cdot\mathbf{r}+\omega_0 t+\varphi) \tag{1.1.34}$$

The continuous electromagnetic waves have a well-defined wavevector, $\mathbf{k}_0$, and frequency, ω_0, and consequently, the distribution function $F(\mathbf{k},\omega)$ is equal to the Dirac delta function, $\delta(\mathbf{k}-\mathbf{k}_0)\,\delta(\omega-\omega_0)$, for both variables. Applying this distribution function for the continuous electromagnetic waves, the vector potential in the polarization direction, $A(\mathbf{r},t)$, is:

$$A(\mathbf{r},t) = A_0 \sin(\mathbf{k}_0\cdot\mathbf{r}+\omega_0 t+\varphi) \tag{1.1.35}$$

and the vector potential, $\mathbf{A}(\mathbf{r},t)$:

$$\mathbf{A}(\mathbf{r},t) = A_0 \sin(\mathbf{k}_0\cdot\mathbf{r}+\omega_0 t+\varphi)\,\mathbf{u}_A \tag{1.1.36}$$

where A_0 is the amplitude of the vector potential and φ is an arbitrary phase. For more complex electromagnetic fields, as the pulses, the distribution function, $F(\mathbf{k},\omega)$, can take other expressions. In addition, the inverse Fourier transform of the distribution function can be expressed in terms of its complementary function in the position and time domains, $f(\mathbf{r},t)$, [125] given a general expression for the vector potential:

$$\mathbf{A}(\mathbf{r},t) = A_0 f(\mathbf{r},t) \sin(\mathbf{k}_0\cdot\mathbf{r}+\omega_0 t+\varphi)\,\mathbf{u}_A \tag{1.1.37}$$

1.1.1 Dipole approximation

The expression for the vector potential, $\mathbf{A}(\mathbf{r},t)$, of the continuous electromagnetic waves in equation 1.1.36, can be written in complex exponential form using the Euler's formula:

$$\mathbf{A}(\mathbf{r},t) = \frac{A_0}{2i}\left\{e^{[i(\mathbf{k}_0\cdot\mathbf{r}+\omega_0 t+\varphi)]} - e^{[-i(\mathbf{k}_0\cdot\mathbf{r}+\omega_0 t+\varphi)]}\right\}\mathbf{u}_A \tag{1.1.38}$$

In the above the equation, both imaginary exponential terms can be expanded in Taylor's series as a function of the position vector:

$$\begin{aligned} e^{[\pm i(\mathbf{k}_0\cdot\mathbf{r}+\omega_0 t+\varphi)]} &= e^{[\pm i(\omega_0 t+\varphi)]}\sum_{n=0}^{\infty}(\pm 1)^n\frac{(i\mathbf{k}_0\cdot\mathbf{r})^n}{n!} = \\ &= e^{[\pm i(\omega_0 t+\varphi)]}\left\{1 \pm i\mathbf{k}_0\cdot\mathbf{r} - \frac{(i\mathbf{k}_0\cdot\mathbf{r})^2}{2} \pm \cdots\right\} \end{aligned} \tag{1.1.39}$$

When the wavelength, $|\lambda|$, of the electromagnetic wave used is larger than the size of the system, the following relation is satisfied:

$$\mathbf{k}_0\cdot\mathbf{r} \simeq \frac{2\pi a_0}{|\lambda|} \ll 1 \tag{1.1.40}$$

and, the imaginary exponential can be considered equal to one:

$$e^{[\pm i\mathbf{k}_0\cdot\mathbf{r}]} \simeq 1 \tag{1.1.41}$$

Thus, the vector potential, $\mathbf{A}(t)$, can be written as:

$$\begin{aligned} \mathbf{A}(t) &= \frac{A_0}{2i}\left\{e^{[i(\omega_0 t+\varphi)]} - e^{[-i(\omega_0 t+\varphi)]}\right\}\mathbf{u}_A \\ \mathbf{A}(t) &= A_0 \sin(\omega_0 t+\varphi)\,\mathbf{u}_A \end{aligned} \tag{1.1.42}$$

which is the dipole approximation. Consequently, equation 1.1.42 indicates that the vector potential of a continuous electromagnetic wave in the dipole approximation, $\mathbf{A}(t)$, does not depend on the position vector, $\mathbf{r}$, being a function only of the time, t.

The expression of the external potential operator, $\widehat{V}(t)$, given in equation 1.1.7, can be now simplified by the use of the dipole approximation. The second term, $\nabla_i \cdot \mathbf{A}(\mathbf{r}_i, t)$, is equal to zero, and the external potential operator, $\widehat{V}(t)$, can be written as:

$$\widehat{V}(t) = \sum_{i=1}^{n} \frac{q_i^2}{2m_i}\mathbf{A}(t)^2 - 2i\sum_{i=1}^{n}\frac{q_i\hbar}{2m_i}\mathbf{A}(t)\cdot\nabla_i + \sum_{i=1}^{n} q_i\phi(\mathbf{r}_i, t) \tag{1.1.43}$$

1.1.2 Gauge transformations

The expression of the Hamiltonian operator , $\widehat{H}(t)$, can be simplified selecting a convenient gauge, fixing the indeterminacy introduced by the vector potential, $\mathbf{A}(\mathbf{r}_i, t)$, and the scalar potential, $\phi(\mathbf{r}_i, t)$. This gauge transformation modifies the expressions for the vector potential, $\mathbf{A}(\mathbf{r}_i, t)$, and the scalar potential, $\phi(\mathbf{r}_i, t)$. Therefore, the Hamiltonian operator, $\widehat{H}(t)$, which is not invariant with the gauge transformation, is modified. However, as it is demonstrated in [118], the physics described by the TDSE remains unchanged. The gauge transformation only adds a relative phase to the original time dependent wavefunction,$\Psi(\mathbf{r}_i, t)$, keeping the physical description given by this time dependent wavefunction. The gauge transformation gives that the vector potential, $\mathbf{A}(t)$, scalar potential, $\phi(\mathbf{r}_i, t)$, and the wavefunction of the Hamiltonian operator, $\Psi(\mathbf{r}_i, t)$ are:

$$\mathbf{A}'(t) = \mathbf{A}(t) + \nabla_i\lambda(\mathbf{r}_i, t) \tag{1.1.44}$$

$$\phi'(\mathbf{r}_i, t) = \phi(\mathbf{r}_i, t) - \frac{\partial\lambda(\mathbf{r}_i, t)}{\partial t} \tag{1.1.45}$$

$$\Psi'(\mathbf{r}_i, t) = \Psi(\mathbf{r}_i, t)\, e^{\left[-\frac{i}{\hbar}\sum_{i=1}^{n} q_i\lambda(\mathbf{r}_i, t)\right]} \tag{1.1.46}$$

where $\lambda(\mathbf{r}_i, t)$ is an arbitrary scalar function. The expression given by the equation 1.1.44 for the gauge transformation of the vector potential is obtained within the dipole approximation. Two gauge transformations are commonly used in light-matter interaction problems: velocity and length gauge.

1.1.2.1 Velocity gauge

The scalar function, $\lambda(\mathbf{r}_i, t)$, in the velocity gauge transformation is expressed as:

$$\lambda(\mathbf{r}_i, t) = \lambda(t) = \frac{q_i}{2m_i} \int_{-\infty}^{t} \mathbf{A}(t')^2 \, dt' \tag{1.1.47}$$

Using this scalar function in the velocity gauge, equations 1.1.44, 1.1.45 and 1.1.46 become:

$$\mathbf{A}'(t) = \mathbf{A}(t) + \frac{q_i}{2m_i} \int_{-\infty}^{t} \nabla_i \left[\mathbf{A}(t')^2\right] dt' \tag{1.1.48}$$

$$\phi'(\mathbf{r}_i, t) = \phi(\mathbf{r}_i, t) - \frac{q_i}{2m_i} \frac{\partial \int_{-\infty}^{t} \mathbf{A}(t')^2 \, dt'}{\partial t} \tag{1.1.49}$$

$$\Psi'(\mathbf{r}_i, t) = \Psi(\mathbf{r}_i, t) \, e^{\left[i \sum_{i=1}^{n} \frac{q_i^2}{2m_i \hbar} \int_{-\infty}^{t} \mathbf{A}(t')^2 dt'\right]} \tag{1.1.50}$$

Assuming the dipole approximation, the vector potential, $\mathbf{A}(t)$, does not depend on the position vector, $\mathbf{r}_i$. Consequently, the gradient of the vector potential square has to be zero, $\nabla_i \left[\mathbf{A}(t')^2\right] = \mathbf{0}$. Moreover, in the second equation, the integral of the derivative of any function is equal to the function itself. Therefore, it is obtained:

$$\mathbf{A}'(t) = \mathbf{A}(t) \tag{1.1.51}$$

$$\phi'(\mathbf{r}_i, t) = \phi(\mathbf{r}_i, t) - \frac{q_i}{2m_i} \mathbf{A}(t)^2 \tag{1.1.52}$$

$$\Psi'(\mathbf{r}_i, t) = \Psi(\mathbf{r}_i, t) \, e^{\left[i \sum_{i=1}^{n} \frac{q_i^2}{2m_i \hbar} \int_{-\infty}^{t} \mathbf{A}(t')^2 dt'\right]} \tag{1.1.53}$$

Substituting the equations 1.1.51 and 1.1.53 in equation 1.1.43, the external potential operator, $\widehat{V}(t)$, for the interaction between any charge particles system and an external electromagnetic field in the dipole approximation with the velocity gauge is:

$$\widehat{V}(t) = -i \sum_{i=1}^{n} \frac{q_i \hbar}{m_i} \mathbf{A}(t) \cdot \nabla_i + \sum_{i=1}^{n} q_i \phi(\mathbf{r}_i, t) \tag{1.1.54}$$

where we can apply a further simplification, through the Coulomb gauge, in which the scalar potential, $\phi(\mathbf{r}_i, t)$, is zero for all spatial and time domains. Thus, scalar potential term, $\sum_{i=1}^{n} q_i \phi(\mathbf{r}_i, t)$, is equal to zero, leading to:

$$\widehat{V}(t) = -i \sum_{i=1}^{n} \frac{q_i \hbar}{m_i} \mathbf{A}(t) \cdot \nabla_i \tag{1.1.55}$$

In summary, the total Hamiltonian operator, $\widehat{H}(t) = \widehat{H}_0 + \widehat{V}(t)$, becomes:

$$\begin{aligned}\widehat{H}(t) = -\sum_{i=1}^{n} \frac{\hbar^2}{2m_i}\nabla_i^2 + \sum_{i=1}^{n}\sum_{j>1}^{n} \frac{1}{4\pi\varepsilon_0}\frac{q_i q_j}{|\mathbf{r}_i - \mathbf{r}_j|} - \\ -i\sum_{i=1}^{n}\frac{q_i\hbar}{m_i}\mathbf{A}(t)\cdot\nabla_i\end{aligned} \tag{1.1.56}$$

1.1.2.2 Length gauge

The scalar function, $\lambda(\mathbf{r}_i, t)$, in the length gauge transformation is expressed as:

$$\lambda(\mathbf{r}_i, t) = -\mathbf{r}_i \cdot \mathbf{A}(t) \tag{1.1.57}$$

Using this scalar function in the length gauge, equations 1.1.44, 1.1.45 and 1.1.46 become:

$$\mathbf{A}'(t) = \mathbf{A}(t) - \nabla_i[\mathbf{r}_i \cdot \mathbf{A}(t)] \tag{1.1.58}$$

$$\phi'(\mathbf{r}_i, t) = \phi(\mathbf{r}_i, t) + \mathbf{r}_i \cdot \frac{\partial \mathbf{A}(t)}{\partial t} \tag{1.1.59}$$

$$\Psi'(\mathbf{r}_i, t) = \Psi(\mathbf{r}_i, t)\, e^{\left[\frac{i}{\hbar}\sum_{i=1}^{n} q_i \mathbf{r}_i \cdot \mathbf{A}(t)\right]} \tag{1.1.60}$$

From the first equation, the gradient of the scalar product of the position vector, $\mathbf{r}_i$, multiplied by the vector potential, $\mathbf{A}(t)$, [29] is:

$$\begin{aligned}\nabla_i[\mathbf{r}_i \cdot \mathbf{A}(t)] = [\mathbf{r}_i \cdot \nabla_i]\mathbf{A}(t) + [\mathbf{A}(t)\cdot\nabla_i]\mathbf{r}_i + \\ +\mathbf{r}_i \times [\nabla_i \times \mathbf{A}(t)] + \mathbf{A}(t) \times [\nabla_i \times \mathbf{r}_i]\end{aligned} \tag{1.1.61}$$

where only the second term survives, since the first and the third terms are zero within the dipole approximation, because $\mathbf{A}(t)$, does not depend on the vector position, $\mathbf{r}_i$, and consequently the rotational and the divergence of the vector potential is zero, $\nabla_i \times \mathbf{A}(t) = \mathbf{0}$ and $\nabla_i \cdot \mathbf{A}(t) = \mathbf{0}$, and the rotational of the position vector is also the zero vector, $\nabla_i \times \mathbf{r}_i = \mathbf{0}$. Because the second terms is equal to the vector potential, $[\mathbf{A}(t)\cdot\nabla_i]\mathbf{r}_i = \mathbf{A}(t)$, the gauge transformations are:

$$\mathbf{A}'(t) = \mathbf{0} \tag{1.1.62}$$

$$\phi'(\mathbf{r}_i, t) = \phi(\mathbf{r}_i, t) + \mathbf{r}_i \cdot \frac{\partial \mathbf{A}(t)}{\partial t} \tag{1.1.63}$$

$$\Psi'(\mathbf{r}_i, t) = \Psi(\mathbf{r}_i, t)\, e^{\left[\frac{i}{\hbar}\sum_{i=1}^{n} q_i \mathbf{r}_i \cdot \mathbf{A}(t)\right]} \tag{1.1.64}$$

Substituting the equations 1.1.62 and 1.1.64 in equation 1.1.43, and operating, the external potential operator, $\widehat{V}(t)$, for the interaction between any multiparticle

system and an external electromagnetic field in the dipole approximation with the length gauge is:

$$\widehat{V}(t) = \sum_{i=1}^{n} q_i \mathbf{r}_i \cdot \frac{\partial \mathbf{A}(t)}{\partial t} + \sum_{i=1}^{n} q_i \phi(\mathbf{r}_i, t) \tag{1.1.65}$$

where, as in the velocity gauge case, we used the Coulomb gauge, which makes the scalar potential, $\phi(\mathbf{r}_i, t)$, equal to zero. From equation 1.1.18, we have that the electric field vector, $\mathbf{E}(\mathbf{r}, t)$, within the Coulomb gauge is:

$$\mathbf{E}(t) = -\frac{d\mathbf{A}(t)}{dt} \tag{1.1.66}$$

Using both Coulomb and length gauges in equation 1.1.65, the external potential operator, $\widehat{V}(t)$, is simplified as:

$$\widehat{V}(t) = \sum_{i=1}^{n} q_i \mathbf{r}_i \cdot \frac{\partial \mathbf{A}(t)}{\partial t} = -\sum_{i=1}^{n} q_i \mathbf{r}_i \cdot \mathbf{E}(t) \tag{1.1.67}$$

In summary, the total Hamiltonian operator, $\widehat{H}(t) = \widehat{H}_0 + \widehat{V}(t)$, becomes:

$$\begin{aligned} \widehat{H}(t) = -\sum_{i=1}^{n} \frac{\hbar^2}{2m_i} \nabla_i^2 + \sum_{i=1}^{n} \sum_{j>1}^{n} \frac{1}{4\pi\varepsilon_0} \frac{q_i q_j}{|\mathbf{r}_i - \mathbf{r}_j|} + \\ + \sum_{i=1}^{n} q_i \mathbf{r}_i \cdot \frac{\partial \mathbf{A}(t)}{\partial t} \end{aligned} \tag{1.1.68}$$

Chapter 2

Ultrashort pulses

The advances in the techniques to generate ultrashort laser pulses, as the HHG and the XFEL, with energies in the XUV region and durations of the order of sub-femtoseconds ($1\,\mathrm{fs} = 10^{-15}\,\mathrm{s}$) and even attoseconds ($1\,\mathrm{as} = 10^{-15}\,\mathrm{s}$), make accessible the investigation of the fundamental processes in matter. Recently, the shortest duration, in the order to 80 as, was obtained using the well-known HHG technique [66, 149, 60]. These ultrashort durations are the perfect tool to explore, trace and even control the dynamics of electrons and fast nuclei in atoms and light molecules, which take place in similar timescales. The ultrashort pulses can be viewed as cameras which take "snapshots" of the electronic and nuclear motion, and therefore, a pulse duration shorter than the timescale of the dynamics explored is needed to resolve it. A complete description and characterization of the ultrashort pulses is fundamental to the theoretical investigation of the dynamics in atoms and molecules.

As discussed in chapter 1, our description of the laser-matter interaction is based on the semiclassical approximation, where the atomic or molecular system is treated by quantum mechanics and the external electromagnetic field by classical electrodynamics. Within classical electrodynamics, the ultrashort pulses are described by the Maxwell's equations (appendix A and chapter 1). Using the solutions of the Maxwell's equations, in the first section of this chapter we describe the pulses in both time and frequency domains. We start this section, presenting the mathematical expression of the vector potential for an isolated pulse and characterizing its most relevant parameters: the finite envelope function, the central frequency and the carrier envelope phase (CEP). In addition, we obtain the representation of the pulse in the frequency (energy) domain, using the well-known Fourier transform, and connect it to the spectral population distribution in our molecular target.

In order to obtain the time-resolved images of the electronic and fast nuclear motions, different experiments in attophysics presented protocols inspired in the infrared (IR) pump - IR probe schemes used in the femtochemistry to explore and trace the nuclear motion in the chemical reaction [187]. In these schemes, the IR pump pulse launches the dynamics and the probe pulse traces it as a function of the time delay between both pulses. The pump - probe schemes can combine two or more pulses, where due to the timescales of the electronic and fast

nuclear motion, the pump has durations of the order of as. This short duration is associated with broad bandwidth, populating a bunch of excited and ionic states of the system, which constitute a wavepacket. The evolution of this wavepacket after the pump is traced by the transition induced by the probe. To give a complete overview of these pump - probe schemes, in the second section of this chapter we discuss their mathematical expressions and their Fourier transforms, specially for the extreme ultraviolet (XUV) pump - IR probe and XUV pump - XUV probe schemes later used in realistic problems.

2.1 Mathematical definition of ultrashort pulses

The laser pulses are described as electromagnetic waves freely propagating in the space, whose spatial and time evolution is determined by their electric field vectors, $\mathbf{E}(\mathbf{r},t)$, and their magnetic field vectors, $\mathbf{B}(\mathbf{r},t)$. The expressions of these physical magnitudes for any electromagnetic field are given by the solutions of the Maxwell's equations, presented in appendix A, plus certain boundary conditions which define the electromagnetic field treated. As was introduced in chapter 1, the electromagnetic waves can be also described by other two physical magnitudes, the vector potential, $\mathbf{A}(\mathbf{r},t)$, and the scalar potential, $\phi(\mathbf{r},t)$, which are associated with the electric field vector, $\mathbf{E}(\mathbf{r},t)$, and the magnetic field vector, $\mathbf{B}(\mathbf{r},t)$. However, the use of these vector potential, $\mathbf{A}(\mathbf{r},t)$, and scalar potential, $\phi(\mathbf{r},t)$, introduce an indeterminacy in the solutions of the Maxwell's equations, which can be fixed by the use of a boundary condition, the gauge. As explained in previous chapter, introducing the Coulomb gauge ($\phi(\mathbf{r},t)=0$) and the velocity or length gauge within the dipole approximation ($\mathbf{A}(\mathbf{r},t)\simeq\mathbf{A}(t)$), the vector potential, $\mathbf{A}(t)$, for linearly polarized light is given by:

$$\mathbf{A}(t)=A_0 f(t)\sin(\omega_0 t+\varphi)\,\mathbf{u}_A \tag{2.1.1}$$

where A_0 is the amplitude of the vector potential, ω_0 is the central frequency of the pulse, φ is an arbitrary phase, called carrier envelope phase, CEP, and $f(t)$ is the shape or envelope function [125], that accounts for the finite duration of the laser pulse. Although, due to the election of the velocity gauge we work with the vector potential, $\mathbf{A}(t)$, which is associated with the electric field vector, $\mathbf{B}(t)$, using the Coulomb gauge and the dipole approximation, by the expression:

$$\mathbf{E}(t)=-\frac{\partial\mathbf{A}(t)}{\partial t} \tag{2.1.2}$$

Time envelopes

Several mathematical expressions can be used for this envelope function, $f(t)$, depending on the laser pulse that we want to theoretically describe [125]. The most widely used envelope functions are: the Gaussian and sine/cosine squared envelopes. First, focusing on the Gaussian type, its vector potential, $A(t)$, is:

$$A(t) = A_0 e^{\left[-\frac{(t-t_0)^2}{2\sigma^2}\right]} \sin\left[\omega_0 (t - t_0) + \varphi\right] \tag{2.1.3}$$

where t_0 is the time center and σ is the standard deviation of the Gaussian pulse [125, 25]. This σ can be defined in terms of the amplitude profile, $|A(t)|$, or the spectral profile, $|\mathcal{F}\{A(t)\}(\omega)|$. In both cases, the standard deviation of the Gaussian pulse is associated with the full width half maximum (FWHM), τ, of one of these profiles. Considering the amplitude profile, $|A(t)|$, the mathematical relation between σ and τ is [25]:

$$\sigma = \frac{\tau}{2\sqrt{2\ln(2)}} \tag{2.1.4}$$

In the left panel of figure 2.1.1, it is plotted the vector potential, $A(t)$, for a Gaussian envelope pulse with a FWHM of 0.8 fs, an energy of 28 eV and an intensity of $10^{12}\,\mathrm{W}\cdot\mathrm{cm}^{-2}$. The Gaussian function is only zero in the infinite range of time. This introduces numerical issues for the finite-time propagation used in our calculations, because the pulse never goes to zero in the integration time. However, the Fourier transform of the vector potential with the Gaussian envelope function gives a Gaussian function for the shape of its spectral representation, which satisfies the same property. This differs from the Fourier transform of the vector potential using a sine squared envelope which goes to zero at a certain values of frequency, as we will present in this chapter.

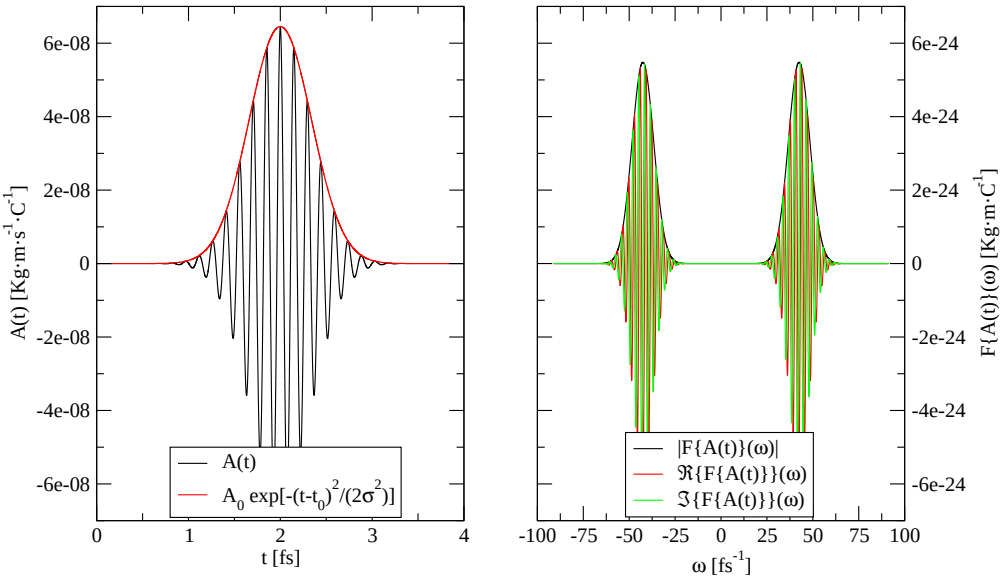

Figure 2.1.1: Left panel: Time representation of the vector potential in the polarization direction, $A(t)$, as a black line, and its Gaussian envelope function multiplied by the amplitude of the vector potential, $A_0 \exp\left[-(t-t_0)^2/(2\sigma^2)\right]$, as a red line. Right panel: Frequency representation of the same vector potential in the polarization direction. The pulse parameters are: $\tau = 0.8$ fs, $\omega_0 = 28$ eV and $I = 10^{12}\,\mathrm{W}\cdot\mathrm{cm}^{-2}$. The CEP, φ, is chosen to obtain the maximum of the vector potential in the center of the pulse ($\varphi = \pi/2$).

Using a sine squared envelope, the vector potential, $A(t)$, is defined as:

$$A(t) = \begin{cases} = A_0 \sin^2\left[\frac{\pi}{T}\left(t - t_0 - \frac{T}{2}\right)\right] \sin\left[\omega_0\left(t - t_0 - \frac{T}{2}\right) + \varphi\right] & t_0 \leq t \leq t_0 + T \\ = 0 & t_0 > t > t_0 + T \end{cases} \tag{2.1.5}$$

where T is the pulse duration, defined as the difference between the initial time, t_0, and final time, $t_0 + T$. The time $t - t_0 - T/2$ is selected to leave the CEP, φ, independent of the pulse frequency and duration. The factor π/T, which multiplies the difference time $t - t_0 - T/2$, in the sine square envelope function satisfies that this is defined as the positive half cycle of a complete oscillation between the initial , t_0, and final, $t_0 + T$, time points. In figure 2.1.2, it is plotted the vector potential in the polarization direction, $A(t)$, and the sine square function multiplied by amplitude of the vector potential, A_0, for a pulse with a duration of 2 fs, an energy of 28 eV and an intensity of $10^{12}\,\mathrm{W \cdot cm^{-2}}$ (corresponding to $2 \cdot 10^{-15}$ s, $4.2539 \cdot 10^{16}\,\mathrm{s^{-1}}$ and $10^{16}\,\mathrm{W \cdot m^{-2}}$ in SI units, respectively).

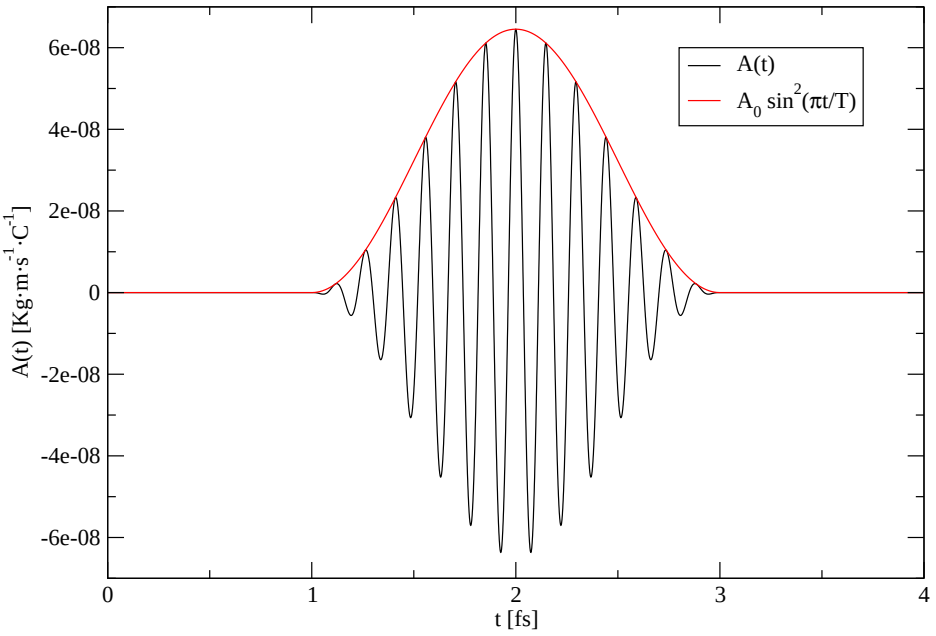

Figure 2.1.2: Time representation of the vector potential in the polarization direction, $A(t)$, as a black line, and its sine squared envelope function multiplied by the amplitude of the vector potential, $A_0 \sin^2(\pi(t - t_0)/T)$, as a red line. The pulse parameters are: $T = 2$ fs, $\omega_0 = 28$ eV and $I = 10^{12}\,\mathrm{W \cdot cm^{-2}}$. The CEP, φ, is chosen to obtain the maximum the vector potential in the center of the pulse ($\varphi = \pi/2$). The pulse starts at 1 fs of initial time, t_0, and finishes at 3 fs, which is equal to $t_0 + T$.

The intensity of the radiation, I, defined as the number of photons in a certain space area per unit of time, is often used to describe the electromagnetic waves. This intensity, I, can be obtained as the time-average value of the module of the Poynting vector, $\mathbf{S}(\mathbf{r}, t)$, which is defined as the directional energy flux density of the electromagnetic field. Using the Poynting theorem [71, 93, 64, 124],

the Poynting vector, $\mathbf{S}(\mathbf{r},t)$, is associated with the electric, $\mathbf{E}(\mathbf{r},t)$, and magnetic, $\mathbf{B}(\mathbf{r},t)$, field vectors by: $\mathbf{S}(\mathbf{r},t) = \mathbf{E}(\mathbf{r},t) \times \mathbf{B}(\mathbf{r},t)/\mu_0$. Since the electric, $\mathbf{E}(\mathbf{r},t)$, and magnetic, $\mathbf{B}(\mathbf{r},t)$, field vectors are associated through the Maxwell's equations, the Poynting vector, $\mathbf{S}(\mathbf{r},t)$, can be written in terms of only one of them. Consequently, the intensity, I, can be written in terms of the electric field vector, $\mathbf{E}(\mathbf{r},t)$, and within the Coulomb gauge, in terms of the vector potential, $\mathbf{A}(\mathbf{r},t)$, [25]:

$$I = \frac{c\varepsilon_0 E_0^2}{2} = \frac{c\varepsilon_0 \omega_0^2 A_0^2}{2} \tag{2.1.6}$$

In figure 2.1.2, it is clear that the envelope function modulates the vector potential, $A(t)$. However, the internal oscillations and the position of these oscillations with respect to the maximum of the vector potential is determined by the central frequency, ω_0, and the CEP. To give deeper comprehension of the pulse characteristics, it is necessary an analysis of these parameters.

Central frequency of the pulse

The most relevant pulse parameter is the central frequency, ω_0, of the pulse, which is defined as the number of full oscillations of the vector potential per unit of time. In figure 2.1.3, it is plotted the vector potential, $A(t)$, for two pulses with the same durations and intensities than the used in figure 2.1.2 (2 fs and $I = 10^{12}\,\mathrm{W}\cdot\mathrm{cm}^{-2}$), but with two different central frequencies: 14 eV ($2.1270 \cdot 10^{16}\,\mathrm{s}^{-1}$) and t 28 eV ($4.2539 \cdot 10^{16}\,\mathrm{s}^{-1}$). In this figure, we can appreciate that the amplitude of the vector potential changes when the frequency varies, fixing the intensity and pulse duration. This can be deduced from equation 2.1.6, where the amplitude of the vector potential, A_0, in terms of the intensity, I, and central frequency of the pulse, ω_0, is:

$$A_0 = \frac{1}{\omega_0}\sqrt{\frac{2I}{c\varepsilon_0}} \tag{2.1.7}$$

where the amplitude of the vector potential is directly proportional to the square root of the intensity and inversely proportional to the central frequency. However, the amplitude of the electric field vector, E_0, does not vary with the pulse frequency for a fixed intensity, as it satisfies the relation: $E_0 = A_0\omega_0$.

Because the envelope function confines the time range in which the pulse is non-zero, determining the maximum number of full oscillations, cycles, in the time domain, the pulses are usually defined using the number of laser optical cycles, n_{cycles}, i.e. the number of the full cycle per unit of time, n_{cycles}. This n_{cycles} is mathematically associated with the central frequency and the pulse duration by:

$$n_{cycles} = \frac{\omega_0}{2\pi}T \tag{2.1.8}$$

The advantage of using this parameter to define the pulses is that we can appreciate directly the limited number of full oscillations of the vector potential, and therefore, if the pulse can be considered within the perturbation regime.

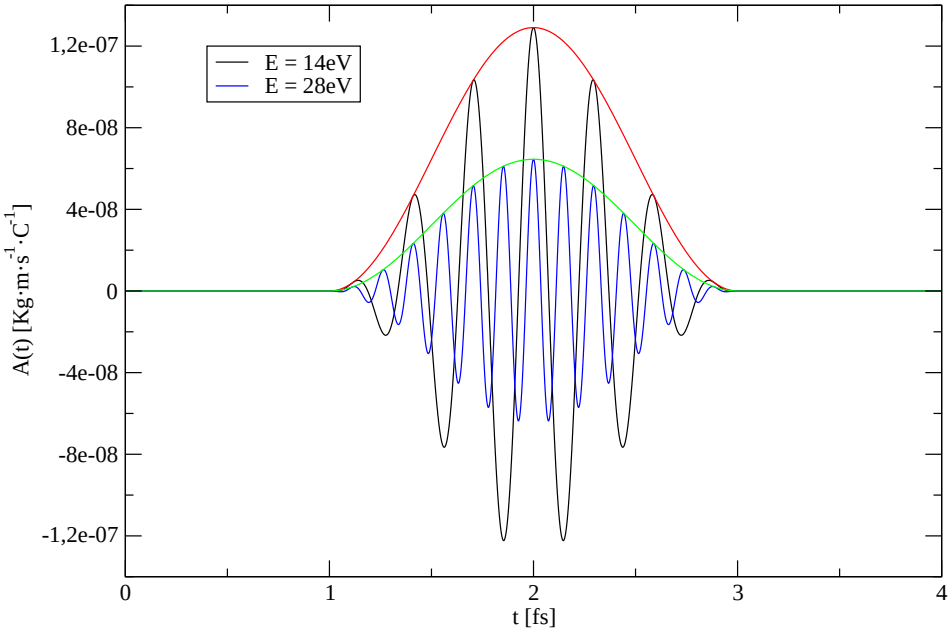

Figure 2.1.3: Vector potential and its sine squared envelope function for two pulses, with $\omega_0 = 14\,\text{eV}$ (black line) and $\omega_0 = 28\,\text{eV}$ (blue line). Both pulses have $T = 2\,\text{fs}$ and $I = 10^{12}\,\text{W}\cdot\text{cm}^{-2}$. In both cases, the CEP, φ, is chosen to give the maximum of the vector potential in the center of the pulse ($\varphi = \pi/2$).

Carrier envelope phase (CEP)

In all the previous examples, the vector potentials have a maximum in the center of the pulse. The position of the maximum of the vector potential with respect to the center of the envelope function is controlled by the carrier envelope phase (CEP), φ. This can be observed in figure 2.1.4, where two pulses are plotted, both with 2 fs of duration, 14 eV of energy and $10^{12}\,\text{W}\cdot\text{cm}^{-2}$ of intensity, but different CEP values: $\varphi = \pi/2$ and $\varphi = 0$. While the first CEP value makes that the vector potential has a positive maximum in the center of the pulse, the other CEP value produces that the vector potential has a minimum, i.e., both pulses have a phase difference of π.

We usually fix the CEP such that the maximum of the vector potential lies in the center of the pulse, assuring that the pulse reaches, in the center of the pulse, the maximum of the intensity. This value of the CEP can be obtained from equation 2.1.5, making the sine function in terms of the central frequency and CEP equal to one, at the time corresponding to the maximum of the envelope function, equal to $t = t_0 + T/2$ for a sine squared envelope:

$$\begin{aligned} \sin\left[\omega_0\left(t_0 + \frac{T}{2} - t_0 - \frac{T}{2}\right) + \varphi\right] &= \sin\left[\varphi\right] = 1 \\ \varphi &= \arcsin\left(1\right) = \frac{\pi}{2} \end{aligned} \tag{2.1.9}$$

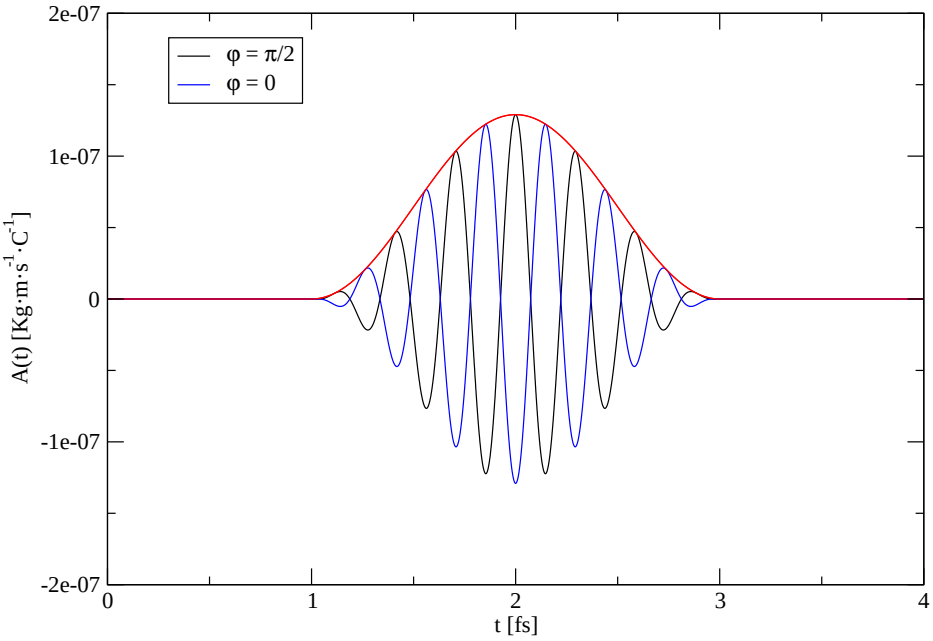

Figure 2.1.4: Vector potential representation with the sine square envelope function for two pulses with $T = 2\,\text{fs}$, $\omega_0 = 28\,\text{eV}$, $I = 10^{12}\,\text{W}\cdot\text{cm}^{-2}$ and different CEP, φ. The CEP is selected to give in the center of the pulse the positive maximum for the pulse, in the right panel, and the negative maximum of the vector potential, in the left panel. Thus, both pulses are the same but with a phase difference of π.

2.1.1 Frequency domain

For analysis purposes, it is convenient to plot the pulses in the frequency domain, specially when working with spectral methods. In this case, the energy distribution of our pulse gives selective information, because we can see in advance the energy region where the pulses can excite or ionize our system after the photoabsorption process. In other words, the pulse representation in the frequency domain allows a straightforward prediction of the states that will play an important role in the excited and ionic dynamics.

The mathematical expression for the pulse representation in the frequency domain is obtained using the well-known Fourier transform. The general expression of the Fourier transform, which brings any time dependent function $f(t)$, to its respective frequency dependent function, $\mathcal{F}\{f(t)\}(\omega)$, is:

$$\mathcal{F}\{f(t)\}(\omega) = \frac{1}{(2\pi)^{1/2}} \int_{-\infty}^{\infty} f(t)\, e^{(-i\omega t)} dt \tag{2.1.10}$$

Using the above definition, the frequency representation of the vector potential, $A(t)$, for a pulse with sine squared envelope function, is:

$$\mathcal{F}\{A(t)\}(\omega) = \frac{A_0}{(2\pi)^{1/2}} \int_{-T/2}^{T/2} \sin^2\left(\frac{\pi}{T}t\right) \sin(\omega_0 t + \varphi)\, e^{[-i\omega(t+t_0+T/2)]} dt \tag{2.1.11}$$

Since the vector potential, $A(t)$, is defined only non-zero in the time region from t_0 to $t_0 + T$, the above interval of integration in the Fourier transform is exactly equivalent to the integration from $-\infty$ to ∞. In addition, to simplify the integral, we can transform the integration variable from t to t', using $t' = t - t_0 - T/2$. An analytical expression for the above integral can be obtained applying the Euler's formula for both sine functions. The Fourier transform can be then written as:

$$\begin{aligned}\mathcal{F}\left\{A(t)\right\}(\omega) = \frac{A_0 e^{[-i\omega(t_0+T/2)]}}{(2\pi)^{1/2}} \int_{-T/2}^{T/2} \left[\frac{e^{\left(i\frac{\pi}{T}t\right)} - e^{\left(-i\frac{\pi}{T}t\right)}}{2i}\right]^2 \cdot \\ \cdot \left[\frac{e^{\{i(\omega_0 t+\varphi)\}} - e^{\{-i(\omega_0 t+\varphi)\}}}{2i}\right] e^{(-i\omega t)} dt\end{aligned} \tag{2.1.12}$$

Expanding the square terms and the different products in this equation, and later joint the exponential terms in different groups, the expression obtained is:

$$\begin{aligned}\mathcal{F}\left\{A(t)\right\}(\omega) = -i\frac{A_0 e^{[-i\omega(t_0+T/2)]}}{8(2\pi)^{1/2}} \cdot \\ \cdot \left\{2e^{(i\varphi)} \int_{-T/2}^{T/2} e^{[i(\omega_0-\omega)t]} dt - 2e^{(-i\varphi)} \int_{-T/2}^{T/2} e^{[-i(\omega_0+\omega)t]} dt - \right. \\ -e^{(i\varphi)} \int_{-T/2}^{T/2} e^{\left[i\left(\omega_0-\omega+\frac{2\pi}{T}\right)t\right]} dt - e^{(i\varphi)} \int_{-T/2}^{T/2} e^{\left[i\left(\omega_0-\omega-\frac{2\pi}{T}\right)t\right]} dt + \\ \left. +e^{(-i\varphi)} \int_{-T/2}^{T/2} e^{\left[-i\left(\omega_0+\omega-\frac{2\pi}{T}\right)t\right]} dt + e^{(-i\varphi)} \int_{-T/2}^{T/2} e^{\left[-i\left(\omega_0+\omega+\frac{2\pi}{T}\right)t\right]} dt \right\}\end{aligned} \tag{2.1.13}$$

All the integrals in the above equation present the same general structure, which corresponds:

$$\int_{-T/2}^{T/2} e^{(\pm iat)} dt = \mp\frac{i}{a}\left[e^{(\pm iaT/2)} - e^{(\mp iaT/2)}\right] = \mp\frac{i}{a} e^{(\mp iaT/2)}\left[e^{(\pm iaT)} - 1\right] \tag{2.1.14}$$

Substituting this general integral for its specific expressions and grouping together the fractions with the same numerator, the Fourier transform of the vector potential, $\mathcal{F}\left\{A(t)\right\}(\omega)$, for a pulse with a sine squared envelope in the dipole approximation, is:

$$\begin{aligned}\mathcal{F}\left\{A(t)\right\}(\omega) = A_0 e^{[-i\omega(t_0+T/2)]} \left(\frac{\pi^3}{2}\right)^{1/2} \cdot \\ \cdot \left\{e^{(i\varphi)} \frac{e^{[-i(\omega_0-\omega)T/2]}\left(e^{[i(\omega_0-\omega)T]} - 1\right)}{(\omega_0-\omega)\left[T^2(\omega_0-\omega)^2 - 4\pi^2\right]} + \right. \\ \left. +e^{(-i\varphi)} \frac{e^{[i(\omega_0+\omega)T/2]}\left(e^{[-i(\omega_0+\omega)T]} - 1\right)}{(\omega_0+\omega)\left[T^2(\omega_0+\omega)^2 - 4\pi^2\right]} \right\}\end{aligned} \tag{2.1.15}$$

The Fourier transform of the vector potential, $\mathcal{F}\{A(t)\}(\omega)$, is a complex function. The vector potential, $A(t)$ of a 2 fs pulse with a frequency of 28 eV (left panel) and its Fourier transform, $\mathcal{F}\{A(t)\}(\omega)$, (right panel) are plotted in figure 2.1.5. Both real and imaginary parts of $\mathcal{F}\{A(t)\}(\omega)$ have fast oscillations with different phases between them. However, as we will illustrate through several examples in the next chapters, we are usually interested in the frequency distribution of the pulse, which corresponds to the module of the Fourier transform, $|\mathcal{F}\{A(t)\}(\omega)|$, plotted as the black line in figure 2.1.5, which gives a well-defined shape function around both positive, ω_0, and negative, $-\omega_0$, values of the central frequency of the pulse. Both terms in equation 2.1.15 can be associated with the absorption $(+\omega)$ or emission $(-\omega)$ processes. The first term dominates at positive frequencies, $+\omega$, and is associated with the absorption process. While the second term dominates at negative frequencies, $-\omega$, and is related with the stimulated emission.

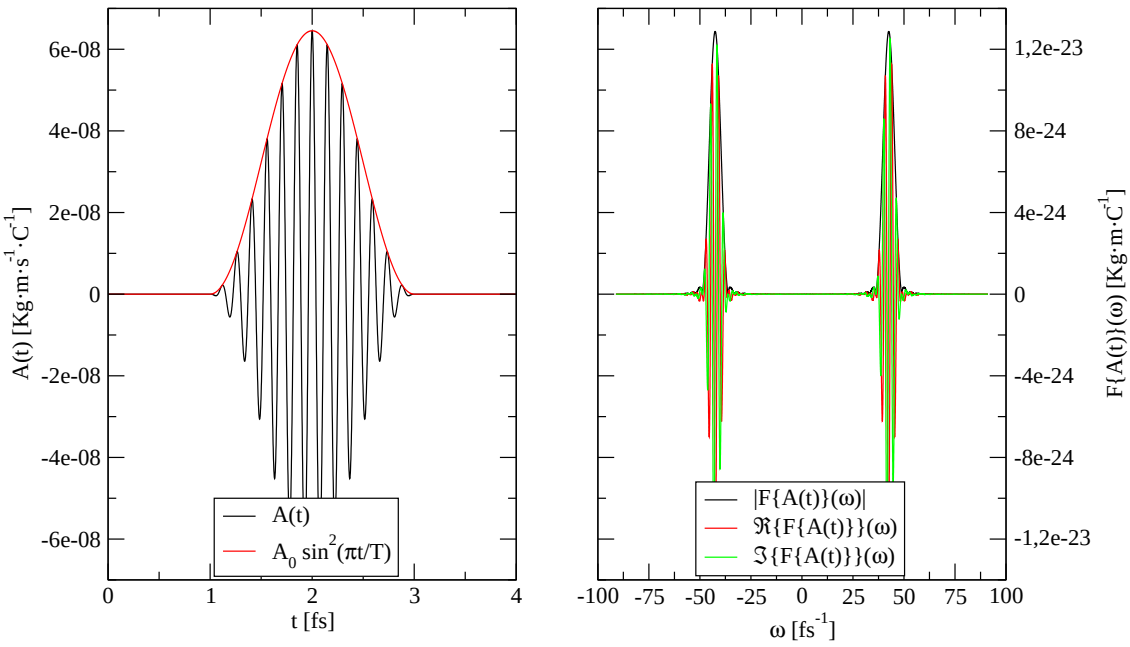

Figure 2.1.5: Right panel: vector potential. Left panel: representation of the Fourier transform of the vector potential for a pulse with a sine squared envelope function. The pulse parameters are: $T = 2$ fs, $\omega_0 = 28$ eV and $I = 10^{12}\,\mathrm{W}\cdot\mathrm{cm}^{-2}$. Black line: Module of the Fourier transform. Red line: Real part of the Fourier transform. Blue line: Imaginary part of the Fourier transform.

To go deeper in the analysis of the frequency distribution of the pulse, it becomes necessary the expansion of the Fourier transform module:

$$
\begin{aligned}
&\left|\mathcal{F}\left\{A\left(t\right)\right\}\left(\omega\right)\right| = A_0\left(\frac{\pi^3}{2}\right)^{1/2}\cdot \\
&\cdot\left\{\frac{2-e^{[i(\omega_0-\omega)T]}-e^{[-i(\omega_0-\omega)T]}}{\left(\omega_0-\omega\right)^2\left[T^2\left(\omega_0-\omega\right)^2-4\pi^2\right]^2}+\frac{2-e^{[i(\omega_0+\omega)T]}-e^{[-i(\omega_0+\omega)T]}}{\left(\omega_0+\omega\right)^2\left[T^2\left(\omega_0+\omega\right)^2-4\pi^2\right]^2}+\right. \\
&\quad+e^{(i2\varphi)}\frac{e^{(-i\omega_0T)}\left(e^{[i(\omega_0-\omega)T]}-1\right)\left(e^{[i(\omega_0+\omega)T]}-1\right)}{\left(\omega_0^2-\omega^2\right)\left[T^2\left(\omega_0-\omega\right)^2-4\pi^2\right]\left[T^2\left(\omega_0+\omega\right)^2-4\pi^2\right]}+ \\
&\quad\left.+e^{(-i2\varphi)}\frac{e^{(i\omega_0T)}\left(e^{[-i(\omega_0-\omega)T]}-1\right)\left(e^{[-i(\omega_0+\omega)T]}-1\right)}{\left(\omega_0^2-\omega^2\right)\left[T^2\left(\omega_0-\omega\right)^2-4\pi^2\right]\left[T^2\left(\omega_0+\omega\right)^2-4\pi^2\right]}\right\}^{1/2}
\end{aligned}
\tag{2.1.16}
$$

where the first two terms are the module of each term from equation 2.1.15, and the last two terms are the crossing terms. It is clear that the module of each term from equation 2.1.15 gives the main contribution to the peaks in figure 2.1.5 while the crossing terms correspond to the overlap between them. Equation 2.1.16 can be simplified by applying the well-known rotating wave approximation, RWA, which implies that only the absorption (or emission) term is considered [2, 154]. The RWA is appropriate for the intensities used in our calculation and is used as a convenience to give a simpler picture in this analysis of the frequency distribution of the pulse. Considering only the positive frequency region, the Fourier transform module of the vector potential, $\left|\mathcal{F}\left\{A\left(t\right)\right\}\left(\omega\right)\right|$, becomes:

$$
\left|\mathcal{F}\left\{A\left(t\right)\right\}\left(\omega\right)\right| = A_0\left(2\pi^3\right)^{1/2}\frac{\sin\left[\frac{(\omega_0-\omega)}{2}T\right]}{\left(\omega_0-\omega\right)\left[T^2\left(\omega_0-\omega\right)^2-4\pi^2\right]} \tag{2.1.17}
$$

where the module of $\left(\exp\left[i\left(\omega_0\pm\omega\right)T\right]-1\right)$ has been transformed in the expression $2^{1/2}\left\{1-\cos\left[\left(\omega_0\pm\omega\right)T\right]\right\}^{1/2}$ applying the Euler's formula, and rewriting as $2\sin\left[\left(\omega_0\pm\omega\right)T/2\right]$, using simple trigonometric relations. Note from equation 2.1.17 that the module of the Fourier transform, $\left|\mathcal{F}\left\{A\left(t\right)\right\}\left(\omega\right)\right|$, does not depend on the initial time, t_0, and the CEP, φ_0. As a consequence, the distributions obtained for photoionization and photoexcitation processes will be independent of the CEP, φ_0, for one-photon transitions.

It is interesting to determine the parameters of the pulse which determine the high and width of the spectral distribution. In figure 2.1.6, it is clear that the highest value is obtained for a frequency equal to the central frequency, ω_0. Consequently, the high of the pulse spectral distribution can be obtained making the limit when this equation approaches to the central frequency, ω_0:

$$
\lim_{\omega\to\omega_0}\left|\mathcal{F}\left\{A\left(t\right)\right\}\left(\omega\right)\right| = \frac{A_0}{4\left(2\pi\right)^{1/2}}T \tag{2.1.18}
$$

where, it is used the L'Hôpital rule to solve the indeterminacy 0/0. As can be observed in equation 2.1.18, the maximum of the Fourier transform module depends explicitly on the pulse duration, T, and implicitly, through the amplitude

of the vector potential, A_0, on the intensity, I, and the central frequency, ω_0, of the pulse. This can be inferred from figure 2.1.6 where the distributions are higher and narrower when we increase the pulse duration, indicating a linear relation between the high of the distribution and the pulse duration.

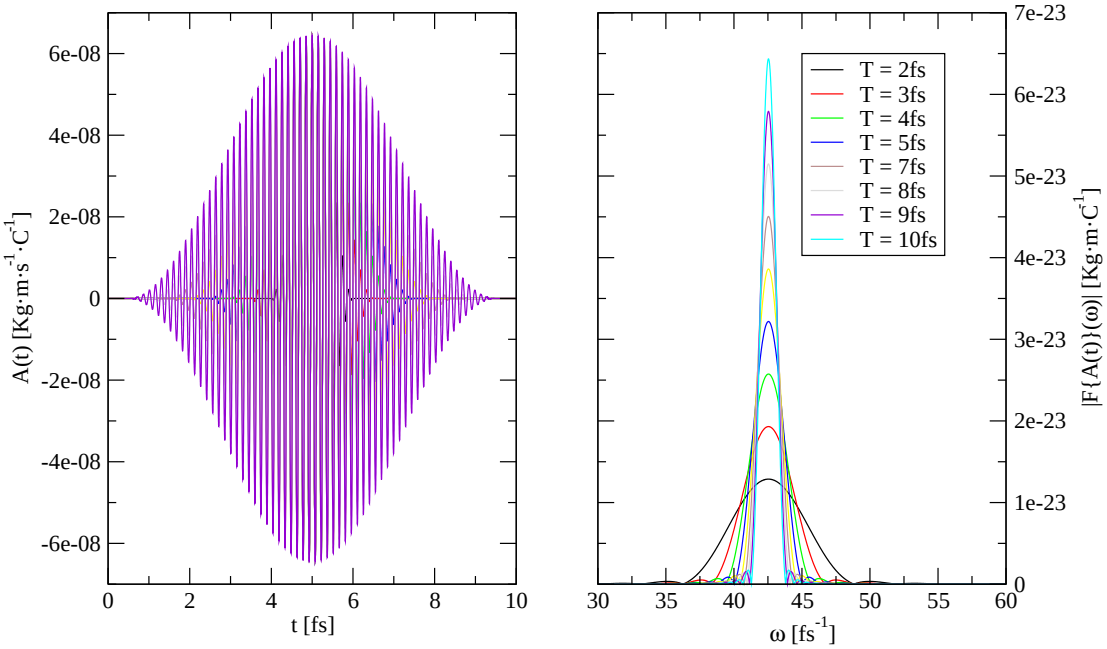

Figure 2.1.6: left panel: vector potentials for several pulses. Right panel: module of the Fourier transform of the vector potential for several pulses. All the pulses have the same central frequency, 28 eV, and intensity, $10^{12}\,\mathrm{W}\cdot\mathrm{cm}^{-2}$, and different pulse duration, from 2 fs to 10 fs (indicated in figure by different color lines).

The bandwidth of the pulse is defined as the full width at half maximum (FWHM) of the Fourier transform module. This definition indicates that the bandwidth of the pulse can be obtained using the above expression for the maximum of the Fourier transform module of the vector potential. Making equal equation 2.1.17 to equation 2.1.18 divided by two, and operating, we have:

$$T\left(\omega_0-\omega\right)\left[T^2\left(\omega_0-\omega\right)^2-4\pi^2\right]=16\pi^2\sin\left[\frac{\left(\omega_0-\omega\right)}{2}T\right] \tag{2.1.19}$$

Now, observing the equation 2.1.19, the left hand side there is a subtraction, and the right hand side there is a sine function. One possible way to solve equation 2.1.19 is to make both terms equal to zero. Therefore, we have two equations:

$$T^2\left(\omega_0-\omega\right)^2-4\pi^2=0 \tag{2.1.20}$$

$$\sin\left[\frac{\left(\omega_0-\omega\right)}{2}T\right]=0 \tag{2.1.21}$$

The two frequencies, $\omega_\pm$, which satisfies simultaneously both equations 2.1.20 and 2.1.21, and consequently, equation 2.1.19, are:

$$\omega_{\pm} = \omega_0 \pm \frac{2\pi}{T} \tag{2.1.22}$$

The bandwidth, $\Delta\omega$, is defined as the difference of these two frequencies. Consequently, the bandwidth of the sine square envelope pulse is:

$$\Delta\omega = \frac{4\pi}{T} \tag{2.1.23}$$

i.e., larger pulse durations produce higher and narrower frequency distributions. This can be observed in figure 2.1.6, where it is plotted the Fourier transform module of the vector potential, $\mathcal{F}\{A(t)\}(\omega)$, using the equation 2.1.17, for several pulses, all of them with an energy of 28.0 eV and an intensity of $10^{12}\,\mathrm{W}\cdot\mathrm{cm}^{-2}$ and different durations, from 2 fs to 10 fs. In the long time duration limit, when the pulse duration is closer to infinite, the spectral representation of the pulse is the delta function, $3\pi T/16 \cdot \delta(\omega_0 - \omega)$.

The frequency representation of the pulse and specially its bandwidth gives selective information about the populated states in the excitation and ionization processes. To illustrate this, we can focus on the one-photon absorption process, where the first order time dependent perturbation theory (TDPT) is valid. This theory simplifies the equation 1.1.9 [142], giving that the first order time dependent coefficient, $c_n^{(1)}(t;\varepsilon)$, is:

$$c_n^{(1)}(t;\varepsilon) = -\frac{i}{\hbar}\sum_{i=1}^{n}\left[\int_{S(\mathbf{r})}\overline{\psi}_n(\mathbf{r};\varepsilon)\,\widehat{V}(t)\,\psi_0(\mathbf{r};0)\,d^3\mathbf{r}\right]\cdot\left[\int_0^t \mathbf{A}(t)\,e^{\left[i\frac{E_n(\varepsilon)-E_0(0)}{\hbar}t\right]}dt\right] \tag{2.1.24}$$

where external interaction potential operator, $\widehat{V}(t)$, can be substituted by its expression in the velocity or length gauge, given in equations 1.1.55 and 1.1.67, respectively. In the above equation, the first term in square brackets is the dipole coupling between the final, $\psi_n(\mathbf{r};\varepsilon)$, and initial states, $\psi_0(\mathbf{r};0)$, and the second term corresponds to the Fourier transform of the pulse, except the normalization factor, where, the frequency is defined by the energy difference between both states. Consequently, larger bandwidth of the pulse gives a wider range of final states populated, as it is shown in figure 2.1.7, where it is plotted the ground state, $X\,{}^1\Sigma_g^+$, the first two lowers ${}^1\Sigma_u^+$ bound states, $B\,{}^1\Sigma_u^+$ and $B'\,{}^1\Sigma_u^+$, of the hydrogen molecule, H_2, and the first ionic state, $1s\sigma_g$, of the hydrogen molecular ion, H_2^+, with their respective bound vibrational states. In this figure, on the y axis it is plotted the module of the Fourier transform for two pulses, both with 14 eV of energy and $10^{12}\,\mathrm{W}\cdot\mathrm{cm}^{-2}$ of intensity, and two different durations, 1 fs in the left panel and 10 fs in the right panel. It is clear that the shortest pulse, which has the larger bandwidth, covers a wider energy region and populates a larger bunch of vibronic (vibrational and electronic) states than the longest pulse. As we are going to see in chapter 4, the shortest pulse generates a vibronic wavepacket constituted by several electronic states, while the longest pulse is creating a vibrational wavepacket associated with a specific electronic state.

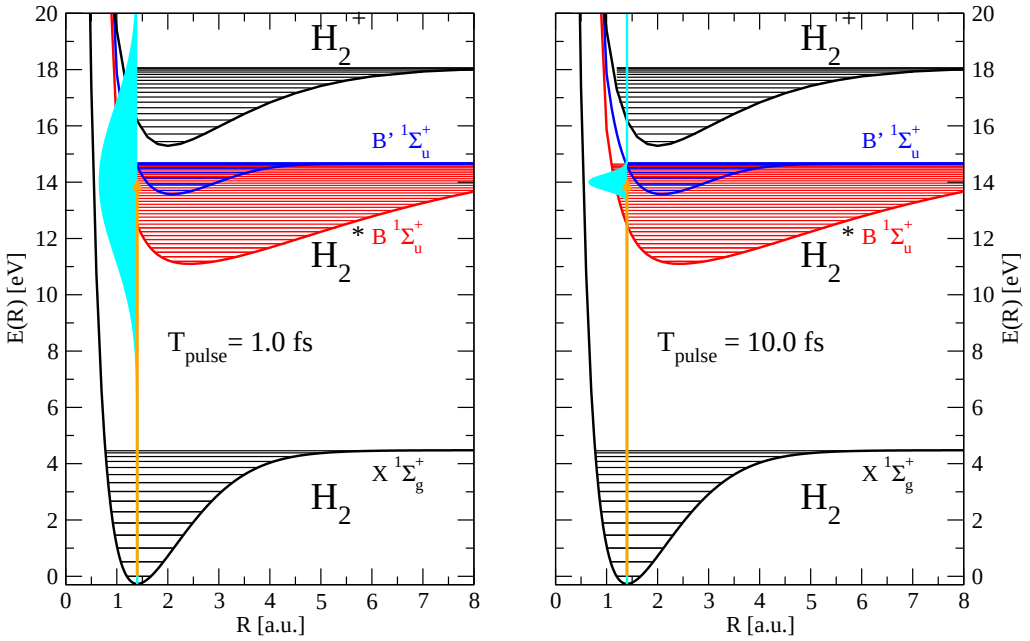

Figure 2.1.7: Representation of the potential energy curves and their corresponding bound vibrational states for the electronic ground state, $X\ ^1\Sigma_g^+$, the two lowest single excited states of Σ_u symmetry, $B\,^1\Sigma_u^+$ and $B'\,^1\Sigma_u^+$, and the first ionic threshold, $1s\sigma_g$, in both panels. Left panel: Energy region, determined by the Fourier transform (yellow shape), in which a sine squared envelope pulse with a duration of 1.0 fs, an energy of 14.0 eV and an intensity of $10^{12}\,\mathrm{W}\cdot\mathrm{cm}^{-2}$, can produce the transition from the ground state. Right panel: The same as the left panel for a pulse with the previous energy and intensity but a duration of 10.0 fs. In both panels, the orange arrow indicates the direct transition from the vibrational ground state of the $X\ ^1\Sigma_g^+$ to the states, whose energy difference is equal to the central frequency of the pulse used.

2.2 Pump-probe schemes

Therefore, the ultrashort single isolated pulses launch the dynamics into excited and/or ionic states of the system, generating vibronic (vibrational and electronic) wavepackets which freely evolve in time and space. Most of the actual techniques are capable of measure the final probabilities and cross sections in the long time limit. However, the dynamical information of the wavepacket is not fully accessible by these techniques. To obtain this dynamical information, we need to take pictures at different times to reconstruct the wavepacket dynamics, as a video camera takes snapshots. Thus, we need to use a combination of different pulses, to first launch the dynamics, and later to trace this dynamics during its evolution.

The pump - probe techniques in attophysics field were inspired in the analog protocols used in femtochemistry. These pump-probe techniques in femtochemistry are the logical evolution of the pump - dump experiments. In the pump - dump experiments [166, 165, 155, 156, 157, 26], applied to the control of chemical reactions, the initial population in the ground state potential energy surface is

excited by the pump, generating a vibronic wavepacket which evolves in time and space to other regions in the excited surface. When the wavepacket arrives to the region of the interested products, the dump pulse induces the stimulated photoemission, depopulating the excited states and populating the searched product channel in the ground state surface. However, in the pump - dump experiments, the dynamical information of the intermediate wavepacket, which constitutes the transition state between the reacts and products, is not fully obtained in the final reaction path. To obtain information about the reaction mechanism, we use a similar idea. In this manner, the pump - probe experiments [16, 15, 187], as several pump - dump protocols, use a combination of IR laser pulses with duration in the femtosecond timescales, where the pump pulse launches the dynamics into excited states of the system, and the probe pulse, through transition to final states, gives the position of the intermediate wavepacket as a function of the time delay between both pulses.

These pump - probe experiments can be extrapolated to attophysics, using as pump, pulses shorter and more energetic than in femtochemistry, because while in the latter the heavy nuclear motion is in the hundreds of femtosecond timescales and the energy difference among the relevant states is in the IR region, in attophysics the electronic and fast nuclear motion is in attosecond regime and the energy difference among states needs the use of XUV pulses. In this way, several works proposed pump – probe protocols in which attosecond XUV pulses have been used to ionize and induce some dynamics in the target, and phase-locked IR probe pulses have been used to trace it, both in atoms [97, 168, 61] and molecules [191, 36]. More recent experiments combine two XUV pulses, as pump and probe, avoiding the perturbation introduced by the IR fields. To obtain the dynamical information, different strategies are used, such as interferometric methods to reconstruct the electron wavepackets in atoms [164] or the attosecond streak camera [61, 69, 83, 121]. In this way, the deep understanding of the photoexcitation and ionization processes [121, 66, 84] can be only accounted by the optical characterization of pump and probe pulses used.

Since we restrict our description of the pulses to linearly polarized light, the total vector potential, $\mathbf{A}(t)$, in the dipole approximation is:

$$\mathbf{A}(t) = \mathbf{A}_1(t) + \mathbf{A}_2(t) \tag{2.2.1}$$

where $\mathbf{A}_1(t)$ is the vector potential of the pump and $\mathbf{A}_2(t)$ is the vector potential of the probe. In addition, restricting our definition to pulses with the same direction of the polarization vector, $\mathbf{u}_A$, the total vector potential can be written as:

$$\mathbf{A}(t) = [A_1(t) + A_2(t)]\,\mathbf{u}_A \tag{2.2.2}$$

With $A_1(t)$ and $A_2(t)$, using a sine squared envelope, equal to:

$$A_1(t) = \begin{cases} = A_{0,1} \sin^2\left[\frac{\pi}{T_1}\left(t - t_{0,1} - \frac{T_1}{2}\right)\right] \sin\left[\omega_{0,1}\left(t - t_{0,1} - \frac{T_1}{2}\right) + \varphi_1\right] & t_{0,1} \leq t \leq t_{0,1} + T_1 \\ = 0 & t_{0,1} > t > t_{0,1} + T_1 \end{cases} \tag{2.2.3}$$

$$A_2(t) = \begin{cases} = A_{0,2} \sin^2\left[\frac{\pi}{T_2}\left(t - t_{0,2} - \frac{T_2}{2}\right)\right] \sin\left[\omega_{0,2}\left(t - t_{0,2} - \frac{T_2}{2}\right) + \varphi_2\right] & t_{0,2} \leq t \leq t_{0,2} + T_2 \\ = 0 & t_{0,2} > t > t_{0,2} + T_2 \end{cases} \tag{2.2.4}$$

where, $A_{0,i}$, $\omega_{0,i}$, $\varphi_{0,i}$, $t_{0,i}$ and T_i are the amplitude of the vector potential, the central frequency, the CEP, the initial time and the pulse duration of the pump ($i = 1$) or probe ($i = 2$) pulses.

The definition of the time delay between the pulses, τ, depends on the convention used. In our calculations, we define the time delay as:

$$\tau = \left(t_{0,2} + \frac{T_2}{2}\right) - \left(t_{0,1} + \frac{T_1}{2}\right) \tag{2.2.5}$$

Using the above equation to define the time delay, τ, we can express the vector potential of the pump or probe pulse as a function of the time delay between both pulses. The label of the pump or probe pulse is associated with the process studied. Focusing on the XUV pump - IR probe and the XUV pump - XUV probe schemes analyzed in next chapters, the pump is the XUV pulse which launches the dynamics into excited and ionized states, generating a vibronic wavepacket, whose motion is traced by the IR field or the second XUV pulse, respectively, which acts as probe. In figure 2.1.6, it is plotted the typical XUV pump - XUV probe scheme with two equal pulse, with a duration of 2 fs, an energy of 14 eV and an intensity of $10^{12}\,\mathrm{W \cdot cm^{-2}}$. In this particular XUV pump - XUV probe scheme, the observables obtained as a function of the time delays are symmetric with respect to its zero value, due to both pulses are indistinguishable. However, in other schemes, when the pulses used present different parameters, the observables as a function of the time delay are not symmetric.

In all our calculation we fix the CEP parameters of both pulses to have the maximum of the amplitude of the vector potential in the center of the pulse, as can be observed in figure 2.2.1. The importance of the CEP value in the laser-matter interaction processes is deeply linked with the number of optical oscillations of the pulse. When the pulse has a frequency, which assures a large number of full oscillations during the pulse, a variation of the CEP does not have a measurable physical consequence, because the pulse practically does not vary. This is the case of the XUV pump - XUV probe schemes, where the XUV pulse has optical cycles large enough that a variation of the CEP of one of them does not modifies the induced processes in the matter. However, when the pulse has a few number of optical cycles, as in short IR pulses, the structure of the pulse is widely affected by a change in the CEP. Consequently, in the XUV pump - IR probe protocols, it is necessary to fix the CEP of the IR.

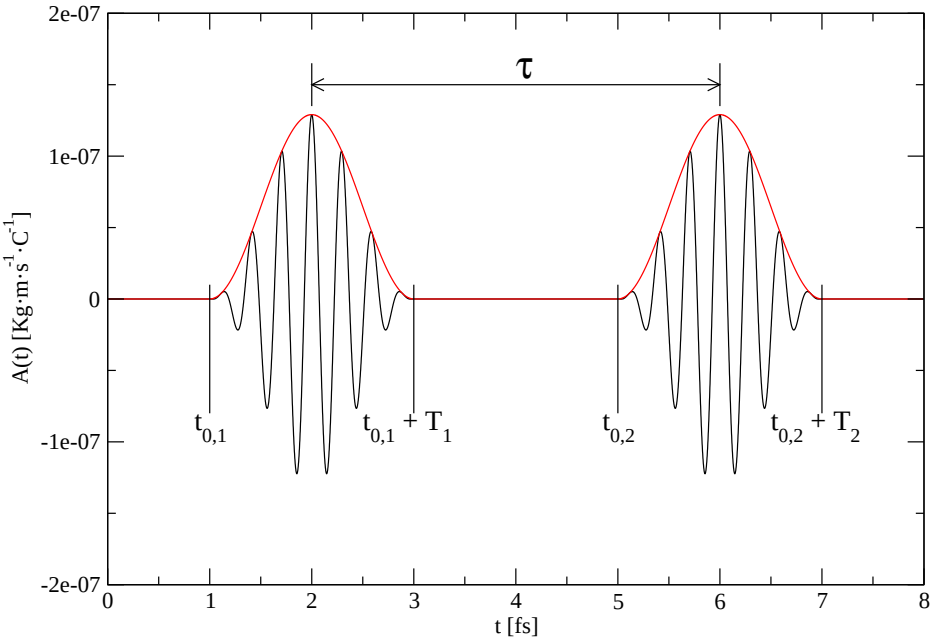

Figure 2.2.1: Vector potential representation in the time domain of both pump and probe pulses with the same duration of 2 fs, energy of 14 eV, and intensity of $10^{12}\,\mathrm{W}\cdot\mathrm{cm}^{-2}$. The separation between the center of the probe and pump pulses is the time delay, τ. In addition, the CEP of both pulses is selected to have the positive maximum of the vector potential in the center of the pulse.

The total vector potential, $A(t)$, of the pump-probe scheme can be expressed in the frequency domain by its Fourier transform, $\mathcal{F}\{A(t)\}(\omega)$:

$$\begin{aligned}\mathcal{F}\{A(t)\}(\omega) &= \frac{1}{(2\pi)^{1/2}}\int_{-\infty}^{\infty}\left[A_1(t)+A_2(t)\right]e^{(-i\omega t)}dt = \\ &= \frac{1}{(2\pi)^{1/2}}\int_{-\infty}^{\infty}A_1(t)\,e^{(-i\omega t)}dt + \frac{1}{(2\pi)^{1/2}}\int_{-\infty}^{\infty}A_2(t)\,e^{(-i\omega t)}dt\end{aligned} \tag{2.2.6}$$

where the total vector potential, $A(t)$, is substituted by the sum of the pump, $A_1(t)$, and probe, $A_2(t)$, vector potentials. Since the Fourier transform is a linear transformation, it satisfies the distributive property of the integrals [5], and the Fourier transform of the pump - probe vector potential, $\mathcal{F}\{A(t)\}(\omega)$, can be expressed as the coherent sum of the separate Fourier transforms of the vector potentials for the pump and probe pulses:

$$\mathcal{F}\{A(t)\}(\omega) = \mathcal{F}\{A_1(t)\}(\omega) + \mathcal{F}\{A_2(t)\}(\omega) \tag{2.2.7}$$

Note in the above expression that the pump and probe Fourier transforms are added coherently, and consequently, the Fourier transform module of the total vector potential, $|\mathcal{F}\{A(t)\}(\omega)|$, does not satisfy $|\mathcal{F}\{A_1(t)\}(\omega)| \neq |\mathcal{F}\{A_1(t)\}(\omega)| + |\mathcal{F}\{A_2(t)\}(\omega)|$. $|\mathcal{F}\{A(t)\}(\omega)|$ contains the cross terms between both pump and probe pulses, which can generate structure in the total spectral representation, as is shown in figure 2.2.2. In this figure, we plot for several time delays the

Fourier transform module for two XUV pump and probe pulses with the same parameters as in figure 2.2.1. Consequently, the probe pulse has the same Fourier transform as the pump, but with and extra phase as a function of the time delay: $\mathcal{F}\{A_2(t)\}(\omega) = \mathcal{F}\{A_1(t)\}(\omega)\exp(i\omega\tau)$. When the time delay is 0 fs, in the upper left panel, the pulses are fully overlapped in time. As both pulses have the same CEP, the sum of the vector potential gives a final pulse equal to a single pulse with 4 times the intensity of each pump or probe pulse. For time delays higher than 2 fs, the spectral distributions of the pump - probe scheme present different fringes, whose number increases with the time delay, by the expression:

$$\mathcal{F}\{A(t)\}(\omega) = \mathcal{F}\{A_1(t)\}(\omega)\left[1 + e^{(i\omega\tau)}\right] \tag{2.2.8}$$

where the fringes resulting from the coherent combination of both pump and probe pulses with different initial time phases, $\exp(i\omega t_{0,i})$, which appears in the crossing terms, and consequently, the shape on these spectral distributions are contained in the shape of the spectral distribution for a time delay equal to 0 fs.

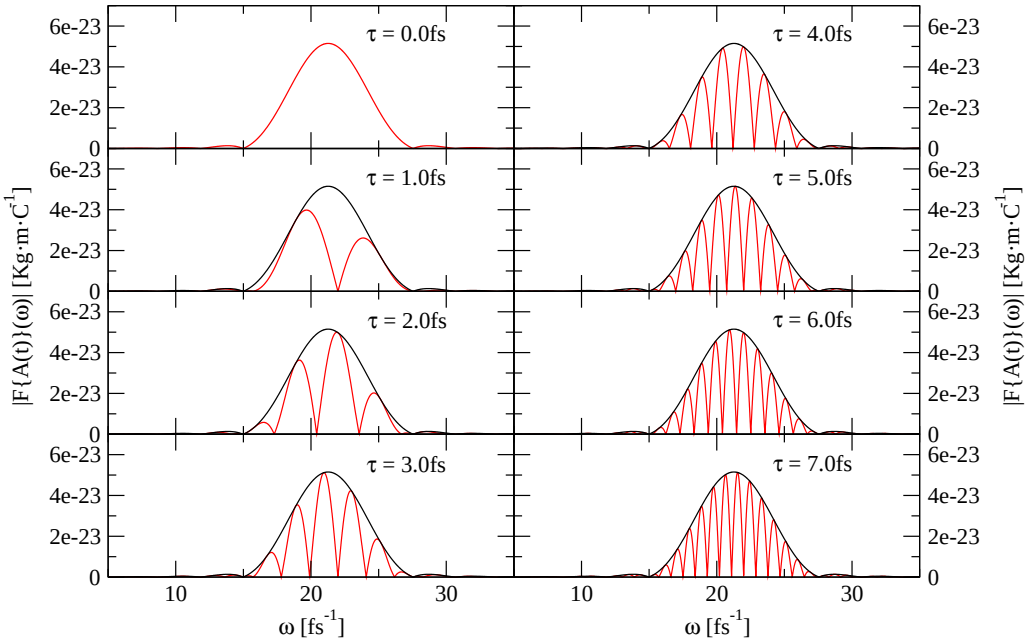

Figure 2.2.2: Fourier transform module of the total vector potential for several time delays. The pump and probe pulses used have the same parameters between them,. The parameters used for the pump and probe pulses are the same as in figure 2.2.1. Each panel corresponds to a different time delay between the pulses, indicated in its corresponding label.

However, if both pump and probe pulses have durations and central frequencies sufficiently different, their peaks of the spectral distributions appear at different regions of the frequency domain, and therefore, the crossing term can be neglected considering that the Fourier transform of both pump and probe pulses are independent. In this case, the spectral distribution for any time delay does not present the fringes observed in figure 2.2.2, and it can be obtained as the sum

of the spectral representation for both pump and probe pulse as single pulses. This can be observed in figure 2.2.3, where it is plotted the module of the Fourier transform of a XUV pump - IR probe scheme for several time delays, in which the XUV pulse has a duration of 1 fs, an energy of 28 eV and an intensity of $10^{10}\,\mathrm{W}\cdot\mathrm{cm}^{-2}$ and the IR probe has a duration of 9 fs, an energy of 1.65 eV and an intensity of $10^{8}\,\mathrm{W}\cdot\mathrm{cm}^{-2}$.

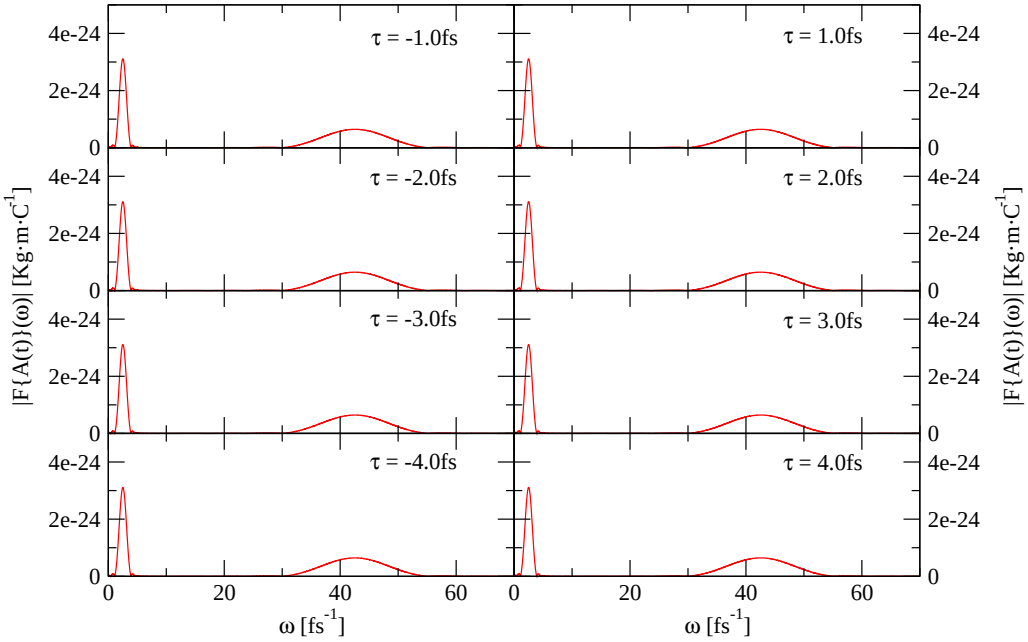

Figure 2.2.3: Fourier transform module of the total vector potential of a XUV pump - IR probe scheme, for several time delays. The XUV pump pulse parameters are: 1 fs, 28 eV and $10^{10}\,\mathrm{W}\cdot\mathrm{cm}^{-2}$. The IR probe parameters are: 9 fs, 1.65 eV and $10^{8}\,\mathrm{W}\cdot\mathrm{cm}^{-2}$. Each panel corresponds to a different time delay between the pulses, indicated in its corresponding label.

2.3 Attosecond pulse train (APT)

In the above sections of the present chapter, we have focused on the SAPs (single attosecond pulses). Nowadays, these SAPs are mainly generated through the HHG techniques, where the HHG process is limited to emit only one pulse from a possible train of attosecond pulses. However, the main electromagnetic waves generated for the HHG techniques are a temporal sequence of attosecond pulses which constitute a train, called attosecond pulse train (APT). The mathematical description of the APT can be considered as the pump - probe schemes extension, where the total vector potential of the APT is a linear combination of different vector potentials for each attosecond pulse in the train:

$$\mathbf{A}(t) = \sum_{i=1}^{N} A_i(t)\, g(t)\, \mathbf{u}_A \tag{2.3.1}$$

where N is the number of the attosecond pulses, which conform the APT and $A_i(t)$ is the vector potential of each harmonic, whose expression follows the equations 2.2.3 or 2.2.4. The APT is modulated by the $g(t)$ function, which usually takes the expression of a Gaussian function. To simplify the description of the APT, the modulation introduced by this shape function can be included in each $A_i(t)$, simply modifying their amplitude of the vector potentials to fix the value of the $g(t)$ function in their pulse center.

All $A_i(t)$ satisfy close relations among them. These relations are intrinsically associated with the HHG process, in which several parameters of the attosecond pulses are associated with the IR generating strong field. Since the harmonic emission is produced each half cycle of the IR generating strong field, the attosecond pulses have the same durations and frequencies and their CEP are alternative opposite as a function of the time. In addition, for similar reasons, the different attosecond pulses which constitute the train are separated between them by a $T_{IR}/2$, where this T_{IR} is the period of the generating IR pulse. This can be appreciated in the left panel of figure 2.3.1, where it is plotted the APT constituted for four attosecond pulses, with a pulse duration of $0,55\,\text{fs}$, a frequency of $14,67\,\text{eV}$ and an intensity of $3.5 \cdot 10\,\text{W} \cdot \text{cm}^{-2}$ (for the first and last harmonic) and $10^9\,\text{W} \cdot \text{cm}^{-2}$ (for the central harmonics).

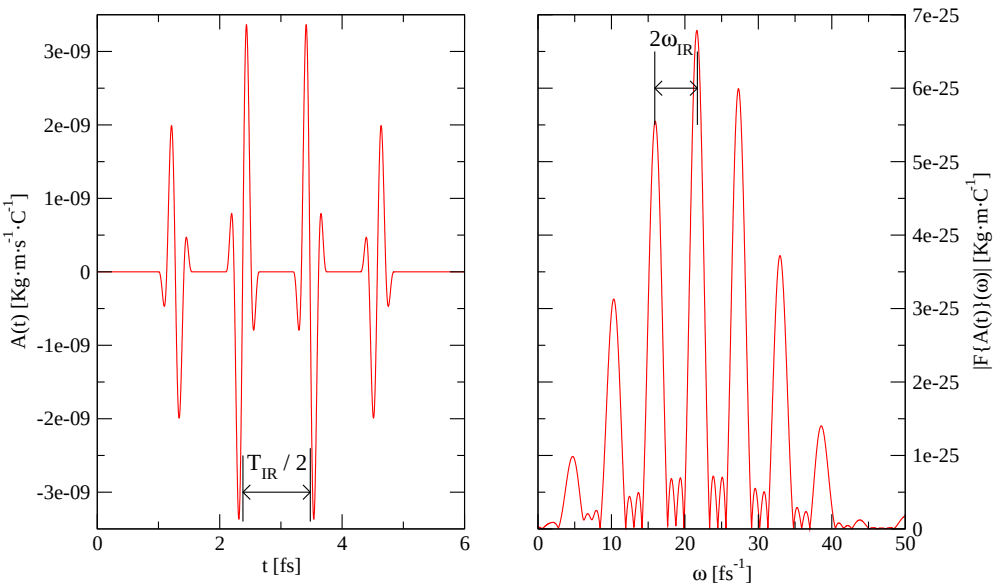

Figure 2.3.1: Left panel: Vector potential representation in the time domain of the APT with a duration of 0.55 fs, an energy of 14.67 eV, and an intensity of $3.5 \cdot 10\,\text{W} \cdot \text{cm}^{-2}$ (for the first and last harmonic) and $10^9\,\text{W} \cdot \text{cm}^{-2}$ (for the central harmonics). Right panel: Fourier transform module of the vector potential for the same APT.

As in the pump - probe schemes, the Fourier transform of the APT vector potential, $\mathcal{F}\{A(t)\}(\omega)$, can be expressed as the coherent sum of the separate Fourier transforms of the vector potentials for each attosecond pulse:

$$\mathcal{F}\left\{A\left(t\right)\right\}\left(\omega\right) = \sum_{i=1}^{N} \mathcal{F}\left\{A_i\left(t\right)\right\}\left(\omega\right) \tag{2.3.2}$$

Again we have a coherent sum, the module of the APT Fourier transform cannot be obtained as the sum of the modules of the Fourier transforms for all attosecond pulses. In fact, the spectral distribution of the APT, which follows the module squared of its Fourier transform, presents different spikes, as can be observed in the right panel of figure 2.3.1, which are consequence of the different temporal phases between the different attosecond pulses with the same central frequency. As in the XUV pump - XUV probe scheme, the Fourier transforms of the vector potential of the all attosecond pulses can be considered equals, $A_{AP}\left(t\right)$, but with a extra modulation (g_i) and phase, which depends on their initial time:

$$\mathcal{F}\left\{A\left(t\right)\right\}\left(\omega\right) = \mathcal{F}\left\{A_{AP}\left(t\right)\right\}\left(\omega\right) \sum_{i=1}^{N} g_i e^{(i\omega t_{0,i})} \tag{2.3.3}$$

Chapter 3

Molecular structure

The hydrogen molecule is the simplest system with more than one electron, that can be studied with *ab initio* methods. Consequently, the hydrogen molecule is the prototypical system to analyze the excitation and ionization processes induced by a laser field from a theoretical point of view. The full dimensional treatment of this system can be obtained using a spectral method, where the time dependent wavefunction is expressed as a linear combination of the eigenstates of the field-free system.

The interest as well as the complexity of this molecular system lies in the accurate representation of the electronic correlation between both electrons and the coupled motion of the electrons and nuclei. For the latter term, the large mass difference between electrons and nuclei allows us to apply the Born-Oppenheimer approximation, that greatly reduces the problem by expressing the total eigenfunction as the product of an electronic wavefunction and an nuclear wavefunction. This approximation simplifies the solution of the TISE for the field-free system in two separate problems, one for the electrons and the other for the nuclei.

In the method, developed in our group [106, 67, 151, 129], we first obtain the electronic wavefunctions and energies as a function of the nuclear position vectors. These electronic wavefunctions are obtained using the configuration interaction method [95, 163], where the electronic wavefunctions of the two-electron hydrogen system are expressed as the antisymmetric product of one-electron wavefunctions. The method is simplified using as one-electron wavefunctions, the eigenfunctions of the hydrogen molecular ion, H_2^+, which satisfy similar symmetry properties that the states of the hydrogen molecular system.

The electronic states H_2 are obtained in the subsection 3.1.2. Due to the different character of the bound and scattering states, these are computed through distinct treatments. The bound electronic states are calculated with the standard CI method, while the scattering states are described using the Feshbach formalism, which builds two complementary subspaces, one for the continuum states, where one electron is ejected from the molecule, and the other for the resonant states, constituted by metastable bound states where both electrons are excited.

Once we obtained the electronic structure (eigenfunctions and energies), we solve

the nuclear problem. Within the Born-Oppenheimer approximation, the electronic energies as a function of the nuclear coordinates are the well-known potential energy surfaces (curves), which the nuclei feel in their motion. For the laser-matter interaction, we restrict our study to the use of ultrashort laser pulses, whose durations are significantly shorter than molecular rotation. Consequently, we can neglect the rotational degrees of freedom.

3.1 Electronic structure of $H_2/H_2^+ + e^-$

As explained in chapter 1, the time dependent Hamiltonian operator, $\widehat{H}(t)$ for the light-matter interaction is written as the sum of the field-free Hamiltonian operator, $\widehat{H}_0$, and the external time dependent potential operator, $\widehat{V}(t)$. This allows to expand the time dependent wavefunction, $\Psi(\mathbf{r},t)$, which describes the evolution of the atomic or molecular system, as a *ly* combination of the TDSE solutions for the field-free Hamiltonian operator, $\widehat{H}_0$. Because the field-free Hamiltonian operator is time invariant, these wavefunctions can be factorized as the product of the eigenfunctions, $\psi(\mathbf{r})$, solutions of the TISE for $\widehat{H}_0$, multiplied by their stationary phases, $\exp[-iEt/\hbar]$, where E are the eigenvalues of the field-free states.

Although we are interested in solving the field-free TISE of the $H_2/H_2^+ + e^-$ system, first we introduce the expressions for a more general system constituted by n electrons and N nuclei. The field-free Hamiltonian operator is given in equation 1.1.6, for a system constituted by several charge particles. Now, equation 1.1.6 is rewritten, specially indicating electrons and nuclei. In this way, the TISE, for a system constituted by n electrons and N nuclei, can be rewritten as:

$$\left[-\sum_{i=1}^{n}\frac{\hbar^2}{2m_e}\nabla_i^2-\sum_{\alpha=1}^{N}\frac{\hbar^2}{2M_\alpha}\nabla_\alpha^2-\sum_{\alpha=1}^{N}\sum_{i=1}^{n}\frac{1}{4\pi\varepsilon_0}\frac{Z_\alpha e^2}{|\mathbf{r}_i-\mathbf{R}_\alpha|}+\right.$$
$$\left.+\sum_{i=1}^{n}\sum_{j>i}^{n}\frac{1}{4\pi\varepsilon_0}\frac{e^2}{|\mathbf{r}_i-\mathbf{r}_j|}+\sum_{\alpha=1}^{N}\sum_{\beta>\alpha}^{N}\frac{1}{4\pi\varepsilon_0}\frac{Z_\alpha Z_\beta e^2}{|\mathbf{R}_\alpha-\mathbf{R}_\beta|}\right]\Psi(\mathbf{r},\mathbf{R})=E\Psi(\mathbf{r},\mathbf{R}) \tag{3.1.1}$$

where, m_e and e are the mass and electric charge of any electron and M_α and $Z_\alpha e$ are the mass and electric charge of the nucleus α. $\mathbf{r}_i$ is the position vector of the electron i and $\mathbf{R}_\alpha$ is the position vector of the nucleus α. In the above TISE, we do not consider the terms due to the mass polarization and relativistic effects in our description of the field-free system. The field-free Hamiltonian operator, $\widehat{H}_0$, given in equation 3.1.1, is constituted by five terms. The first two terms correspond to the kinetic energy operator for the electrons and nuclei, respectively, and the last three terms are the electrostatic interaction terms: the electron-nucleus attraction term, the electron-electron repulsion term and the nucleus-nucleus repulsion term.

The wavefunction, $\Psi(\mathbf{r},\mathbf{R})$, can be written as the product of an electronic wavefunction, $\psi(\mathbf{r},\mathbf{R})$, which depends on the electronic and nuclear coordinates, $\mathbf{r}$

and $\mathbf{R}$, and a nuclear wavefunction, $\chi(\mathbf{r},\mathbf{R})$, which only depends on the nuclear coordinates, $\mathbf{R}$ [163]:

$$\Psi(\mathbf{r},\mathbf{R}) = \psi(\mathbf{r};\mathbf{R})\,\chi(\mathbf{R}) \tag{3.1.2}$$

Substituting this expression of the wavefunction $\Psi(\mathbf{r},\mathbf{R})$, in equation 3.1.1, the TISE becomes:

$$\begin{aligned} &-\chi(\mathbf{R})\sum_{i=1}^{n}\frac{\hbar^2}{2m_e}\nabla_i^2\psi(\mathbf{r};\mathbf{R}) - \psi(\mathbf{r};\mathbf{R})\sum_{\alpha=1}^{N}\frac{\hbar^2}{2M_\alpha}\nabla_\alpha^2\chi(\mathbf{R}) - \\ &-2\sum_{\alpha=1}^{N}\frac{\hbar^2}{2M_\alpha}\left[\nabla_\alpha\psi(\mathbf{r};\mathbf{R})\right]\left[\nabla_\alpha\chi(\mathbf{R})\right] - \chi(\mathbf{R})\sum_{\alpha=1}^{N}\frac{\hbar^2}{2M_\alpha}\nabla_\alpha^2\psi(\mathbf{r};\mathbf{R}) + \\ &+\frac{1}{4\pi\varepsilon_0}\left[-\sum_{\alpha=1}^{N}\sum_{i=1}^{n}\frac{Z_\alpha e^2}{|\mathbf{r}_i-\mathbf{R}_\alpha|} + \sum_{i=1}^{n}\sum_{j>i}^{n}\frac{e^2}{|\mathbf{r}_i-\mathbf{r}_j|} + \sum_{\alpha=1}^{N}\sum_{\beta>\alpha}^{N}\frac{Z_\alpha Z_\beta e^2}{|\mathbf{R}_\alpha-\mathbf{R}_\beta|}\right]\cdot \\ &\cdot\Psi(\mathbf{r};\mathbf{R})\,\chi(\mathbf{R}) = E\psi(\mathbf{r};\mathbf{R})\,\chi(\mathbf{R}) \end{aligned} \tag{3.1.3}$$

In the above equation, the third term, $\sum_{\alpha=1}^{N}\frac{\hbar^2}{2M_\alpha}\left[\nabla_\alpha\psi(\mathbf{r};\mathbf{R})\right]\left[\nabla_\alpha\chi(\mathbf{R})\right]$, prevents the separation of the electronic and nuclear terms. However, because the nuclear mass is around 2000 times the electronic mass, for a similar momentum, the electrons have to move faster than the nuclei, and consequently, we can consider that the electrons feel the nuclei as static charges in their motion [135]. This is the well-known Born-Oppenheimer approximation. The validity of this approximation is based on the large difference in the velocity of nuclei and electrons. The mathematical expression of this approximation is that the gradient with respect to the nuclear coordinates of the electronic wavefunction has to be equal to zero:

$$\nabla_\alpha\psi(\mathbf{r};\mathbf{R}) = \mathbf{0} \tag{3.1.4}$$

Within the Born-Oppenheimer approximation, the third and fourth terms in equation 3.1.3 vanish. Thus, it allows the solution of the TISE in two separate electronic and nuclear TISE. The expressions of these two electronic and nuclear TISE are:

$$\begin{aligned} &\left[-\sum_{i=1}^{n}\frac{\hbar^2}{2m_e}\nabla_i^2 - \sum_{\alpha=1}^{N}\sum_{i=1}^{n}\frac{1}{4\pi\varepsilon_0}\frac{Z_\alpha e^2}{|\mathbf{r}_i-\mathbf{R}_\alpha|} + \sum_{i=1}^{n}\sum_{j>i}^{n}\frac{1}{4\pi\varepsilon_0}\frac{e^2}{|\mathbf{r}_i-\mathbf{r}_j|} + \right. \\ &\left. +\sum_{\alpha=1}^{N}\sum_{\beta>\alpha}^{N}\frac{1}{4\pi\varepsilon_0}\frac{Z_\alpha Z_\beta e^2}{|\mathbf{R}_\alpha-\mathbf{R}_\beta|}\right]\psi(\mathbf{r};\mathbf{R}) = E(\mathbf{R})\,\psi(\mathbf{r};\mathbf{R}) \end{aligned} \tag{3.1.5}$$

$$\left[-\sum_{\alpha=1}^{N}\frac{\hbar^2}{2M_\alpha}\nabla_\alpha^2 - E(\mathbf{R})\right]\chi(\mathbf{R}) = E\chi(\mathbf{R}) \tag{3.1.6}$$

In equation 3.1.5, the nuclear position vectors, $\mathbf{R}_\alpha$, only contribute as linear parameters in the nucleus-electron attraction and nucleus-nucleus repulsion terms. Therefore, the electronic TISE can be solved using different sets of the nuclear position vectors, being the solution absolutely independent for each set. This procedure gives the electronic energy, $E(\mathbf{R})$, as a function of the nuclear position vectors, i.e., potential energy surface/curve (PES/PEC). It will be used as the potential term in the solution of the nuclear TISE. Note that, since the position vectors of the nuclei are parameters in the electronic TISE, the nucleus-nucleus repulsion term gives a constant energy term. It does not modify the electronic wavefunction, $\psi(\mathbf{r};\mathbf{R})$, and only contributes with a constant value to the electronic energy, $E(\mathbf{R})$. In this manner, we can solve the electronic TISE, giving in equation 3.1.5, without the nucleus-nucleus repulsion term, and later adds its value to the electronic energy, $E(\mathbf{R})$.

3.1.1 Electronic states of the H_2^+

We first solve the TISE of the hydrogen molecular ion, H_2^+, which is a one-electron problem. The wavefunctions and energies of the H_2^+ system will be later used as a basis set to obtain the bound, resonant and continuum states of the two-electron system, $H_2/H_2^+ + e^-$. The electronic TISE for the hydrogen molecular ion, H_2^+, is:

$$\left[-\frac{\hbar^2}{2m_e}\nabla^2 - \sum_{\alpha=1}^{2}\frac{1}{4\pi\varepsilon_0}\frac{e^2}{|\mathbf{r}-\mathbf{R}_\alpha|} + \frac{1}{4\pi\varepsilon_0}\frac{e^2}{R}\right]\phi_{n,\lambda,\sigma}(\mathbf{r};\mathbf{R}) = \\ = E_{n,\lambda,\sigma}(R)\,\phi_{n,\lambda,\sigma}(\mathbf{r};\mathbf{R}) \tag{3.1.7}$$

where $\mathbf{r}$ is the position vector of the electron, $\mathbf{R}_\alpha$ is the position vector of each nucleus ($\alpha = 1$ or $\alpha = 2$) and R is the internuclear distance between both nuclei, $R = |\mathbf{R}_1 - \mathbf{R}_2|$. The states in equation 3.1.7, are defined by the set of quantum numbers n, λ, σ, related with the different physical magnitudes which are conserved in the dynamics of the system. These physical magnitudes are those whose operators commute with the electronic Hamiltonian operator [29], constituting the complete set of commuting observables, CSCO. For the hydrogen molecular ion, H_2^+, the CSCO is constituted by the electronic Hamiltonian operator, $\widehat{H}_0$, the angular momentum operator in the z axis, $\widehat{L}_z$, and the symmetry operator of the central plane, perpendicular to the internuclear axis, $\widehat{\sigma}$. All these operators of the CSCO have a complete set of common eigenfunctions, defined by the quantum numbers n, λ, σ. The quantum number n determines the state energy, taken the values $1s$, $2s$, $2p$, $3s$, $3p$, $3d$, etc., of the atomic hydrogen, in the limit of the separated atoms. λ is the azimuthal quantum number of the electron, which is equal to the module of the quantum number, m, of the angular momentum operator in the z axis, L_z, $\lambda = |m|$, taking the values $\lambda = 0 \Rightarrow \sigma$, $\lambda = 1 \Rightarrow \pi$, $\lambda = 2 \Rightarrow \delta$, etc.. Finally, σ is the parity of the function with respect to the plane perpendicular to the molecular axis and placed at the center of mass. σ can take the values g or u, where g, "gerade" (even in German) indicates that

the wavefunction has an even parity with respect to the perpendicular plane and u, "ungerade" (odd in German) represents the odd symmetry states.

Equation 3.1.7 is separable in the prolate spheroidal coordinates, also called parabolic coordinates [14]. Although these coordinates give the correct symmetry of the system, their implementation to use them later as a basis for a two-electron problem (H_2) introduces a huge complexity. It is more affordable to solve the equation 3.1.7 using the spherical coordinates. To use this coordinates, the one-electron wavefunction, $\phi_{n,\lambda,\sigma}(\mathbf{r};\mathbf{R})$, is expressed as a central angular expansion of spherical harmonics, $Y_l^{\pm\lambda}(\theta,\varphi)$:

$$\phi_{n,\lambda,\sigma}(\mathbf{r};\mathbf{R}) = \sum_{l=0}^{l_{max}} \frac{U_{n,\sigma,l}(r;\mathbf{R})}{r} Y_l^{\pm\lambda}(\theta,\varphi) \tag{3.1.8}$$

where $U_{n,\sigma,l}(r;\mathbf{R})$ is the radial wavefunction. According to the linear variational principle [95, 163], the above equation should include an infinite expansion of angular momenta. However, for practical computational reasons, we truncate the expansion at a certain value of the angular quantum number, l_{max}. In addition, the radial wavefunction, $U_{n,\sigma,l}(r;\mathbf{R})$, is expanded as a linear combination of B-spline functions, $B_{i,l}^{n,\sigma}(r;\mathbf{R})$, [103]:

$$U_{n,\sigma,l}(r;\mathbf{R}) = \sum_{i=0}^{N_l} c_{i,l}^{n,\sigma} B_i^{n,\sigma}(r;\mathbf{R}) \tag{3.1.9}$$

where N_l indicates the total number of B-splines used in the basis set. In our calculations, we use the same number of B-splines for each angular momenta in the expansion. The B-splines are polynomial functions which are defined over a sequence of inner turning points in the radial position interval $[0, r_{max}]$. A complete overview of the B-splines properties and their use as a basis set of functions can be found [37, 67, 129, 10, 103, 106].

Equation 3.1.7 can be solved using the linear variational principle. Inserting the expansions given in equations 3.1.8 and 3.1.9 in the TISE defined in equation 3.1.7, we obtain a system of linear equations. The solutions of this system are the coefficients, $c_{i,l}^n$, of the expansion. The matrix form of this system of linear equations constitutes an eigenvalue problem, whose expression is:

$$\widetilde{H}\mathbf{c} = E\widetilde{S}\mathbf{c} \tag{3.1.10}$$

where E are the energies of the different states of the H_2^+ and $\mathbf{c}$ is the vector formed by the coefficients of the B-splines expansion, $c_{i,l}^n$. In the above eigenvalue problem, $\widetilde{H}$ and $\widetilde{S}$ are the Hamiltonian and overlap matrices between the functions of the basis set, whose elements have the general expressions:

$$H_{i,l;i',l'}^{n,\lambda,\sigma} = \int_0^{r_{max}} \int_0^{\pi} \int_0^{2\pi} \overline{B_i^{n,\sigma}}(r;\mathbf{R})\, \overline{Y_l^{\pm\lambda}}(\theta,\varphi)\, \widehat{H}_{el} B_{i'}^{n,\sigma}(r;\mathbf{R})\, Y_{l'}^{\pm\lambda}(\theta,\varphi) \sin(\theta)\, dr d\theta d\varphi \tag{3.1.11}$$

$$S_{i,l;i',l'}^{n,\lambda,\sigma} = \int_0^{r_{max}} \overline{B_i^{n,\sigma}}\left(r;\mathbf{R}\right) B_{i'}^{n,\sigma}\left(r;\mathbf{R}\right) dr\delta_{l,l'} \tag{3.1.12}$$

where $\widehat{H}_{el}$ in the Hamiltonian matrix elements, $H_{i,l;i',l'}^{n,\sigma,\lambda}$, is the electronic Hamiltonian operator for the hydrogen molecular ion, given in equation 3.1.7. As the B-splines are not orthonormal, the overlap between the different B-splines functions is not zero and the overlap matrix cannot be considered equal to the identity matrix, $\widetilde{I}$, being necessary its calculation. Finally, to obtain the wavefunctions, $\phi_{n,\lambda,\sigma}\left(\mathbf{r};\mathbf{R}\right)$, from equation 3.1.7, we have to impose the boundary conditions to the wavefunctions obtained in the diagonalization of the matrix problem. We impose that the radial wavefunctions, $U_{n,\sigma,l}\left(r;\mathbf{R}\right)$, and therefore, the wavefunctions, $\phi_{n,\lambda,\sigma}\left(\mathbf{r};\mathbf{R}\right)$, have to be zero in the limits of the box in which we define the B-splines, $U_{n,\sigma,l}\left(r=0;\mathbf{R}\right)=0$ and $U_{n,\sigma,l}\left(r=r_{max};\mathbf{R}\right)=0$.

3.1.2 Electronic states of the H_2

The field-free electronic states of the hydrogen molecule ($H_2/H_2^+ + e^-$), are solutions of the TISE:

$$\begin{aligned}\left[-\frac{\hbar^2}{2m_e}\sum_{i=1}^{2}\nabla_i^2 - \sum_{\alpha=1}^{2}\sum_{i=1}^{2}\frac{1}{4\pi\varepsilon_0}\frac{e^2}{|\mathbf{r}_i-\mathbf{R}_\alpha|} + \frac{1}{4\pi\varepsilon_0}\frac{e^2}{|\mathbf{r}_1-\mathbf{r}_2|} + \right.\\ \left. + \frac{1}{4\pi\varepsilon_0}\frac{e^2}{R}\right]\psi_{n,\sigma,\Lambda}^{S}\left(\mathbf{r};\mathbf{R}\right) = E_{n,\sigma,\Lambda}\left(\mathbf{R}\right)\psi_{n,\sigma,\Lambda}^{S}\left(\mathbf{r};\mathbf{R}\right)\end{aligned} \tag{3.1.13}$$

where $\mathbf{r}_i$ is the position vector of each electron, $\mathbf{R}_\alpha$ is the position vector of each nucleus and R is the internuclear distance between both nuclei, $R=|\mathbf{R}_1-\mathbf{R}_2|$. In the above TISE, the electronic Hamiltonian operator includes the kinetic energy and nucleus-electron attraction terms for both electrons, as well as the electron-electron and nucleus-nucleus repulsion terms.

The electronic wavefunctions, $\psi_{n,\sigma,\Lambda}^{S}\left(\mathbf{r};\mathbf{R}\right)$, and energies, $E_{n,\sigma,\Lambda}\left(\mathbf{R}\right)$, of this system are obtained using the configuration interaction method, CI [95, 163]. In this method, the wavefunction, $\psi_{n,\sigma,\Lambda}^{S}\left(\mathbf{r};\mathbf{R}\right)$, is expanded as a linear combination of the antisymmetric product of two one-electron wavefunctions, $\phi_{n_k,\lambda_k,\sigma_k}\left(\mathbf{r}_i;\mathbf{R}\right)$:

$$\begin{aligned}\psi_{n,\sigma,\Lambda}^{S}\left(\mathbf{r}_1,\mathbf{r}_2;\mathbf{R}\right) = \sum_{n_1}\sum_{n_2>n_1}\sum_{\lambda_1} c_{n_1,n_2;\sigma_1,\sigma_2}^{\lambda_1,\lambda_2}\cdot\\ \cdot\left[\phi_{n_1,\lambda_1,\sigma_1}\left(\mathbf{r}_1;\mathbf{R}\right)\phi_{n_2,\lambda_2,\sigma_2}\left(\mathbf{r}_2;\mathbf{R}\right) \pm \phi_{n_1,\lambda_1,\sigma_1}\left(\mathbf{r}_2;\mathbf{R}\right)\phi_{n_2,\lambda_2,\sigma_2}\left(\mathbf{r}_1;\mathbf{R}\right)\right]\cdot\\ \cdot\left[s_\alpha\left(1\right)s_\beta\left(2\right) \mp s_\beta\left(1\right)s_\alpha\left(2\right)\right]\end{aligned} \tag{3.1.14}$$

where $s_x\left(i\right)$ ($x=\alpha,\beta$ and $i=1,2$) are the spin wavefunctions of each electron. Because the electrons are fermions, the above two-electron wavefunctions have to satisfy the Pauli principle. The Pauli principle [28] indicates that the wavefunction has to be antisymmetric with respect to the exchange of both electrons. The antisymmetry can be introduced in the spatial or spin part of the wavefunction.

In the two-electron wavefunction given in equation 3.1.14, when the antisymmetry is introduced in the spin part $(s_\alpha(1)\, s_\beta(2) - s_\beta(1)\, s_\alpha(2))$, the total spin is singlet, S, and the spatial part is symmetric. While, when the spin part is symmetric $(s_\alpha(1)\, s_\beta(2) + s_\beta(1)\, s_\alpha(2),\ s_\alpha(1)\, s_\alpha(2)$ or $s_\beta(1)\, s_\beta(2))$, the state is triplet, T, and the spatial part introduces the antisymmetry.

In our particular case, we use the calculated wavefunctions for the hydrogen molecular ion, $\phi_{n_k,\lambda_k,\sigma_k}(\mathbf{r}_i;\mathbf{R})$, as the one-electron wavefunctions in the CI expansion. These one-electron wavefunctions satisfy the symmetry properties of the system. In this way, the total parity of the wavefunction, $\psi^S_{n,\sigma,\Lambda}(\mathbf{r};\mathbf{R})$, is equal to the product of the parities of the one-electron wavefunctions, $\sigma = \sigma_1 \cdot \sigma_2$, knowing that these symmetry products satisfy the relations: $g \cdot g = u \cdot u = g$ and $g \cdot u = u \cdot g = u$, and the total azimuthal quantum number is the sum of the module of the angular momentum quantum numbers of each one-electron wavefunctions, $\Lambda = |m_1 + m_2|$. The expression of the total wavefunction, $\psi^S_{n,\sigma,\Lambda}(\mathbf{r};\mathbf{R})$, can be obtained by a diagonalization procedure of the CI matrix. This CI matrix is obtained with the same linear variational principle used in the hydrogen molecular ion, in which, we substitute the expansion of the wavefunction $\psi_{n,\sigma,\Lambda,S}(\mathbf{r};\mathbf{R})$, in the electronic TISE, given in equation 3.1.13, and later we project into the basis set used, obtaining a system of linear equations which constitute a eigenvalue problem. Its diagonalization gives the energies, $E_{n,\sigma,\Lambda}(\mathbf{R})$, and the CI coefficients, $c^{\lambda_1,\lambda_2}_{n_1,n_2;\sigma_1,\sigma_2}$, which determine the wavefunctions, $\psi^S_{n,\sigma,\Lambda}(\mathbf{r};\mathbf{R})$, and therefore, describe the bound states of the hydrogen molecule, H_2.

The continuum states, $H_2^+ + e^-$, which describe the ejection of one electron from the molecular system, constitute a scattering problem. The solutions of the global scattering problem, including the continuum and resonant states, are determined by the appropriate boundary conditions to describe the system. Each boundary condition imposed to the system gives a set of quantum number, which can determine one or more wavefunctions for each energy. Each set of quantum numbers, which defines a scattering wavefunction, is called channel [49]. Analyzing the asymptotic form of the channels, they can be separated in two groups, the open and close channels. The open channels have an oscillatory behavior of the wavefunctions in the asymptotic region, which correspond to the continuum states, also called non-resonant states. On the other hand, in the close channels, the wavefunctions tend to zero in the asymptotic region, and therefore, have a bound-like behavior, corresponding to the resonant states. Although the direct solution of the Hamiltonian operator, presented in equation 3.1.13, gives the full set of continuum and resonant states of our system, these states are mixed as stationary eigenfunctions of this Hamiltonian operator, and therefore, we can not use to obtain the nuclear wavefunction in the Born-Oppenheimer approximation. To give an electronic and nuclear description of the system, the Hilbert's space of the scattering states, in which all the resonant and continuum wavefunctions are contained, has to be separated in two subspaces. To make this separation of the non-resonant scattering and resonant bound-like states, we use the Feshbach formalism [47, 46, 73], in which we define two projector operators, $\widehat{P}$ and $\widehat{Q}$. As the total wavefunction, $\psi^S_{n,\sigma,\Lambda}(\mathbf{r};\mathbf{R},\varepsilon)$, contains both continuum and resonant states, represented by the quantum numbers n and ε, the $\widehat{P}$ and $\widehat{Q}$ operators project

this total wavefunction in one of the two subspaces. The $\widehat{P}$ operator projects the total wavefunction, $\psi^S_{n,\sigma,\Lambda}(\mathbf{r};\mathbf{R})$, in the subspace of the non-resonant scattering states, $\widehat{P}\psi^S_{n,\sigma,\Lambda}(\mathbf{r};\mathbf{R},\varepsilon)$, and the $\widehat{Q}$ operator project in the subspace of the resonant bound-like states, $\widehat{Q}\psi^S_{n,\sigma,\Lambda}(\mathbf{r};\mathbf{R},\varepsilon)$. Since both operators divide the space in two complementary subspaces, they satisfy the completeness and orthogonality properties:

$$\widehat{P} + \widehat{Q} = \widehat{I} \tag{3.1.15}$$

$$\widehat{P}\widehat{Q} = \widehat{Q}\widehat{P} = 0 \tag{3.1.16}$$

where $\widehat{I}$ is the identity operator. In addition, both operator satisfy the idempotent property, $\widehat{P}^2 = \widehat{P}$ and $\widehat{Q}^2 = \widehat{Q}$. Using the completeness property of both operators, $\widehat{P}$ and $\widehat{Q}$, the total wavefunction, $\psi^S_{n,\sigma,\Lambda}(\mathbf{r};\mathbf{R})$, can be written as a linear combination of the continuum wavefunctions, $\widehat{P}\psi^S_{n,\sigma,\Lambda}(\mathbf{r};\mathbf{R})$, plus the resonant wavefunctions, $\widehat{Q}\psi^S_{n,\sigma,\Lambda}(\mathbf{r};\mathbf{R})$:

$$\psi^S_{n,\sigma,\Lambda}(\mathbf{r};\mathbf{R},\varepsilon) = \widehat{P}\psi^S_{n,\sigma,\Lambda}(\mathbf{r};\mathbf{R},\varepsilon) + \widehat{Q}\psi^S_{n,\sigma,\Lambda}(\mathbf{r};\mathbf{R},\varepsilon) \tag{3.1.17}$$

Introducing this expression for the total wavefunction, $\psi_{n,\sigma,\Lambda,S}(\mathbf{r};\mathbf{R},\varepsilon)$, in equation 3.1.13, the electronic TISE in the Feshbach formalism can be written as:

$$\begin{aligned}\widehat{H}\widehat{P}\psi^S_{n,\sigma,\Lambda}(\mathbf{r};\mathbf{R},\varepsilon) + \widehat{H}\widehat{Q}\psi^S_{n,\sigma,\Lambda}(\mathbf{r};\mathbf{R},\varepsilon) = \\ E_{n,\sigma,\Lambda}(\mathbf{R})\,\widehat{P}\psi^S_{n,\sigma,\Lambda}(\mathbf{r};\mathbf{R},\varepsilon) + E_{n,\sigma,\Lambda}(\mathbf{R})\,\widehat{Q}\psi^S_{n,\sigma,\Lambda}(\mathbf{r};\mathbf{R},\varepsilon)\end{aligned} \tag{3.1.18}$$

where $\widehat{H}$ is the Hamiltonian operator given in equation 3.1.13. Now, projecting on the right hand side into the $\widehat{P}$ or $\widehat{Q}$ operators and reordering the result equations, we obtain two coupled equations:

$$\left[E_{n,\sigma,\Lambda}(\mathbf{R},\varepsilon) - \widehat{P}\widehat{H}\widehat{P}\right]\widehat{P}\psi^S_{n,\sigma,\Lambda}(\mathbf{r};\mathbf{R},\varepsilon) = \widehat{P}\widehat{H}\widehat{Q}\psi^S_{n,\sigma,\Lambda}(\mathbf{r};\mathbf{R},\varepsilon) \tag{3.1.19}$$

$$\left[E_{n,\sigma,\Lambda}(\mathbf{R},\varepsilon) - \widehat{Q}\widehat{H}\widehat{Q}\right]\widehat{Q}\psi^S_{n,\sigma,\Lambda}(\mathbf{r};\mathbf{R},\varepsilon) = \widehat{Q}\widehat{H}\widehat{P}\psi^S_{n,\sigma,\Lambda}(\mathbf{r};\mathbf{R},\varepsilon) \tag{3.1.20}$$

To solve this system of coupled equations, we take the second equation to obtain a general expression in the Feshbach formalism for the resonant wavefunctions, $\widehat{Q}\psi^S_{n,\sigma,\Lambda}(\mathbf{r};\mathbf{R},\varepsilon)$:

$$\widehat{Q}\psi^S_{n,\sigma,\Lambda}(\mathbf{r};\mathbf{R},\varepsilon) = \frac{\widehat{Q}\widehat{H}}{\left[E_{n,\sigma,\Lambda}(\mathbf{R},\varepsilon) - \widehat{Q}\widehat{H}\widehat{Q}\right]}\widehat{P}\psi^S_{n,\sigma,\Lambda}(\mathbf{r};\mathbf{R},\varepsilon) \tag{3.1.21}$$

In this equation, the term $1/\left[E_{n,\sigma,\Lambda}(\mathbf{R},\varepsilon) - \widehat{Q}\widehat{H}\widehat{Q}\right]$ is called the resolvent and is associated with its respective Green's functions. Introducing this expression of the resonant wavefunction in equation 3.1.19, and reordering, we obtain the general expression to be satisfied by the continuum states in the Feshbach formalism:

$$\widehat{P}\left[\widehat{H}+\widehat{H}\widehat{Q}\frac{1}{\left[E_{n,\sigma,\Lambda}\left(\mathbf{R},\varepsilon\right)-\widehat{Q}\widehat{H}\widehat{Q}\right]}\widehat{Q}\widehat{H}-E_{n,\sigma,\Lambda}\left(\mathbf{R},\varepsilon\right)\right]\widehat{P}\psi^{S}_{n,\sigma,\Lambda}\left(\mathbf{r};\mathbf{R},\varepsilon\right)=0 \tag{3.1.22}$$

However, the solution of this system of equations is very complicated, therefore, first we solve the equation 3.1.20, neglecting the coupling with the continuum wavefunctions, $\widehat{Q}\widehat{H}\widehat{P}\psi^{S}_{n,\sigma,\Lambda}\left(\mathbf{r};\mathbf{R}\right)$:

$$\left[E_{r,\sigma,\Lambda}\left(\mathbf{R}\right)-\widehat{Q}\widehat{H}\widehat{Q}\right]\psi_{r,\sigma,\Lambda}\left(\mathbf{r};\mathbf{R}\right)=0 \tag{3.1.23}$$

whose solutions, the wavefunctions $\psi_{r,\sigma,\Lambda}\left(\mathbf{r};\mathbf{R}\right)$, are eigenfunctions of the operator $\widehat{Q}\widehat{H}\widehat{Q}$. Because the eigenfunction of an operator is also eigenfunction of any function of this operator, these resonant wavefunctions, $\psi_{r,\sigma,\Lambda}\left(\mathbf{r};\mathbf{R}\right)$, are also eigenfunctions of the resolvent operator, $1/\left[E_{n,\sigma,\Lambda}\left(\mathbf{R},\varepsilon\right)-\widehat{Q}\widehat{H}\widehat{Q}\right]$. Then, we can expresses the resolvent operator in the terms of the complete set of the wavefunctions $\psi_{r,\sigma,\Lambda}\left(\mathbf{r};\mathbf{R}\right)$, which is the spectral representation of the resolvent operator:

$$\frac{1}{\left[E_{r,\sigma,\Lambda}\left(\mathbf{R},\varepsilon\right)-\widehat{Q}\widehat{H}\widehat{Q}\right]}=\sum_{r}\frac{\left|\psi_{r,\sigma,\Lambda}\right\rangle\left\langle\psi_{r,\sigma,\Lambda}\right|}{E_{n,\sigma,\Lambda}\left(\mathbf{R},\varepsilon\right)-E_{r,\sigma,\Lambda}\left(\mathbf{R}\right)} \tag{3.1.24}$$

where $\left|\psi_{r,\sigma,\Lambda}\right\rangle$ is the representation of the resonant state vector in the Hilbert's space, associated with the wavefunctions $\psi_{r,\sigma,\Lambda}\left(\mathbf{r};\mathbf{R}\right)$. The relation of the wavefunction, $\psi_{r,\sigma,\Lambda}\left(\mathbf{r};\mathbf{R}\right)$, and its state vector in the Hilbert's space can be obtained by the projection of the state vector into the basis set of the position vectors, $\psi_{r,\sigma,\Lambda}\left(\mathbf{r};\mathbf{R}\right)=\left\langle\mathbf{r};\mathbf{R}\mid\psi_{r,\sigma,\Lambda}\right\rangle$, both in the Hilbert's space. Substituting this expression of the resolvent in terms of the $\widehat{Q}\widehat{H}\widehat{Q}$ operator wavefunctions, equation 3.1.19 becomes:

$$\widehat{P}\left[\widehat{H}+\sum_{r}\widehat{H}\widehat{Q}\frac{\left|\psi_{r,\sigma,\Lambda}\right\rangle\left\langle\psi_{r,\sigma,\Lambda}\right|}{E_{n,\sigma,\Lambda}\left(\mathbf{R},\varepsilon\right)-E_{r,\sigma,\Lambda}\left(\mathbf{R}\right)}\widehat{Q}\widehat{H}-E_{n,\sigma,\Lambda}\left(\mathbf{R},\varepsilon\right)\right]\widehat{P}\psi^{S}_{n,\sigma,\Lambda}\left(\mathbf{r};\mathbf{R},\varepsilon\right)=0 \tag{3.1.25}$$

which can be written in a more compact form as:

$$\left[\widehat{P}\widehat{H}\widehat{P}+\widehat{H}'-E_{\alpha}\left(\mathbf{R},\varepsilon_{\alpha}\right)\right]\psi_{\alpha,l_{\alpha},m}\left(\mathbf{r};\mathbf{R},\varepsilon_{\alpha}\right)=0 \tag{3.1.26}$$

The wavefunction $\psi_{\alpha,l_{\alpha},m}\left(\mathbf{r};\mathbf{R},\varepsilon_{\alpha}\right)$ is the continuum wavefunction obtained by projecting the total wavefunction, $\psi^{S}_{n,\sigma,\Lambda}\left(\mathbf{r};\mathbf{R},\varepsilon\right)$, into the $\widehat{P}$ operator. This continuum wavefunction depends on the quantum number of the molecular ion, $\alpha=n,\sigma,\lambda$, and the corresponding quantum numbers of the ejected electron, ε_{α}, l_{α} and m. In addition, the operator $\widehat{H}'$ presented in equation 3.1.26 is the so-called optical potential:

$$\widehat{H}' = \sum_r \widehat{P}\widehat{H}\widehat{Q}\frac{|\psi_{r,\sigma,\Lambda}\rangle\langle\psi_{r,\sigma,\Lambda}|}{E_{n,\sigma,\Lambda}(\mathbf{R},\varepsilon) - E_{r,\sigma,\Lambda}(\mathbf{R})}\widehat{Q}\widehat{H}\widehat{P} \tag{3.1.27}$$

The resonant states, which include the coupling with the continuum states, can be calculated by a perturbative method of any order, using the continuum states given in equation 3.1.26. The presented Feshbach formalism split the Hamiltonian operator as $\widehat{H} = \widehat{P}\widehat{H}\widehat{P} + \widehat{Q}\widehat{H}\widehat{Q} + \widehat{Q}\widehat{H}\widehat{P} + \widehat{P}\widehat{H}\widehat{Q}$, where the last two terms are the couplings between both subspaces. These couplings are the responsible for the resonances decay into the continua [44]. In practice, instead of solving the coupled problem presented between both subspaces, we solve the resonance states and continuum states without the coupling terms, and later we introduce these $\widehat{Q}\widehat{H}\widehat{P}$ and $\widehat{P}\widehat{H}\widehat{Q}$ couplings, in the solution of the TDSE. In this way, the real scattering states with their electrostatic couplings are constructed in the time domain, instead of constructing in the usual time independent framework. Therefore, we can now neglect the electrostatic coupling terms in the calculation of the stationary states of both subspaces.

First, we obtain the continuum states of the non-resonant subspace. These states are the solution of equation 3.1.25, neglecting the optical potential which couples the continuum states with the resonant states:

$$\left[\widehat{P}\widehat{H}\widehat{P} - E_\alpha(\mathbf{R},\varepsilon_\alpha)\right]\psi^0_{\alpha,l_\alpha,m}(\mathbf{r};\mathbf{R},\varepsilon_\alpha) = 0 \tag{3.1.28}$$

where the superindex 0 in the wavefunction $\psi^0_{\alpha,l_\alpha,m}(\mathbf{r};\mathbf{R},\varepsilon_\alpha)$ indicates that the coupling term with the resonant subspace is neglected. This conforms the static-exchange approximation for the non-resonant states. As in the solutions of the TISE for the bound states of the H_2, the wavefunction is obtained using an expansion of the basis set of the H_2^+ wavefunctions. The channels can be considered as the antisymmetric product of the H_2^+ wavefunctions multiplied by the ejected electron wavefunctions. As it can be demonstrated [49], the Hamiltonian operator of the H_2^+ does not commute with the Hamiltonian operator of the H_2 system in the spherical coordinates used. Therefore, the channels formed by the antisymmetric product of the H_2^+ wavefunctions with the ejected electron wavefunctions have to be coupled to obtain the correct boundary conditions of the scattering problem. This constitutes a multichannel problem. To solve this multichannel continuum problem, we use the L^2 close-coupling method [158, 159, 10, 103]. This method is based on separating the scattering problem in two parts. In the first part, we transform the multichannel problem in a sum of several single-channel problems, in which the channels are not coupled. In the second part, the solutions of single-channel problems are coupled with the Lipmann-Schwinger formalism [73], which includes the correct boundary conditions to the total scattering problem treated.

The first step, in the L^2 close-coupling method, is to obtain the scattering wavefunctions of the single-channel problem. We define the uncoupled-continuum states, UCS, whose wavefunctions, $\Phi_{\alpha,l_\alpha,m}(\mathbf{r};\mathbf{R},\varepsilon_\alpha)$, are equal to the antisymmetric product of the H_2^+ wavefunctions, $\phi_\alpha(\mathbf{r};\mathbf{R})$, with the ejected electron scattering wavefunctions, $\xi_{l_\alpha,m}(\mathbf{r};\mathbf{R},\varepsilon_\alpha)$:

$$\Phi_{\alpha,l_\alpha,m}(\mathbf{r};\mathbf{R},\varepsilon_\alpha)=\frac{1}{\sqrt{2}}\left[\phi_\alpha(\mathbf{r}_1;\mathbf{R})\,\xi_{\alpha,l_\alpha,m}(\mathbf{r}_2;\mathbf{R},\varepsilon_\alpha)+\phi_\alpha(\mathbf{r}_2;\mathbf{R})\,\xi_{\alpha,l_\alpha,m}(\mathbf{r}_1;\mathbf{R},\varepsilon_\alpha)\right] \tag{3.1.29}$$

where the H_2^+ wavefunction, $\phi_\alpha(\mathbf{r}_i;\mathbf{R})$, has been previously calculated for the hydrogen molecular ion. The above UCS is selected to give a singlet state, where the antisymmetry is carried by the spin part $(s_\alpha(1)\,s_\beta(2)-s_\beta(1)\,s_\alpha(2))$. These H_2^+ wavefunctions determine the ionization threshold. The solution of the scattering problem gives the expressions for the ejected electron wavefunction, $\xi_{\alpha,l_\alpha,m}(\mathbf{r}_i;\mathbf{R},\varepsilon_\alpha)$. To solve this scattering problem, the ejected electron scattering wavefunctions, $\xi_{\alpha,l_\alpha,m}(\mathbf{r};\mathbf{R},\varepsilon_\alpha)$, are written as a combination of a radial part, $U_{\alpha,l_\alpha}(r;\mathbf{R},\varepsilon_\alpha)/r$, multiplied by a spherical harmonics, $Y_{l_\alpha}^m(\theta,\varphi)$:

$$\xi_{\alpha,l_\alpha,m}(\mathbf{r}_i;\mathbf{R},\varepsilon_\alpha)=\frac{U_{\alpha,l_\alpha}(r;\mathbf{R},\varepsilon_\alpha)}{r}Y_{l_\alpha}^m(\theta,\varphi) \tag{3.1.30}$$

where, α is the ionic state, defined by the quantum number n, λ and σ of the residual ion H_2^+, l_α is the partial wave of the ejected electron associated with the ionic state α, and ε_α is the energy of the channel. The UCS wavefunctions, $\Phi_{\alpha,l_\alpha,m}(\mathbf{r};\mathbf{R},\varepsilon_\alpha)$, are solutions of the uncoupled Hamiltonian operator of order zero:

$$\sum_{\alpha'}\sum_{l'_\alpha}\widehat{P}_{\alpha',l'_\alpha}\widehat{H}\widehat{P}_{\alpha',l'_\alpha}\Phi_{\alpha,l_\alpha,m}(\mathbf{r};\mathbf{R},\varepsilon_\alpha)=\varepsilon_\alpha\Phi_{\alpha,l_\alpha,m}(\mathbf{r};\mathbf{R},\varepsilon_\alpha) \tag{3.1.31}$$

where $\widehat{P}_{\alpha',l'_\alpha}$ is the projection operator into the partial wave l_α. This operator satisfies the relations:

$$\widehat{P}_{\alpha,l_\alpha}\Phi_{\alpha,l_\alpha,m}(\mathbf{r};\mathbf{R},\varepsilon_\alpha)=\Phi_{\alpha,l_\alpha,m}(\mathbf{r};\mathbf{R},\varepsilon_\alpha) \tag{3.1.32}$$

$$\widehat{P}_{\alpha,l_\alpha}\widehat{P}_{\alpha',l'_\alpha}=\delta_{\alpha,\alpha'}\delta_{l_\alpha,l'_\alpha}\widehat{P}_{\alpha,l_\alpha} \tag{3.1.33}$$

After separately solving of the uncoupled scattering problems, we combine the UCS wavefunctions, $\Phi_{\alpha,l_\alpha,m}(\mathbf{r};\mathbf{R},\varepsilon_\alpha)$, to obtain the scattering wavefunctions, $\psi^0_{\alpha,l_\alpha,m}(\mathbf{r};\mathbf{R},\varepsilon_\alpha)$. This combination is achieved through the Lipmann-Schwinger equation, which introduces the correct boundary conditions which define the final scattering wavefunctions, $\psi^0_{\alpha,l_\alpha,m}(\mathbf{r};\mathbf{R},\varepsilon_\alpha)$:

$$\psi^0_{\alpha,l_\alpha,m}(\mathbf{r};\mathbf{R},\varepsilon_\alpha)=\Phi_{\alpha,l_\alpha,m}(\mathbf{r};\mathbf{R},\varepsilon_\alpha)+\widehat{G}(\varepsilon_\alpha)\,\widehat{V}\Phi_{\alpha,l_\alpha,m}(\mathbf{r};\mathbf{R},\varepsilon_\alpha) \tag{3.1.34}$$

where $\widehat{G}(\varepsilon_\alpha)$ is the Green's function associated with the Hamiltonian operator, $\widehat{H}$, and $\widehat{V}$ is the coupling potential between the UCS with different partial waves:

$$\widehat{G}(\varepsilon_\alpha)=\lim_{\eta\to0}\frac{1}{\varepsilon_\alpha-\widehat{H}-i\eta} \tag{3.1.35}$$

$$\widehat{V} = \sum_{\alpha} \sum_{l_\alpha} \sum_{\alpha' \neq \alpha} \sum_{l'_\alpha \neq l_\alpha} \widehat{P}_{\alpha,l_\alpha} \widehat{H} \widehat{P}_{\alpha',l'_\alpha} \tag{3.1.36}$$

To describe the continuum problem, we will discretize it in a finite box. The continuum wavefunction are transformed in bound-like states and the scattering states are obtained in the L^2 clouse-coupling [146, 35, 103, 106] method with the discretized wavefunctions. The discretization procedure is based on the use of a basis set constituted by L^2 integrable functions. This assures that the UCS are normalized as bound states. The radial part, $U_{\alpha,n_\alpha,l_\alpha}(r;\mathbf{R},\varepsilon_\alpha)$, is expanded in a linear combination of B-splines, $B_i^{\alpha,l_\alpha}(r;\mathbf{R},\varepsilon_\alpha)$ which is introduced in the central spherical expansion of $\xi_{\alpha,l_\alpha,m}(\mathbf{r};\mathbf{R},\varepsilon_\alpha)$:

$$\xi_{\alpha,n_\alpha,l_\alpha,m}(\mathbf{r}_i;\mathbf{R}) = \sum_i \frac{c_i^{\alpha,n_\alpha,l_\alpha} B_i^{\alpha,n_\alpha,l_\alpha}(r;\mathbf{R})}{r} Y_{l_\alpha}^m(\theta,\varphi) \tag{3.1.37}$$

where n_α is the discrete quantum number for the energy state. Using the L^2 clouse-coupling method, the discretized UCS wavefunctions are the solutions of the TISE in a finite box. However, to satisfy the boundary conditions of the problem, the discretized continuum wavefunctions have to introduce the correct asymptotic behavior of the real continuum wavefunctions. Focusing on the single-channel problems, the discretized wavefunctions can reproduce exactly the real continuum wavefunctions, except for a normalization factor. This normalization factor, is the density of states, $\rho(\varepsilon_{n_\alpha})$:

$$\Phi_{\alpha,l_\alpha,m}(\mathbf{r};\mathbf{R},\varepsilon_\alpha) = \rho^{1/2}(\varepsilon_{n_\alpha})\,\Phi_{\alpha,n_\alpha,l_\alpha,m}(\mathbf{r}_i;\mathbf{R}) \tag{3.1.38}$$

The density of states, $\rho(\varepsilon_{n_\alpha})$, can be obtained by two different methods. The most direct method consists of the comparison in the asymptotic region with the exact continuum wavefunction, which can be obtained analytically or numerically. For this, the discretized wavefunction has to be calculated in a far enough region, where it can be considered that the state has reached the asymptotic behavior. However, this method can be only applied to systems in which the exact continuum wavefunction is known in the asymptotic region. Therefore, it is limited to several particular scattering problems. In the second method, the density of states is extracted from the discretized energy spectrum. These energies, obtained in the diagonalization of the discretized wavefunctions, depend on the quantum number, n_α. Using the L^2 integrable functions, the density of states, $\rho(E_n)$, is equal to the inverse of the change of the discrete energy as a function of the quantum number, n_α:

$$\rho(\varepsilon_{n_\alpha}) = \left| \frac{\partial \varepsilon_{n_\alpha}}{\partial n_\alpha} \right|^{-1} \tag{3.1.39}$$

Although the energy does not depend on the continuous variable, if the energy difference among the successive n_α quantum numbers is close enough, the derivative can be transformed in the difference between the two closer energies around

the energy of the state n_α. Applying this approximation, the derivative can be approximated as:

$$\left|\frac{\partial \varepsilon_{n_\alpha}}{\partial n_\alpha}\right| \simeq \frac{\varepsilon_{n_\alpha+1} - \varepsilon_{n_\alpha-1}}{(n_\alpha+1)-(n_\alpha-1)} = \frac{\varepsilon_{n_\alpha+1} - \varepsilon_{n_\alpha-1}}{2} \tag{3.1.40}$$

As in the non-discretized case presented before, after obtaining the discretized UCS wavefunction, $\Phi_{\alpha,n_\alpha,l_\alpha,m}(\mathbf{r}_i;\mathbf{R})$, they are coupled by the Lipmann-Schwinger equation, which includes the correct boundary conditions, to obtain the scattering wavefunction, $\psi^0_{\alpha,l_\alpha,m}(\mathbf{r};\mathbf{R},\varepsilon_\alpha)$:

$$\begin{aligned}\psi^0_{\alpha,l_\alpha,m}(\mathbf{r};\mathbf{R},\varepsilon_\alpha) = \rho^{1/2}(\varepsilon_{n_\alpha})\,\Phi_{\alpha,n_\alpha,l_\alpha,m}(\mathbf{r}_i;\mathbf{R}) + \\ +\widehat{G}(\varepsilon_\alpha)\,\widehat{V}\rho^{1/2}(\varepsilon_{n_\alpha})\,\Phi_{\alpha,n_\alpha,l_\alpha,m}(\mathbf{r}_i;\mathbf{R})\end{aligned} \tag{3.1.41}$$

These continuum wavefunctions of the $H_2/H_2^+ + e^-$ system, constitute the P subspace in the static-exchange approximation of the Feshbach formalism.

On the other hand, resonant states, solutions of the Q subspace in the Feshbach formalism, are solutions of the TISE:

$$\left[E_{r,\sigma,\Lambda}(\mathbf{R}) - \widehat{Q}\widehat{H}\widehat{Q}\right]\psi_{r,\sigma,\Lambda}(\mathbf{r};\mathbf{R}) = 0 \tag{3.1.42}$$

where we neglect the coupling with the P subspace. However, instead of solving this equation, we can solve the equivalent but simpler TISE for an effective Hamiltonian operator, $\widehat{H}_{eff}$. This effective Hamiltonian operator, $\widehat{H}_{eff}$, is constituted by the Hamiltonian operator of the H_2, $\widehat{H}$, plus the Phillips-Kleinman pseudopotential, $M\widehat{P}$, where $\widehat{P}$ is the projection operator into the non-resonant continuum subspace and M is a large real number. As it can be demonstrated [105], the solutions of the TISE with this effective Hamiltonian operator, $\widehat{H}_{eff} = \widehat{H} + M\widehat{P}$, are the same than the solutions obtained with equation 3.1.42:

$$\left[\widehat{H} + M\widehat{P}\right]\psi_{r,\sigma,\Lambda}(\mathbf{r};\mathbf{R}) = E_{r,\sigma,\Lambda}(R)\,\psi_{r,\sigma,\Lambda}(\mathbf{r};\mathbf{R}) \tag{3.1.43}$$

In this equation, the effect of $M\widehat{P}$ is project to upwards the wavefunctions corresponding to the P subspace, so the first wavefunctions and energies obtained by the variational principle are the corresponding resonant states. To solve this TISE, we have to know the expression of the $\widehat{P}$ projection operator. Following our description for the bound and continuum states, the resonant wavefunctions are CI wavefunctions, constituted by the antisymmetric product of the H_2^+ wavefunction, $\phi_{n,\lambda,\sigma}(\mathbf{r}_i;\mathbf{R})$. These resonant states are bound state embedded in the different continua, in which both electrons are excited. This double excitation of both electrons gives the name of doubly excited states. In addition, the resonant states are joint in groups, called series, over the different ionization threshold. To obtain the resonant states, we express the $\widehat{P}$ operator in terms of the one-electron wavefunctions, corresponding to the ionization threshold under the energy region where serie of the resonant states, in which we are interested, appears. Consequently, the Q_1 serie of the resonant states, associated with the first ionization

threshold, $1s\sigma_g$, can be obtained making the $\widehat{P}$ operator equal to the one-electron wavefunction of this threshold, $\widehat{P} = \phi_{1s\sigma_g}(\mathbf{r}_i;\mathbf{R})$. If we apply this operator in the CI expansion, all the states with a non-zero contribution of the configurations which contain the one-electron wavefunction $\phi_{1s\sigma_g}(\mathbf{r}_i;\mathbf{R})$, will increase their energies and the states with the lower energies obtained in the CI diagonalization will be the Q_1 resonant states. Following this procedure, Q_2 series of resonant states are calculated using the $\widehat{P}$ operator, $\widehat{P} = \phi_{1s\sigma_g}(\mathbf{r}_i;\mathbf{R}) + \phi_{2p\sigma_u}(\mathbf{r}_i;\mathbf{R})$, where $\phi_{2p\sigma_u}(\mathbf{r}_i;\mathbf{R})$ is the residual ion wavefunction of the second ionization threshold. Including more one-electron wavefunctions of the upper ionic threshold in the expression of the $\widehat{P}$ operator, we can obtain all the resonant state series.

In our case, as the eigenstates of the hydrogen molecular ion are orthonormal, the Phillips-Kleinman method is analogous to use a truncated basis set to describe the doubly excited states. In this method we diagonalize the Hamiltonian operator using an expansion for the resonant states, without including the configuration of the one-electron wavefunction for the first ionization threshold, $\phi_{1s\sigma_g}(\mathbf{r}_i;\mathbf{R})$, for the Q_1 serie, the one-electron wavefunction of the first and second ionization threshold, $\phi_{1s\sigma_g}(\mathbf{r}_i;\mathbf{R})$ and $\phi_{2p\sigma_u}(\mathbf{r}_i;\mathbf{R})$, for the Q_2 serie, etc.. In practice, the TISE of the resonant states is solved as the bound states of the H_2, where we neglect some configuration terms depending on the resonant series treated.

3.2 Vibrational structure

Once we have the electronic structure, we have the full set of PES/PEC as a function of the nuclear coordinates, $\mathbf{R}$. Now, we can solve the TISE for the nuclei. The nuclear TISE given in equation 3.1.6 is written for two nuclei as:

$$\left[-\frac{\hbar^2}{2M_1}\nabla_1^2 - \frac{\hbar^2}{2M_2}\nabla_2^2 + E(\mathbf{R})\right]\chi(\mathbf{R}) = E\chi(\mathbf{R}) \tag{3.2.1}$$

where the electronic energies, $E(\mathbf{R})$, obtained from equations 3.1.7 and 3.1.13, are the potential terms which the nuclei feel in their motion. The above nuclear TISE can be solved using as reference system the center of mass [119], where the relations between the position vectors in both reference system are:

$$\begin{aligned}\mathbf{R}_{CM} &= \frac{M_1\mathbf{R}_1 + M_2\mathbf{R}_2}{M_1 + M_2}\\ \mathbf{R} &= \mathbf{R}_2 - \mathbf{R}_1\end{aligned} \tag{3.2.2}$$

In these expressions, $\mathbf{R}_1$ and $\mathbf{R}_2$ represent the position vectors of each nucleus, $\mathbf{R}_{CM}$ is the position vector of the center of mass and $\mathbf{R}$ is the position vector between both nuclei, so-called internal position vector. Equation 3.2.1 can be written in the center of mass reference system as:

$$\begin{aligned}\left[-\frac{\hbar^2}{2M}\nabla_{CM}^2 - \frac{\hbar^2}{2\mu}\nabla^2 + E_N(\mathbf{R})\right]\chi_{N,v_N,J}(\mathbf{R},\mathbf{R}_{CM};\mathbf{k}_{CM}) =\\ = E_{N,v_N}(\mathbf{k}_{CM})\,\chi_{N,v_N,J}(\mathbf{R},\mathbf{R}_{CM};\mathbf{k}_{CM})\end{aligned} \tag{3.2.3}$$

where ∇^2_{CM} is the Laplacian of the center of mass and ∇^2 is the Laplacian of the internal coordinates. M is the total nuclear mass, defined as $M = M_1 + M_2$, and μ is the reduced nuclear mass, defined as $\mu = M_1 M_2 / (M_1 + M_2)$, where M_1 and M_2 are the nuclear masses of both nuclei. Finally, R is the internuclear distance between both nuclei and $E_N(R)$ is the electronic energy for an electronic state N as a function of the internuclear distance. The quantum number N is a condensation of different electronic quantum numbers. This quantum number N represents to n, λ, σ, for the H_2^+ or n, Λ, σ for the H_2 case. Because the kinetic energy term of the center of mass is the unique term which depends on the center of mass coordinates, the nuclear TISE can be separated in two TISE, one for the center of mass and the other for the internal coordinates. The center of mass TISE is analogous to the TISE for a free particle moving in the space:

$$-\frac{\hbar^2}{2M}\nabla^2_{CM}\phi(\mathbf{R}_{CM};\mathbf{k}_{CM}) = E(\mathbf{k}_{CM})\,\phi(\mathbf{R}_{CM};\mathbf{k}_{CM}) \tag{3.2.4}$$

whose solutions are the plane waves. While, the TISE for the internal coordinates is:

$$\left[-\frac{\hbar^2}{2\mu}\nabla^2 + E_N(\mathbf{R})\right]\psi_{N,v_N,J}(\mathbf{R}) = E_{N,v_N}\psi_{N,v_N,J}(\mathbf{R}) \tag{3.2.5}$$

This equation contains the electronic energy because it only depends on the internuclear distance. This dependence with the internuclear distance of the electronic energy indicates that this equation 3.2.5, can be separated in the three space components using the spherical coordinates. The Laplacian operator, ∇^2, in the spherical coordinates, is:

$$\nabla^2 = \frac{1}{R^2}\frac{\partial}{\partial R}\left(R^2\frac{\partial}{\partial R}\right) - \frac{\left|\widehat{\mathbf{L}}\right|^2}{\hbar^2 R^2} \tag{3.2.6}$$

where $\left|\widehat{\mathbf{L}}\right|^2$ is the module square of the angular momentum operator. The nuclear wavefunction, $\psi_{n,\Lambda,\sigma v_n}(\mathbf{R})$, can be expressed in the spherical coordinates as the product of a radial wavefunction, $\chi_{N,v_N,J}(R)/R$, multiplied by a spherical harmonic, $Y_J^M(\theta,\varphi)$:

$$\psi_{N,v_N,J}(\mathbf{R}) = \frac{\chi_{N,v_N,J}(R)}{R}Y_J^M(\theta,\varphi) \tag{3.2.7}$$

These spherical harmonics, $Y_J^M(\theta,\varphi)$, are the eigenfunctions of the module square of the angular momentum operator, $\left|\widehat{\mathbf{L}}\right|^2 Y_J^M(\theta,\varphi) = J(J+1)\,Y_J^M(\theta,\varphi)$. Consequently, introducing the expression in spherical coordinates for the nuclear wavefunction, $\psi_{N,v_N,J}(\mathbf{R})$, in equation 3.2.5, the angular term of the Laplacian operator is transformed in an extra potential term, called centrifugal barrier [73]. In addition, as it can be demonstrated, the radial wavefunction, $\chi_{N,v_N,J}(R)/R$, transforms the radial terms of the Laplacian in a simple second derivative as a function of the internuclear distance, $\partial^2/\partial R^2$. Finally, the absence of any term

which depends on the angular variables, θ and φ, allows to eliminate the spherical harmonics from the equation, obtaining the nuclear TISE [30]:

$$\left[-\frac{\hbar^2}{2\mu}\frac{\partial^2}{\partial R^2}+\frac{J\left(J+1\right)}{2\mu R^2}+E_N\left(R\right)\right]\chi_{N,v_N,J}\left(R\right)= \\ =E_{N,v_N}\chi_{N,v_N,J}\left(R\right) \tag{3.2.8}$$

The nuclear radial wavefunction, $\chi_{N,v_N,J}\left(R\right)$, is expanded as a linear combination of a basis set. We again use B-splines functions as the underlying basis set:

$$\chi_{N,v_N,J}\left(R\right)=\sum_{i=1}^{N}c_i^{N,v_N,J}B_i^{N,v_N,J}\left(R\right) \tag{3.2.9}$$

Introducing the above expression for $\chi_{N,v_N,J}\left(R\right)$ in equation 3.2.8 and projecting into the same expansion, we obtain a eigenvalue problem (system of linear equation), that will be solved by means of a diagonalization procedure. The boundary conditions are imposed by making the nuclear radial wavefunction to go to zero in the extremes of the box: $\chi_{N,v_N,J}\left(R=0\right)=$ and $\chi_{N,v_N,J}\left(R=R_{max}\right)=0$, where the maximum size of the box is R_{max}.

The nuclear wavefunction depends on the quantum number N, v_N and J. This dependence with the nuclear angular quantum number, J, indicates that for each vibrational state of the system, we will have several nuclear rotational states. In this way, we have to solve the vibrational problem for all the possible vibrational states available. However, as we are interested in the transition processes induced by the ultrashort laser fields, the possible rotational states populated by this transition are determined by the dipole selection rules. Using the dipole selection rules for the rotational transitions in diatomic molecules between different electronic and vibrational states [180], we can simplify the possible states populated. If the transition is between two Σ bound states of the H_2, the rotational transition are only with $\triangle J=\pm1$, and when are between two other bound states of the H_2 which are not two Σ states, the rotational transition are only with $\triangle J=0,\pm1$. As we can consider that our system is in the ground rotational state before the interaction with the field, we can calculate only the rotational state in which the transition is possible, depending on the number of photon absorbed or emitted. On the other hand, when the transition is between the bound states and the continuum states of the H_2, the dipole selection rules are not the same as between bound states. The dipole selection rules, for the transition between a bound state and a continuum states, imply that $\triangle J=l+3/2,l+1/2,\ldots,-l-1/2,-l-3/2$, where l is the angular quantum number of the ejected electron [179, 40]. However, in several experimental techniques, it can be considered that the detection of the ionic fragments produced in the photoionization processes have the same orientation than this fragments before the ionization in the initial bound state. This approximation, called axial recoil approximation [184], indicates that the photoionization process is several times faster than the rotation dynamics. Consequently, we can consider that the rotation is fixed. This can be interpreted from the theoretical point of view, that the rotation of the molecule is not excited in the

photoionization processes, and therefore, we can calculate the vibrational wavefunction for the continuum electronic states of the $H_2/H_2^+ + e^-$system, fixing the rotational state.

3.3 Computational details

In the first stages of our method, we compute the one-electron wavefunctions, eigenstates of the field-free Hamiltonian operator of H_2^+. The TISE, given in equation 3.1.7, is solved in a grid of internuclear distances, R. The radial wavefunction for the expansion in equation 3.1.9, is written in a basis set of 180 B-splines of order $k = 8$ [37, 129, 67, 145, 144]. This basis set is defined in a radial box with a outer limit in $r_{max} = 60$ a.u.. In this box, the B-splines are defined in a linear sequence of points, breakpoints, as the product of these radial wavefunctions multiplied by the spherical harmonics, $Y_l^m(\theta, \varphi)$, in a center spherical expansion with an angular momentum quantum number from $l = 0$ to $l = 16$:

$$\phi_{n,\lambda,\sigma}(\mathbf{r};\mathbf{R}) = \sum_{l=0}^{l_{max}=16} \frac{U_{n,\sigma,l}(r;\mathbf{R})}{r} Y_l^m(\theta,\varphi) \tag{3.3.1}$$

The grid of internuclear distances, R, in which we solve the electronic TISE, is not linear, and it has a higher density of points in the region close to the equilibrium distance of the ground state, to ensure a good description of it.

The two-electrons wavefunctions of the hydrogen system are obtained as an antisymmetric product of two H_2^+ one-electron wavefunctions previously calculated. Because these one-electron wavefunctions are used, the H_2 electronic wavefunctions are defined in same finite box of $r_{max} = 60$ a.u., by 180 B-splines of order $k = 8$. We use the CI method, discussed in subsection 3.1.2, to obtain the bound states (ground and single excited states) and the resonant states (doubly excited states). The difference between the bound and resonant states comes in the one-electrons wavefunction used in the configurations. In the case of the Π_u states, the configurations used, after a convergence procedure, are:

- $^1\Pi_u$: $n\sigma_g n'\pi_u$ ($n = 1-9$, $n' = 1-9$), $n\sigma_u n'\pi_g$ ($n = 1-8$, $n' = 1-8$,), $n\delta_g n'\pi_u$ ($n = 1-7$, $n' = 1-9$), $n\delta_u n'\pi_g$ ($n = 1-5$, $n' = 1-5$)

where in the notation used, n indicates the energetic position of the one-electron wavefunction obtained in the diagonalization. In the above expression, the Π_u bound states contain configurations with the ground state of the H_2^+, the $1s\sigma_g$ ($1\sigma_g$). However, the configurations used to obtain the doubly excited states within our treatment of the Feshbach formalism do not have to contain this ground state. As example, the configuration used for the $Q_1\,^1\Sigma_g^+$ is:

- $Q_1\,^1\Sigma_g^+$: $2\sigma_g n\sigma_g$ ($n = 2-35$), $3\sigma_g n\sigma_g$ ($n = 3-35$), $1\pi_g n\pi_g$ ($n = 1-10$), $1\delta_g n\delta_g$ ($n = 1-10$), $1\sigma_u n\sigma_u$ ($n = 1-70$), $2\sigma_u n\sigma_u$ ($n = 2-18$), $1\pi_u n\pi_u$ ($n = 1-70$), $2\pi_u n\pi_u$ ($n = 2-10$)

Focusing on the continuum states of the $H_2^+ + e^-$ system, they are calculated using the L^2 close-coupling method, presented in subsection 3.1.2. In this method, the two-electron wavefunction is calculated as the antisymmetric product of the H_2^+ one-electron wavefunction, which constitutes the residual ion state, with a scattering wavefunction of the ejected electron. The solution of this scattering problem gives the expression for this scattering wavefunction in a grid of energies determined in the diagonalization. However, this energy grid can be artificially modified. One can redefine it using an interpolation method. In this case, one can vary the box size, until one of the original electron energies, ε, coincides with the artificial electron energy imposed. In our particular case, the new electron grid imposed to the ejected electron spectrum is selected to assure that the vector potential are equidistant, $k_e = \sqrt{2m\varepsilon}/\hbar$. Therefore, this imposed grid to the ejected electron energies simulated the spectrum which would be obtained for a particle in a finite box. Because the discretization converts the continuum in a discrete energy distribution, to correctly simulate the transition to them, it is needed that the energy difference between the states of the artificial grid imposed are smaller than the bandwidth of the pulse ($\Delta\varepsilon < \Delta\omega_{pulse}$).

Finally, to include the nuclear motion in the description of the $H_2/H_2^+ + e^-$ system, we solve the nuclear TISE, presented in section 3.2, for the different electronic states of the $H_2/H_2^+ + e^-$ system. The PECs for each different electronic state obtained are used as the potential felt by the nuclei as a function of the internuclear distance, R. These nuclear wavefunctions are obtained in a central spherical expansion, where the nuclear radial wavefunction is also expanded in a basis set of B-splines. This basis set is constituted by 240 B-splines of the order $k = 8$ in a radial nuclear box with a maximum longitude of $R_{max} = 12$ a.u.. Note that the size for the nuclear box is appreciable smaller than the electronic box used, since the nuclear motion is slower due to the larger mass of the nuclei.

3.4 Dipole selection rules: Optical allowed states

The use of the dipole selection rules greatly reduces the size of our calculations. Moreover, as we discussed in chapters 1 and 2, in our calculations we use linearly polarized light. The polarization direction of the vector potential, $\mathbf{A}(t)$, given by the polarization vector, $\mathbf{u}_A$, can present any orientation with respect to the molecular axis. In the case of homonuclear diatomic molecules, any orientation can be expressed as a combination of the parallel (when the polarization vector has the same direction with respect to the molecular axis) and perpendicular (when the polarization vector has a perpendicular direction with respect to the the molecular axis) orientation. As a function of the orientation presented, parallel, perpendicular or a mixture of then, the dipole selection rules impose different symmetric conditions to the dipole transitions.

The dipole selection rules fix the molecular symmetries that will be optically allowed/forbidden. These dipole selection rules, for the homonuclear diatomic molecules, as the hydrogen molecule, determine that the total angular momentum over the z axis, Λ, cannot change for a parallel orientation of the molecule

in the transition between two electronic states. This means that the change of Λ has to be zero, $\Delta\Lambda = 0$, and therefore, the transition always have to occur between states with the same total angular momentum, as $\Sigma \rightarrow \Sigma$, $\Pi \rightarrow \Pi$, etc. However, for perpendicular transition, the dipole selection rules indicate that the angular momentum in the z axis has to change one positive or negative unit, $\Delta\Lambda = \pm 1$, and therefore, are allowed transition between states of different total angular momentum. In addition, for both orientations, parallel or perpendicular, the dipole selection rules establish than the symmetry quantum number, σ, with respect to the perpendicular plane to the molecular axis, which determine the symmetry gerade, g, or ungerade, u, have to change in any photoabsorption transition. In this way, the parallel and perpendicular transitions have to satisfy than $g \rightarrow u$ or $u \rightarrow g$. The total spin of both electron, defined by the Pauli rules, determines the multiplicity of the electronic states: singlet when both electron have opposite directions, and triplet when both are in the same direction. Rigorously, the dipole selection rules do not forbid the transitions between electronic states with the same or different multiplicity [180]. However, the dipole selection rules establish than the transition between states of the same multiplicity is several order of magnitude more probable than between states with different multiplicity. Therefore, we restrict the allowed transition when occur between same multiplicity states.

On the other hand, the dipole selection rules do not forbid the transitions between different vibrational states of different electronic states. Therefore, we can populate any vibrational state, bound and continuum, of any electronic state from any vibrational state of other electronic state, always than this transition between the electronic states are allowed by the others dipole selection rules. Consequently, in diatomic homonuclear molecules, the transitions between vibrational states of a particular electronic state are not allowed due to the electronic transition does not satisfy $g \rightarrow u$ or $u \rightarrow g$.

We focus on the parallel case, where only the transitions between states of the same total angular momentum in the z axis are allowed. Our simulations always start from the ground state of H_2, which is the $X\ ^1\Sigma_g^+$, and therefore, after the interaction, only the singlet states with Σ symmetry can be populated by the absorption of one or more photons. Note that the dipole selection rules establish that the transition has to occur between states of different gerade/ungerade symmetry, but we will be describing not only one, but also multiphoton absorption. Therefore, the singlet Σ states with gerade an ungerade inversion symmetries constitute a complete basis to represent the photoexcitation and photoionization processes when the molecular axis has a parallel orientation with respect to the polarization direction of the electromagnetic field.

Chapter 4

Observables

The use of a spectral method to study excitation and single ionization processes in small molecules presents several advantages with respect to other numerical approaches. Firstly, the most straightforward advantage to emphasize is the fact that the amplitudes associated with each function in the basis set have a physical meaning, and it is easy to extract information contained in the wavepackets, as we present in second section. Secondly, one can use relatively small basis sets, taking into account energetic criteria as well as symmetry considerations due to the dipole selection rules.

The amplitudes are directly given by the time dependent coefficients of the eigenstates of the field-free Hamiltonian operator in the expansion of the time dependent wavefunction. The different observables, densities of probability and probabilities, are extracted by projection of the final time dependent wavefunction into the eigenstates of the field-free Hamiltonian. The use of the stationary states as the basis set reduces the TDSE to a system of coupled first order differential equations, whose solutions can be obtained using any standard integration method. Specially, we choose the Runge-Kutta algorithm, briefly presented in first section.

Our method also simplifies the analysis of the dynamics associated with a given electronic state of the system, through its corresponding vibrational wavepacket. The time evolution of this wavepacket and its properties are determined by the potential energy curve (PEC) in which it moves. In this way, in last section we present an analysis of the time and spatial evolution of the vibrational wavepackets in terms of the electronic potential anharmonicity.

4.1 TDSE solution of the $H_2/H_2^+ + e^-$ system

The time evolution of the system is given by the solution of the TDSE, presented in chapter 1, whose expression is:

$$i\hbar\frac{\partial}{\partial t}\Psi\left(\mathbf{r},R,t\right)=\widehat{H}\left(t\right)\Psi\left(\mathbf{r},R,t\right) \tag{4.1.1}$$

where the time dependent wavefunction of the hydrogen molecular system, $\Psi(\mathbf{r}, R, t)$, can be expressed as:

$$\begin{aligned}\Psi(\mathbf{r}, R, t) = &\sum_n \sum\!\!\!\!\!\!\int_{v_n} c_{n,v_n}(t)\, \Phi_{n,v_n}(\mathbf{r}, R)\, e^{\left[-i\frac{E_{n,v_n}}{\hbar}t\right]} dv_n + \\ + \sum_\alpha \sum\!\!\!\!\!\!\int_{v_\alpha} \int_\varepsilon \sum_l &c^{l,m}_{\alpha,v_\alpha}(t;\varepsilon)\, \Phi^{l,m}_{\alpha,v_\alpha}(\mathbf{r}, R;\varepsilon)\, e^{\left[-i\frac{E_{\alpha,v_\alpha}(\varepsilon)}{\hbar}t\right]} d\varepsilon dv_\alpha + \\ &+ \sum_r \sum\!\!\!\!\!\!\int_{v_r} c_{r,v_r}(t)\, \Phi_{r,v_r}(\mathbf{r}, R)\, e^{\left[-i\frac{E_{r,v_r}}{\hbar}t\right]} dv_n\end{aligned} \tag{4.1.2}$$

In the above expansion, $\sum\!\!\!\!\!\!\int$ indicates that all discrete quantum numbers are summed and all continuum are integrated. n is the bound (ground or single excited) electronic state and v_n is a vibrational state of it, r and v_r indicates the same for the resonant (doubly excited) states. Finally, α indicates the ionic threshold, ε, l and m the energy and partial wave of the ejected electron and v_α the vibrational state in this ionic threshold. $\Phi_{n,v_n}(\mathbf{r}, R)$ and E_{n,v_n} are the vibronic wavefunctions and energies of the ground and the single excited states (H_2), $\Phi_{r,v_r}(\mathbf{r}, R)$ and E_{r,v_r} are the vibronic wavefunctions and energies of the doubly excited states (resonances), and $\Phi^{l,m}_{\alpha,v_\alpha}(\mathbf{r}, R;\varepsilon)$ and $E_{\alpha,v_\alpha}(\varepsilon)$ are the vibronic wavefunctions and energies of the continuum states $(H_2^+ + e^-)$, all of them presented in chapter 3.

As shown in chapter 1, from equation 1.1.12 to 1.1.17, inserting the above expansion in the TDSE, and projecting into the same eigenstates, we obtain a system of first order coupled differential equations for the coefficients $c_{n,v_n}(t)$, $c_{r,v_r}(t)$ and $c^{l,m}_{\alpha,v_\alpha}(t;\varepsilon)$, which can be presented in matrix form as:

$$\begin{pmatrix} \frac{dc_{n',v'_{n'}}(t)}{dt} \\ \frac{dc^{l',m'}_{\alpha',v'_{\alpha'}}(t;\varepsilon)}{dt} \\ \frac{dc_{r',v'_{r'}}(t)}{dt} \end{pmatrix} = -\frac{i}{\hbar}\left[\widetilde{A} + \widetilde{E}\right] \begin{pmatrix} c_{n,v_n}(t) \\ c^{l,m}_{\alpha,v_\alpha}(t;\varepsilon) \\ c_{r,v_r}(t) \end{pmatrix} \tag{4.1.3}$$

where the $\widetilde{A}$ is the dipole coupling matrix, and the $\widetilde{E}$ is the electrostatic coupling matrix, whose general expressions in the velocity gauge are:

$$\widetilde{A} = \frac{e}{m_e\hbar}\mathbf{A}(t)\cdot \begin{pmatrix} \left\langle \Phi_{n',v'_{n'}} \middle| \hat{\mathbf{p}} \middle| \Phi_{n,v_n} \right\rangle & \left\langle \Phi_{n',v'_{n'}} \middle| \hat{\mathbf{p}} \middle| \Phi^{l,m}_{\alpha,v_\alpha}(\varepsilon) \right\rangle & \left\langle \Phi_{n',v'_{n'}} \middle| \hat{\mathbf{p}} \middle| \Phi_{r,v_r} \right\rangle \\ \left\langle \Phi^{l',m'}_{\alpha',v'_{\alpha'}}(\varepsilon') \middle| \hat{\mathbf{p}} \middle| \Phi_{n,v_n} \right\rangle & \left\langle \Phi^{l',m'}_{\alpha',v'_{\alpha'}}(\varepsilon') \middle| \hat{\mathbf{p}} \middle| \Phi^{l,m}_{\alpha,v_\alpha}(\varepsilon) \right\rangle & \left\langle \Phi^{l',m'}_{\alpha',v'_{\alpha'}}(\varepsilon') \middle| \hat{\mathbf{p}} \middle| \Phi_{r,v_r} \right\rangle \\ \left\langle \Phi_{r',v'_{r'}} \middle| \hat{\mathbf{p}} \middle| \Phi_{n,v_n} \right\rangle & \left\langle \Phi_{r',v'_{r'}} \middle| \hat{\mathbf{p}} \middle| \Phi^{l,m}_{\alpha,v_\alpha}(\varepsilon) \right\rangle & \left\langle \Phi_{r',v'_{r'}} \middle| \hat{\mathbf{p}} \middle| \Phi_{r,v_r} \right\rangle \end{pmatrix} \tag{4.1.4}$$

$$\widetilde{E} = \begin{pmatrix} 0 & 0 & 0 \\ 0 & 0 & \left\langle \Phi^{l',m'}_{\alpha',v'_{\alpha'}}(\varepsilon') \right| \widehat{P}\widehat{H}\widehat{Q} \left| \Phi_{r,v_r} \right\rangle \\ 0 & \left\langle \Phi_{r',v'_{r'}} \right| \widehat{Q}\widehat{H}\widehat{P} \left| \Phi^{l,m}_{\alpha,v_\alpha}(\varepsilon) \right\rangle & 0 \end{pmatrix} \tag{4.1.5}$$

where $\hat{\mathbf{p}}$ runs over both electrons: $\hat{\mathbf{p}} = \hat{\mathbf{p}}_1 + \hat{\mathbf{p}}_2$. The $\widetilde{A}$ carries the information about the dipole coupling between the stationary states of the field-free system due to the interaction with the external electromagnetic field, described through its vector potential, $\mathbf{A}(t)$, in the velocity gauge. Within the Feshbach formalism, the scattering states are built during the time evolution, through a time interaction procedure. This is accounted by the $\widetilde{E}$ matrix, which contains the $\widehat{P}\widehat{H}\widehat{Q}$ and $\widehat{Q}\widehat{H}\widehat{P}$ couplings between the resonant and continuum states.

Equation 4.1.3 is solved using an implicit Runge-Kutta integration method of 3^{rd} order [22], which gives the values of the coefficients $c_{n,v_n}(t)$, $c_{r,v_r}(t)$ and $c^{l,m}_{\alpha,v_\alpha}(t;\varepsilon)$ for a certain integration time. The Runge-Kutta integrations are a well-known iterative methods to solve systems of differential equations. The order of this method indicates the number of points used for the integration at each time step, in our case, three intermediate points. It presents several advantages with respect to other integration procedures. First, we can use an adaptive time step, based on norm criteria and on the variation of the potential felt by the system. The larger the field perturbation, the shorter the time step is. The advantage of the norm criteria is that this method assures that the norm of the time dependent wavefunction is conserved equal to one, with a precision of 10^{-5} or higher, during the integration steps, as a function of the order used. The presented method has been successfully employed in previous works [114, 51, 133].

For the solution of TDSE, given in equation 4.1.3, we impose as initial condition that the system starts in its ground state, $X\,{}^1\Sigma^+_g$. In this implementation ($\Psi(\mathbf{r}, R, t) = \psi_{0,0}(\mathbf{r}, R)$), where all coefficients of the expansion given in equation 4.1.3 are zero except for the ground state.

In figure 4.1, we have represented the electronic energy curves, that we obtained by solving the equation 3.1.13 as a function of the internuclear distance, R. On the left graphic, we have plotted the 6 lowest ${}^1\Sigma^+_g$ and ${}^1\Sigma^+_u$ and the 4 lowest ${}^1\Pi^+_u$ electronic bound states of H_2; the six ionization thresholds: $1s\sigma_g$, $2p\sigma_u$, $2p\pi_u$, $2s\sigma_g$, $3d\sigma_g$ and $3d\pi_g$ states of H_2^+. We also include the six lowest states for each series of the doubly excited states with the following total symmetries: $Q_1\,{}^1\Sigma^+_g$, $Q_1\,{}^1\Sigma^+_u$, $Q_1\,{}^1\Delta^+_g$, $Q_2\,{}^1\Sigma^+_g$ and $Q_2\,{}^1\Sigma^+_u$ states of H_2^{**}. We have already a truncated basis, with only the lowest states in energy. The oscillator strengths from the ground state decreases as we go to higher states. Consequently, we can reduce even more the number of these states included in the basis set through symmetry and energetic criteria. At this point, we can select those states that will be populated due to the dipole selection rules, given in section 3.4. When the linearly polarized light parallel to the internuclear axis are selected and the initial population is concentrated in the ground states of symmetry Σ_g , we can take only the states with Σ_g and Σ_u total symmetry. On the other hand, we explore photoionization processes with schemes that will only reach the first two

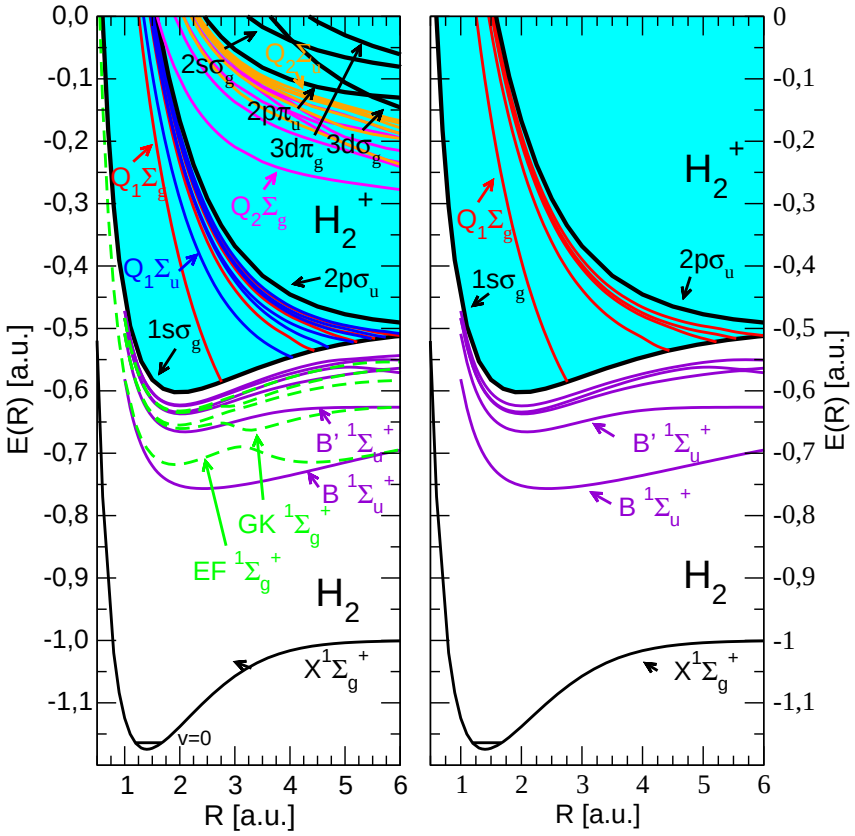

Figure 4.1.1: On the left, representation of the 6 lowest ${}^1\Sigma_g^+$ (including the ground state) and ${}^1\Sigma_u^+$ and the 4 lowest ${}^1\Pi_u^+$ electronic bound states of H_2; the $1s\sigma_g$, $2p\sigma_u$, $2p\pi_u$, $2s\sigma_g$, $3d\sigma_g$ and $3d\pi_g$ states of H_2^+; and the 6 lowest $Q_1{}^1\Sigma_g^+$, $Q_1{}^1\Sigma_u^+$, $Q_1{}^1\Delta_g^+$, $Q_2{}^1\Sigma_g^+$ and $Q_2{}^1\Sigma_u^+$ states of H_2^{**}. On the right, representation of the truncated basis, with the relevant states of a typical pump - probe scheme. In this graph, it is selected the ground state ($X\,{}^1\Sigma_g^+$), the 6 lowest ${}^1\Sigma_u^+$ bound states of H_2, the $1s\sigma_g$ and $2p\sigma_u$ states of H_2^+, and the 6 lowest $Q_1{}^1\Sigma_g^+$ states of H_2^{**}.

ionization thresholds. Attending to the dipole selection rules and the energy of the states, we can select the ground state ($X\,{}^1\Sigma_g^+$), the 6 lowest ${}^1\Sigma_u^+$ electronic bound states of H_2, the $1s\sigma_g$ and $2p\sigma_u$ states of H_2^+, and the 6 lowest $Q_1{}^1\Sigma_g^+$ doubly excited states. Thus, in the right graph of figure 4.1, we have represented this truncated basis set for the typical pump - probe schemes here used, with linearly polarized light parallel to the internuclear axis. In this way, the selection of the relevant states of our basis set is a great advantage, because this reduces the memory size that we need and the computational effort. Note that for one-photon ionization, we can also remove all singly excited states of the basis.

4.2 Energy differential probability distributions

The probability of finding the system in a molecular asymptotic state at a certain time, t, is obtained projecting the time dependent wavefunction into this state.

The differences between the bound and scattering states indicate that each of them reaches the asymptotic regime at different times. The bound states, ground and single excited states, reach the aymptotic limit just after the pulse. However, within the Feshbach formalism, the stationary regime is only reached when the resonant states have fully decayed into the continuum states. At this time, we can consider that the $\widehat{P}\widehat{H}\widehat{Q}$ and $\widehat{Q}\widehat{H}\widehat{P}$ become zero. A practical way of choosing the time at which the system reaches the asymptotic regime is by checking the projection of the time dependent wavefunction at different times, until the contributions to both subspaces, $\widehat{P}$ and $\widehat{Q}$, remain constant.

In this asymptotic limit, the density of probability for the excitation processes corresponds to the population in the single excited states after the photoabsorption process. The density of probability, $dP_{n,v_n}(t)/dv_n$, of finding the system in the single excited state n, v_n, can be calculated as:

$$\frac{dP_{n,v_n}(t)}{dv_n} = \left| \int_{S(\mathbf{r}_1)} \int_{S(\mathbf{r}_2)} \int_{S(R)} \overline{\Phi}_{n,v_n}(\mathbf{r}, R)\, \Psi(\mathbf{r}, R, t)\, d^3\mathbf{r}_1 d^3\mathbf{r}_2 dR \right|^2 \tag{4.2.1}$$

where $\Phi_{n,v_n}(\mathbf{r}, R)$ are the vibronic wavefunction of the single excited state. Substituting equation 4.1.2 in equation 4.2.1, and considering that the wavefunctions of the bound, resonant and continuum states are orthonormal among them, this density of probability becomes:

$$\frac{dP_{n,v_n}(t)}{dv_n} = |c_{n,v_n}(t)|^2 \tag{4.2.2}$$

This density of probability depends on the module of the time dependent coefficient, the amplitude, of the vibronic state. In the above equation, we take into account the bound as well as the continuum vibrational states. While the bound vibrational states give peaks around their corresponding energy level, the continuum vibrational states present a continuum distribution.

We can define an energy-differential distribution for the doubly excited states. Operating as in the single excited states, the density of probability, $dP_{r,v_r}(t)/dv_r$, of finding the system in the doubly excited state r, v_r, is:

$$\frac{dP_{r,v_r}(t)}{dv_r} = |c_{r,v_r}(t)|^2 \tag{4.2.3}$$

where the above expression only depends on the square of the amplitude of resonant states. As can be observed in figure 4.1, the resonances are pure dissociative states, only constituted by continuum vibrational states. This makes that their energy distributions are similar to continuum contributions studied for the single excited states.

As commented before, although the densities of probability for the single and doubly excited states give important information, the experimental access to these distributions is usually complicated, and consequently, they focus on the energy-differential distributions of the ionization processes. In this manner, we present

the densities of probability in terms of the charge fragment energies generated in the photoionization process.

First, we define the electronic and nuclear energy-differential distributions, so-called fully energy-differential distributions, as the density of ionization probability in terms of the energies of all ejected photofragments (the electron and the residual ion or the proton plus the atomic hydrogen). The procedure to obtain this density of probability, $dP^{l,m}_{\alpha,v_\alpha}(t;\varepsilon)/dv_\alpha d\varepsilon$, is similar to the previous used for the single and doubly excited states. In this case, the time dependent wavefunction, $\Psi(\mathbf{r},R,t)$, is projected into the vibronic wavefunctions of the continuum states, $\Phi^{l,m}_{\alpha,v_\alpha}(\mathbf{r},R;\varepsilon)$:

$$\frac{dP^{l,m}_{\alpha,v_\alpha}(t;\varepsilon)}{dv_\alpha d\varepsilon} = \left| \int_{S(\mathbf{r}_1)} \int_{S(\mathbf{r}_2)} \int_{S(R)} \overline{\Phi^{l,m}_{\alpha,v_\alpha}}(\mathbf{r},R;\varepsilon)\, \Psi(\mathbf{r},R,t)\, d^3\mathbf{r}_1 d^3\mathbf{r}_2 dR \right|^2 \quad (4.2.4)$$

where substituting the expression of the time dependent wavefunction, given in equation 4.1.2, the density of probability $dP^{l,m}_{\alpha,v_\alpha}(t;\varepsilon)/dv_\alpha d\varepsilon$, becomes:

$$\frac{dP^{l,m}_{\alpha,v_\alpha}(t;\varepsilon)}{dv_\alpha d\varepsilon} = \left| c^{l,m}_{\alpha,v_\alpha}(t;\varepsilon) \right|^2 \quad (4.2.5)$$

The fully energy-differential distribution depends on the amplitudes for the continuum states, similar to the vibrational distributions of the single and doubly excited states. As it is observed, the spectral method is revealed as a very straightforward method to obtain the different densities of probability from the TDSE solution. Because our vibronic wavefunctions are calculated in a center spherical expansion, the final amplitudes are expressed in terms of partial waves, determined by the angular quantum number l. The sum over all partial waves included in the calculation gives the total fully energy-differential distributions. The vibrational quantum number, v_α, in equation 4.2.5, includes the bound, if the continuum electronic state presents them, and continuum vibrational states. Equation 4.2.5 can be separated in the dissociative and non-dissociative fully energy-differential distributions, including only the corresponding bound or continuum vibrational states. In addition, as in the dissociation processes, the residual ion is fragmented in one proton and one hydrogen atom, the fully differential energy distributions can be expressed in terms of the proton kinetic energy.

On the other hand, the nuclear and electronic energies can be redefined in terms of the total energy and the energy sharing, where the total energy is the available energy after the absorption of one or more photons and the energy sharing is the percentage of the total energy which is contained for the ejected electron or nuclei, being both definitions complementary. Using these two energies, equation 4.2.5 can be transformed to give the population in terms of the absorbed photon energy and the distribution of this energy among the ejected fragments.

Although the fully energy-differential distributions give all accessible information of the ionization process, to obtain them the ejected charge fragments have to be measured in coincidence. However, several experimental techniques measure only the energy-differential distributions of one particle averaging over the other.

These energy-differential probability distributions can be measured and calculated for the energies of the residual ion or its fragments (proton and hydrogen atom) as well as for the ejected electron, given the nuclear kinetic energy (NKE) and electron kinetic energy (EKE) distributions. These NKE, $dP^{l,m}_{\alpha,v_\alpha}(t)/dv_\alpha$, and EKE, $dP^{l,m}_{\alpha,v_\alpha}(t)/dv_\alpha$, distributions can be calculated from equation 4.2.5 integrating over the electronic energies or sum and integrating over the nuclear energies, respectively:

$$\frac{dP^{l,m}_{\alpha,v_\alpha}(t)}{dv_\alpha} = \int_\varepsilon \frac{dP^{l,m}_{\alpha,v_\alpha}(t;\varepsilon)}{dv_\alpha d\varepsilon} d\varepsilon = \int_\varepsilon \left|c^{l,m}_{\alpha,v_\alpha}(t)\right|^2 d\varepsilon \tag{4.2.6}$$

$$\frac{dP^{l,m}_{\alpha}(t;\varepsilon)}{d\varepsilon} = \sum_{v_\alpha} \frac{dP^{l,m}_{\alpha,v_\alpha}(t;\varepsilon)}{dv_\alpha d\varepsilon} dv_\alpha = \sum_{v_\alpha} \left|c^{l,m}_{\alpha,v_\alpha}(t;\varepsilon)\right|^2 dv_\alpha \tag{4.2.7}$$

The dependence of the NKE distributions with the vibrational states, allows the separation of them for the dissociative and non-dissociative ionization processes, where the bound vibrational states only contribute for the non-dissociative NKE distribution and the continuum for the dissociative NKE distributions. In addition, as in the electronic and nuclear energy-differential distributions, the NKE distributions for the dissociative ionization can be expressed as the proton kinetic energy (PKE) distributions, where the nuclear kinetic energy is divided by two. Contrary to the NKE distributions, the dissociative and non-dissociative ionization contributions of the EKE distributions cannot be extracted from equation 4.2.7, because the EKE distributions are obtained by integrating and sum over all vibrational states. In this case, the EKE distributions for the non-dissociative and dissociative ionization can be only obtained from equation 4.2.5, sum over the bound or integrating over the continuum vibrational states, separately.

Finally, we can obtain the ionization probability, $P^{l,m}_{\alpha}(t)$, so-called ionization yield, for the total population over a certain final ionic state. This can be obtained by integration and sum over the electronic and nuclear energies of the fully energy-differential distributions:

$$P^{l,m}_{\alpha}(t) = \sum_{v_\alpha} \int_\varepsilon \frac{dP^{l,m}_{\alpha,v_\alpha}(t;\varepsilon)}{dv_\alpha d\varepsilon} d\varepsilon dv_\alpha = \sum_{v_\alpha} \int_\varepsilon \left|c^{l,m}_{\alpha,v_\alpha}(t)\right|^2 d\varepsilon dv_\alpha \tag{4.2.8}$$

As in the EKE distributions, to obtain the dissociative and non-dissociative contributions to the ionization probability, we have to sum the bound or integrate the continuum vibrational states separately in equation 4.2.5.

4.2.1 Randomly oriented molecules

Along this chapter we have focused on a parallel orientation of the molecule with respect to the polarization vector of the electromagnetic field. Experimentally, widely used techniques as the COLTIRMS [41, 171], distinguish parallel from perpendicular orientations by reconstructing the molecular position through momentum analysis. However, this information is not always accessible if all charged

particles are not measured in coincidence. In many cases, the experimental spectrum is obtained averaged over all possible orientations of the electromagnetic field with respect to the molecular axis. In order to give a theoretical description for these experiments, the orientation has to be included in the above expressions for the densities of probability and probabilities as an extra variable. Restricting our description to linear polarized light, this orientation is defined through the angle, θ, formed by the polarization vector of the electromagnetic field with respect to the internuclear axis, given a expression of the external interaction potential operator, $\widehat{V}(t)$, in the velocity gauge:

$$\widehat{V}(t) = \frac{e}{m_e}\sum_{i=1}^{2}\mathbf{A}(t)\cdot\widehat{\mathbf{p}}_i = \frac{e}{m_e}\sum_{i=1}^{2}\left[A(t)\cos(\theta)\,\widehat{p}_z + A(t)\sin(\theta)\,\widehat{p}_y\right] \tag{4.2.9}$$

where the polarization direction of the electromagnetic field is contained in the yz plane and the molecular axis is defined along the z axis. In the above equation, it is clear that for an angle $\theta = 0\,\text{rad}$, the orientation of the electromagnetic field is parallel with respect to the molecular axis and $\theta = \pi/2\,\text{rad}$ gives the perpendicular orientation. Introducing the above expression for the external interaction potential operator, $\widehat{V}(t)$, in equation 1.1.17, indicates that the time dependent coefficients of our expansion, $c_{n,v_n}(t,\theta)$, $c_{r,v_r}(t,\theta)$ and $c^{l,m}_{\alpha,v_\alpha}(t,\theta;\varepsilon)$, explicitly depend on the angle θ, and consequently, the densities of probability and the probabilities also depend on θ. The density of probability is then written as a function of the nuclear and electronic kinetic energies and the angle θ:

$$\frac{dP^{l,m}_{\alpha,v_\alpha}(t,\theta;\varepsilon)}{d\theta dv_\alpha d\varepsilon} = \left|c^{l,m}_{\alpha,v_\alpha}(t,\theta;\varepsilon)\right|^2 \tag{4.2.10}$$

Integrating the above equation over the solid angle, the density of probability as a function of the nuclear and electronic kinetic energies averaged over all possible orientations of the electromagnetic field with respect to the molecular axis, is:

$$\frac{dP^{l,m}_{\alpha,v_\alpha}(t;\varepsilon)}{dv_\alpha d\varepsilon} = \frac{1}{4\pi}\int_0^{\pi}\int_0^{2\pi}\left|c^{l,m}_{\alpha,v_\alpha}(t,\theta;\varepsilon)\right|^2\sin(\theta)\,d\theta d\varphi \tag{4.2.11}$$

If we restrict our simulations to the one-photon absorption, which is a first order process, in the perturbative regime, the first order time dependent perturbation theory (TDPT) applies. In the TDPT, the time dependent coefficients, $c_{n,v_n}(t,\theta)$, $c_{r,v_r}(t,\theta)$ and $c^{l,m}_{\alpha,v_\alpha}(t,\theta;\varepsilon)$, are given by:

$$\begin{aligned} c_{n,v_n}(t,\theta) = -\frac{e}{m_e}\sum_{i=1}^{2}&\left[\langle\Phi_{n,v_n}|\,\widehat{p}_z\,|\Phi_{0,0}\rangle\cos(\theta) + \right.\\ &\left.+\langle\Phi_{n,v_n}|\,\widehat{p}_y\,|\Phi_{0,0}\rangle\sin(\theta)\right]\int_0^t A(t)\,e^{\left[i\frac{E_{n,v_n}-E_{0,0}}{\hbar}t\right]}dt \end{aligned} \tag{4.2.12}$$

$$
\begin{aligned}
c_{\alpha,v_\alpha}^{l,m}(t,\theta;\varepsilon) = -\frac{e}{m_e}\sum_{i=1}^{2}\Big[\big\langle\Phi_{\alpha,v_\alpha}^{l,m}(\varepsilon)\big|\,\widehat{p}_z\,|\Phi_{0,0}\rangle\cos(\theta) + \\
+\big\langle\Phi_{\alpha,v_\alpha}^{l,m}(\varepsilon)\big|\,\widehat{p}_y\,|\Phi_{0,0}\rangle\sin(\theta)\Big]\int_0^t A(t)\,e^{\left[i\frac{E_{\alpha,v_\alpha}(\varepsilon)-E_{0,0}}{\hbar}t\right]}dt
\end{aligned}
\tag{4.2.13}
$$

$$
\begin{aligned}
c_{r,v_r}(t,\theta) = -\frac{e}{m_e}\sum_{i=1}^{2}\big[\langle\Phi_{r,v_r}|\,\widehat{p}_z\,|\Phi_{0,0}\rangle\cos(\theta) + \\
+\langle\Phi_{r,v_r}|\,\widehat{p}_y\,|\Phi_{0,0}\rangle\big]\int_0^t A(t)\,e^{\left[i\frac{E_{r,v_r}-E_{0,0}}{\hbar}t\right]}dt
\end{aligned}
\tag{4.2.14}
$$

where we used the braket notation. In the above expressions, it is clear that the time dependent coefficients are proportional to the dipole transition matrix elements and the Fourier transform of the electromagnetic field used and they are independent of the population in other excited of ionic states. Thus, the time dependent coefficients can be defined as the composition of the time dependent coefficients for the parallel orientation, $c_{n,v_n}(t,\theta=0)$, $c_{r,v_r}(t,\theta=0)$ and $c_{\alpha,v_\alpha}^{l,m}(t,\theta=0;\varepsilon)$, and for the perpendicular orientation, $c_{n,v_n}(t,\theta=\pi/2)$, $c_{r,v_r}(t,\theta=\pi/2)$ and $c_{\alpha,v_\alpha}^{l,m}(t,\theta=\pi/2;\varepsilon)$, as:

$$
\begin{aligned}
c_{n,v_n}(t,\theta) &= c_{n,v_n}(t,\theta=0)\cos(\theta) + c_{n,v_n}(t,\theta=\pi/2)\sin(\theta) \\
c_{r,v_r}(t,\theta) &= c_{r,v_r}(t,\theta=0)\cos(\theta) + c_{r,v_r}(t,\theta=\pi/2)\sin(\theta) \\
c_{\alpha,v_\alpha}^{l,m}(t,\theta;\varepsilon) &= c_{\alpha,v_\alpha}^{l,m}(t,\theta=0;\varepsilon)\cos(\theta) + c_{\alpha,v_\alpha}^{l,m}(t,\theta=\pi/2;\varepsilon)\sin(\theta)
\end{aligned}
\tag{4.2.15}
$$

Using the above expression for the coefficients of the ionic states, the density of probability as a function of the nuclear and electronic kinetic energies and the angle θ, becomes:

$$
\frac{dP_{\alpha,v_\alpha}^{l,m}(t,\theta;\varepsilon)}{d\theta dv_\alpha d\varepsilon} = \left|c_{\alpha,v_\alpha}^{l,m}(t,\theta=0;\varepsilon)\cos(\theta) + c_{\alpha,v_\alpha}^{l,m}(t,\theta=\pi/2;\varepsilon)\sin(\theta)\right|^2 \tag{4.2.16}
$$

To obtain the average over all possible values of the angle θ, we integrate the above expression over the solid angle:

$$
\begin{aligned}
\frac{dP_{\alpha,v_\alpha}^{l,m}(t;\varepsilon)}{dv_\alpha d\varepsilon} = \frac{1}{4\pi}\int_0^{\pi}\int_0^{2\pi}\big|c_{\alpha,v_\alpha}^{l,m}(t,\theta=0;\varepsilon)\cos(\theta) + \\
+c_{\alpha,v_\alpha}^{l,m}(t,\theta=\pi/2;\varepsilon)\sin(\theta)\big|^2\sin(\theta)\,d\theta d\varphi
\end{aligned}
\tag{4.2.17}
$$

where the integral over the φ angle is equal to 2π. The expansion of the module square gives four terms:

$$\frac{dP^{l,m}_{\alpha,v_\alpha}(t;\varepsilon)}{dv_\alpha d\varepsilon d} = \left|c^{l,m}_{\alpha,v_\alpha}(t,\theta=0;\varepsilon)\right|^2 \frac{1}{2}\int_0^\pi \cos^2(\theta)\sin(\theta)\,d\theta + \\ + \left|c^{l,m}_{\alpha,v_\alpha}(t,\theta=\pi/2;\varepsilon)\right|^2 \frac{1}{2}\int_0^\pi \sin^3(\theta)\,d\theta + \\ + \left[\overline{c^{l,m}_{\alpha,v_\alpha}}(t,\theta=0;\varepsilon)\,c^{l,m}_{\alpha,v_\alpha}(t,\theta=\pi/2;\varepsilon) + c^{l,m}_{\alpha,v_\alpha}(t,\theta=0;\varepsilon)\,\overline{c^{l,m}_{\alpha,v_\alpha}}(t,\theta=\pi/2;\varepsilon)\right]\cdot \\ \cdot\frac{1}{2}\int_0^\pi \sin^2(\theta)\cos(\theta)\,d\theta \tag{4.2.18}$$

where the different integrals can be solved analytically. Thus, the density of probability averaged over all possible values of the angle θ, as a function of the nuclear and electronic kinetic energy is:

$$\frac{dP^{l,m}_{\alpha,v_\alpha}(t;\varepsilon)}{dv_\alpha d\varepsilon d} = \frac{1}{3}\left|c^{l,m}_{\alpha,v_\alpha}(t,\theta=0;\varepsilon)\right|^2 + \frac{2}{3}\left|c^{l,m}_{\alpha,v_\alpha}(t,\theta=\pi/2;\varepsilon)\right|^2 \tag{4.2.19}$$

The above expression is the well-known composition for the one-photon processes. However, our study is focused on multiphoton processes induced by electromagnetic fields. In this case, the final time dependent coefficients cannot be expressed as the composition of the parallel and perpendicular contributions, and consequently, the density of probability as a function of the nuclear and electronic kinetic energy averaged over all possible orientations, is given in equation 4.2.11. Specifically, we numerically evaluate this integral using a Gauss-Legendre quadrature, whose details are given in appendix B.

4.3 Angular distributions

Some experimental techniques, as COLTRIMS [41, 171], allow the measurement in coincidence of the ejected charge fragments, giving the fully energy-differential angular distributions. These electron angular distributions can be presented in two reference systems: the laboratory or molecular frames. In the laboratory frame, the reference origin is external to the molecular system, and therefore, the ejected electron and proton momentum vectors are randomly oriented. While in the molecular frame, the nuclear center of mass is taken as the zero reference system. Thus, we measure the ejected electron direction with respect to arbitrarily orientated proton momentum vector.

Focusing on the molecular frame, the detected electrons are not associated with a well-defined ionic threshold, because they are measured in terms of a well-defined proton momentum vector. To theoretically obtain these angular distributions, our time dependent wavefunction has to be projected into a combination of those ionic states with the same threshold energy, which gives the same proton momentum vector. The possible partial waves of the electron momentum vector are included through a center spherical expansion [39]. In the present PhD thesis, we focus on

the ionization into the two lowest, $1s\sigma_g$ and $2p\sigma_u$, states of H_2^+ which have the same threshold energy, given:

$$\Phi^{l,m}_{\pm,v_\pm}(\mathbf{r},R;\theta_e,\varphi_e,\varepsilon)=\frac{1}{\sqrt{2}}\sum_l\sum_{m=-l}^{l}\Big[\Phi^{l,m}_{\alpha=1s\sigma_g,v_\alpha}(\mathbf{r},R;\varepsilon)\,Y_l^m(\theta_e,\varphi_e)\pm \\ \pm\Phi^{l,m}_{\alpha=2p\sigma_u,v_\alpha}(\mathbf{r},R;\varepsilon)\,Y_l^m(\theta_e,\varphi_e)\Big] \tag{4.3.1}$$

where $\Phi^{l,m}_{\alpha,v_\alpha}(\mathbf{r},R;\varepsilon)$ is the continuum vibronic wavefunction, $Y_l^m(\theta_e,\varphi_e)$ is the spherical harmonic associated with the momentum of the ejected electron, for a partial wave with quantum numbers l and m, and $1/\sqrt{2}$ is a normalized factor. In the above equation, the symbol $\pm$ indicates that the combination is positive or negative as a function of the orientation of the proton momentum vector. The angular density of probability, $dP^{l,m}_{\pm,v_\pm}(t;\varepsilon,\theta_e,\varphi_e)/dv_\pm d\varepsilon$, is obtained as the projection of the time dependent wavefunction into the above wavefunction:

$$\frac{dP^{l,m}_{\pm,v_\pm}(t;\varepsilon,\theta_e,\varphi_e)}{dv_\pm d\varepsilon}=\left|\int_{S(\mathbf{r}_1)}\int_{S(\mathbf{r}_2)}\int_{S(R)}\overline{\Phi^{l,m}_{\pm,v_\pm}}(\mathbf{r},R;\theta_e,\varphi_e,\varepsilon)\,\Psi(\mathbf{r},R,t)\,d^3\mathbf{r}_1d^3\mathbf{r}_2dR\right|^2 \tag{4.3.2}$$

Using the equation 4.1.2, the density of probability as a function of the nuclear and electronic energies and the electron momentum direction, θ_e and φ_e, is:

$$\frac{dP^{l,m}_{\pm,v_\pm}(t;\varepsilon,\theta_e,\varphi_e)}{dv_\pm d\varepsilon}=\frac{1}{2}\left|\sum_l\sum_{m=-l}^{l}\left[c^{l,m}_{\alpha=1s\sigma_g,v_\alpha}(t)\pm c^{l,m}_{\alpha=2p\sigma_u,v_\alpha}(t)\right]\cdot \\ \cdot Y_l^m(\theta_e,\varphi_e)\,e^{\left[-i\frac{E_{\alpha,v_\alpha}(\varepsilon)}{\hbar}t\right]}\right|^2 \tag{4.3.3}$$

As with the fully energy-differential probability distributions, this fully energy-differential angular distribution can be integrated over the nuclear or electronic kinetic energies, obtaining the electron or nuclear energy-differential angular distributions, respectively, whose expression as a function of the nuclear kinetic energy is:

$$\frac{dP^{l,m}_{\pm,v_\pm}(t;\theta_e,\varphi_e)}{dv_\pm}=\frac{1}{2}\int_\varepsilon\left|\sum_l\sum_{m=-l}^{l}\left[c^{l,m}_{\alpha=1s\sigma_g,v_\alpha}(t)\pm c^{l,m}_{\alpha=2p\sigma_u,v_\alpha}(t)\right]\cdot \\ \cdot Y_l^m(\theta_e,\varphi_e)\,e^{\left[-i\frac{E_{\alpha,v_\alpha}(\varepsilon)}{\hbar}t\right]}\right|^2 d\varepsilon \tag{4.3.4}$$

and the energy-differential angular distribution as a function of the electron kinetic energy is:

$$\frac{dP_{\pm}^{l,m}(t;\varepsilon,\theta_e,\varphi_e)}{d\varepsilon} = \frac{1}{2}\sum_{v_\alpha}\left|\sum_{l}\sum_{m=-l}^{l}\left[c_{\alpha=1s\sigma_g,v_\alpha}^{l,m}(t) \pm c_{\alpha=2p\sigma_u,v_\alpha}^{l,m}(t)\right]\cdot \right. \\ \left. \cdot Y_l^m(\theta_e,\varphi_e)\, e^{\left[-i\frac{E_{\alpha,v_\alpha}(\varepsilon)}{\hbar}t\right]}\right|^2 dv_\alpha \tag{4.3.5}$$

The electron angular distributions give much information of the dissociative ionization processes. However, the complexity to obtain a wide enough experimental sampling for all the energies and directions, makes difficult the measurement of clear electron angular distributions. To avoid this, we can use the asymmetry parameters, which can be obtained for any of the before electron angular distributions. All these asymmetry parameters are defined as:

$$A = \frac{I_{up} - I_{down}}{I_{up} + I_{down}} \tag{4.3.6}$$

where I_{up} corresponds to the integration of the electron angular distribution in the hemisphere region upwards the plane contained in the inversion center and perpendicular to the molecular axis, and the I_{down} corresponds to the integration in the hemisphere downwards this plane. The sum of both integrated hemispheres in the divisor is to normalize. When the emission of the electron is symmetric with respect to the perpendicular plane, the asymmetry parameter is zero. However, there are several phenomenas which can break this symmetry, given a non-zero contribution to the asymmetry parameter.

4.3.1 Vibrational wavepackets

The time dependent wavefunction, given in equation 4.1.2, contains the dynamical information for the time evolution of the system. However, we can study the dynamics of a particular electronic state, looking into its associated vibrational wavepacket. One can thus project the full time dependent wavefunction into a given electronic state, and keep the evolution with respect to the nuclear degrees of freedom. The total density of the vibrational wavepacket, $\rho(R,t)$, is obtained by integrating the module square of the time dependent wavefunction, $\Psi(\mathbf{r},R,t)$, over the electronic coordinates:

$$\rho(R,t) = \left|\int_{S(\mathbf{r}_1)}\int_{S(\mathbf{r}_2)} \overline{\Psi}(\mathbf{r},R,t)\,\Psi(\mathbf{r},R,t)\,d^3\mathbf{r}_1 d^3\mathbf{r}_2\right|^2 \tag{4.3.7}$$

Using the equation 4.1.2, the total density of the vibrational wavepacket, $\rho(R,t)$, can be written as:

$$\rho\left(R,t\right)=\sum_{n}\left|\sum\!\!\!\!\!\!\int_{v_n} c_{n,v_n}\left(t\right)\chi_{n,v_n}\left(R\right)e^{\left[-i\frac{E_{n,v_n}}{\hbar}t\right]}dv_n\right|^2+$$
$$+\sum_{\alpha}\int_{\varepsilon}\sum_{l}\left|\sum\!\!\!\!\!\!\int_{v_\alpha} c^{l,m}_{\alpha,v_\alpha}\left(t;\varepsilon\right)\chi_{\alpha,v_\alpha}\left(R\right)e^{\left[-i\frac{E_{\alpha,v_\alpha}(\varepsilon)}{\hbar}t\right]}dv_\alpha\right|^2 d\varepsilon+ \tag{4.3.8}$$
$$+\sum_{r}\left|\sum\!\!\!\!\!\!\int_{v_r} c_{r,v_r}\left(t\right)\chi_{r,v_r}\left(R\right)e^{\left[-i\frac{E_{r,v_r}}{\hbar}t\right]}dv_r\right|^2$$

In the above equation each module square can be associated with a function of the vibrational wavepacket of one electronic state. For a bound electronic state n, its vibrational wavepacket, $\phi_n\left(R,t\right)$, is:

$$\phi_n\left(R,t\right)=\sum\!\!\!\!\!\!\int_{v_n} c_{n,v_n}\left(t\right)\chi_{n,v_n}\left(R\right)e^{\left[-i\frac{E_{n,v_n}}{\hbar}t\right]}dv_n \tag{4.3.9}$$

where $\chi_{n,v_n}\left(R\right)$ and E_{n,v_n} are the vibrational wavefunctions and energies. The time dependent coefficients become constant when the system arrives the stationary regime, and consequently, the time evolution of the system is only dictated by the stationary phase. This stationary regime is reached for the vibrational wavepackets of the electronic bound states just after the end of the pulse duration. However, the vibrational wavepackets of the resonant and continuum electronic states need larger times than the pulse duration, due to the electrostatic coupling among them within the Feshbach formalism.

Equation 4.3.9, defines the wavepacket function, but the observable is the total density of the vibrational wavepacket, $\rho_n\left(R,t\right)$, which is defined as the module square of this vibrational wavepacket:

$$\rho_n\left(R,t\right)=\sum\!\!\!\!\!\!\int_{v_n}\left|c_{n,v_n}\left(t\right)\right|^2\left|\chi_{n,v_n}\left(R\right)\right|^2 dv_n+$$
$$+\sum\!\!\!\!\!\!\int_{v'_n}\sum\!\!\!\!\!\!\int_{v_n>v'_n}\left(\Re\left[c_{n,v'_n}\left(t\right)\chi_{n,v'_n}\left(R\right)\right]\Re\left[c_{n,v_n}\left(t\right)\chi_{n,v_n}\left(R\right)\right]+\right.$$
$$\left.+\Im\left[c_{n,v'_n}\left(t\right)\chi_{n,v'_n}\left(R\right)\right]\Im\left[c_{n,v_n}\left(t\right)\chi_{n,v_n}\left(R\right)\right]\right)\cos\left[\frac{E_{n,v'_n}-E_{n,v_n}}{\hbar}t\right]dv_n dv'_n \tag{4.3.10}$$

where the module square of equation 4.3.9 has been separated in three summations, one for the $v_n=v'_n$ and the other two for the $v_n>v'_n$. The above equation can be simplified more, if we work with real wavefunction, $\overline{\chi}_{n,v_n}\left(R\right)=\chi_{n,v_n}\left(R\right)$, and even real coefficients, $\overline{c}_{n,v_n}\left(t\right)=c_{n,v_n}\left(t\right)$. As can be observed, the temporal dependence is carried by the crossing terms, while the module of each vibrational wavefunction by its coefficient is a constant.

The vibrational wavefunctions are determined by the potential energy curves (PEC), which are anharmonic potentials. Consequently, their vibrational states

are not equidistant in energy, at a difference with the harmonic potential, $V(r) = k(R - R_{eq})^2/2$, used in several works to describe the vibrational states in the region closer to the equilibrium distance, R_{eq}. The use of harmonic potential wavefunctions [95, 142, 141], $\chi_{n,v_n}(R)$, whose associated energies are $E_{n,v_n} = \hbar\omega_n(v_n + 1/2)$, where ω_n is the oscillation frequency and v_n is the vibrational level, which would give a vibrational wavepacket, $\phi_n(R,t)$:

$$\phi_n(R,t) = \sum_{v_n} c_{n,v_n}(t)\,\chi_{n,v_n}(R)\left[\cos\left[\omega_n(v'-v)\,t\right] - i\sin\left[\omega_n(v'-v)\,t\right]\right] \quad (4.3.11)$$

where the complex exponential from equation 4.3.9 is expressed as trigonometric functions. Using the Euler's formula and taking into account that the quantum number, v, of the harmonic oscillator is discrete, the integral part disappear. For an harmonic potential, the difference between v'_n and v_n is an integer number, and $E_{n,v'_n} - E_{n,v_n}$, becomes equal to $2\pi k/\omega_n$, with $k = 0, \pm1, \pm2, ...$ Two or more superposition of vibrational states of the harmonic potential thus give simple sine or cosine functions, as can be observed in figure 4.3.1.

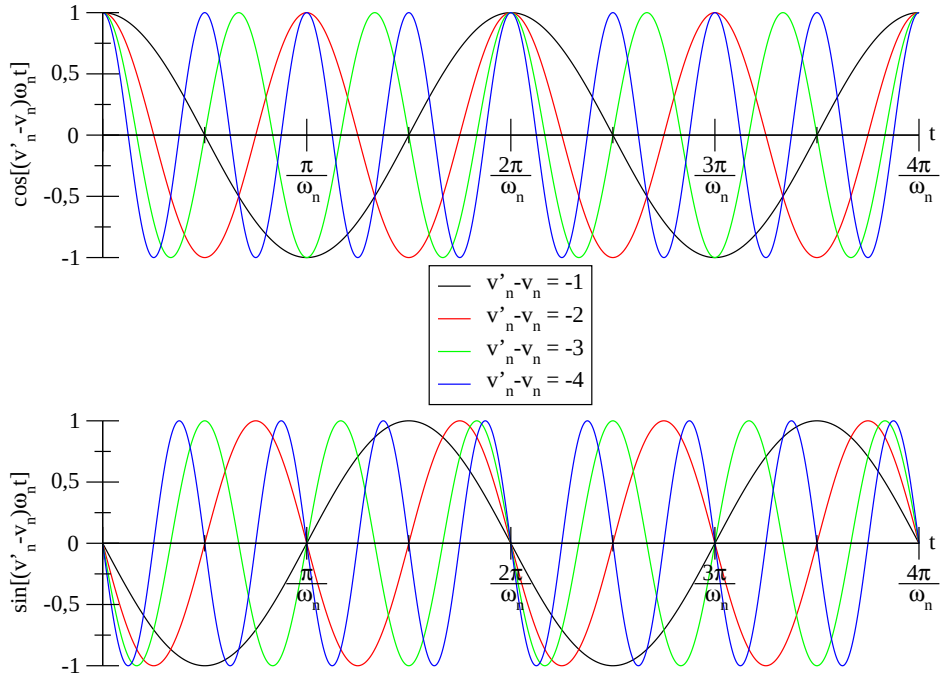

Figure 4.3.1: Time representation of cosine and sine functions, whose frequencies are equal to the energy difference between two different vibrational states of the harmonic oscillator, $(E_{n,v'} - E_{n,v})/\hbar = \omega_n(v' - v)$. Upper panel: Time representation of the cosine function for several values of the difference $(v' - v)$. Lower panel: Time representation of the sine function for several values of the difference $(v' - v)$.

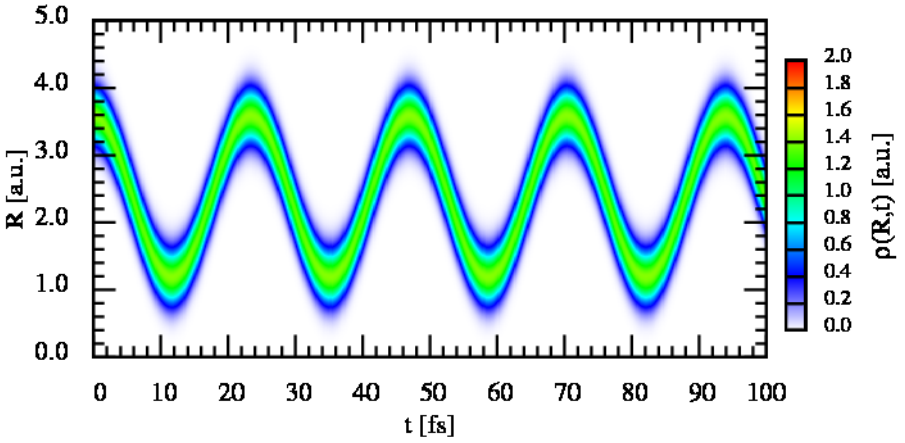

Figure 4.3.2: Representation of the density of the vibrational wavepacket for an approximated $B\,^1\Sigma_u^+$ potential, within the harmonic oscillation, as a function of the internuclear distance, R, in the y axis and time, t, in the x axis. The basis set of vibrational wavefunction is constituted by the harmonic potential wavefunction with an ω_n which fit the PEC in the region near to the equilibrium distance.

As the time evolution of the vibrational wavepacket is determined by the cosine and sine functions, the same periodicity, $2\pi k/\omega_n$, for all the possible energy differences between vibrational states using the wavefunctions and energies of the harmonic potential, indicates that the vibrational wavepacket cannot spread during its time evolution. This is clearly shown in figure 4.3.2, where it is plotted the density of the vibrational wavepacket as a function of the internuclear distance, R, and time, t, obtained using an harmonic potential whose frequency, ω_n, is selected to fit the PEC in the region near to the equilibrium distance for the $B\,^1\Sigma_u^+$ electronic bound state of the H_2 molecule.

However, since the vibrational energies of the PECs for the $H_2/H_2^+ + e^-$ system, are not separated by a linear relation, this periodicity is not satisfied. This can be observed in figure 4.3.3, where it is plotted the cosine, in the upper panel, and sine, in the lower panel, expressions for the energy difference between several vibrational states, obtained for the $B\,^1\Sigma_u^+$ electronic bound state. In this figure 4.3.3, it is clear that the cosine and sine functions for the different energy difference present the different values at any time.

Therefore, the absence of a common period for the different components of the vibrational wavepacket induces that the wavepacket is not well reconstructed and spreads during its time evolution. This can be observed in figure 4.3.4, where it is plotted the vibrational wavepacket for the state $B\,^1\Sigma_u^+$, generated by the one-photon absorption using a XUV pulse with a duration of 2 fs, a central energy of 14 eV and an intensity of $10^{12}\,\mathrm{W}\cdot\mathrm{cm}^{-2}$.

However, the vibrational wavepacket of any anharmonic potential is partially reconstructed each oscillation period. The magnitude and time position of these reconstructions can be analyzed by the autocorrelation function, $R_n\,(t - t_0)$, which

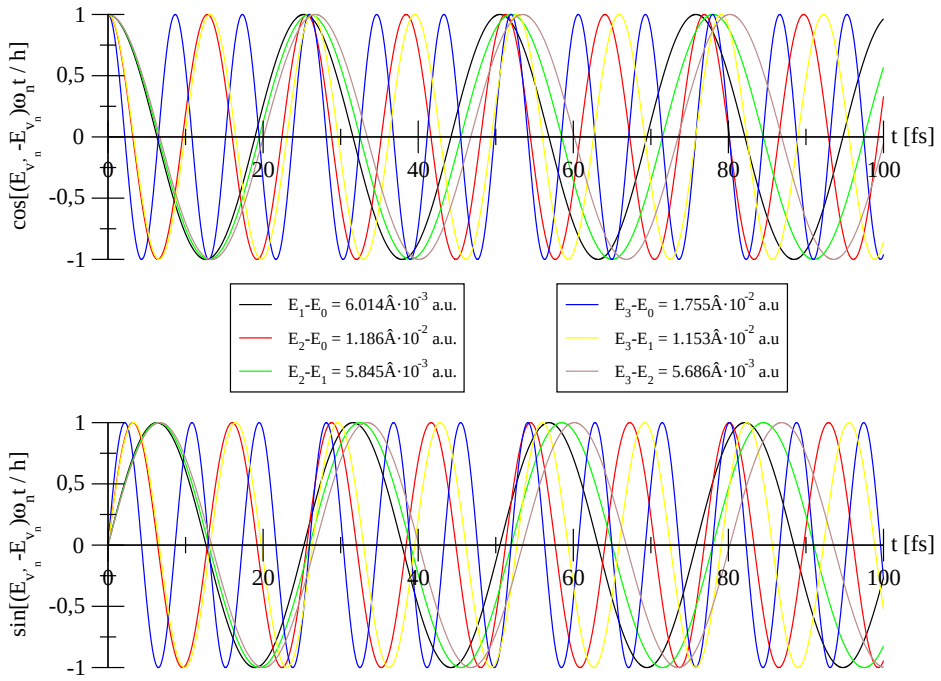

Figure 4.3.3: Time representation of cosine and sine functions, whose frequencies are equal to the difference between two different vibrational states of the $B\,^1\Sigma_u^+$ electronic bound state, $(E_{n,v'} - E_{n,v})/\hbar$. Upper panel: Time representation of the cosine function for several values of the difference $(E_{n,v'} - E_{n,v})/\hbar$. Lower panel: Time representation of the sine function for several values of the difference $(E_{n,v'} - E_{n,v})/\hbar$.

is defined as the projection of the vibrational wavepacket at any time, t, into the same wavepacket at the initial time of propagation, t_0:

$$R_n(t - t_0) = \int_{-\infty}^{\infty} \overline{\phi}_n(R, t_0)\, \phi_n(R, t)\, dR \tag{4.3.12}$$

Using the expression for the vibrational wavepacket in the n bound electronic states, given in equation 4.3.9, the autocorrelation function becomes:

$$R_n(\triangle t) = \sum_{v_n} \int |c_{n,v_n}(T)|^2\, e^{\left[-i\frac{E_{n,v_n}}{\hbar}\triangle t\right]} dv_n \tag{4.3.13}$$

where $\triangle t$ is $t - t_0$. In figure 4.3.5, it is plotted the autocorrelation function for the $B\,^1\Sigma_u^+$ obtained for a XUV pulse with a duration of 2 fs, a central energy of 12.25 eV and an intensity of $10^{12}\,\mathrm{W}\cdot\mathrm{cm}^{-2}$. As can be observed, during the time evolution of the wavepacket, the time points 30 fs and 1075 fs correspond to the maxima in which the vibrational wavepacket reaches the maximum reconstruction possible, around a 70%. In other words, these time points correspond to the time values in which the vibrational wavepacket is roughly located in the inner turning point. When the time points correspond to 12 fs and 993 fs, the wavepacket is spread over a the internuclear distance.

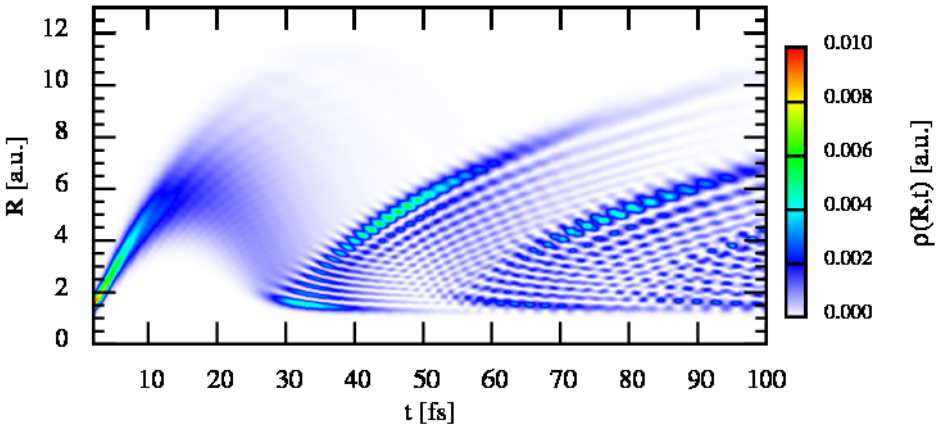

Figure 4.3.4: Representation of the density of the vibrational wavepacket for the $B\,^1\Sigma_u^+$ state as a function of the internuclear distance, R, in the y axis and time, t, in the x axis. The wavepacket was generated by one-photon absorption process using a 2 fs, 14 eV and $10^{12}\,\mathrm{W}\cdot\mathrm{cm}^{-2}$ pulse.

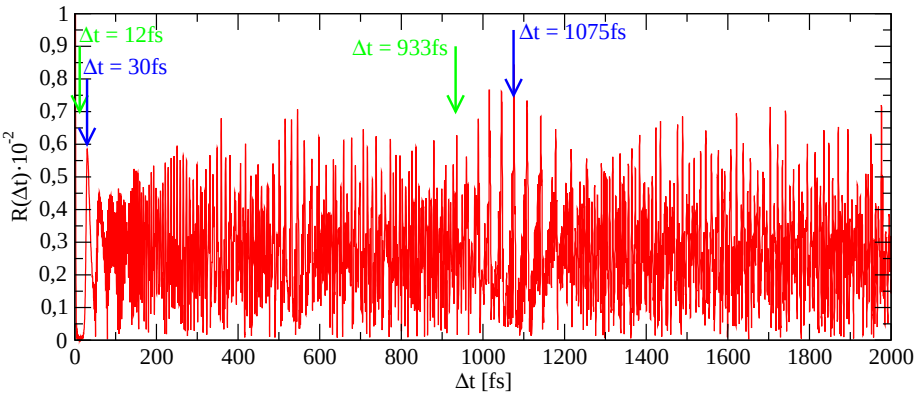

Figure 4.3.5: Autocorrelation function for the $B\,^1\Sigma_u^+$ state as a function of the time, t. The blue arrows indicate the times associated with the maximum reconstruction of the wavepacket and the green arrows to the minimum.

Chapter 5

One-photon absorption processes

The detection of dissociative neutral fragments after electron impact in 1960's [94] was the first experimental evidence of the doubly excited states (DES) existence in the H_2. The H_2 DES are highly correlated electronic states in which both electrons are simultaneously excited. These states are embedded in the single ionization continuum of the H_2 and may decay into these continuum states producing the dissociative or non-dissociative ionization of the H_2 molecule in a timescale comparable to the nuclear motion. This decay process, called autoionization, has an important role in the ionization process of the H_2 molecule. Several experimental and theoretical works have focused on obtaining the structural and dynamical information of DES in H_2 to characterize their contributions to the photoionization processes. Twenty years after the first experimental evidence of their existence, experimental measurements on photodissociation [53, 54, 6] and the first theoretical calculations of their potential energy curves (PECs) [65] were obtained. In the 1990's, new theoretical works focused on the characterization of these states by obtaining energy positions, autoionization widths [144, 147, 148, 160] and photoionization cross sections [146, 147, 148, 76, 77]. Only very recently, combined experimental and theoretical efforts have captured the interferences in the autoionization process involving both electrons and nuclei, in randomly oriented molecules subject to linearly polarized light [140] or in aligned molecules irradiated with circularly polarized light leading to an unexpected circular dichroism in H_2 molecules [42].

In the first section of the present chapter, we study the coherent superposition of continuum states, due to direct photoionization and the contribution of the DES decay into those states. The resulting interference leaves a signal in the photoionization spectra which contain the dynamical information of the autoionization. We discuss the observables and pulse parameters that are required in order to obtain a time image for the dynamics of the DES decay. After the analysis of the autoionization dynamics, in the second section we present a semiclassical model, developed by A. Palacios et al [128], to obtain and explain the shapes and the positions of the signals in the photoionization spectra due to the DES decay. In the last section, we show the signature of autoionization in the angular-resolved ejected electron photoionization spectra, and use the same semiclassical model to explain the fingerprints due to the autoionization.

5.1 Time-resolved imaging of H_2 autoionization

We explore the one-photon ionization of the H_2 molecule, using photon energies to produce the transition from the ground state to the energy region where the DES are embedded. We use linearly polarized light parallel to the molecular axis. Following the dipole selection rules, discussed in chapter 3, only the states whose total symmetry is $^1\Sigma_u^+$ can be populated by photoabsorption. In figure 5.1.1, we represent the relevant potential energy curves of the H_2 molecule. In full thick lines, it is plotted the ground state of the neutral molecule ($X\ ^1\Sigma_g^+$), the six lowest single ionization thresholds of H_2^+ ($1s\sigma_g$, $2p\sigma_u$, $2p\pi_u$, $2s\sigma_g$, $3p\sigma_u$ and $3d\sigma_g$), and the double ionization threshold, the $1/R$ potential curve corresponding to the full Coulomb breakup of the system. The lowest singly excited states of $^1\Sigma_g^+$ and $^1\Sigma_u^+$ symmetries are also plotted. The DES of H_2 lie above its first ionization threshold. Each one of the higher ionization thresholds have their associated series of DES. In figure 5.1.1, there are only shown the first two series, Q_1 and Q_2. It is clear that the potential energy curves of the DES of H_2 are purely repulsive, and consequently, all their vibrational states are dissociative. After the population of DES by photoabsorption, the evolution of the DES can take different channels, which compete among them:

- DES dissociation in neutral atoms:

$$H_2^{**} \rightarrow H(n,l) + H(n',l') \tag{5.1.1}$$

- DES dissociation in ionic fragments:

$$H_2^{**} \rightarrow H^+ + H^- \tag{5.1.2}$$

- DES Autoionization into non-dissociative and dissociative electronic continua:

$$H_2^{**} \rightarrow H_2^+ + e^- \tag{5.1.3}$$

$$H_2^{**} \rightarrow H + H^+ + e^- \tag{5.1.4}$$

Despite the large amount of structural information on photoionization obtained by means of synchrotron radiation [89, 55, 99], characterization of DES with time-resolution requires the use of ultrashort UV/XUV pulsed radiation. In principle, pump - probe techniques using fs pulses can track the combined dynamics of molecular dissociation (nuclear motion lays in the range of tens of fs) and autoionization, which takes place in a few fs for the lowest series of DES in H_2. However, some important considerations on the time and energy domains are required. On the one hand, pulse durations shorter than those lifetimes should be used in order to subsequently trace the field-free evolution of the molecular autoionization triggered after photoabsorption. In addition, the large energy bandwidths (few eV) of such short pulses usually imply more complicated detection techniques in order to obtain full coincidence detection of ejected fragments. This is illustrated in figure 5.1.2, which shows the densities of ionization probability for two different pulse durations, 1 fs (shorter than the lifetime of the DES)

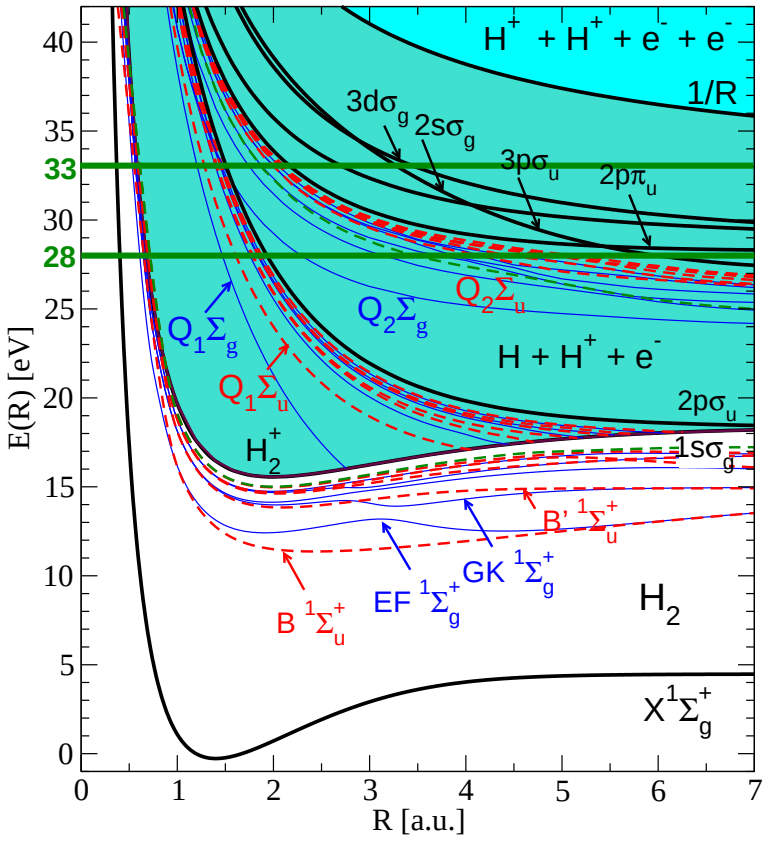

Figure 5.1.1: Potential energy curves of H_2. The six lowest $^1\Sigma_g^+$ and $^1\Sigma_u^+$ single excited states of the neutral are plotted and accordingly labeled. Thick full lines correspond to the ground state of H_2 ($X\ ^1\Sigma_g^+$), the consecutive ionization thresholds (i.e., the six lowest H_2^+ electronic states) and the double ionization threshold ($1/R$) for the full break up of the molecule ($H^+ + H^+ + e^- + e^-$). Shadowed areas indicate the single and double electronic continua, respectively. Embedded in the single electronic continua the first two series of DES, Q_1 and Q_2, are represented. The two horizontal thick lines at 28 eV and 33 eV, indicate the photon energies used for the results presented in this section.

and 10 fs (larger than the lifetime), plotted as a function of proton (left panels) and electron (right panels) kinetic energies. As can be observed, the results present a strong dependence on the pulse duration for a given photon energy. The calculations have been performed considering a laser intensity of $10^{12}\,\mathrm{W}\cdot\mathrm{cm}^{-2}$ for two central frequencies, 28 eV and 33 eV, indicated in figure 5.1.1. For 28 eV, direct photoionization and autoionization from the Q_1 series of DES, both into the first ionization threshold $1s\sigma_g$, are possible. For 33 eV, in addition to the former open channels, there are also contributions from direct photoionization through the second ionization threshold, $2p\sigma_u$, and autoionization from the Q_2 series.

First, note that EKE distributions contain all dissociative and non-dissociative ionization channels, while, as we presented in chapter 4, the PKE distributions only account for dissociative ionization. However, as the non-dissociative ioniza-

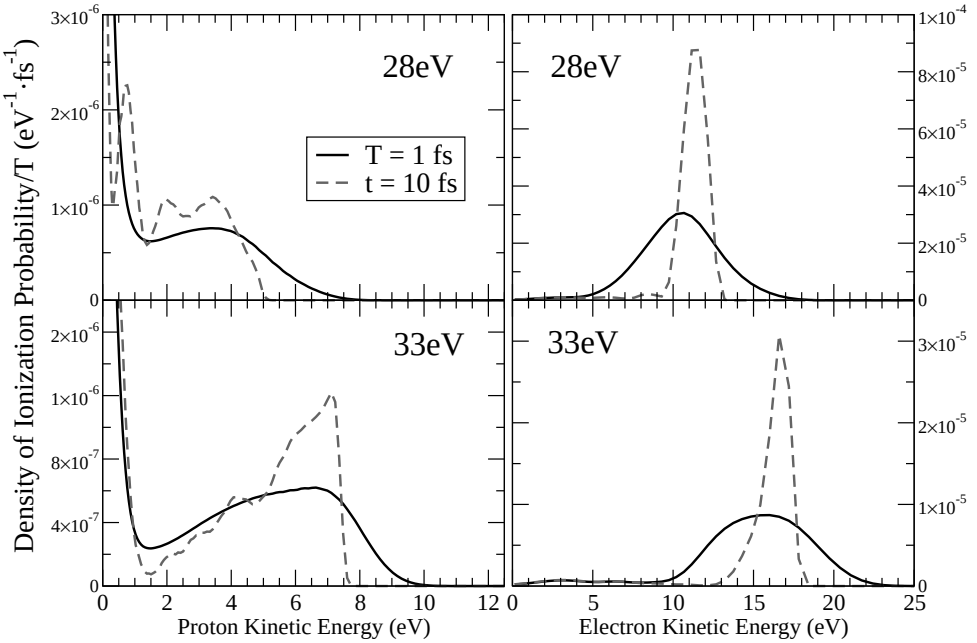

Figure 5.1.2: Density of ionization probability as a function of proton (left panels) and electron (right panels) kinetic energies. Results are plotted for two different pulse durations, 1 fs and 10 fs, and two central photon energies, 28 eV and 33 eV. The intensity is fixed at $10^{12}\,\mathrm{W}\cdot\mathrm{cm}^{-2}$.

tion is the major channel (98%) in photoionization, it dominates in the smooth electron distributions, which reflect the energy bandwidth of the pulse. EKE distributions are centered at the expected values of excess electron energy given by the direct vertical transition from the ground state of the neutral. In contrast, PKE distributions show different structures varying with photon energy and pulse duration. As shown in figure 5.1.2, for 28 eV, the signature of autoionization of the Q_1 series appears at $2-8$ eV of PKE. These structures, due to the autoionization process, are more visible in the dissociative ionization channel [128, 145, 147]. For a central photon energy of 33 eV, the peak at around 7 eV of PKE corresponds to the direct dissociative ionization associated with the $2p\sigma_u$ ionization threshold. The exponential decay of the probability observed at low proton energies corresponds to direct photoionization and it equally manifests in the PKE distributions for any photon energy above the dissociative ionization potential of H_2 (18.15 eV) [145, 151]. The sharp features in the PKE distributions for a 10 fs pulse completely disappear for 1 fs, which is the consequence of the large spectral bandwidth of the pulse.

The figure 5.1.3 shows the densities of dissociative ionization probability for a 1 fs pulse, centered at 28 eV and 33 eV, respectively, as a function of both electron and proton kinetic energies. Here, it is clear that integration over electron energies with such a broad bandwidth leads to smooth PKE distributions when short pulses are used. For a 10 fs pulse (whose energy bandwidth is 0.6 eV), only narrow distributions centered at diagonal total energies of 10 eV (for $\omega = 28$ eV) and 15 eV (for $\omega = 33$ eV) appear [59], which therefore allow for the distinction

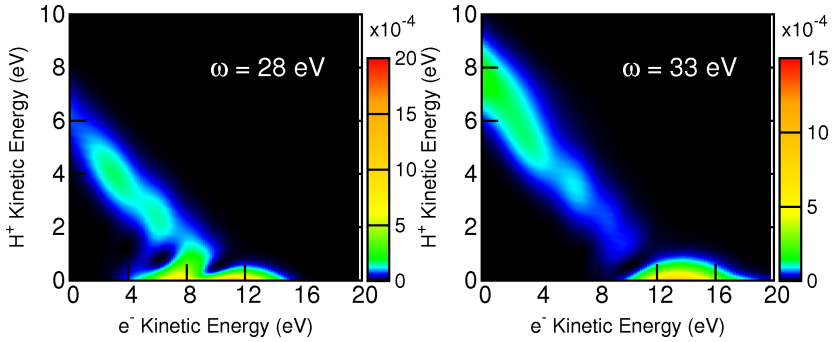

Figure 5.1.3: Densities of dissociative ionization probability as a function of proton and electron kinetic energies for a 1 fs pulse with a central energy of 28 eV, on the left, and 33 eV, on the right panel.

of the autoionization structures after integration over electron energy. The pulse duration dependence of the PKE distributions partly contains information on the time scale for autoionization dynamics. For pulses long enough, the sharp signatures of autoionization appear and the PKE distribution is almost identical to that obtained with monochromatic light (i.e., in the continuous wave limit), which in the energy domain implies that $T > 1/\Gamma$, where Γ is an averaged autoionization width over the relevant internuclear distances. However, for pulses shorter than the average resonance lifetime ($T < 1/\Gamma$), structures are not well-defined and even disappear, therefore photoionization fragments should be measured in coincidence to obtain such information.

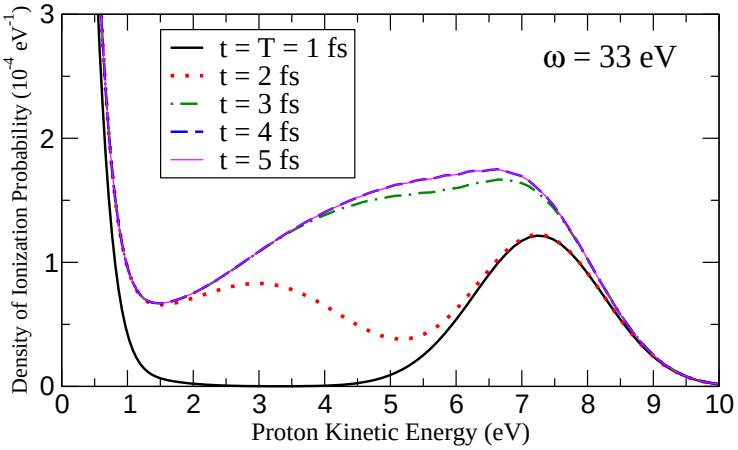

Figure 5.1.4: Density of dissociative ionization probability as a function of the proton kinetic energies for a 1 fs pulse with a central energy of 33 eV and an intensity of $10^{12}\,\mathrm{W}\cdot\mathrm{cm}^{-2}$. Ionization probabilities have been integrated over all possible electron energies. Each curve corresponds to the ionization yield at different times, once the pulse is turned off.

The previous conclusion is further visualized through a time-resolved imaging of the autoionization events. Figure 5.1.4 shows the evolution of the PKE distributions after the interaction with a 1 fs pulse. The density of ionization probability increases with time in the region of intermediate PKE due to the delayed decay

of the DES. The stationary limit is reached 3 fs after the end of the pulse, which is thus the lifetime of the DES that is being significantly populated (the first DES of $Q1\Sigma_u$ series). Moreover, the timescales at which nuclei are moving in the DES potential energy curve are also reflected in the time tracing shown in figure 5.1.4. For $t = 2$ fs, autoionization leads to protons with and energy around 3 eV. This proton energy corresponds to an internuclear distance around 1.8 a.u. in the first $Q_1\Sigma_u$ potential energy curve. At $t = 3$ fs, the density of probability has increased in the region of proton kinetic energies up to $6 - 7$ eV, which indicates that autoionization occurs when the nuclei have moved at least 3 a.u. apart. The probability distributions at 4 and 5 fs are identical, i.e., 4 fs after the end of the pulse non appreciable autoionization takes place. These results suggest the possibility to trace molecular autoionization in time when it is launched with pulses of 3 fs duration or shorter.

5.2 The molecular autoinization model

In the present section, the model developed by A. Palacios et al [128] is introduced and compared with *ab initio* calculations, in order to elucidate the origin of the structures found in the energy-differential ionization probability distributions. In the previous section, we showed the important contribution of the autoionization processes to the final probabilities in the asymptotic regime. Obviously, the study of the resonances was treated first in atoms. One of the most important theoretical works in this area was the Fano's paper [44], in which the quantum treatment of the embedded bound electronic states in the continua explains the interferences signals observed in the atomic energy-differential cross sections as the well-known Fano lineshapes. These Fano lineshapes are due to the coherence interferences between the autoionization decay and the direct photoionization. However, these Fano lineshapes are not observed in the total nor in the energy-differential ionization probability distributions for the hydrogen molecule. It absence is explained within the timescales of the nuclear motion, which can induce effects non-present in atoms for two main reasons: a) the DES can be resonantly excited over a wide range of photon energies due to the nuclear dependence of the energy levels within the Franck-Condon region, which already implies an averaging effect, b) nuclear motion proceeds on similar timescales as autoionization, making the phase accumulated in nuclear propagation relevant. Consequently, the dependence of the decay rate (width), $\Gamma(R)$, with the internuclear distance is behind the absence of the well-known Fano lineshape in the energy-differential ionization probability distributions of molecules, contrary to the clear signature in the atoms ionization cross sections. Although the combination of these two effects renders the absence of Fano profiles in H_2 photoionization spectra, the interference peaks observed in the proton energy-differential distributions for the long pulses, indicate that the dynamics is fully coherent. To explain the autoionization in H_2 and the absence of the Fano profiles in the energy-differential photoionization probability distributions, we use a semiclassical model, developed by A. Palacios et al [128], which describes the autoionization processes in the hydrogen molecule.

The model included the coherent superposition between both autoionization and direct processes. In the dissociative ionization process over the H_2, the system can follow two paths: the direct ionization, which consists in the direct transition from the ground state to the final ionic states, and through the DES, where the photon populates the resonant states, and they evolve in time to larger internuclear distances and finally decay into the continua, reaching the same final states than the direct ionization. This two paths showed in previous section, are also presented in the ionization processes in atoms with resonant states.

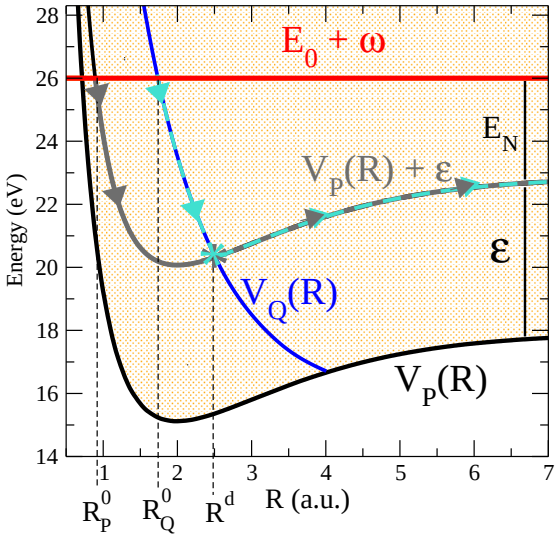

Figure 5.2.1: Representation of the potential energy curves (PECs) for the H_2^+ ground state, $V_P\,(R)$, and the lowest $Q_1\,{}^1\Sigma_u^+$ DES of the H_2, $V_Q\,(R)$. It is indicated the semiclassical nuclear paths included in the presented model, for both the DES and the electronic continuum, $V_P\,(R) + \varepsilon$, where ε represents the energy of the ejected electron. The total energy $E_0 + \omega$ reached after photoabsorption from the lowest vibronic state of the $X\,{}^1\Sigma_g^+$ ground state, not included in the figure, is distributed among the photofragments (nuclei with energy E_{v_α} and the electron with energy ε) such that $\varepsilon + E_{v_\alpha} + V_P\,(R) = E_0 + \varepsilon$. R_P^d and R_Q^d denote the classical turning points for the $V_P\,(R)$ and $V_Q\,(R)$ curves, respectively, for the given total energy, and R^d indicates the internuclear distance at which the DES eventually decays into a continuum state with energy $V_P\,(R) + \varepsilon$. The energy scale starts at $E_0 = 0$, and the y axis thus directly indicates the photon energy in eV.

As in atoms, in molecules the transition probability, and therefore, the photoionization cross section is composed by the two contributions from the continua and from the DES. Thus, in figure 5.2.1, we plot the relevant PEC, corresponding to the PEC of the H_2^+ ground state $1s\sigma_g$, $V_P\,(R)$, and the first DES of symmetry Σ_u, $1Q_1\,{}^1\Sigma_u$, $V_Q\,(R)$. As can be observed, only the first and lower in energy DES are introduced in the model. When the photon is absorbed by the system, the energy of the photon, ω, produces the transition from the ground state, whose energy is E_0, to a final state with total energy $E_0 + \omega$. In addition, when this energy is enough to reach the continua, this energy is distributed between the photofrag-

ments emitted, the proton (or residual ion) and the electron, and therefore, the distribution satisfies: $\varepsilon + E_{v_\alpha} + V_P(R) = E_0 + \omega$. Different from the atomic case, in molecules, the DES position and width depend on the internuclear distance, due to this extra degree of freedom, and the photon can populate a broad range of energies around the center of the resonance. As a consequence of this averaging effect in the center energy of the resonance, the phase jump closed to the resonance center observed in atoms disappears, and therefore, the Fano profile may become absent in a molecule. The relative phase of the nuclear motion in our transition amplitude has to be included for molecules. This internuclear distance dependence of the population of the resonant and continuum states produces a second effect in the transient amplitude, because the contributions from the autoionization and direct ionization paths for the same final proton and electron energies cannot be originated over the same initial internuclear distance value. In this way, the transition amplitude of our molecular ionization has to include the phase contribution of two different nuclear motions from the two different paths.

Taking into account the similarities with atoms, one can part from the Fano expression for the atomic ionization, modifying and including the relative phases of the nuclear motion. In this way, as in the atomic case, the $c_P(\omega, \varepsilon)$ and $a_Q(\omega)$ are the transition matrix elements between the ground state and the final ionic state and DES, respectively, ε is the ejected electron energy and ω is the photon energy. Therefore, the dissociative ionization probability as a function of the photon and ejected electron energy, $P(\omega, \varepsilon)$, can be expressed as (following the model proposed in [128]):

$$P(\omega, \varepsilon) = \left| c_P(\omega, \varepsilon) e^{(-i\theta_P)} e^{(-i\delta_c)} + a_Q(\omega) e^{\left(-i\theta_Q\right)} \right|^2 \tag{5.2.1}$$

where δ_c is an arbitrary phase to take into account the phase difference between the electronic dipole couplings and θ_P and θ_Q are the accumulated phases of the nuclei moving on the continuum and DES potential energy curves, $V_P(R)$ and $V_Q(R)$, respectively. In addition, the energy dependence of the transition matrix elements, $c_P(\omega, \varepsilon)$ and $a_Q(\omega)$, is neglected. The WKB approximation, presented in appendix C, is used to obtain the accumulated phases of the nuclei motion, θ_P and θ_Q, which are:

$$\theta_P = \int_{R_P^0}^{R^d} \left\{ 2\mu \left[\omega - V_p(R) - \varepsilon \right] \right\}^{1/2} dR \tag{5.2.2}$$

$$\theta_Q = \int_{R_Q^0}^{R^d} \left\{ 2\mu \left[\omega - V_Q(R) \right] \right\}^{1/2} dR \tag{5.2.3}$$

where μ is the reduced mass formed for both nuclei and ω is the total energy available equal to the photon energy. In these equations 5.2.2 and 5.2.3, each nuclear phase, and therefore, each amplitude follows a single classical path, which for the one-photon absorption from the ground state with energy E_0, are plotted in figure 5.2.1. R_P^d and R_Q^d are the R values in which the $1s\sigma_g$ PEC plus the electron energy, $V_P(R) + \varepsilon$, and the first DES PEC, $V_Q(R)$, are equal to the

total energy available by the photon, $E_0 + \omega$. These initial internuclear distance values are based on the reflection approximation, explained in appendix C. As commented before, the excess total energy, E_T, which is the total energy available over the dissociation limit of the first ionic state, $E_T = \omega - V_p(R \to \infty)$, is shared between the nuclei and electrons, $E_T = \omega - V_p(R \to \infty) = \varepsilon + E_N$. Because the nuclei are heavier than the electrons, the main peak in the distribution gives all the maximum available energy to the electrons and the nuclei have the minimum value. In the direct path, the probability distribution presents an exponential decay as a function of the nuclear kinetic energy. In the DES case, the excess of total energy represents the decay width of the DES and it is reflected into the initial internuclear distance R_Q^d , which has to be added coherently in a more complex model. However, in this model, this is neglected, as well as the variation of the phase shift, Δ, with the internuclear distance, R, across the resonance, being replaced in this model by the δ_c phase, which is independent of the energy. On the other hand, following the WKB approximation, equations 5.2.2 and 5.2.3 have to be integrated until infinitive value of R. However, after the decay of the resonance, both states evolve in the same potential energy curve, $V_P(R)$, the nuclear phase accumulation in both states are the same. Thus, for the upper integration limit, R^d, is taking the same R value in which both potential energy curves are equal, $V_P\left(R^d\right) + \varepsilon = V_Q\left(R^d\right)$. This R^d is the larger value of the internuclear distance in which the DES can decay and eject an electron.

Focusing on the autoionization path from a semiclassical point of view, the amplitude $a_Q(\omega)$ can be expressed as a product of the direct transition from the ground state to the DES, $c_Q(\omega)$, multiplying by the amplitude which describes the decay of the resonance into the continuum states. To introduce these two factors in the autoionization amplitude, one can follow the Miller's paper [112], to describe the decay probability of the resonant state into the continuum. The density of probability of the DES, $P(R)$, is defined as the probability of the decay into the continuum for a infinitesimal increment of the internuclear distance, R, whose expression is:

$$P(R)\,dR = \left[1 - \int_R^\infty P(R')\,dR'\right] \frac{\Gamma(R)}{\hbar v(R)} dR \tag{5.2.4}$$

where $\Gamma(R)$ is the decay width of the resonance as a function of the internuclear distance, $v(R)$ is the velocity of the nuclei and the term inside the brackets is the probability that the resonance does not decay into the continuum in all the internuclear distance interval. This expression is solved by converting it in a differential equation, one obtain an expression to describe the decay of the resonance into the continuum:

$$P(R) = \frac{\Gamma(R)}{\hbar v(R)} e^{\left[-\int_R^\infty \frac{\Gamma(R')}{\hbar v(R')} dR'\right]} \tag{5.2.5}$$

Using the relation $P(R)\,dR = P(\varepsilon)\,d\varepsilon$, the above probability as a function of the internuclear distance, $P(R)$, can be written as:

$$P(\varepsilon) = \frac{P(R(\varepsilon))}{|\varepsilon'(R)|} \tag{5.2.6}$$

As explained in paper [128], the autoionization amplitude, $a_Q(\omega)$, can be expressed as the square root of the decay probability, $P(\varepsilon)$. Using the above equation, equation 5.2.5 and the relation $\varepsilon = V_Q(R) - V_P(R)$ of the electron energy, ε, with the PEC of the DES, $V_Q\left(R^d\right)$, and the ionic threshold, $V_P(R)$, the autoionization amplitude, $a_Q(\omega)$, is written as:

$$a_Q(\omega) = \sqrt{\frac{1}{\left|V'_Q\left(R^d\right) - V'_P\left(R^d\right)\right|}}\sqrt{\frac{\Gamma\left(R^d\right)}{\hbar v\left(R^d\right)}} c_Q(\omega)\, e^{\left[-\frac{1}{2}\int_{R_Q^d}^{R^d}\frac{\Gamma(R)}{\hbar v(R)}dR\right]} \tag{5.2.7}$$

On the other hand, $c_P(\omega,\varepsilon)$ and $c_Q(\omega)$ are the transition amplitudes from the initial ground state, $\psi_0(\mathbf{r},R)\,\chi_{0,0}(R)$, to the final ionic continuum state, $\psi_P(\mathbf{r},R;\varepsilon)\,\chi_P(R)$, and to the DES, $\psi_Q(\mathbf{r},R)\,\chi_Q(R)$, respectively:

$$c_P(\omega,\varepsilon) = d_P(\varepsilon)\int_0^\infty \overline{\chi}_P(R)\,\chi_{0,0}(R)\,dR \tag{5.2.8}$$

$$c_Q(\omega) = d_Q\int_0^\infty \overline{\chi}_Q(R)\,\chi_{0,0}(R)\,dR \tag{5.2.9}$$

where both equations 5.2.8 and 5.2.9 are expressed within the Franck-Condon approximation, in which it is considered that the dipole couplings, $d_P(\varepsilon)$ and d_Q, are independent of the internuclear distance. This approximation is valid if the dipole coupling between both initial and final electronic wavefunctions changes very smoothly with the internuclear distance. These electronic dipole couplings are defined in the Franck-Condon approximation as:

$$d_P(\varepsilon) = \langle\psi_P(R_e,\varepsilon)|\,\widehat{D}\,|\psi_0(R_e)\rangle \tag{5.2.10}$$

$$d_Q = \langle\psi_Q(R_e)|\,\widehat{D}\,|\psi_0(R_e)\rangle \tag{5.2.11}$$

where $\widehat{D}$ is the electronic dipole operator, which can be expressed in any gauge, i.e., the velocity or length gauge presented in chapter 1, and the electronic wavefunctions are taking in the equilibrium distance of the ground state, R_e, due to the Franck-Condon approximation.

Equation 5.2.1 was evaluated using as inputs the calculated vibronic ground state, the PEC $V_Q(R)$ and $V_P(R)$, and the $\Gamma(R)$ function; only leaving free the values of δ_c, θ_Q and θ_P in a fit to the cross sections. For the vibrational overlaps in equations 5.2.8 and 5.2.9 the reflection approximation, in appendix C, was used. The PEC $V_P(R)$ for the first ionization threshold, $1s\sigma_g$, was calculated analytically and the $1Q_1\,{}^1\Sigma_u$ potential energy curve, $V_Q(R)$, was taken from our *ab initio* calculations, where both potential energy curves are plotted in figure 5.2.1. For the vibrational ground state of H_2 and D_2, we have solved the one dimension TISE using the accurate electronic energies obtained by Wolnievicz [178, 177]. In reference [128],

the results for the dissociative photoionization of H_2 and D_2 as a function of the proton (PKE) or deuteron kinetic energy (DKE) of this model, were compared with the accurate time independent calculations published in reference [147] for photoionization at four different photon energies using linearly polarized light parallel to the molecular axis. Because the δ_c, θ_Q and θ_P parameters only depend on the electronic structure, their values should be the same for both isotopes. This requirement was imposed to fit the model PKE and DKE distributions with the accurate data. In addition, for simplicity it was also imposed δ_c, θ_Q and θ_P to be independent of photon and electron energies, assuming negligible the variation in the relatively narrow photon energy range we are fitting, from 25 eV to 28 eV. For the results shown in reference [128], they found $\delta_c \approx 4\pi/3$ and $\theta_Q/\theta_P \approx 0.15$, where the remaining global scale depends on whether one compares with a cross section or a density of probability obtained from a short pulse calculation. This compares well with the ratio obtained by averaging the actual value over the Franck-Condon region and contributing electron energies, which is $|d_Q/d_P| \approx 0.09$. The agreement of the model with the time dependent calculations of [147] was remarkable, specially because all the electron energy dependencies have been neglected for the amplitudes.

Focusing on this model, one could go further and try to use it to extract resonance decay rates, $\Gamma(R)$, from a given photoionization cross section. Note that the width, $\Gamma(R)$, contains the actual electron–electron correlation information among direct and autoionization paths. In this way, the last decades, there were several experimental and theoretical [91, 90, 70] studies which were focused on obtaining the dynamical properties, as the widths, $\Gamma(R)$, of the resonances. However, some of these works, as reference [91, 90], attempted to extract the autoionization widths as a function of the internuclear distances, $\Gamma(R)$, with a semiclassical expression, analogous to equation 5.2.5, for the decay probability in which the non-resonant contribution into the continua was neglected. Although this formula is valid for some resonances in H_2, like the Q_2 and higher series for symmetries $^1\Pi_u$, an accurate description of the autoionization has to be accounted for the direct photoionization path. In this way, the previous semiclassical model used to characterize the proton energy-differential ionization probability distributions, can be used to obtain the resonance widths. This choice was appropriate since the $1Q_1\,{}^1\Sigma_u$ state is the main state contributing in the photon energy region of 28 eV. However, other DESs also contribute to the actual photoionization process, so that the agreement with the model is expected to be worse for a more complete calculation or an experiment, making extraction of $\Gamma(R)$ significantly more challenging.

Using the method of [151], we have performed our calculations with the *ab initio* spectral method in which all the DESs of the Q_1 series are included, obtaining the nuclear and electronic energy-differential distributions with short pulse. The photon energy and bandwidth of this pulse have been selected to give a non-zero contribution in the energy-differential distribution in the region of interest. After, divided by the Fourier transform (FT) of the used short pulse, we extract the cross sections as described in reference [57]. The results for the latter calculations, as well as for the model using the calculated and fitted $\Gamma(R)$, are plotted

in figure 5.2.2. It shows the photoionization cross sections as a function of photon energy and energy sharing among nuclei and electrons (the ratio between the nuclear kinetic energy and the available total energy, E_T). The upper panel (panel a) of figure 5.2.2 corresponds to the *ab initio* calculation including the complete Q_1 series. The newly calculated cross sections are extremely similar to those in upper-middle panel (panel b) of figure 5.2.2 where only the first DES of the series is included, that is, results as in reference [147]. There are only appreciable differences for photon energies above 28 eV and for energy sharing above 20–30%, where, as expected, we find slightly larger ionization probability due to the contribution from higher DESs in the $Q_1\,{}^1\Sigma_u$ series. The two lowest panels in figure 5.2.2 correspond to the cross sections obtained with the semiclassical model using the calculated width, in lower-middle panel (panel c) of figure 5.2.2, and, more interestingly, when fitting the $\Gamma(R)$ function, in lower panel (panel d) of figure 5.2.2. For this last case, δ_c, c_P and c_Q are left as free energy-independent parameters and we find the function $\Gamma(R)$ that leads to the best agreement of equation 5.2.1 with the *ab initio* calculated cross sections including a single DES, i.e. panel b of figure 5.2.2.

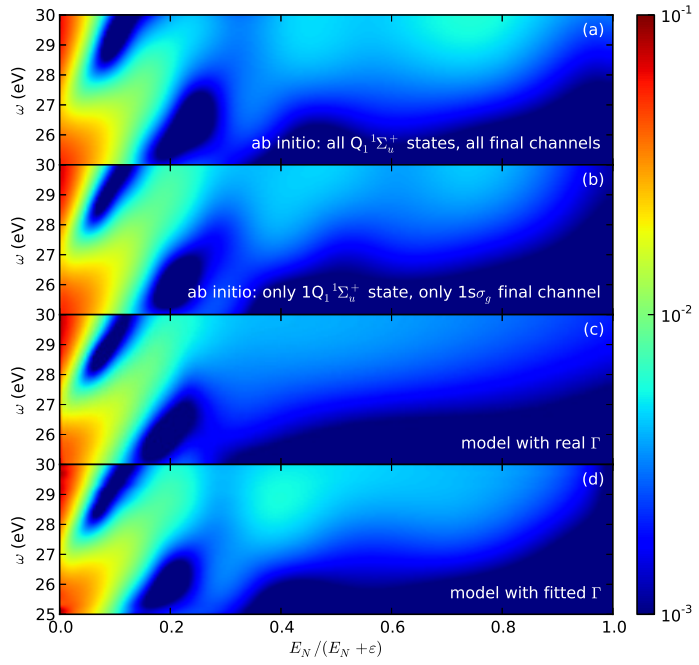

Figure 5.2.2: Density of dissociative ionization probability as a function of photon energy (y axis) and energy sharing (x axis, ratio of nuclear and total kinetic energy available). (a) Full *ab initio* calculations. (b) $1s\sigma_g$ final channel from *ab initio* calculations including only the first DES in the $Q_1\,{}^1\Sigma_u$ series. (c) Simple model in equation 5.2.1 using the calculated values for $\Gamma(R)$ given in reference [147]. (d) Simple model in equation 5.2.1 with $\Gamma(R)$ obtained by fitting to (b).

The corresponding fitted $\Gamma(R)$ is shown in figure 5.2.3 in dashed thick lines and compared with the calculated width, correspond to the full thick line. The fitted values start at around $R = 1.42$ a.u. since this is the smallest internuclear distance that is reached by the largest photon energy, $\omega = 30$ eV, included for the fit. The

agreement is quite reasonable up to an internuclear distance of 3 a.u., that is, well beyond the Franck–Condon region. At larger internuclear distance values, the width is overestimated. This could be expected from the assumptions that are implicit in the semiclassical model: First, it is assumed that the autoionization events eject electrons with a well-defined energy at a given internuclear distance, while in the quantum treatment the electron ejection occurs in an interval of energies with a bandwidth of $\Gamma(R)$ around the energy of the DES, $V_Q(R)$; and second, the amplitudes are approximated by using the reflection approximation and neglecting the energy and R dependencies of the transition elements, whose error is expected to accumulate in the integrals performed in increasingly larger intervals of internuclear distances. In order to further check the validity of the fit, in figure 5.2.3, we have also included the values of $\Gamma(R)$ obtained from an additional fit in which the actual Franck-Condon overlaps between the vibrational ground state and the final resonant and non-resonant states are included. As expected, the extracted widths do not differ from those resulting from the previous fit, because the steep shape of the PEC in the region of maximum vibrational overlap validates the reflection approximation assumed in the first fit.

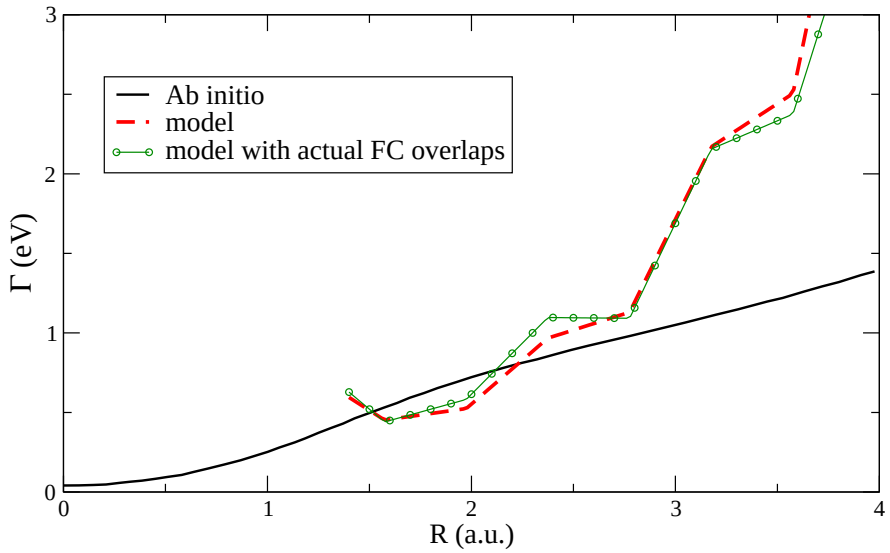

Figure 5.2.3: Autoionization decay width $\Gamma(R)$ (in eV) obtained by fitting equation 5.2.1 to *ab initio* H_2 data. Red dashed line: fit using the reflection approximation. Green line with circles: fit using the actual FC overlaps.

The appropriateness of the model in describing energy-differential cross sections, in particular, the interferences resulting from different dissociation pathways, and in providing a reasonable value of $\Gamma(R)$ up to relatively large values of R, raises the challenge of its applicability in the time domain in order to understand the outcome of pump - probe experiments aimed at getting insight in the autoionization dynamics. These experiments have already been performed on atoms [52] and on hydrogenic molecules [51]. The ultimate goal is to trace molecular autoionization in time. In the following we show the temporal build-up of the interference by means of both time-dependent *ab initio* calculations and the simple model, where we now introduce the time dependence of the nuclear position.

5.2.1 The time-resolved image of DES decay

The time-resolved image of the autoionization process can be obtained with a pulse whose duration is shorter than the average resonance lifetime ($T < 1/\Gamma$). We perform a calculation with a 500 as, 28 eV and $10^{12}\,\mathrm{W \cdot cm^{-2}}$ pulse and extract the cross section in the range 25–28 eV, for which the energy components of the FT of the pulse are appreciably non-zero. As the cross section is only well-defined in the asymptotic limit, we will talk about apparently cross section. We take snapshots every 500 as after the end of the pulse. The time evolution of the apparent cross section is plotted in the left-side panels of figure 5.2.4 for four different photon energies. The thin full line in each panel corresponds to the long-time limit. For completeness, we have also included the time independent calculations from reference [147], corresponding to the dashed lines. We compare to the time dependent calculations where only the lowest DES is included, as in upper-middle panel of figure 5.2.3 and reference [147]. Just at the end of the pulse ($t = T = 0.5$ fs), only direct photoionization is observable. 500 as later ($t = 1.0$ fs), autoionization leads to ions with energies up to 2.5 eV and interferes with the direct ionization channel. As time passes, larger proton kinetic energies are observed, and the interference builds up. At $t = 3.0$ fs, that is, 2.5 fs after the end of the 500 as pulse, autoionization has practically finished and the apparent cross sections have reached their asymptotic form.

In order to distinguish if the evolution is due to the electron correlation, and thus comparable to structures in atomic systems, or nuclear motion, and thus of purely molecular origin, we investigate the nuclear dynamics in more detail. While the direct contribution "instantaneously" populates the nuclear continuum, the contribution from the DES depends on time. The laser pulse creates a vibrational wavepacket in the DES, which then slides down the $V_Q(R)$ curve, accelerating in the process. Snapshots of this wavepacket, extracted from the full *ab initio* calculation, are shown in figure 5.2.5. When the wavepacket arrives passes over a given internuclear distance R, it ejects electrons at the associated energy $\varepsilon = V_Q(R) - V_P(R)$, which also determines the asymptotic nuclear energy $E_N = E_T - \varepsilon$. A time dependent version of the semiclassical model is also proposed by A. Palacios et al [128]. In this extended model, the expression for the ionization probability as a function of the time is given by:

$$P\left(\varepsilon, E_N, t\right) = \left| c_P e^{-i\theta_P} e^{-i\delta_c} + g\left(t, \varepsilon\right) a_Q e^{-i\theta_Q} \right|^2 \tag{5.2.12}$$

where $g(t, \varepsilon)$ is a time-dependent filter, approximating to a Gaussian function, representing the accumulated amplitude of the vibrational wavepacket, ϕ_Q, passing over the internuclear distance in which $V_Q(R)$ curve cuts the $V_P(R)$ curve (see reference [128] for details on the time dependent model).

The time dependent probabilities obtained with this simple model appear in the right-side panels of figure 5.2.4. Again, the agreement with the *ab initio* calculations is excellent, except at high proton energies. Apart from the interference with the P background, the observed temporal dependence is simply that of the vibrational wavepacket motion in the metastable Q electronic state. The snapshots at different times reveal the expected profile of electron ejection from the

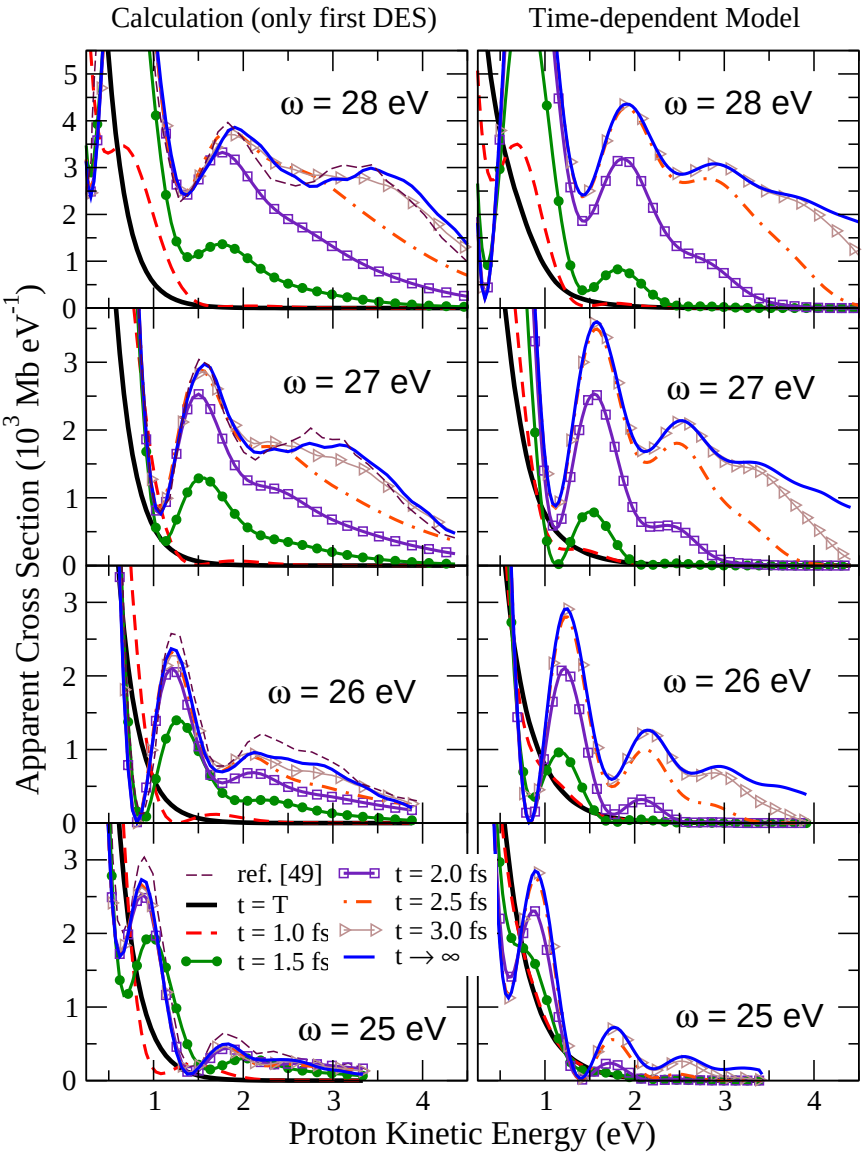

Figure 5.2.4: Field-free evolution of H_2 dissociative ionization apparent cross sections at different times after the end of a T=500 as pulse. Left panels: *ab initio* calculations including the first $1Q_1\ ^1\Sigma_u^+$ DES. Right panels: time-dependent model, explained in the text. Each row corresponds to a given photon energy. Blue full thick lines correspond to the probabilities in the long-time limit. Dotted lines are time-independent calculations taken from reference [147].

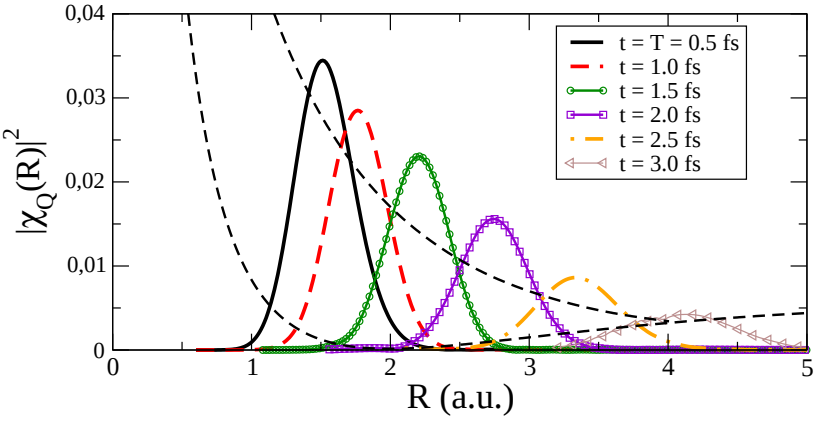

Figure 5.2.5: Field-free propagation of the vibrational wavepacket associated with the $1Q_1\,{}^1\Sigma_u^+$ state, launched from the ground state by a 500 as pulse centered at 28 eV.

moving vibrational wavepacket. Thus, we demonstrated that the nuclear motion indeed determines the time at which the contribution at a given proton kinetic energy appears in the spectrum. Electron correlation only governs the local decay rate $\Gamma(R)$, which dictates how much autoionization occurs.

5.3 Asymmetry in angular distributions

The modern detection techniques, as the reaction microscope [171], allow to measure the individual momenta of all charge particles emerging from an ionization process. These detection techniques open the way to study more complex observables which can include more dynamical information of the ionization process. Therefore, in the present section we will go further than in previous sections and we will study not only autoionization effects over the energy-differential distributions, unless also the energy and angular-differential distributions of the ejected electron in the molecular frame, i.e. with respect to the internuclear axis of the molecule. Several works show that as in multiphoton, treated in chapter 7 [58], as even in the one-photon absorption processes [57], the symmetric photoionization can be broken. This is a consequence of the combination of two scattering states with the same final energy but with different parity. As in previous sections, the autoionization of the DES plays an important role in this asymmetry, because the decay of the resonance into certain energy regions can increases dramatically the population of the scattering states whose coherent superposition gives the non-zero contribution to the asymmetry parameter.

As it was presented in section 5.1, although the autoionization takes place over both non-dissociative and dissociative ionization channels, the larger contribution of the non-dissociative ionization with respect to the dissociative one, makes that autoionization effects are more clear in the last one. Therefore, in this section we focus on the electron angular distributions in the molecular frame for the dissociative ionization of the H_2. As in previous sections, our calculations are performed

considering the parallel orientation of the electromagnetic field with respect to the molecular axis. Because measuring the electron angular distribution is usually a difficult task, in the present section, we study the more convenient asymmetry parameter, A, of the ejected electron as a function of the proton and electron kinetic energies, presented in chapter 4 by the equation 4.3.6:

$$A = \frac{I_{up} - I_{down}}{I_{up} + I_{down}} \tag{5.3.1}$$

where I_{up} and I_{down} are the electronic and nuclear energy-differential electron angular distributions integrated with respect to up and down regions separated by the plane containing the inversion center and perpendicular to the molecular axis.

In the present section, the theoretical asymmetry parameter is compared not only with the previously semiclassical model, also with an experimental measurement. The experiment was performed in Heidelberg laboratory by the group of Prof. J. Ullrich and Prof. Robert Moshammer. Details of the experiment can be found in [48]. In the experiment, the system is irradiated by an APT, with a photon energy between $16 - 37\,\text{eV}$. The photofragments are detected by a reaction microscope obtaining the asymmetry parameter. To compare with the experimental data, we perform a theoretical calculation with an APT pulse which contains 4 pulses, whose durations are 600 as and have a central energy of 29.3 eV. The Fourier transform of both experimental and theoretical APT are very similar, claiming the validity of the comparison in the one-photon absorption process observed. The photon energy of the APT is enough to ensure that both first, $1s\sigma_g$, and second, $2p\sigma_u$, ionization threshold and the first $Q_1\,{}^1\Sigma_u^+$ are reached in the ionization process.

The application of the semiclassical model in reference [128], allows us to unravel the main contributions in the quantum interferences observed in the asymmetry parameter. To compute the asymmetry parameter in equation 5.3.1 within the semiclassical model, one has to take into account the final scattering wavefunctions. In this problem, only the first two ionic states are considered, so the wavefunction has to be a linear combination of both ionization thresholds, $1s\sigma_g$ and $2p\sigma_u$, in which we represent every possible ejected electron partial waves:

$$\begin{aligned} |\Psi\rangle = &\sum_{l=0,2,\ldots} c_1^l \left|\phi_{1s\sigma_g,v_{1s\sigma_g}}\right\rangle \left|\xi_{l,0}^g(\varepsilon)\right\rangle + \sum_{l=1,3,\ldots} c_2^l \left|\phi_{1s\sigma_g,v_{1s\sigma_g}}\right\rangle \left|\xi_{l,0}^u(\varepsilon)\right\rangle + \\ &+ \sum_{l=1,3,\ldots} c_3^l \left|\phi_{2p\sigma_u,v_{2p\sigma_u}}\right\rangle \left|\xi_{l,0}^u(\varepsilon)\right\rangle + \sum_{l=0,2,\ldots} c_4^l \left|\phi_{2p\sigma_u,v_{2p\sigma_u}}\right\rangle \left|\xi_{l,0}^g(\varepsilon)\right\rangle \end{aligned} \tag{5.3.2}$$

where we used the Dirac's notation in the Hilbert space to simplify the actual maths. In the above equation, c_i^l are the corresponding ionization amplitude, the wavefunctions $\left|\phi_{1s\sigma_g,v_{1s\sigma_g}}\right\rangle$ and $\left|\phi_{2p\sigma_u,v_{2p\sigma_u}}\right\rangle$ represent the first and second ionization threshold, $\left|\xi_{l,0}^x(\varepsilon)\right\rangle$ is the wavefunction of the ejected electron, in which, l is the angular momentum and x is the parity of the ejected electron (note the

redundant notation, because all l odd have a u parity and all l even have a g parity). This equation can be simplified, attending to the physical properties of the one-photon transition. Because the dipole selection rules establish that the one-photon absorption from the ground state ($X\ ^1\Sigma_g^+$) can only populate final states with Σ_u total symmetry, for the transition in which the internuclear axis of the molecule is parallel with respect to the field polarization vector. In addition, attending to the symmetry multiplication rules ($g \otimes g = u \otimes u = g$ and $g \otimes u = u \otimes g = u$), to give a final state with Σ_u total symmetry, the first ionization threshold with a symmetry Σ_g, can only eject electrons with l odd (symmetry Σ_u), and the second ionization threshold, whose symmetry is Σ_u, eject electrons with l even (symmetry Σ_g). In this case, the coefficients c_1^l and c_3^l have to be zero, and therefore, can be neglected in equation 5.3.2 for the studied one-photon absorption process. Moreover, the transition amplitudes are larger to the scattering states in the expansion with lower angular momenta, i.e. we can consider that only the $l = 1$ partial wave for the $1s\sigma_g$ and $l = 0$ for the $2p\sigma_u$ and in the equation 5.3.2. Applying these simplifications, equation 5.3.2 becomes:

$$|\Psi\rangle = c_2 \left|\phi_{1s\sigma_g, v_{1s\sigma_g}}\right\rangle \left|\xi^u_{1,0}(\varepsilon)\right\rangle + c_4 \left|\phi_{2p\sigma_u, v_{2p\sigma_u}}\right\rangle \left|\xi^g_{0,0}(\varepsilon)\right\rangle \tag{5.3.3}$$

where the $c_2 = c_2^1$ and $c_4 = c_4^0$. On the other hand, as we introduced in chapter 4, to project the final wavefunction into the localized electron and proton final states is necessary the "left-right" basis:

$$\begin{aligned} |\Phi_+\rangle &= \frac{1}{\sqrt{2}} \left(\left|\phi_{1s\sigma_g, v_{1s\sigma_g}}\right\rangle + \left|\phi_{2p\sigma_u, v_{2p\sigma_u}}\right\rangle\right) \\ |\Phi_-\rangle &= \frac{1}{\sqrt{2}} \left(\left|\phi_{1s\sigma_g, v_{1s\sigma_g}}\right\rangle - \left|\phi_{2p\sigma_u, v_{2p\sigma_u}}\right\rangle\right) \end{aligned} \tag{5.3.4}$$

On the other hand, to define the direction of the ejected electron contribution into the upper and lower hemispheres of the asymmetry parameter, we separate the residual ion and the ejected electron wavefunctions, where these electron wavefunctions can be written as:

$$\begin{aligned} |\phi_{up}\rangle &= \frac{1}{\sqrt{2}} \left(\left|\xi^g_{0,0}(\varepsilon)\right\rangle + \left|\xi^u_{1,0}(\varepsilon)\right\rangle\right) \\ |\phi_{down}\rangle &= \frac{1}{\sqrt{2}} \left(\left|\xi^g_{0,0}(\varepsilon)\right\rangle - \left|\xi^u_{1,0}(\varepsilon)\right\rangle\right) \end{aligned} \tag{5.3.5}$$

For a fixed ejected proton direction we measure the electron distribution with respect to the plane contained in the inversion center and perpendicular to the molecular axis. Consequently, the final localized states have to be the product of one of the "left-right" basis, in our case the $|\Phi_+\rangle$, combined with the upper and lower ejected electron states from equation 5.3.5 to obtain the final electron and proton localized final states:

$$\begin{aligned} |\psi_{up}\rangle &= |\Phi_+\rangle\, |\phi_{up}\rangle \\ |\psi_{down}\rangle &= |\Phi_+\rangle\, |\phi_{down}\rangle \end{aligned} \tag{5.3.6}$$

To obtain the I_{up} and I_{down} densities of probability defined in the asymmetry parameter, equation 5.3.1, we project into the final localized states defined in equation 5.3.6 the final wavefunction given in equation 5.3.3:

$$\begin{aligned} N_{up} &= |\langle \psi_{up} | \Psi \rangle|^2 = \frac{1}{4}\left(|c_2|^2 + |c_4|^2 + c_2^* c_4 + c_2 c_4^*\right) \\ N_{down} &= |\langle \psi_{down} | \Psi \rangle|^2 = \frac{1}{4}\left(|c_2|^2 + |c_4|^2 - c_2^* c_4 - c_2 c_4^*\right) \end{aligned} \tag{5.3.7}$$

And finally, introducing the I_{up} and I_{down} densities of probability from equation 5.3.7 in the asymmetry parameter, equation 5.3.1, the final asymmetry parameter is:

$$A = \frac{2\Re\left[c_2^* c_4\right]}{|c_2|^2 + |c_4|^2} \tag{5.3.8}$$

where the coefficients c_2 and c_4 correspond to the first and second ionization thresholds, respectively. Now, attending to the semiclassical model presented in section 5.2, the c_2 and c_4 coefficients have to be separated in our treatment. While the c_2 coefficient has two contributions, the direct ionization amplitude from the ground state and the autoionization amplitude from the DES; the c_4 coefficient is only given by the direct photoionization amplitude, so:

$$\begin{aligned} c_2 &= c_P^{1s\sigma_g} e^{-i\theta_P^{1s\sigma_g}} e^{-i\delta_c^{1s\sigma_g}} + a_Q e^{-i\theta_Q} \\ c_4 &= c_P^{2p\sigma_u} e^{-i\theta_P^{2p\sigma_u}} e^{-i\delta_c^{2p\sigma_u}} \end{aligned} \tag{5.3.9}$$

where $\theta_P^{1s\sigma_g}$, θ_Q and $\theta_P^{2p\sigma_u}$ are the dynamical nuclear phases, obtained with the WKB method (given in equations 5.2.2 and 5.2.3 for the first ionic threshold) and $\delta_c^{1s\sigma_g}$ and $\delta_c^{2p\sigma_u}$ are the phases acquired in the transitions between electronic states. These $\delta_c^{1s\sigma_g}$ and $\delta_c^{2p\sigma_u}$ phases are accessible by the full quantum calculation or by comparing spectra obtained from different isotopes.

In figure 5.3.1, the asymmetry parameter as a function of nuclear and electron kinetic energies is plotted for the experimental data, the semiclassical method and quantum calculation, from the upper to the lower panel, respectively. The result of the simulation (where we set $\delta_c^{1s\sigma_g} - \delta_c^{2p\sigma_u} = \pi$), in the middle panel, is in a very good agreement with the experimental measurement by the group of Prof. Ullrich and Prof. Robert Moshammer, in the upper panel, and our quantum mechanical calculation, in the lower panel of figure 5.3.1. The value $\delta_c^{1s\sigma_g} - \delta_c^{2p\sigma_u} = \pi$ is close to that obtained by averaging the phase difference resulting from the *ab initio* calculation in the Franck-Condon region and in the photon energy range considered in this work. The black contour lines of symmetric ejection, $a = 0$, are calculated by the simulation and overlaid on both energy correlation maps to enable better comparison with the measurement. All phases are inherently accounted for in a fully quantum mechanical treatment of the problems, which we have performed using a previously described method.

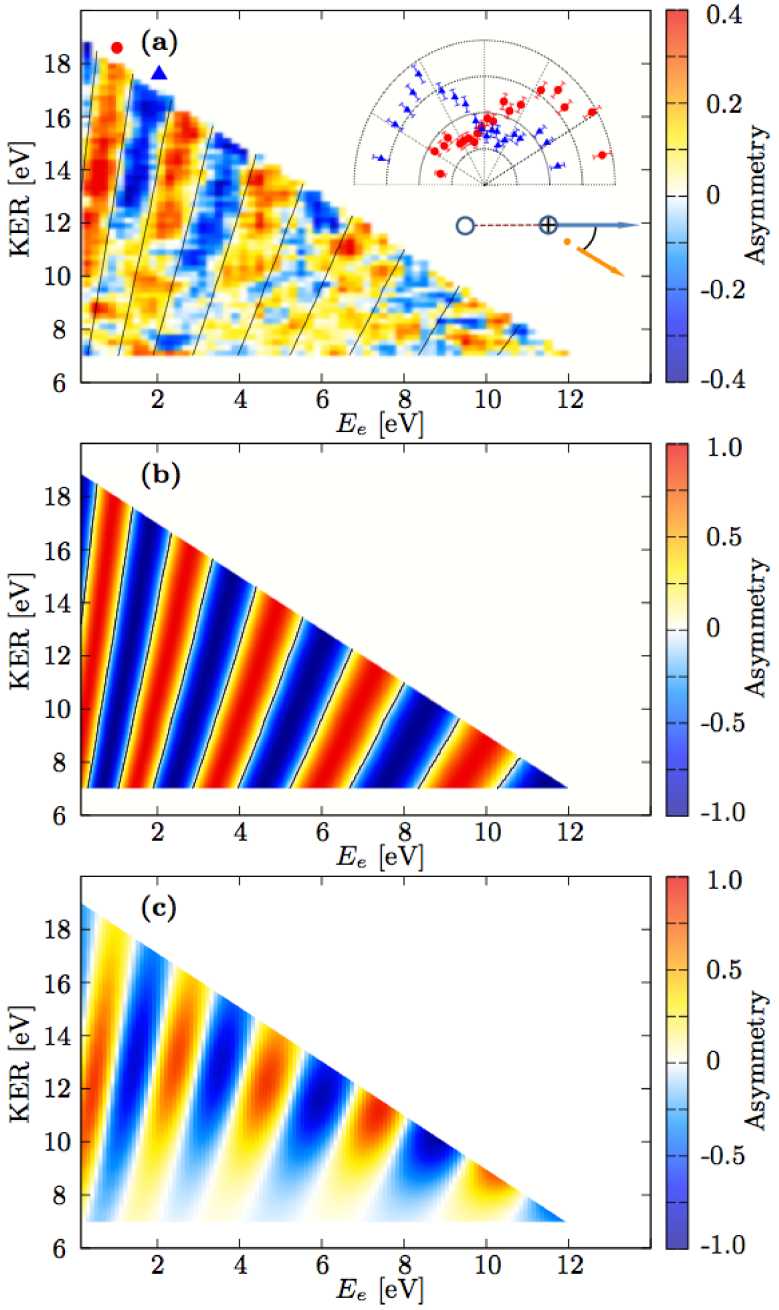

Figure 5.3.1: Asymmetry parameter of the ejected electron as a function of the electron, in the x axis, and proton, in the y axis, kinetic energies for dissociative photoionization of H_2. The panel (a) shows experimental asymmetry parameter measured. The inset in the panel (a) features the distribution of the electron and proton angle, α, for positive, as circles, and negative, as triangles, values of A. The panel (b) gives the asymmetry parameter obtained with the semiclassical model. The black contours are lines which correspond to constant values of the asymmetry parameter equal to zero, copied to the experimental plot for comparison. The panel (c) shows the asymmetry parameter for the fully quantum mechanical calculation.

In the present case, the obtained asymmetry results from the combination of different parity molecular states from the first $1s\sigma_g$, and second, $2p\sigma_u$, ionization threshold reached by the one-photon absorption. However, to obtain this asymmetry the photon has to be capable of populating molecular states of both threshold with the same electron and nuclear energies. In figure 5.1.1, it is clear that just after the pulse the DESs do not have enough time to decay, so the main contribution to the probability came from the direct photoionization from the ground state. In this case, the first and second threshold are populated at different nuclear and electron energies, and therefore, cannot produce any asymmetry in the electron angular distributions. However, the evolution of the system after the pulse allows that the Q_1 DES decay into the first ionization threshold in the energy region where the second ionization threshold was populated by the direct photoabsorption process. Since the decay process from the DES to the continua states conserve the parity, the combination of the continuum states of both threshold, with different parity, gives a non-zero oscillation pattern in the asymmetry parameter observed in figure 5.3.1. Therefore, the autoionization plays the main role to induce an electron angular distribution asymmetry in the ionization process, where the oscillation pattern obtained is mainly dependence with the electron energy, E_e.

Chapter 6

UV pump - IR probe scheme

The time-resolved image of the autoionization decay, shown in chapter 5, confirms the suitability of the isolated extreme UV (XUV) pulses to launch and explore the dynamics in the H_2 molecules at its natural timescales [66, 33, 87, 62, 150]. Based on these XUV pulses, the pump - probe schemes are capable of extracting the temporal dynamical information of the ionization process. Within these pump - probe techniques, the use of an ultrashort XUV pump combined with an IR pulse have been particularly successful in providing temporal information in photoionization processes in atoms [97, 164, 98, 52] and in the hydrogen molecule [82, 51]. In all these works, the XUV launches the photoionization dynamics which is then probed by the IR field as a function of the time delay between them. The ideal situation is when the IR field arrives after the end of the XUV, and therefore, both pulses are not overlapping in time. However, the longer duration of the IR field with respect to the XUV pulse makes that these experiments also measure the fragments emitted when both pulses are overlapping. In this case, the system is being pumped and probed at the same time and is usually called laser-assisted photoionization [27, 36].

Following the previous chapter, the first part of the present chapter is devoted to explore the role of the autoionization when the XUV pulse reaches the system joint with and IR field. Consequently, we focus on the ionization of the laser-assisted photoionization of the H_2 in the region where the autoionization takes place. Our goal is trace the electron dynamics launched by the XUV pulse and recorded by the IR field in the fully or integrated energy-differential distributions. As in chapter 5, we restrict our description of the laser to linearly polarized light parallel with respect to the molecular axis. Thus, based on the dipole selection rules and the $^1\Sigma_g^+$ symmetry of the ground state, the absorption of an odd number of photons leaves the system in final states with $^1\Sigma_u^+$ symmetry, and for an even number of photons, populates final states of $^1\Sigma_g^+$ symmetry. In our analysis of the final observables, we extract the role of the IR field to vary the population in both ionization channels, the direct ionization and the autoionization. Finally, we explore the driving effects of the IR field over the ejected electron in the ionization process, the streaking.

In the second part of this chapter, we present a similar XUV pump - IR probe scheme, but using a train of attosecond pulses combined with an phase-locked

IR to pump the target and other IR field to probe it. The use of a train instead of a single attosecond pulse (SAP), strongly modified the induced phenomena. Moreover, we employ this scheme to probe the dynamics associated to the single excited states of the hydrogen molecule. Previous experimental works have used a combination of XUV and IR pulses to probe and even control the excitation and ionization in He by interfering electron wavepackets [139, 74]. These experiments extended the Brumer-Shapiro works [18, 19, 130, 192, 96, 56] of two-path interference coherent control concept to the attosecond timescales and XUV frequency domains. However, the IR field used as a probe distorts the potential energy curves, so the dynamics extracted is affected by it. In this way, the state-of-art to obtain the dynamics of these states with a weak external perturbations is the use of a XUV pump - XUV probe scheme, studied in next chapter.

6.1 Molecular streaking in the autoionization region (SAP + IR)

We propose the study of the laser-assisted photoionization in the region where the doubly excited states (DESs) decay into the continuum states by autoionization. As widely discussed in chapter 5, autoionization leaves a clear signature into the continuum states, whose dynamics can be obtained using the present XUV pump - IR probe technique. Although several experimental and theoretical works for atoms [52, 123, 27, 167, 134] and molecules [92, 51], were devoted to elucidate the electron dynamics induced by the combination of a XUV pulse and an IR field, the autoionization effects manifested in the differential observables are not well-described in H_2. In addition, the similar timescales of the nuclear motion and the autoionization in the H_2 molecule introduce a complexity in the assignment of the paths following after the photoionization. We focus on a complete analysis of the energy-differential distributions to elucidate the different competing paths that reach the same final states, as well as the mechanisms that can be triggered by the simultaneous interaction of the XUV pulse and the IR field. A similar scheme was previously used in our group [51] to simulate attosecond photoionization of H_2 and D_2 molecules. This work focuses on the analysis of the NKE distributions as a function of the time delay between both pulses. However, in the present section we expand our analysis to the NKE and EKE distributions as well as the densities of probability measured in coincidence for all emitted charge particles.

For these simulations, we use a XUV pulse with an intensity of $10^9\,\mathrm{W}\cdot\mathrm{cm}^{-2}$, a photon energy of 28 eV and a duration of 1 fs. The IR used has an intensity of $3\cdot 10^{12}\,\mathrm{W}\cdot\mathrm{cm}^{-2}$ and a photon energy of 1.65 eV, equivalent to a 750 nm wavelength and a period around 2.5 fs. In our theoretical simulation we use two IR durations, 6 fs and 9 fs. Both pulses, XUV and IR, are phase-locked, so the time delay can be defined as the time difference at which the maximum amplitude is reached of the IR field with respect to the XUV pulse. In this way, the pulses overlap for time delays between -3.5 fs and 3.5 fs for the 6 fs IR pulse and between -5.0 fs and 5.0 fs for the 9 fs IR probe pulse. As was explained in chapter 2, the negative time delays represent the IR arriving before than the XUV pulse. In figure 6.1.1,

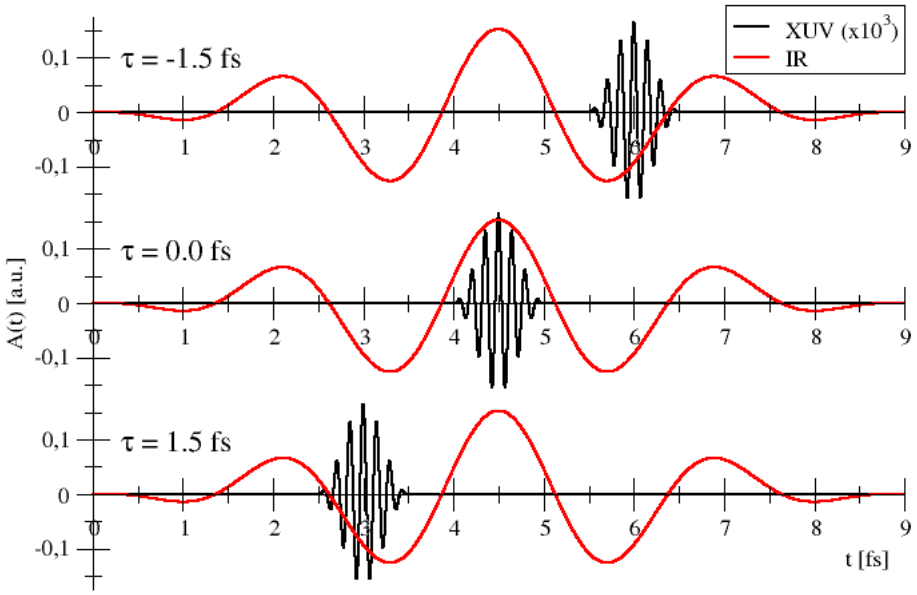

Figure 6.1.1: Vector potential of the of the final XUV pump - IR probe scheme for three different time delays: $\tau = -1.5\,\text{fs}$ in the upper panel, $\tau = 0.0\,\text{fs}$ in the middle panel and $\tau = 1.5\,\text{fs}$ in the lower panel. The XUV vector potential is plotted in black and it is increased 10^3 time to compare with the IR. The IR vector potential is plotted in red.

it is plotted the vector potentials of the XUV and 9 fs IR pulses for three different time delays. The IR field with a carrier energy of 1.65 eV cannot ionize the target by itself, because the neutral molecule should absorb around 10 photons to reach the dissociative ionization threshold, which is unprovable for the intensities of $3 \cdot 10^{12}\,\text{W} \cdot \text{cm}^{-2}$. Similarly, the absorption of more than one XUV photon would lead to very small probabilities, since the intensity of the XUV laser pulse is even smaller than that of the IR pulse ($10^9\,\text{W} \cdot \text{cm}^{-2}$ versus $3 \cdot 10^{12}\,\text{W} \cdot \text{cm}^{-2}$). Besides, two XUV photon absorption would already lead to ionization in a higher energy region than considered in this work.

The broad bandwidth of the XUV pulse and the multiphoton absorption or emission of the IR after the XUV absorption (XUV, XUV+IR, XUV−IR, ...) allow to reach several final states for a given final energy, leading to different open reaction channels. Figure 6.1.2 shows the PECs of the relevant electronic states that can be reached by absorption of the UV±IR light. Due to the large energy bandwidth of the XUV pulse, also plotted in figure 6.1.2 on the energy axis, the ionization can proceed through the two lowest ionization thresholds, $1s\sigma_g$ and $2p\sigma_u$. Only the ground state of the ion, $1s\sigma_g$, presents vibrational bound states. In the energy range considered, the non-dissociative ionization dominates ($> 90\%$), due

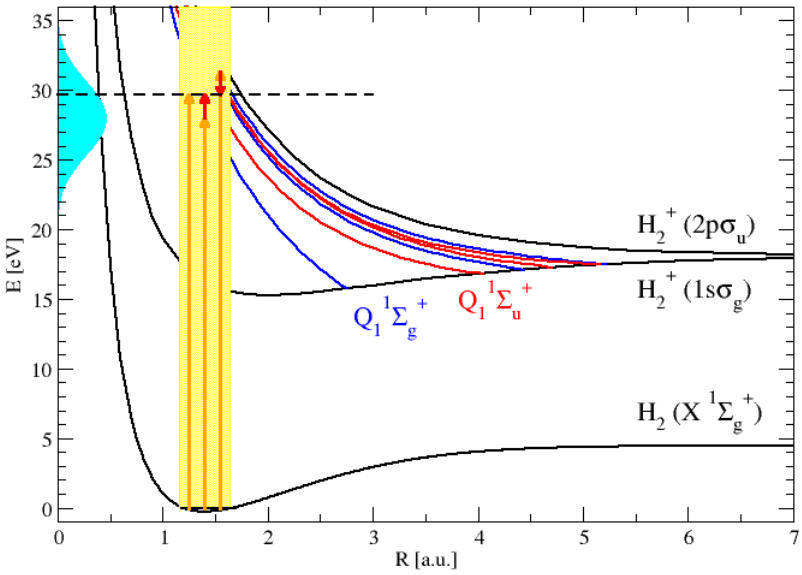

Figure 6.1.2: Relevant potential energy curves of H_2 and H_2^+. The ground states of the neutral, $X\ ^1\Sigma_g^+$ and the two lowest ionization thresholds, $1s\sigma_g$ and $2p\sigma_u$, are plotted. The three lowest states for each symmetry of the Q_1 series are also plotted, where the blue curves are the $Q_1\ ^1\Sigma_g^+$ and the red curves are the $Q_1\ ^1\Sigma_u^+$. The vertical yellow shadow indicates the Franck-Condon region delimited by the ground state. The spectral distribution of the attosecond XUV pump is plotted in cyan. Orange and red arrows represent the XUV and IR photons absorbed or emitted by the system. We illustrate three photon-absorption paths: Left: Indicates absorption of a single XUV photon with an energy of 29.65 eV. Middle and right: Two-photon absorption process of second order, involving the absorption and/or emission of an IR photon after absorption of the 28 eV or 33 eV XUV photon, respectively.

to the favorable Franck–Condon overlap [144, 57]. The excess energy given to the system will be shared between electrons and nuclei. Because we have a broad bandwidth, electrons and/or nuclei ejected with a given energy may be associated with final states of different total excess energy. The only way to distinguish the different paths is to detect the ejected fragments (electrons and residual ions) in coincidence. As was presented in chapter 5, the autoionization from DES of the neutral molecule is possible for the photon energies above 25 eV [144]. In figure 6.1.2, it is also plotted the first series of DES of H_2, which decay by autoionization into first threshold of the H_2^+ $(1s\sigma_g)$. Autoionization contributes to both dissociative and non-dissociative ionization channels, and consequently, interferes with the direct ionization process leading to characteristic features in the nuclear kinetic energy distributions shown in chapter 5. In the following, we seek to answer the question: How does the presence of the IR field modify the

autoionization signal that is observed by one-photon absorption of a single XUV pulse?

6.1.1 Nuclear kinetic energy distributions

First, we explore the NKE distributions in the dissociative ionization channel, where autoionization is expected to leave a larger signal in both ionic states of the residual ion, H_2^+. In figure 6.1.3, we plot the density of ionization probability as a function of the nuclear kinetic energy, NKE, and the time delay, τ. We analyze the NKE distributions using as a probe the 6 fs IR pulse, whose vector potential is superimposed in the left panel (panel a) of figure 6.1.3. The rest of the pump - probe scheme parameters are the same presented before. For analysis purposes, we include in panels b and c the contributions from the optically allowed final symmetries, Σ_u and Σ_g, of the system. As expected, for time delays smaller than -3.5 fs, when the IR pulse arrives first and the pulses do not overlap, the NKE distribution is equivalent to the obtained witn an isolated XUV pulse [57]. The same distributions are obtained even when both pulses overlap, for negative time delays, $-3.5\,\text{fs} < \tau < -2.5\,\text{fs}$, when only the last period of the IR overlap with the XUV, i.e., the overlap is only effective for time delays larger than -2.5 fs. For time delays $-2.5\,\text{fs} < \tau < 3\,\text{fs}$, the laser-assisted photoionization is observed. In this interval, the IR pulse strongly modifies the photoionization distributions and induces an oscillatory behavior with the time delay, showing an increase of the ionization signal at given time delays, particularly in the NKE region where the DESs decay, which correspond to NKE larger than 4 eV. The oscillation with the time delay in the ionization probability can be understood when we look at the Σ_g and Σ_u symmetry contributions. The Σ_u symmetry is dominated by the one-photon absorption of the XUV pulse, only depleted at given time delays (at $\tau = -1.25$ fs and 1.25 fs) where the vector potential of the IR is maximum. When the IR is maximum, the $1Q_1\,{}^+\Sigma_u$ DES is partly depopulated and the autoionization signal into the Σ_u channel decreases. This is manifest in the total ionization distribution, panel a of figure 6.1.3, due to a favorable combination of one-photon absorption of the XUV pulse following by the absorption or emission of one IR photon, which transfers population into the Σ_g channel, increasing its signal, as was observed in panel c. The oscillating patterns in the Σ_g channel appear at NKE between $2\,\text{eV} - 8\,\text{eV}$, indicating the UV+IR transitions enhanced through the $1Q_1\,{}^+\Sigma_u$ DES.

In order to ensure that the localization of these oscillating patterns in the region from -2 fs to 3 fs of time delay, it is due to the IR field, and unrelated to the lifetime of the $1Q_1\,{}^+\Sigma_u$ DES, which is in fact 3 fs [144], we use the calculations using the longer IR probe pulse of 9 fs. Results are shown in figure 6.1.4. The upper row corresponds to the total ionization (a) and the Σ_g (b) and Σ_u (c) final symmetry contributions, as shown in figure 6.1.3 for the 6 fs IR probe pulse. For a complete description of the problem, in this case, we include for each of them their corresponding contributions from each ionization threshold, the $1s\sigma_g$, in the middle row, and $2p\sigma_u$, in the lowest row of figure 6.1.4. All panels are accordingly labeled. First, it is confirmed that the oscillatory behavior purely

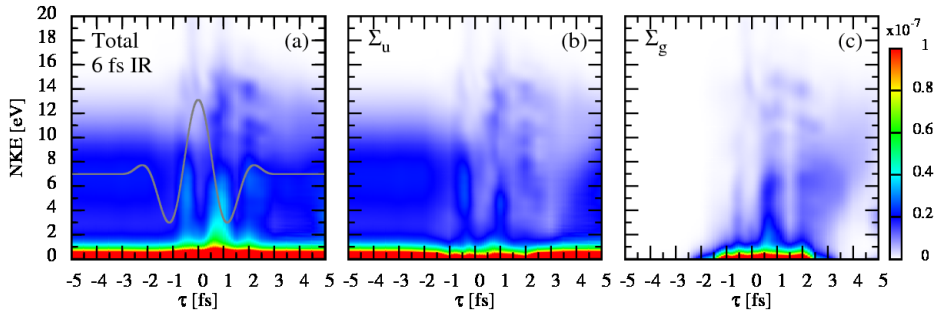

Figure 6.1.3: Density of ionization probability as a function of nuclear kinetic energy (NKE), in the y axis, and time delay, in the x axis. The NKE distributions are for the 6 fs IR probe pulse. (a) Total ionization probability. (b) Total ionization probability leaving the ionized system in a Σ_u total symmetry by the absorption of an odd number of photons. (c) Total ionization probability leaving the ionized system in a Σ_g total symmetry by the absorption of an even number of photons.

follows the IR vector potential, reaching now from -3 fs to 4 fs of time delays, leading to a maximum every half period of the IR. In both cases, 6 fs and 9 fs, the nuclear fragments produced in the ionization reach energies above the 10 eV, as can be observed in panel a of figures 6.1.3 and 6.1.4. As can be observed in panels b and c of both figures 6.1.3 and 6.1.4, these features appear in both final symmetries, Σ_g and Σ_u, of the total ionization. However, while the lower energy fragments came from the first ionic threshold, $1s\sigma_g$, the higher energy fragments are due to ionization to the second ionic threshold, $2p\sigma_u$, as it is observed in panels g, h and i of the figure 6.1.4. This is consequence of a net absorption of one XUV photon plus one or two IR photons, which leaves in a final symmetry Σ_g or Σ_u, respectively, of the $2p\sigma_u$ threshold. That is only available as long as both pulses overlap and particularly for positive time delays, which implies that the transition is enhanced through the existence of DES, whose PEC run almost parallel to the $2p\sigma_u$ state.

On the other hand, for time delays longer than 4 fs, where the XUV and IR pulses barely overlap, panels a, b and c of figure 6.1.4 show a strong signal in the low NKE region, between 0 eV $-$ 5 eV. This feature comes entirely from the $2p\sigma_u$ threshold, as it is demonstrated in the panels g, h and i of figure 6.1.4. At these time delays, the vibrational wavepacket generated by the XUV pulse in the first ionic threshold, $1s\sigma_g$, has time to move and reach to internuclear distances of 3 a.u. $-$ 4 a.u. At these large internuclear distances, the $1s\sigma_g$ and $2p\sigma_u$ ionic states are much closer in energy, as it is appreciable in figure 6.1.2, and can be resonantly coupled by a few IR photons. This phenomena has been widely described in other works as bond-softening [185, 20, 101, 51]. As can be observed in panels h and i, this structure appears in both final symmetries, Σ_g and Σ_u, for the $2p\sigma_u$ ionic state, and therefore, we can ensure that not only one IR photon is being absorbed

but higher order processes are taking place such that the electron gains angular momentum while the residual ion remains unperturbed.

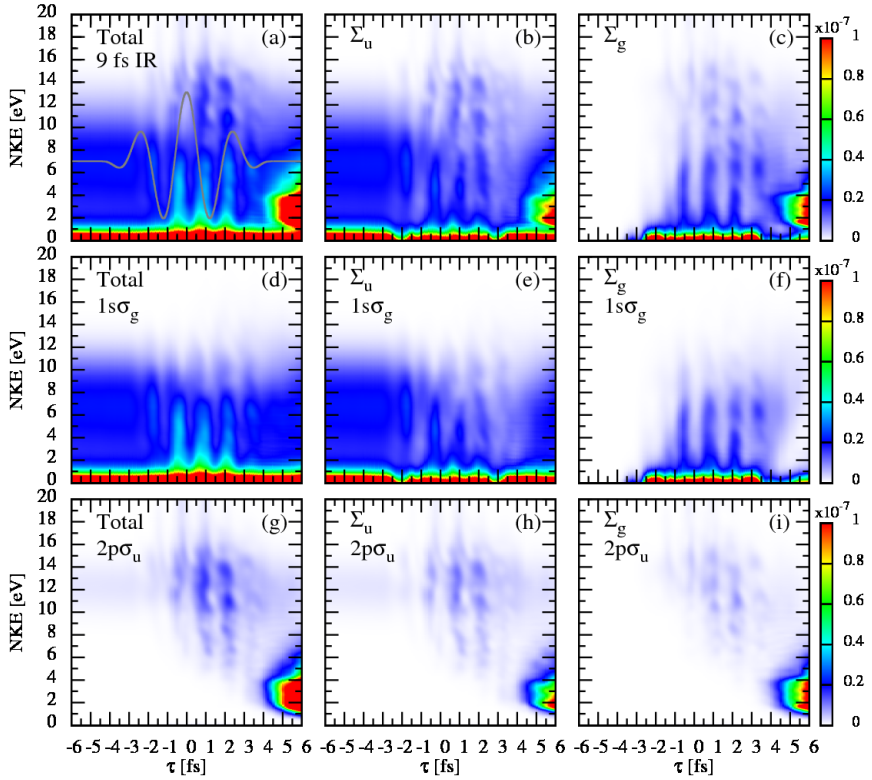

Figure 6.1.4: As in figure 6.1.3, density of ionization probability as a function of nuclear kinetic energy (NKE), in the y axis, and time delay, in the x axis, between the pulses, using the 9 fs IR probe pulse. Left column: Total ionization probabilities. Middle column: Total ionization into channels of Σ_u total symmetry. Right column: Total ionization into channels of Σ_g total symmetry. The upper row corresponds to the total, the middle row corresponds to the contribution in the first ionization threshold, $1s\sigma_g$, and the lower row corresponds to the contribution in the second ionization threshold, $2p\sigma_u$.

Since the different photoionization paths with different net absorption energies can leave signals in the NKE distribution at the same nuclear kinetic energy, these paths are mixed in the NKE distributions and cannot be directly separated. As, the total amount of energy absorbed is sharing between the ejected electrons and the nuclear fragments, for different net absorbed energy, identical nuclear kinetic energies are associated with different electrons kinetic energies. Consequently, the contribution of each different ionization path can be separated, analyzing the electronic and nuclear energy-differential distributions, which give the density of probability as a function of the energy of both ejected charge fragments, measure in coincidence.

6.1.2 Electronic and nuclear energy-differential distributions

The excess energy of the fragments after the photoionization with a photon energy ω_0, will be shared between electrons and nuclei such that $E_{v_\alpha} + \varepsilon = \omega_0 - IP_d$, where $IP_d = 18.15\,\text{eV}$ is the dissociative ionization potential. The photon energy of our pulse, 28 eV, is expected to populate energies in a diagonal approximately centered at around 10 eV of excess energy. This is shown in the electronic and nuclear energy-differential distributions that are plotted in figure 6.1.5 for the simulation using a 9 fs IR pulse. We show panels for seven different time delays. For the same delay between the pump and the probe, but positively or negatively delayed, we obtain significantly different distributions. For $\tau = -4\,\text{fs}$, the distribution is strictly the same as that obtained for a isolated XUV pulse, as can be observed in figure 5.1.2 from the first section of the chapter 5. The direct ionization probability, which is the probability observed in the hypothetical absence of DES, would follow the exponential decay shown at low energies reaching up to $3\,\text{eV} - 4\,\text{eV}$. Ionization at larger nuclear kinetic energies comes from autoionization process. Both direct and autoionization processes interfere giving rise structures shown at low NKE [128], as was discussed in the previous chapter. For negative time delays where XUV and IR pulses overlap, corresponding to $\tau = -1.2\,\text{fs}$ and $\tau = -0.6\,\text{fs}$ in figure 6.1.5, we observe well defined diagonals with a separation equal to the IR energy, of 1.65 eV. This feature is a consequence of the interference between the broad bandwidth of the XUV pulse with its own IR shifted replica. This indicates that the autoionization is being launched by the net absorption of $\omega_0 = 28\,\text{eV}$ and also through third order processes, corresponding to the absorption of one XUV photon with energy $\omega_0 + \omega_{IR}$ or $\omega_0 - \omega_{IR}$ plus the absorption or emission of two IR photons. These ionization paths allow that the fully energy-differential distributions present fringes at excess energies of ω_0, $\omega_0 + \omega_{IR}$ and $\omega_0 - \omega_{IR}$. For positive time delays, this clear pattern at negative time delays vanishes, because the maximum amplitude of the IR pulse reaches the target after the XUV has been absorbed, the vibrational wavepacket associated with the DES has time to move. This produces that the ionization comes partly from autoionization of the $Q_1\,{}^+\Sigma_u$ states and partly from the depopulation of these states, through transition induced by the Ir field. i.e., we are observing the wide energy range of final states capturing the autoionization through the $Q_1\,{}^+\Sigma_u$ states, and a sequential process in which the XUV populates the DES and the IR pulse couples these states with the background continua.

The energy-differential distributions as a function of the NKE and time delay selecting a given excess energy allows us a better visualization of the laser-assisted photoionization and the time delay dependence of different ionization paths. This is shown in figure 6.1.6, where we have selected three values for the excess energy, respectively, to the effective absorption of 26.35 eV, corresponding to an energy of $\omega_0 - \omega_{IR}$; 28 eV, corresponding to an energy of ω_0: and 29.65 eV, corresponding to an energy of $\omega_0 + \omega_{IR}$. In other words, we are taking now a diagonal in figure 6.1.5 and plot it as a function of time. Note that these NKE distributions are different from the presented in figures 6.1.3 and 6.1.4, where we integrated

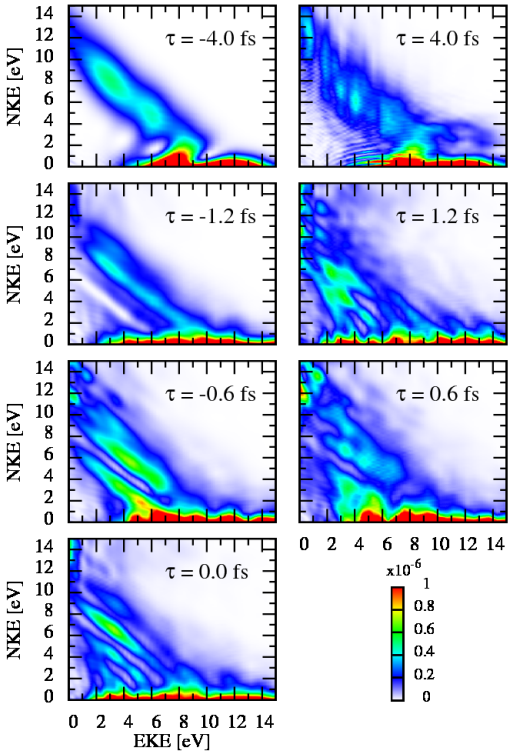

Figure 6.1.5: Density of ionization probability as a function of both electronic (EKE), in the x axis, and nuclear (NKE), in the y axis, kinetic energies for different time delays using the 9 fs IR probe pulse. Each row corresponds to a negative time delay, in the left column, and its corresponding positive value, in the right column.

over the ejected electron energies, and therefore, different excess of energies was mixed from different photoabsorption paths. At time delays $\tau \approx -0.6$ fs and $\tau \approx -1.875$ fs, when the IR vector potential is zero, we observe a depletion for low kinetic energies accompanied with a more intense signal for the structure due to the autoionization, between 4 eV−8 eV of NKE. On the other hand, for positive time delays $\tau \approx 0.6$ fs and $\tau \approx 1.875$ fs, the maximum amplitude of the IR pulse is reached after the XUV pulse, therefore transferring population from the DES to the background continua and preventing autoionization with the expected excess energy of 28 eV.

Coming back to the panels from d to f in figure 6.1.4, It is clear that the effect of the IR field is mainly driving the electron in the presence of the molecular ion, which keeps in its ground state, $1s\sigma_g$. To a given extent, the molecular residual ion remains an expectator and the electron in the continuum is increasing/decreasing its angular momenta. The ionization into $2p\sigma_u$ is only taking place at higher NKE than 10 eV in a sequential process through DES and in the bond softening structure [185]. These are the only remarkable features which we could assign to a UV pump - IR probe processes instead of the laser-assisted photoionization phenomena. Therefore, it is reasonable to explore now the ionization signal as a

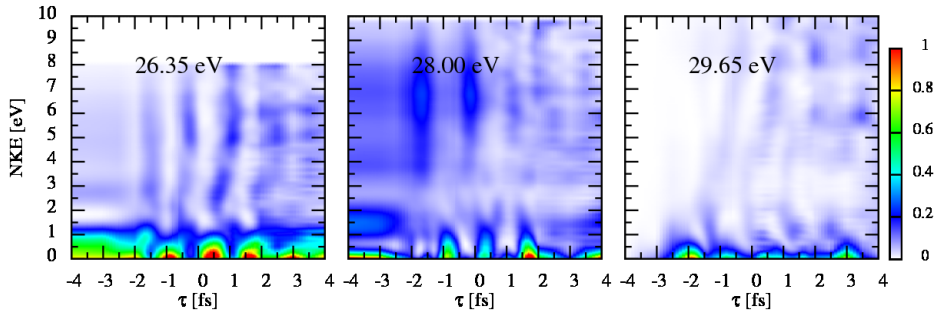

Figure 6.1.6: Density of ionization probability for a total final energy, as a function of nuclear kinetic energy (NKE), in the y axis, and time delay, in the x axis, between the pulses for the 9 fs IR probe pulse. It is plotted for three different excess energy.

function of the electron kinetic energy. Note that in all previous results, we have focused on the events implying dissociation upon ionization, but one could also detect all ejected electrons upon photoionization, therefore including the non-dissociative ionization signal, which is in fact one order of magnitude larger than dissociative ionization.

6.1.3 Streaking patterns in the electron energy distributions

We consider now electronic energy-differential distributions, i.e., the densities of ionization probability integrated and/or summed over all nuclear energies as a function of electron energy. In the previous subsections, as well as in previous works [51], only dissociative ionization is examined. However, we are going to consider all ionization events, dissociative and non-dissociative, because the sole detection of electrons does not allow to separate them. Therefore, the calculated densities of ionization probability are integrated over the energies of the dissociative vibrational states and summed over the bound vibrational states of H_2^+. Figure 6.1.7 shows the total densities of ionization probability as a function of the electron kinetic energy, EKE, and the time delay between the pulses. We show results for both IR pulses used: the 6 fs IR pulse in the upper row and the 9 fs IR pulse in the lower row. Figure 6.1.7 includes the total density of ionization probability in the left column, and the contributions from the $^1\Sigma_u^+$ and $^1\Sigma_g^+$ final symmetries in the middle and right columns, respectively. We can see the streaking patterns for the electron ejection. Within the SFA (strong field approximation), the well-known streaking patterns can be characterized as the ejected electron, emitted at a well-defined time, feels instantaneously the strong IR field, and consequently, its motion follows the IR vector potential as a function of the time delay between the XUV and the IR field [83]. A simple description of streaking is provided by a classical approach [69], where the momentum of the

electron emitted after the interaction with the XUV pulse is given by:

$$\mathbf{p}(t) = \mathbf{p}_0 - \mathbf{A}_{IR}(t) \tag{6.1.1}$$

In the above expression, $\mathbf{p}_0$ is the momentum of the electron at the instant of ejection and $\mathbf{A}_{IR}(t)$ is the vector potential of the IR pulse. Thus, in this approximation, the only effect of the IR field is to shift the electron momentum. This is only true when the photoelectron instantaneously feels the IR field and the potential created by the residual ion is ignored. Refinements of this model to include the effect of the ion potential has been recently proposed [161]. According to equation 6.1.1, the electron energy is approximately given by:

$$\begin{aligned} E(t) &= p_0^2 + A_{IR}^2(t) - p_0 A_{IR}\cos(\theta) \\ E(t) &\simeq p_0^2 - p_0 A_{IR}\cos(\theta) \end{aligned} \tag{6.1.2}$$

where θ is the angle between the electron ejection and polarization directions, and we have taken into account that, for the low IR intensities considered in this work, $A_{IR}^2(t)$ is much smaller than the other two terms. From this equation we see that, in the absence of any interaction between the ejected electron and the remaining electron and ion, the variation of the photoelectron spectrum with time delay should follow the negative IR vector potential, $-A_{IR}(t)$. However, the best contrast will be obtained for $\theta = 0°$ (following $-A_{IR}(t)$) and 180° (following $A_{IR}(t)$), which correspond when the electron escapes along the polarization direction, which in the present simulations also coincide with the molecular axis.

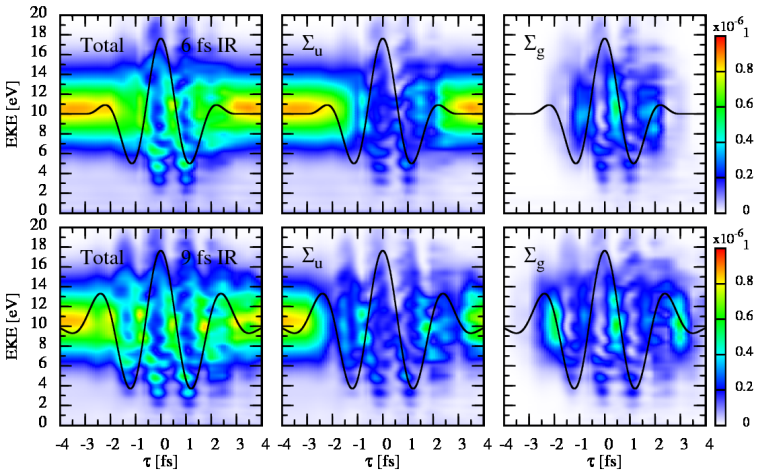

Figure 6.1.7: Density of ionization probability as a function of electron kinetic energy (EKE) and time delay for the 6 fs, in the upper row, and 9 fs in the lower row, IR probe pulse. The total probability, the Σ_u total symmetry contribution and the Σ_g total symmetry contribution are plotted in the left, middle and right panels respectively.

Figure 6.1.8 shows the total density of ionization probability as a function of electron energy and time delay for three different ejection angles of the electron

with respect to the field, 0°, 90° and 180°. We can see that the electron energy distributions at 0° and 180° perfectly match minus the IR field and the IR field, respectively. As expected, at 90°, the signal is an order of magnitude smaller, but not zero as it would be in He atom that only absorbed a XUV photon, due to the lost of spherical symmetry in the molecule and the absorption of the IR photons, the contribution of partial waves with different angular momenta is possible. It is appreciable that this EKE distribution follows the IR field, although this time it only shows up in the region where the IR field is significantly different from zero. The latter is the consequence of the fact that, at 90°, the density of ionization probability resulting from absorption of a single XUV photon is very small, due to the populated states have symmetry, so that electron density in a direction perpendicular to the molecular axis is small. Electron emission at angles different from 0° and 180° is also affected by geometrical effects [181] not accounted for by equation 6.1.1. Since these effects are minor compared to those described above, they will not be discussed here.

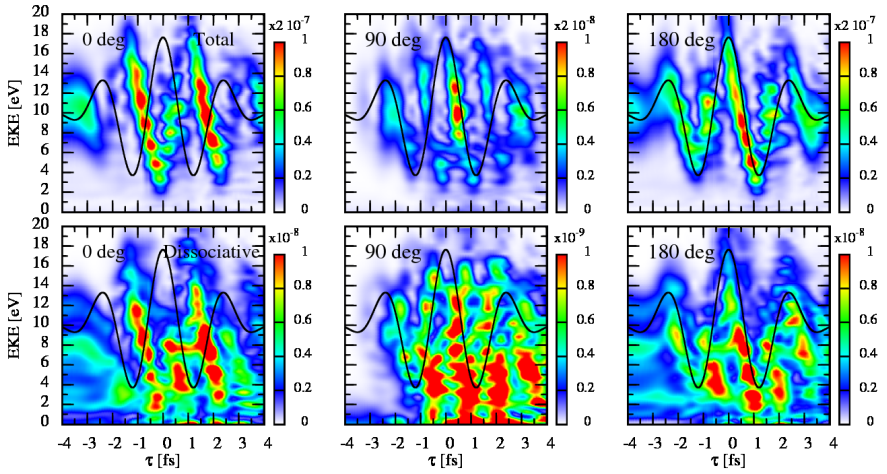

Figure 6.1.8: Density of ionization probability as a function of the electron kinetic energy (EKE), in the y axis, and the time delay, in the x axis, for three different ejection angles with respect to the polarization vector. The calculations are performed for the 9 fs IR probe pulse. Upper row: Total ionization probability. Lower row: Contribution from the dissociative ionization channel. Left column: electron angular and energy distributions for a 0°. Middle column: For the 90°. Right column: For the 180°.

In figure 6.1.7, we have integrated over all ejection angles, and consequently, the results shown in this figure correspond to electrons emitted in all directions. Therefore, this figure includes the behaviors observed in figure 6.1.8, mainly those observed at 0° and 180°, which are the angles with the largest contrast. As a consequence, the angle-integrated electron energy-differential distribution is very close to a superposition of the streaking patterns observed at 0° and 180°. This is true for the two IR pulse durations considered in this work. The above results do not allow us to identify any feature related to the presence of the DES. For this, we should look at the dissociative ionization channel, because in this channel,

the contributions from direct ionization and autoionization are comparable. The lower row of figure 6.1.8 shows the corresponding photoelectron spectra in the dissociative channel. As can be observed, the probabilities are more than an order of magnitude smaller than those shown in the upper row of figure 6.1.8. This information should be experimentally accessible, since as we mentioned, previous experiments devoted to other observables have almost exclusively considered this channel. As can be seen, for the three angles, the observed patterns are much more complex, far from the simple streaking picture described above. These patterns are the signature of autoionization and IR induced ionization of the DES. Both processes can only be described by including electron correlation, which is not taken into account by the simple classical picture with a single active electron under consideration.

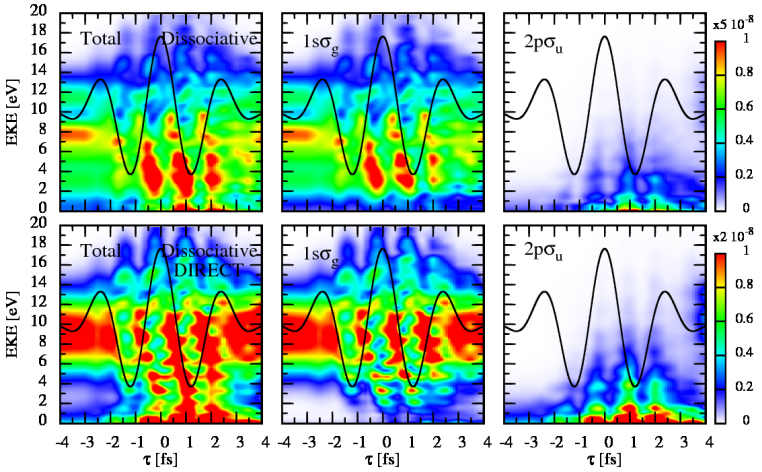

Figure 6.1.9: Density of ionization probability as a function of electron kinetic energy (EKE) and time delay for the 9 fs IR probe pulse. Upper row: dissociative ionization probability. Lower row: same as upper but only including the direct photoionization probability and removing the contribution from autoionization. Left column: Total contribution. Middle column: Contribution from the first ionization threshold, $1s\sigma_g$. Right column: Contribution from the second ionization threshold, $2p\sigma_u$.

The imprint of the DES, which modifies the streaking signal of the photoelectron ejection accompanying dissociation into $H + H^+$, is better illustrated in figure 6.1.9. We show results for two sets of calculations: i) the first simulation, whose results are plotted in the upper row in figure 6.1.9, corresponds to the full calculation presented through the manuscript for the 9 fs IR probe; ii) the second one, whose results are plotted in the lower row in figure 6.1.9, corresponds to a calculation where the DES are removed. For both simulations we plot the total density of dissociative ionization probability, in the left column, and its contributions from each ionization threshold, $1s\sigma_g$ in the left and $2p\sigma_u$ in the right. We observe that a clean streaking signal is obtained in the absence of autoionization. Even in this case, the possibility of extracting photoemission times from

a molecular streaking signal with the presence such of complex structures would be a rather adventurous challenge.

6.2 Coherent control of excited states (APT + IR)

In the previous section, we focused our attention on the signatures of the autoionization into the direct ionization process occurring due to the XUV pump - IR probe schemes. However, a similar scheme can be used to explore the idea of characterize and control the single excited states of the neutral hydrogen molecule. At a difference with the previous simulations, in the present XUV pump - IR probe schemes, the SAP is substituted by an APT as a pump pulse. The APT combine two advantage front the SAP, one, comented before, the APT are more accessible for the experimentalist through the HHG techniques. In addition, at a difference with the SAP whose spectral distributions are extended for a widely range of energies around the central photon frequency, the APT present a series of spikes, odd multiples of the generation laser field used in the HHG, whose distributions are narrower than in a SAP, increasing the precision and control of the states populated. Although the present pump - probe scheme is the most extended protocol to explore and control the dynamical process, the presence of the IR pulse as the probe disturbs the single excited state dynamics. In this way, the state-of-art to explore and even control the vibronic dynamics in the single excited states corresponds to the XUV pump - XUV probe schemes, which will be studied in the next chapter.

In the present section, we compare experimental measurements performed by the group of Prof. M. Murname and H. Kapteyn in JILA (USA) with theoretical calculations to explore the coherent control in the vibronic wavepackets generated simultaneously into the excited and ionic states of the H_2 by the interaction with a complex XUV pump - IR probe scheme. The XUV - IR scheme allows us to control the different population into the excited states by interferences between the vibronic wavepackets, by tuning the photon energies and time delays between the pulses. These interferences turn on or off the different possible ionization paths from the single excited states, and therefore, allow the control over the final dissociative and non-dissociative ionization yields. In addition, because these intermediate dynamics affect over the final ionic states, the fingerprint of the intermediate dynamics of the single excited states can be observed over the final ionization signal.

We use a phase-locked combination of a XUV APT with two IR fields. One IR is combined with the XUV, forming the pump, and the other IR pulse constitutes the probe. This phase-locked between the XUV and IR pump indicates that the relative CEP of both pulses are fixed. The fs APT is composed of a combination of several attosecond pulses, whose frequency domain spectrum has a mountain-like shape, with narrower peaks. As show in figure 2.2.15, this spectrum with narrowly distributed peaks populates selected states compared with the SAP, whose broad bandwidth populates a huge amount of vibronic states. In our simulations, this APT pulse is formed by four attosecond pulse with an intensity of $10^9\,\mathrm{W}\cdot\mathrm{cm}^{-2}$

for the two central pulses and $3.5 \cdot 10^8\,\mathrm{W \cdot cm^{-2}}$ for the other two pulses. Each of these pulses has a duration of 0.55 fs, which correspond to an envelop of 3 fs FWHM and laser intensity of $1.14 \cdot 10^9\,\mathrm{W \cdot cm^{-2}}$ for the APT. Because the attosecond pulse is produced by HHG, their possible frequencies, called harmonics, are multiples of the generating IR frequency, ω_{HHG}. The main reason is that the ejected electron in the HHG process gain an kinetic energy which is a multiple of the photon energy used. When the electron is recaptured by the parent ion, this excess energy is emitted as a unique photon, whose energy is equal to an even or odd multiple of the IR generating photon, called harmonic [87]. As the emission and recombination process is repeated every half-cycle of the generating IR, the coherent combination of the different photons emitted generates constructive and destructive interferences which eliminates the even harmonics, surviving only the odd harmonics. In our particular case, three different HHG generating IR frequencies were selected: 784 nm ($\omega_{HHG} = 1.58\,\mathrm{eV}$), 760 nm ($\omega_{HHG} = 1.63\,\mathrm{eV}$) and 740 nm ($\omega_{HHG} = 1.68\,\mathrm{eV}$), giving three different frequencies for the XUV: 14.22 eV, 14.67 eV, 15.12 eV, respectively. The phase-locked IR field with the XUV pulse has an intensity of $3 \cdot 10^{11}\,\mathrm{W \cdot cm^{-2}}$, while the probe IR has an intensity of $5 \cdot 10^{12}\,\mathrm{W \cdot cm^{-2}}$. However, both IR fields have an energy of 1.6 eV, corresponding to 755 nm. Again, we will mainly focus on time delays when the probe and the pump are overlapping, corresponding to time delays between -4 fs to 4 fs. The experimental setup uses a XUV APT of 10 fs and pump and probe IR pulses of 30 fs. The intensity of the pump IR is $3 \cdot 10^{11}\,\mathrm{W \cdot cm^{-2}}$ while the probe IR is $4 \cdot 10^{12}\,\mathrm{W \cdot cm^{-2}}$. Although these pulses are longer and present slightly different intensities than the used in the theoretical calculations, we checked that a direct comparison between the theory and the experiment is valid when both pump and probe pulses overlap.

In figure 6.2.1, it is plotted the representative PEC which play a role in the pump - probe scheme presented before. The states plotted are the ground state, $X\,^1\Sigma_g^+$, and the first single excited states of symmetries Σ_g and Σ_u, the $B\,^1\Sigma_u^+$ and $EF\,^1\Sigma_g^+$ respectively, of the H_2. In addition, we have the PEC of the two first ionic threshold, $1s\sigma_g$ and $2p\sigma_u$, of the molecular ion H_2^+. Although the theoretical calculations were performed over the H_2 and the experimental measurements were realized over the D_2, for practical reasons, both molecules have the same PECs diagram presented in figure 6.2.1. In the y axis, the different harmonics of the APT are plotted as black arrows and with red arrows the IR one-photon absorptions. As can be observed in figure 6.2.1, the hydrogen molecule can be excited and ionized by the APT due to the absorption from the 7^{th} ($7\omega_{HHG}$) to the 13^{th} ($13\omega_{HHG}$) harmonics. The phase-locked IR, coming with the pump, is capable of inducing more transitions in the Franck-Condon region, around 1.4 a.u. of internuclear distance, as can be observed with the red arrows in this internuclear distance region. The second IR, acting as a probe, is delayed in time with respect to the pump XUV+IR combination and induces the transition between the states outside to the Franck-Condon region, represented for the red arrows at internuclear distances larger than 3 a.u.. The interference between these vibronic wavepackets in the excited states, whose motion depends on the laser parameter used, will be used to manipulate the final ionization probabilities.

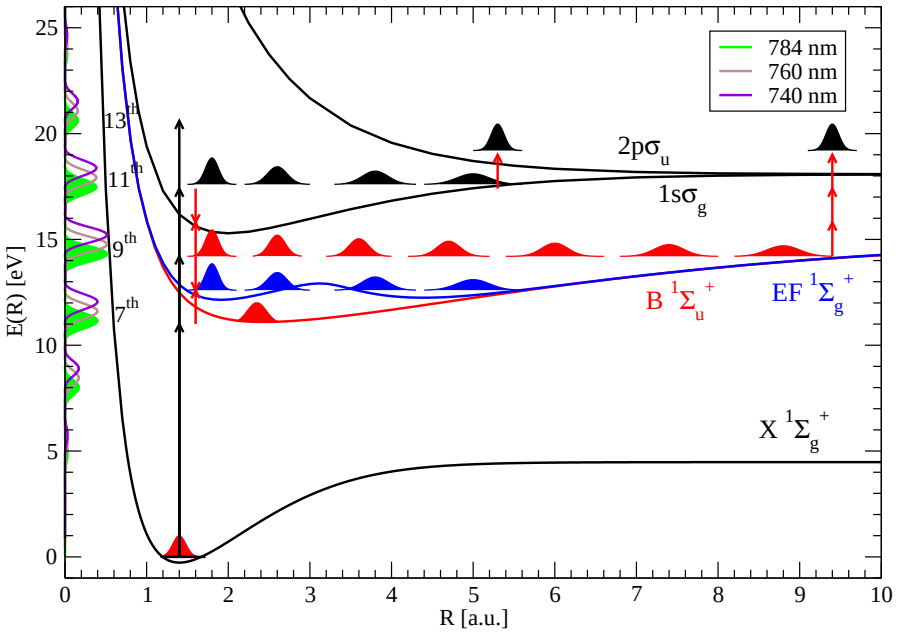

Figure 6.2.1: Representative potential energy curves of H_2 and H_2^+. It is plotted the ground state of the neutral, $X\ ^1\Sigma_g^+$, the two lowest singly excited states of Σ_g symmetry ($EF\ ^1\Sigma_g^+$) and Σ_u symmetry ($B\ ^1\Sigma_u^+$) and the two lowest ionization thresholds, $1s\sigma_g$ and $2p\sigma_u$. The spectral form of the three APT pulses, for the energies 14.22 eV, 14.67 eV, 15.12 eV is plotted in green, brown and violet, respectively. The black arrows represent the absorption of the different harmonics from the XUV APT pulse and the red arrows represent IR absorbed or emitted photons by the system. The evolution of the nuclear wavepackets in the different excited and ionic states are plotted as scheme example. The color of these nuclear wavepackets are the corresponding to the energy potential curve in which they move.

In this scheme, the absorption of the 7^{th} and 9^{th} harmonics of the XUV APT produces a transition from the ground state to different vibrational states of the first single excited state with Σ_u symmetry, the $B\ ^1\Sigma_u^+$. In addition, 11^{th} harmonics of the XUV APT can ionize the molecule into the first ionic threshold, the $1s\sigma_g$. On the other hand, the combined IR field can induce a transition from this state with odd parity, the $B\ ^1\Sigma_u^+$, to the first single excited state of the even parity, the $EF\ ^1\Sigma_g^+$. Due to the energy of the 7^{th} ($7\omega_{HHG}$), 9^{th} ($9\omega_{HHG}$) and 11^{th} ($11\omega_{HHG}$) harmonics of the APT, there are two quantum interference paths to create the vibronic wavepackets over the $EF\ ^1\Sigma_g^+$ state: The absorption of $7\omega_{HHG}+\omega$ and $9\omega_{HHG}-\omega$, i.e., the absorption of the 7^{th} harmonic of the APT plus the IR and the absorption of the 9^{th} harmonic of the APT plus the emission of one IR photon. These paths generate two wavepackets into the same excited states, whose interference determine their evolution [16]. We will observe the same two interference paths by the absorption of $9\omega_{HHG}+\omega$ and $11\omega_{HHG}-\omega$.

The population of the first excited states with odd and even symmetries are plotted in figure 6.2.2. They oscillate with the half-cycle periodicity of the IR for time delays positives, analogous to the oscillation of the NKE distributions observed

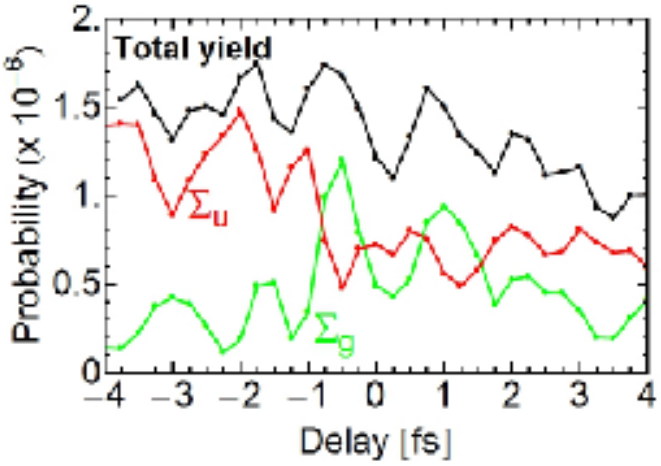

Figure 6.2.2: Theoretical data for excitation probability in the first single excited states with even, $EF\,^1\Sigma_g^+$, and odd parity, $B\,^1\Sigma_u^+$, as a function of the time delay between the pulses.

in previous section. Thus, a two-pathway quantum interference of the electronic wavepackets driven by the lower two harmonics and the delayed IR field can be used as an ultrafast population switch between even, $EF\,^1\Sigma_g^+$, and odd parity, $B^1\Sigma_u^+$, potentials. This demonstrates that the interference of electronic wavepackets can be used to switch and steer the electronically excited states on attosecond time scales, allowing simultaneous control of the electronic and vibrational excitation. This oscillation effect is also appreciable in figure 6.2.3, in which it is plotted the dissociative and non-dissociative ionization probabilities as a function of the time delay. These ionization yields are for the three APT photon energies, 784 nm, 760 nm and 740 nm in the panels from the left to the right, respectively. The suboptical cycle modulation is consequence of the optical interferences between the two IR pulses and the quantum interferences of the vibronic wavepacket generated by the pump. Therefore, the modulation of the oscillation strongly depends on the XUV harmonics, because the amplitudes and phases depend on the intermediate vibronic states populated by the combination of the XUV plus the IR pump pulse. Thus, the change in the periodicity oscillation of the 784 nm compared with the rest can be interpreted as the higher energy of this pulse populates single excited states with higher energy than the $B\,^1\Sigma_u^+$. This would produce a new interference in the vibronic wavepacket evolution which affects the final ionic state populations. Note that higher order processes are possible, like the absorption of 3 IR photons, given absorption processes like $7\omega_{HHG} + 3\omega$ or $11\omega_{HHG} - 3\omega$, which compete with the absorption of $9\omega_{HHG} + \omega$ or $9\omega_{HHG} - \omega$, respectively. However, this process can be neglected in our analysis due to the absorption of 4 photons is less probable than the absorption of 2 photons.

The different ionization and dissociation pathways are depicted in figure 6.2.4. The Fourier transform of the different APTs, for generating IR field frequencies of 784 nm, 760 nm and 740 nm, is plotted in the y axis. As explained before, the combination of the absorption of the 9ω from the XUV alone and $7\omega_{HHG} + \omega$

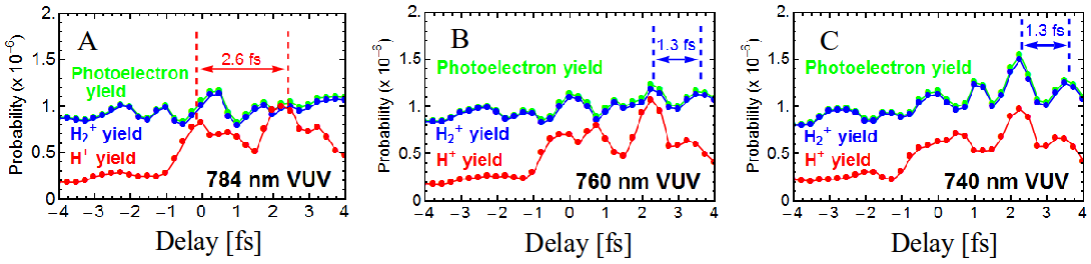

Figure 6.2.3: Theoretical data for total, dissociative and non-dissociative ionization probabilities as a function of the time delay. There are plotted three different XUV APT energies: 784 nm, in the left panel, 760 nm, in the middle panel, and 740 nm, in the right panel. The total ionization yield switches to half-cycle periodicity due to different vibronic wavepacket interferences, thus demonstrating attosecond coherent control over the interfering vibronic wavepackets and ionizing pathways in molecules.

or $9\omega_{HHG} - \omega$ from the XUV plus the pump IR pulses coherently populate the $B\ ^1\Sigma_u^+$ and $EF\ ^1\Sigma_g^+$ states, respectively. These vibronic wavepackets oscillate with periods that depend on the exact energy of the XUV and IR photon energies which populate them, and can couple the ground state to different vibronic bands of the $B\ ^1\Sigma_u^+$ and $EF\ ^1\Sigma_g^+$ potentials. The probe IR pulse can then ionize and dissociate hydrogen molecules from these single excited states through different paths. In this way, we can distinguish three different ionization paths following the absorption of the XUV plus IR pump and probed by a second IR: Two-steps B mechanism, one-step B mechanism and two-step EF mechanism. These three ionization paths are plotted in figure 6.2.4 in the left panel (panel A) for the two-steps B mechanism, in the middle panel (panel B) for the one-step B mechanism and in the right panel (panel C) for the two-step EF mechanism. In the two-steps B mechanism (panel A), the 9^{th} harmonic of the XUV pump APT generates a vibrational wavepacket into the $B\ ^1\Sigma_u^+$. This wavepacket does not have time to evolve, because the pump IR pulse produces in the region of the inner turning point of the $B\ ^1\Sigma_u^+$ potential energy curve the ionization from this single excited state to the first ionic threshold, $1s\sigma_g$. The vibronic wavepacket generated in the first ionic state by the IR photon absorption, evolves in time to larger internuclear distance. When this wavepacket is close to the outer turning point of the $1s\sigma_g$ potential energy curve, the presence of the probe IR can induce the absorption, and therefore, the transition from the ground state of the residual ion to the second ionic state, the $2p\sigma_u$. This above threshold ionization (ATI) process is the bond-softening that efficiently couples both ionic states. The bond softening also appears in the previous XUV pump - IR probe scheme, and leaves the system in dissociative states of low proton kinetic energies releases, around 0.7 eVand 0.9 eV.

In the one-step B mechanism (panel B), the vibrational wavepacket generated in the $B\ ^1\Sigma_u^+$ by the 9^{th} harmonic of the XUV pump APT, evolves to larger internuclear distances. When the wavepacket arrives to the outer turning point

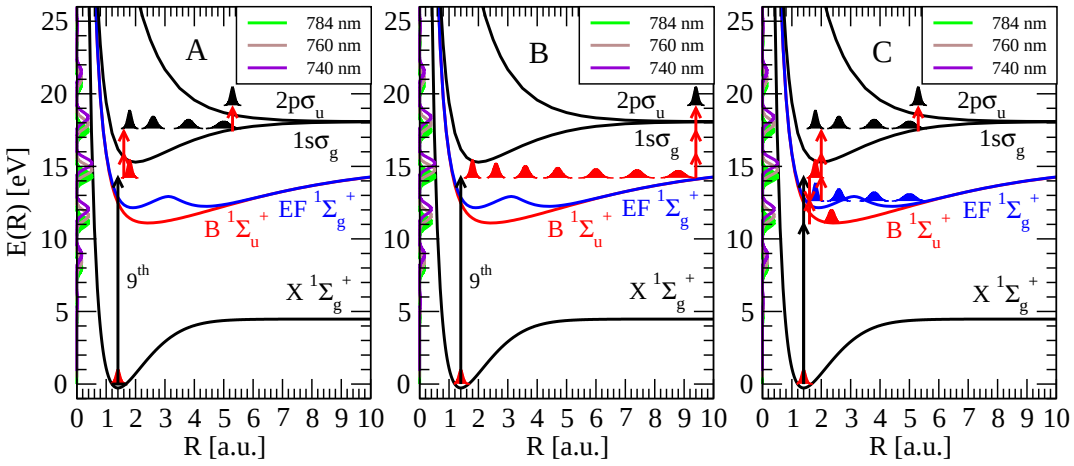

Figure 6.2.4: Different coherent control mechanism of the vibronic wavepacket dynamics on longer timescales. Left panel (A): Two-step B mechanism, whose signal is at high proton kinetic energy. Middle panel (B): One-step B mechanism, whose signal is at low proton kinetic energy. Right panel (C): Two-step EF mechanism, whose signal is at high proton kinetic energy. The spectral form of the three APT pulses, for the energies 14.22 eV, 14.67 eV, 15.12 eV is plotted in green, brown and violet, respectively.

region, the presence of the probe IR induces a transition from this single excited state directly to the second ionic continua, $2p\sigma_u$, by 3 photon absorption. This mechanism also leaves the system in a dissociative states of the ion. In the last ionization path, the two-step EF mechanism, panel C of figure 6.2.4, the combined absorption of the 7^{th} and 9^{th} harmonic of the APT with the simultaneous absorption or emission of one pump IR photon, given a total energy absorption of $7\omega_{HHG} + \omega$ or $9\omega_{HHG} - \omega$, respectively, generates a vibrational wavepacket into the $EF\ ^1\Sigma_g^+$ states. This wavepacket is ionized by the absorption of three photons from the probe IR, when the $EF\ ^1\Sigma_g^+$ vibrational wavepacket is around the inner turning point region. This transition from this $EF\ ^1\Sigma_g^+$ single excited state produces a second vibrational wavepacket into the the first ionic threshold, which evolves with time to larger internuclear distances. As in the two-steps B mechanism, when this wavepacket arrives to the outer turning point of the $1s\sigma_g$ PEC, the presence of the probe IR can induce a transition to the $2p\sigma_u$, due to the bond-softening process. However, becuase this mechanism implies a larger number of photons to be absorbed than the other mechanism, it is less probable. The analysis of the densities of probability as a function of the NKE and the time delay are expected to reflect the contributions from each mechanism.

The experimental proton energy-differential distributions are shown for each different photon energy of the generating IR, 784 nm, 778 nm and 760 nm, in the left column of figure 6.2.5. The Fourier transforms of these experimental distributions are plotted in the right column as a function of the frequency (lower x axis) and period (upper x axis). As can be observed in A and D panels, there is an oscillation around 0.7 eV and 0.9 eV, with periodicities of 58 fs and 83 fs. These periodicities can be assigned to the vibrational oscillation periods of the

wavepackets created by 784 nm XUV over the $EF\,^1\Sigma_g^+$ and $B\,^1\Sigma_u^+$ states, respectively. Taking into account the energy and periodicity, it is clear that the 83 fs period is due to the two-step B mechanism and the 58 fs period is due to the two-step EF mechanism. The more intense signal in the FT of the proton-energy distribution for the two-step B than two-step EF mechanism confirms that three photon absorption of the first are more probable than the four photon absorption. On the other hand, the signal appearing around 0.3 eV of proton kinetic energy, with oscillation period of 90 fs corresponds to the one-step B mechanism. As can be observed in A panel, the bigger signal at higher proton energies, 0.7 eV and 0.9 eV, compared to the lower proton energies, around 0.3 eV, indicates that the transition from the $B\,^1\Sigma_u^+$ to the continuum is more effective when it is produced in the inner turning point region, the Franck-Condon region of the PEC, due to the best vibrational couplings between the ionic and single excited states. In addition, the phase difference observed in the panel A of figure 6.2.4 between the two-step B and one-step B mechanism is because the vibrational wavepacket is probed at different times in those channels. This allows for steering of a desired dissociative route by precisely timing the second IR laser pulse as the neutral molecule vibrates.

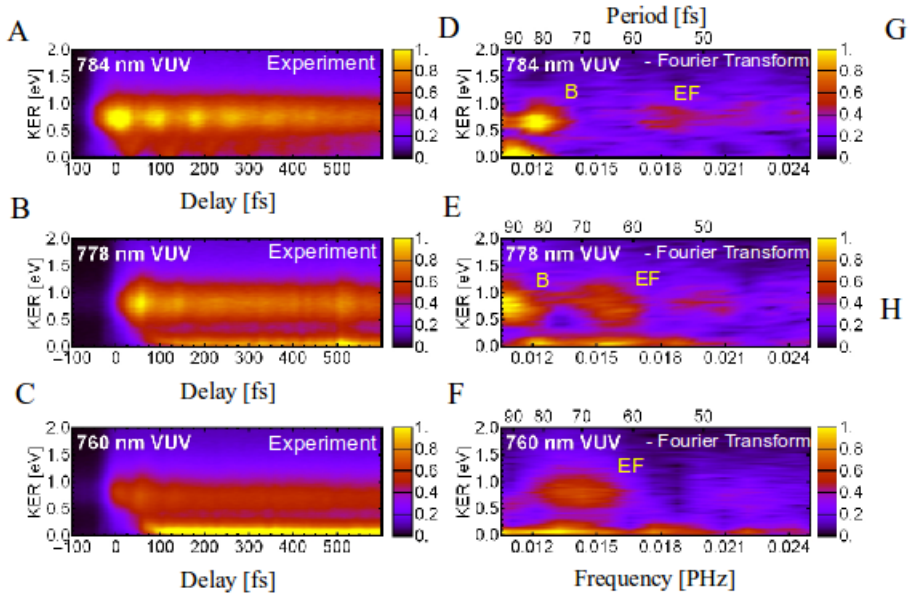

Figure 6.2.5: Controlling the dissociation channels by tuning the photon energy and through vibronic wavepacket dynamics. Panels from A to C: PKE distributions for the D_2 molecule, resulting from dissociation using three different XUV frequency combs that can be tuned to excite different electronic and vibrational single excited states of the neutral states. Panels from D to F: FT of the PKE distributions for the D_2 molecule, as a function of the proton kinetic energy releases and the FT frequency (or period).

In order to give a deeper insight on the dynamics associated with these mechanisms, we theoretically simulate the motion of the vibrational wavepackets associated to the the single excited states populated by the XUV plus IR pump pulses.

As was discussed in chapter 4, the vibrational wavepacket function, $\phi_n(R,t)$, as a function of the internuclear distance, R, and the propagation time, t, for any bound states of the H_2, is given by:

$$\phi_n(R,t) = \sum_{v_n} \int c_{n,v_n}(t)\, \chi_{n,v_n}(R)\, e^{\left[-i\frac{E_{n,v_n}}{\hbar}t\right]} dv_n \tag{6.2.1}$$

where c_{n,v_n}, χ_{n,v_n} and E_{n,v_n} are the coefficient extracted from the solution of the TDSE at $t = T$, the wavefunction and the energy of the vibrational state v_n in the bound electronic state n. The vibrational wavepackets associated to the $B\,^1\Sigma_u^+$ and $EF\,^1\Sigma_g^+$ states are plotted in figure 6.2.6 for the 784 nm and the 760 nm APT. These wavepackets are obtained of a simulation using the H_2. Although the PECs for both systems, H_2 in theoretical simulations and D_2 the experimental results, are the same, the difference of the nuclear masses between both systems produces vibrational states shifted in energy, which change the periods of the vibrational wavepacket evolution. Consequently, for comparison with the experimental results on the D_2, the theoretical H_2 result has to be rescaled with a factor of $\sqrt{2}$, to account difference in the reduced mass between the H_2 and D_2.

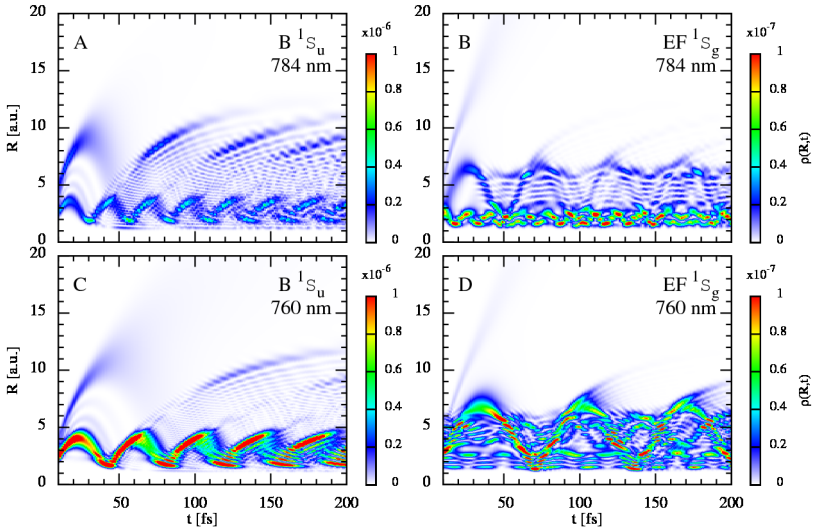

Figure 6.2.6: Representation of the time evolution of the vibrational wavepacket as a function of the time after the pump pulse, in the x axis, and the internuclear distance, in the y axis. In the left column, the $B\,^1\Sigma_u^+$ vibrational wavepackets are plotted in the A and C panels, and the $EF\,^1\Sigma_g^+$, in the B and D panels of right column. In the upper row the the vibrational wavepackets are calculated using a 784 nm XUV APT and, in the low row, using a 760 nm XUV APT.

Looking at the $B\,^1\Sigma_u^+$ state, the vibrational wavepacket is clearly constituted by two main components, one whose outer turning point is around 4 a.u. for the 784 nm and around 5 a.u. for the 760 nm case, while the outer turning point of

the other component is around 10 a.u. for the 784 nm and around 12 a.u. for the 760 nm. Taking into account the $B\,^1\Sigma_u^+$ PEC, the different oscillation amplitudes indicates that the component with $4-5$ a.u. outer turning point is mainly constituted by the lower bound vibrational states and the $10-12$ a.u. component for bound vibrational states of higher energy. Each component is associated with the absorption of different harmonics from the XUV APT, which can be clearly determined by analyzing the figure 6.2.4. In this way, the component with shorter oscillation amplitude is populated by the 7^{th} harmonic of the APT, while the other component is populated by the 9^{th} harmonic.

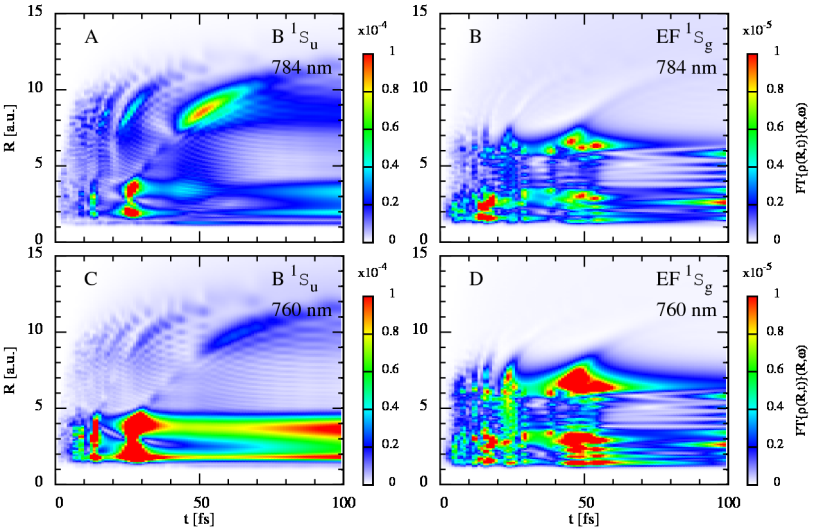

Figure 6.2.7: FT of the vibrational wavepackets from figure 6.2.6. The different states and photon energies of the XUV APT are in the same position that in figure 6.2.6.

Apart of the different oscillation amplitudes, each component present different oscillation periods, which can be extracted from figure 6.2.7, where the corresponding FT for these wavepackets are shown. The component with shorter oscillation amplitude presents an oscillation periodicity around 25 fs for the 784 nm case and around 50 fs for the 760 nm case. While the other component has a periodicities around 50 fs for the 784 nm case and around 83 a.u. for the 760 nm case. To explain the difference between the oscillation periods and amplitudes we have to take into account the energy differences between the both APTs used. As can be observed in figures 6.2.1 and 6.2.4, for the 784 nm APT the spectral maximum of the 7^{th} harmonic has an energy just below the minimum of the $B\,^1\Sigma_u^+$ PEC, while for the 760 nm case, this maximum arrives to the region of the lower vibrational states of the $B^1\Sigma_u^+$ state, and therefore, the coupling with the ground state is more effective. This improves the vibrational wavepacket density observed for the component with shorter oscillation amplitude. However, for the 9^{th} harmonic, the increase of the energy position of its maximum reduces the effective coupling with the ground state due to the increase of the coupling with the second single

excited states, $B'\,^1\Sigma_u^+$. This can be observed in figure 6.2.8, where is plotted the vibrational wavepackets of the second single excited states of both symmetries, $B'\,^1\Sigma_u^+$ and $GK\,^1\Sigma_g^+$. Therefore, this change in the predominant single excited state population by the absorption, decreases the vibrational wavepacket density of the component with larger oscillation amplitude from the 784 nm to the 760 nm APT case. This effect, observed also in the XUV pump - XUV probe presented in chapter 7, produces the disappearance of the two-step mechanism observed in the 760 nm case (F panel of figure 6.2.5). All these show how tunable attosecond XUV radiation can be used to precisely control excitation of different electronic and vibrational states.

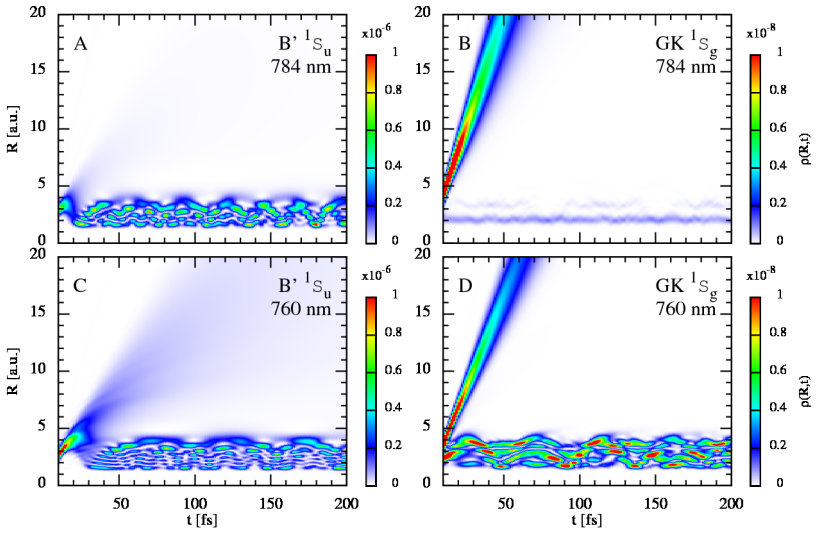

Figure 6.2.8: Representation of the time evolution of the vibrational wavepacket as a function of the time after the pump pulse, in the x axis, and the internuclear distance, in the y axis. In the left column, the $B'\,^1\Sigma_u^+$ vibrational wavepackets are plotted in the A and C panels, and the $GK\,^1\Sigma_g^+$, in the B and D panels of right column. In the upper row the the vibrational wavepackets are calculated using a 784 nm XUV APT and, in the low row, using a 760 nm XUV APT.

The $EF^1\Sigma_g^+$ PEC has a double well (see figure 6.2.4), where the vibrational states under the barrier have to tunneling to reach longer internuclear distances. The wavepacket created in this single excited state by the combined absorption of the $7\omega_{HHG}+\omega$ or $9\omega_{HHG}-\omega$, contains a mixture of vibrational states of this double well. The vibrational wavepacket in the $EF\,^1\Sigma_g^+$, generating in the inner well, starts reflecting in the inner barrier at a internuclear distance around 3 a.u., 10 fs after the excitation. We also see that this wavepacket tunnels with around a 20% probability compared with the main wavepacket motion occurring in the inner well of the $EF^1\Sigma_g^+$ double potential well. In addition, the other striking feature of this calculation starts around 45 fs, when the vibrational wavepacket in the inner well tunnels through the inner barrier for the second time and meets the outer-well vibrational wavepacket on its way back from the outer classical turning point.

The interference of the different vibrational wavepackets is clearly visible from 45 fs onward. As the time evolves, multiple reflections/tunneling events from both sides of the inner barrier and the interferences of the vibrational wavepackets in the $EF\,^1\Sigma_g^+$ PEC are responsible for the fast decoherence. The effect of increasing the generating IR frequency to 760 nm, shifts the maximum population to higher vibrational states, giving a vibrational wavepacket which can tunnel the barrier easily. This increases the vibrational wavepacket density, as can be observed between the panels corresponding to the 784 nm and 760 nm APT wavelength, and the relative visibility of the two-step EF mechanism with respect to the two-step B mechanism. Moreover, the population of higher energy vibrational states allows the vibrational wavepacket to move to larger internuclear distances and to have vibrational periods similar to the wavepacket over the $B\,^1\Sigma_u^+$ state, as can be observed in the increase of the repetition period of the signal from the 760 nm to the 784 nm in the F, E and D panels. Thus, this blue shift of the XUV allows the control of the relative population of the different neutrally excited states of the hydrogen molecules.

6.3 UV pump - IR probe perspectives

The streaking effects of the IR field over the ejected electron presented in the first part of the present chapter is not limited to its kinetic energy distributions. In addition, the IR field modifies the partial waves in which the electron is emitted. In this way, a natural extension of the present work is based on the analysis of the electron angular distributions, to give a full overview of the streaking effect, including the play role of the autoionization. On the other hand, in both pump - probe protocols presented, the strong IR used disturbs the PECs which electrons feel, and consequently, the dynamics observed is driving by the presence of this field as probe. In this way, the XUV pump - IR probe schemes, as was presented in the second part, can be used to control the dynamical processes occurred in the molecular system, but not to explore the natural dynamics of the target, which requires a more appropriated scheme, as the XUV pump - XUV probe schemes presented in next chapter.

Chapter 7

XUV pump - XUV probe schemes

As discussed in chapter 6, the dynamics associated with the single excited states can be followed using a XUV pump - XUV probe scheme. This protocol implies different paths, through different single excited states which populate the same final ionic states. Consequently, the coherent combination of the wavepacket generated by the different quantum paths produces interferences which contain the dynamical information of the intermediate states.

The idea of the interferometry using pump - probe techniques has been previously used in femtochemistry to explore the nuclear dynamics in molecules [43, 16, 15], where due to the hundreds of femtosecond timescale of the nuclear motion, the used pump and probe IR pulses have durations of tens of femtoseconds to obtain a time resolution enough. The interferometry is based on the coherent superposition of wavepackets generated at different times. The pump generates a first wavepacket which evolves in time. After a given time, the probe pulse produces a second identical wavepacket, but delayed with respect to the first IR. In quantum mechanics, the phases are associated with the energies of the eigenstates which constitute the wavepacket. Since both wavepackets have different evolution phases at a certain spatial and time point, the coherent combination of both gives a constructive or destructive interferences, which contain the information of these relative evolution phases. The interfering wavepakets can be generated not only by a "direct" transition from the ground state at different times, but also by multiphoton "sequential" process, in which the final wavepacket contains information about the dynamics of intermediate wavepackets. Similar interferometric schemes have been used in attophysics to explore the electrons and fast nuclei motion in atoms and molecules. The mayor experiments make use of a XUV pump phase-locked with and strong IR probe pulse [97, 168, 36, 51]. As we shown in chapter 6, the XUV pump launches the wavepacket dynamics into an excited or ionic state, and the IR probe traces this dynamics by the interferometry between the different paths followed by the system. Different observables are used to obtain the atomic interferometer, as the angular electron distribution [164, 107] or the ionization yield and its Fourier transform in terms of the kinetic energy release (KER) [108, 86], all of them as a function of the time delay.

However, as discussed in chapter 6, the strong IR pulses used in the above experiments can disturb the potential which electrons feel, and even induce the

well-known electron streaking effect [36]. Therefore, one of the most promising approaches to explore and trace the motion of the electrons and light nuclei without the field perturbation is the use of attosecond or sub-femtosecond "weak" XUV pulses for both pump and probe, with intensities within the perturbation regime. This pump - probe technique has been recently explored theoretically in atoms [169] and experimentally in molecules [23]. One of the current limitations is that although the HHG technique can provide XUV pulses with these temporal resolutions, the achieved intensity is still too low. Rapid improvements in the different source techniques are opening the way to explore these kind of pump - probe schemes, soa theoretical background which guides future experiments is needed.

Following this idea, in the present chapter we propose a molecular interferometer generated by two identical XUV pulses separated a time delay. We aim to use two-photon "direct" transition from the ground state as a reference path that will interfere with a two-photon "sequential" transition, through the single excited states of the molecule. The induced interference encodes the dynamical information of the wavepackets formed within the single excited states. These interferences are presented in several observables, as the ionization probabilities or the fully energy differential probability distributions measured in coincidence for both ejected particles (electron and residual ion or proton) or averaged over one of them. In addition, the experimental access to these observables is relatively easy, in the case of dissociative ionization, by detecting electrons and protons in coincidence, through techniques as the COLTRIMS [115, 170, 111]. Thus, the analysis of these observables allows us to extract and unravel the vibronic dynamics into the different intermediate states.

7.1 Ionization probability yields

Our theoretical XUV pump - XUV probe scheme uses two identical pulses. We propose two set of simulations with different XUV pulses. In the first set, both pulses have durations of 2 fs, photon energies of 12.25 eV and intensities of $10^{12}\,\mathrm{W{\cdot}cm^{-2}}$, and in the second set, the pulses have the same durations and intensities but with photon energies of 14.0 eV.

The different transitions processes that the pump - probe scheme can induce in the hydrogen molecule, are plotted in figure 7.1.1, for the case in which it is used 14.0 eV pulses. In the upper panels of this figure, there are showed the potential energy curves (PEC) of the relevant states populated by the one or two-photon absorption process for three different times. In addition, in the lower panel, it is plotted the vector potentials of the pump and probe pulses as a function of time. In this way, when the pump pulse initially arrives to the system, its short duration of the 2 fs, which gives a broad bandwidth of around 1 eV, can induce the one-photon absorption into the single excited states, $B\,^1\Sigma_u^+$ and $B'\,^1\Sigma_u^+$, from the ground state and even the one-photon ionization into the bound vibrational states of the first ionic threshold ($1s\sigma_g$). In addition, the two-photon absorption of the pump pulse can ionize the molecule by resonant enhanced multi-photon

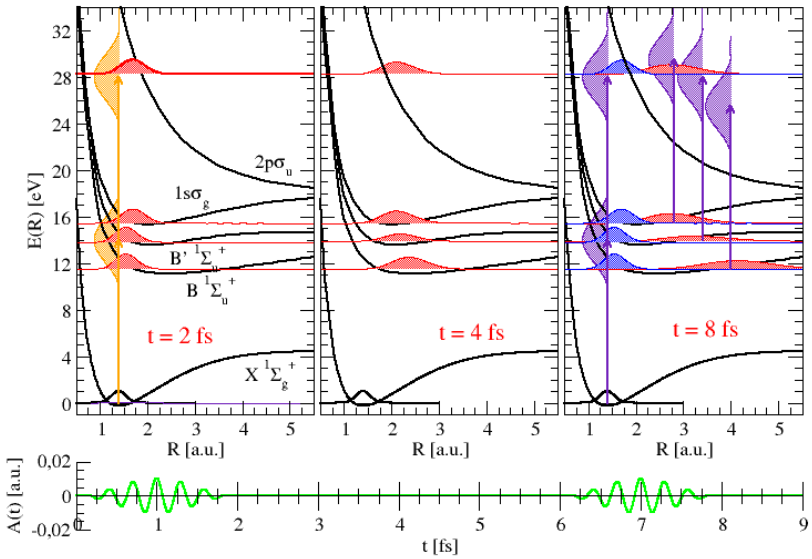

Figure 7.1.1: Schematic representation of the induced process by the pump - probe scheme with 14.0 eV pulses. In the upper panels, we plot the potential energy curves of the relevant states: The ground state, $X\ ^1\Sigma_g^+$, the two first Σ_u single excited states, $B\ ^1\Sigma_u^+$ and $B'\ ^1\Sigma_u^+$, and the two first ionic states, $1s\sigma_g$ and $2p\sigma_u$. The orange and violet arrows represent the one photon absorption due to pump and probe pulses, respectively, and the orange and violet shaded areas are the Fourier Transform, FT, of their vector potentials. The red shaded areas are the vibrational wavepackets over the different electronic (excited and ionic) states generated by the pump. The blue areas are the wavepacket generated by the probe. In the low panel, it is represented the vector potential of the total field (the sum of the pump and probe pulses) as a function of time.

ionization (REMPI) through the single excited states and by above threshold ionization (ATI) process through the ionic state. These different transition processes, generate vibrational wavepackets in the populated electronic states, plotted just after the pulse, for time equal to 2 fs, in the left upper panel. These wavepackets have a spatial and temporal evolution after the pump transition, moving to larger internuclear distances, as can be observed in the middle panel of figure 7.1.1, for a 4 fs after the pump arrives to the system. When the probe pulse arrives, there are two new possible paths for ionization: the "direct" and "sequential" processes, plotted in the right panel of figure 7.1.1. The "direct" path, in which the probe excites and ionizes the system from the ground state as the pump, generates a second set of wavepackets equal to the generated by pump into the same final states, but delayed in time. In the "sequential" path, the probe ionizes the the system from the intermediate states populated by the pump pulse, to the same final ionic states than the "direct" two-photon absorption. Focusing on the finals ionic states, the wavepackets generated by the "direct and "sequential" paths interfere.

Note that the presence of resonant states embedded into the continuum, which can be populated by the pump and probe pulses, generates other interference when they decay into the same ionic states than the direct photoionization.

We first analyze the total ionization yields that are expected to reveal the interferometric signals. As detailed in chapter 4, the ionization probability as a function of the time delay is given by:

$$P(\tau) = \sum_{\alpha} \sum_{l} \sum\!\!\!\!\!\!\int_{v_\alpha} \int_{\epsilon} \left| c^{l}_{\alpha,v_\alpha}(2T+\tau;\epsilon) \right|^2 dv_\alpha d\epsilon \tag{7.1.1}$$

where α is the ionic state ($1s\sigma_g$ and $2p\sigma_u$, in this simulations), v_α is the bound or continuum vibrational state of the residual ion, ϵ and l are the energy and angular momentum, respectively, of the ejected electron. T is the pulse duration and τ is the time delay between both pulses. The ionization yield as a function of the time delay for the 12.25 eV and 14.0 eV pulses are plotted in figures 7.1.2 and 7.1.3, respectively. For each scheme, we show the dissociative ionization probability (DI) in the lower panel, the non-dissociative ionization probability (NDI) in the middle panel, and the sum of both DI and NDI, which is the total ionization (TI) in the upper panel. In addition, we include for each ionization yield the contributions of Σ_g and Σ_u symmetries. It is clear that the 12.25 eV scheme has the same structure among the NDI, DI and TI yields, while the 14.0 eV case, the DI yield presents a different structure with respect to the NDI and TI yields. To explain these differences, we look at the different final symmetries, Σ_g and Σ_u. For the 12.25 eV case, the main contribution for TI, NDI and DI yields, comes from the Σ_g symmetry. The dipole selection rules, previously exposed in other chapters, for the parallel orientation, indicate that the unique transition allowed is from the Σ_g symmetry to Σ_u symmetry or viceversa. Consequently, for a final Σ_g symmetry it is necessary that the system absorbs two photons. We neglect in this analysis the absorption processes of four, six, and higher number of photons, which populate higher energy states, because their transition probabilities are orders of magnitude smaller.

For the 14.0 eV case, the main contribution to the DI yield comes from the same Σ_g symmetry. However, in the NDI yield comes from the Σ_u symmetry, corresponding to a one-photon absorption process, because the broad bandwidth and the photon energy of the 14.0 eV pulse allow to reach vibronic states with higher energy than the 12.25 eV pulse. Consequently, the 14.0 eV pulse can effectively produce the one-photon ionization to the bound vibrational states of the $1s\sigma_g$ threshold from the ground state. This first order transition process presents a higher probability than the two-photon absorption and dominates in the NDI yield. Finally, the TI yield for the 14.0 eV scheme has a contribution for both one- and two-photon transitions, which can be separated making a spectral analysis, as we will see later.

It is obvious that the ionization yields, showed in figure 7.1.3, present very fast oscillation patterns inside the yield structure, and a slower one, which can be observed looking at the shape of the probability as a function of time delay. Focusing on the TI, NDI and DI yields for the scheme with 12.25 eV pulses, the

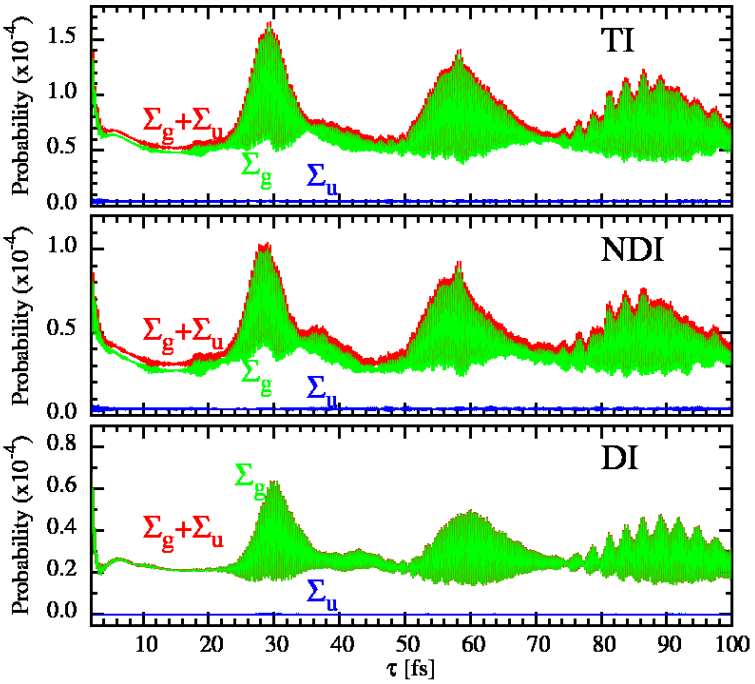

Figure 7.1.2: Ionization yields as a function of time delay, for pump - probe scheme with pulses of12.25 eV photon energy. Upper panel: Total (dissociative plus non-dissociative) ionization yield (TI). Middle panel: Non-dissociative ionization yield (NDI). Lower panel: Dissociative ionization yield (DI).

slow oscillation has a periodicity around 30.0 fs. However, in TI and DI yields for the scheme with 14.0 eV pulses, the slow oscillation is not so clear, and presents maxima every 20.0 fs and 30.0 fs. While the slow oscillation has a periodicity around 15.0 fs in the NDI yield.

These oscillation patterns are consequence of the accumulated phases in the different quantum paths followed by the system to reach the final ionic channels. These relative phases, imprinted in the ionization yields, can be easily extracted using the short-time Fourier transform (STFT), so-called short-term Fourier transform or windowed Fourier transform. As a difference with the standard Fourier transform, which transforms any time dependent function to its complementary expression in the frequency domain, the STFT gives an observable defined in both time and frequency domains. To this purpose, the STFT uses a window function, which limits the time region where the original time dependent function is not zero. Mathematically, the general expression for the STFT is:

$$\mathcal{F}_{STFT}\left[f\left(t\right)\right]\left(w;\tau,\sigma\right)=\int_{-\infty}^{\infty}f\left(t\right)g\left(\frac{\left(t-\tau\right)}{\sigma}\right)e^{\left(-i\omega t\right)}dt \tag{7.1.2}$$

where, $\mathcal{F}_{STFT}\left[f\left(t\right)\right]\left(w;\tau,\sigma\right)$ is the STFT of the function $f\left(t\right)$ and $g\left(\left(t-\tau\right)/\sigma\right)$ is the temporal window function, whose parameters are τ, the center time point,

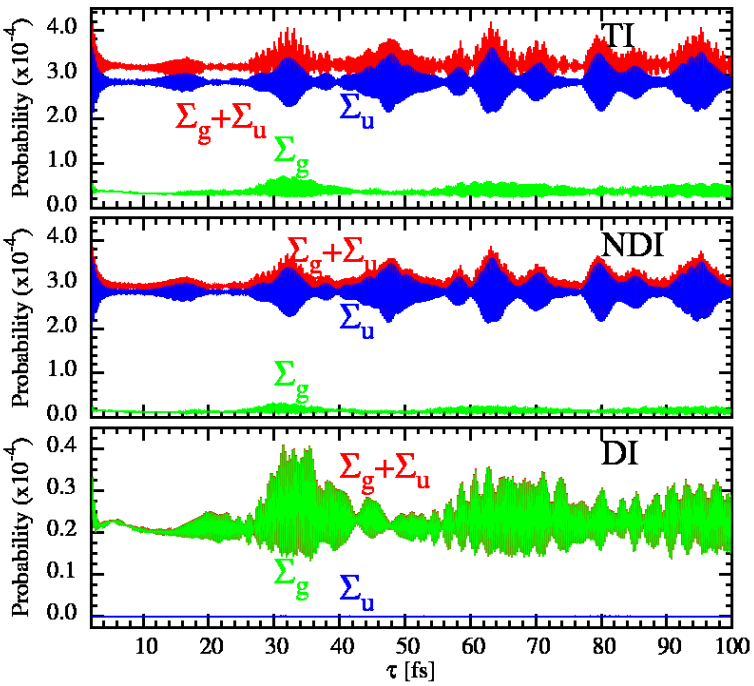

Figure 7.1.3: Same as in figure 7.1.2, but for pump-probe pulses with 14.0 eV of photon energy.

and σ, the time width. For the window function, we can choose several functions, but the most usual is the Gaussian type:

$$g\left(\frac{(t-\tau)}{\sigma}\right) = \frac{1}{\sqrt{2\pi}\sigma} e^{\left(-\frac{(t-\tau)^2}{2\sigma^2}\right)} \tag{7.1.3}$$

where $1/\sqrt{2\pi}\sigma$ is the normalization factor. The time limitation introduced by the window function gives to the STFT a certain time resolution, which is directly associated with the width used. As the time and frequency domains are complementary, an increase in the time resolution (smaller width) decreases the frequency resolution and viceversa. Consequently, only when the window function is larger than the periodicity of the structures from the original function, these can be discomposed in their corresponding frequencies. This can be appreciated in figure 7.1.4, where it is plotted the STFT of the DI yield of the pump - probe scheme with 12.25 eV pulses as a function of the frequency, ω, and time, τ, for different widths of the Gaussian window function in each panel. The width used in the left upper panel, around 100 fs, is several times larger than the slow oscillation in the DI yield, and therefore, the frequency resolution is shorter enough to discompose all the oscillation patterns, slower and fast, in its frequency components. This width makes that the STFT becomes a standard FT of the DI yield. A smaller width, with similar timescales of the oscillation patterns,

decreases the frequency resolution and starts to appear the temporal periods of the slow oscillations, as it is observed from the right upper panel, with a 25 fs width to the left lower panel, with a 10 fs width. Only when the width used is several times shorter than the slow oscillation but several times larger than the faster oscillation, the slower one is discomposed in its frequency components but the fast oscillation is represented in the temporal domain, as is clearly observed in the right lower panel, for a 2 fs width.

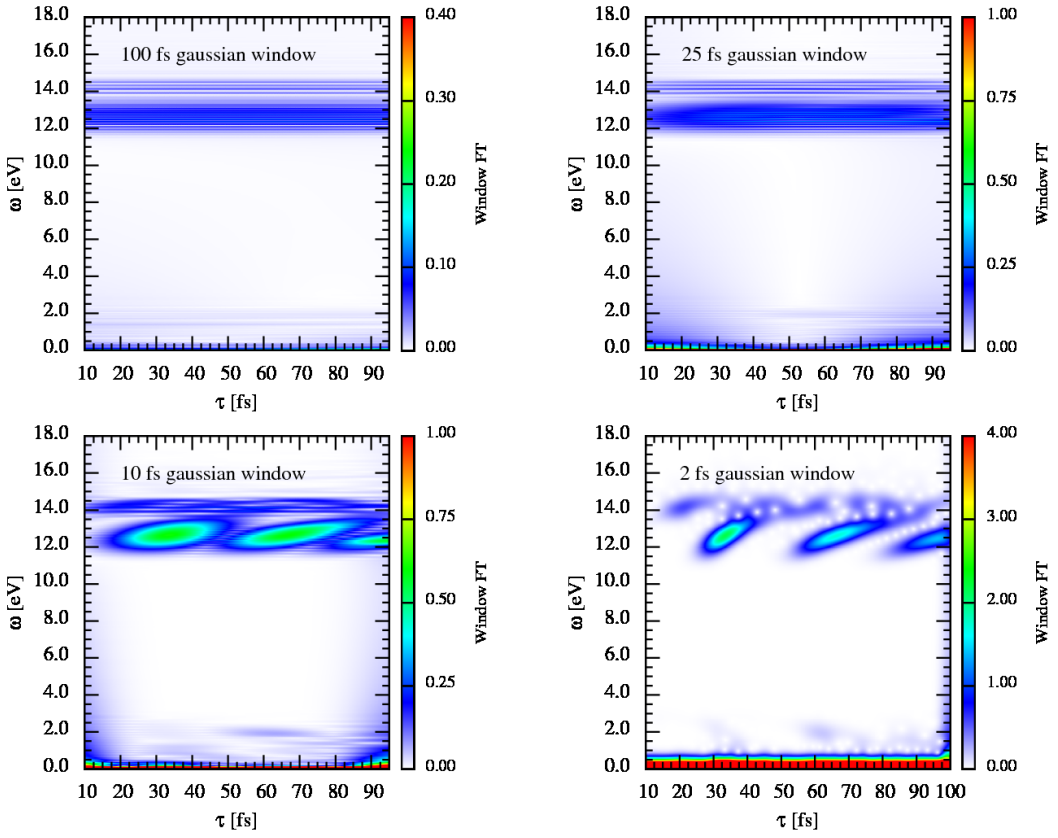

Figure 7.1.4: Short-Term Fourier Transform (STFT) so-called window Fourier transform of the DI yield, for a pump - probe scheme with pulses of 14.0 eV. Each panel corresponds to the STFT with different widths of Gaussian window function. Upper left panel: 100 fs width. Upper right panel: 25 fs width. Lower left panel: 10 fs width. Lower right panel: 2 fs width.

The STFT of the different ionization yields in figures 7.1.2 and 7.1.3, are given in figures 7.1.5 and 7.1.6, respectively. For all the ionization yields, we used a Gaussian window function with a 2 fs width. For each figure, we plot the STFT spectrum for the TI (upper panel), NDI (middle panel) and DI yields (lower panel). Focusing on figure 7.1.5, which corresponds to the TI, NDI and DI yields for the 12.25 eV case, it is clear that the maxima appear around an energy of 12.0 eV, which corresponds to the energy region of $B\,^1\Sigma_u^+$ electronic state. The oscillation period of the vibrational wavepacket in this electronic states is given by the repetition rate observed in the STFT, around 30.0 fs. On the other hand,

the increase of the tilt in the different maxima as a function of time indicates that the vibrational wavepacket is spreading. This is due to the anharmonicity of the PEC, as discussed in chapter 4.

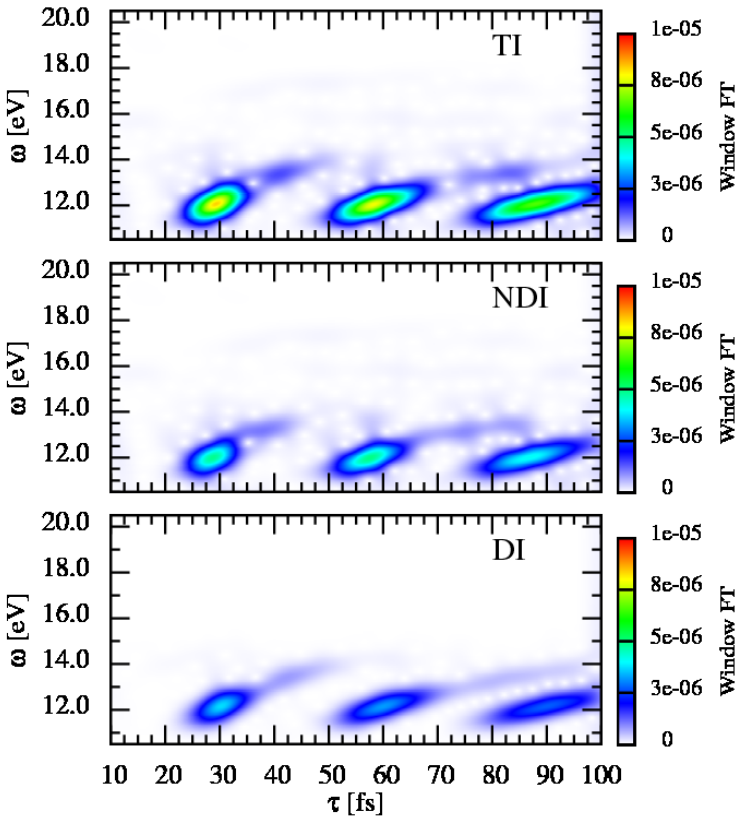

Figure 7.1.5: STFT of the ionization yield with a 2 fs width of the Gaussian window function for a pump - probe scheme with 12.25 eV pulses. Upper panel: STFT of the total ionization yield (TI). Middle panel: STFT of the non-dissociative ionization yield (NDI). Lower panel: STFT of the dissociative ionization yield (DI).

This STFT analysis confirms that the main contribution into the final ionic states only comes from the first single excited state of Σ_u symmetry, the $B\,^1\Sigma_u^+$. However, for the 14.0 eV pump - probe scheme, in figure 7.1.6, it is obvious that more intermediate states are present. Focusing on the DI yield, in which the two-photon absorption is dominant, the two groups of maxima at different FT frequencies indicate that two electronic wavepackets are generated. The signal at the energy region around 12.0 eV with a repetition rate of 30.0 fs corresponds to the vibrational wavepacket in the $B\,^1\Sigma_u^+$ electronic state, while the features at energies around 14.0 eV, with a periodicity of 20.0 fs, which correspond to the $B'\,^1\Sigma_u^+$ electronic state. The difference in the oscillation period between both electronic states can be explained observing the figure 7.1.1. It is clear that the $B'^1\Sigma_u^+$ PEC is narrower than the $B^1\Sigma_u^+$, and therefore, the vibrational wavepacket

of the $B'^1\Sigma_u^+$ state, associated with a shorter oscillation period, spreads in shorter times than the wavepacket in the $B\,^1\Sigma_u^+$ state.

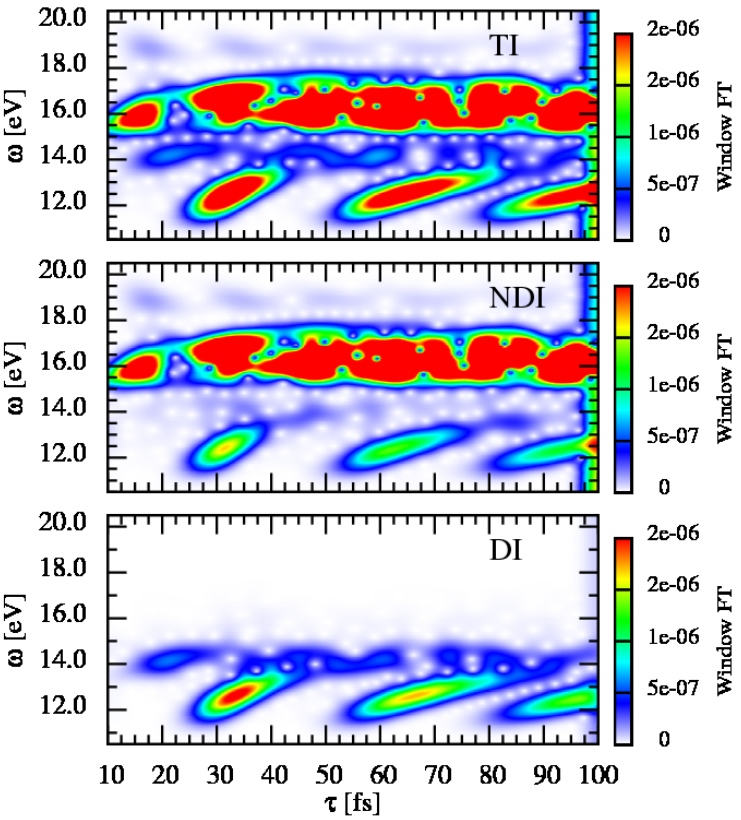

Figure 7.1.6: Same as in figure 7.1.5, but for a pump - probe scheme with 14.0 eV pulses

In the NDI yield for the scheme with 14.0 eV pulses, there are two two-photon ionization processes, the "direct" and the "sequential", and one one-photon ionization process. As we previously discussed, the one-photon transition is several times more probable than the two-photon absorption, so the features from the bound vibrational states of the first ionic threshold, $1s\sigma_g$, have a larger contribution in the NDI yield. These features are consequence of the interferences between the wavepacket generated by the pump pulse and its delayed replica due to the probe pulse, given a signal over the STFT around 16.0 eV. The periodicity of 15.0 fs, indicates that the wavepacket generated has a shorter period than the single excited state wavepackets, due to the narrower PEC of the $1s\sigma_g$ state. Finally, the STFT of the TI yield is the sum of the NDI and DI STFT spectra, so the same features observed in both DI and NDI spectra are present.

To characterize the different quantum path contributions in the interferometric signals observed in the probabilities, a second order approximation is developed. in this approximation, the time dependent wavefunction, $\Psi(\mathbf{r}, R, t)$, can be expressed as the product of three time evolutions operators applied into the initial

wavefunction:

$$\Psi\left(\mathbf{r},R,t\right)=\widehat{U}_{probe}\left(t-\tau\right)e^{\left[-i\widehat{H}_{0}(\tau-T)/\hbar\right]}\widehat{U}_{pump}\left(T\right)\Phi_{0,0}\left(\mathbf{r},R\right) \tag{7.1.4}$$

where $\Phi_{0,0}\left(\mathbf{r},R\right)$ is the initial state (the vibronic wavefunction of the ground state), $\widehat{U}_{pump}\left(T\right)$ and $\widehat{U}_{probe}\left(t-\tau\right)$ are the time evolution operators associated with the pump and probe electromagnetic fields and $\exp\left[-i\widehat{H}_{0}\left(\tau-T\right)/\hbar\right]$ is the free-field time evolution operator. In our spectral method, the eigenstates of the isolated Hamiltonian operator, $\widehat{H}_{0}$, constitute a complete basis set, satisfying the closure relation. As is presented in appendix D, the application of the closure relation to the above equation projected into the final continuum states gives the amplitudes for these states. Consequently, the electronic and nuclear energy-differential probability distributions are:

$$\begin{aligned}\frac{d^{2}P_{f,v_{f}}^{l_{f}}\left(\tau;\epsilon\right)}{dE_{v_{f}}dE\left(\epsilon\right)}=\Bigg|a_{f,v_{f}}^{l}\left(\epsilon\right)\left\{1+e^{\left[i\left(E_{f,v_{f}}(\epsilon)-E_{0}\right)\tau/\hbar\right]}\right\}+\\ \sum_{m}\sum\!\!\!\!\!\!\int_{v_{m}}b_{f,v_{f},l}^{m,v_{m}}\left(\epsilon\right)e^{\left[i\left(E_{f,v_{f}}(\epsilon)-E_{m,v_{m}}\right)\tau/\hbar\right]}\Bigg|^{2}\end{aligned} \tag{7.1.5}$$

where $a_{f,v_{f}}^{l}\left(\epsilon\right)$ is the "direct" two-photon transition amplitude from the ground to the final state, $b_{f,v_{f},l}^{m,v_{m}}\left(\epsilon\right)$ is "sequential" transition amplitude induced by the one-photon pump transition from the ground to the intermediate state, m,v_{m}, and later, as a function of the time delay, the probe transition to the final state. Finally, $E_{f,v_{f}}\left(\epsilon\right)$, $E_{m,v_{m}}$ and E_{0} are the energies of the ionic, single excited and ground states, respectively. Because the pump can populate a bunch of vibronic states, the "sequential" transition to the final states comes from all of them, running both coherent sums over the vibrational states associated with several electronic intermediate states. Developing the square module of equation 7.1.5, we can separate the fully energy-differential distribution into three components:

- The alpha contribution, corresponding to the interference between the pump and the probe replica due to the two-photon "direct" transition from the ground state:

$$\frac{d^{2}\alpha_{f,v_{f}}^{l}\left(\tau;\epsilon\right)}{dE_{v_{f}}dE\left(\epsilon\right)}=2\left|a_{f,v_{f}}^{l}\left(\epsilon\right)\right|^{2}\left\{1+\cos\left[\frac{E_{f,v_{f}}\left(\epsilon\right)-E_{0}}{\hbar}\tau\right]\right\} \tag{7.1.6}$$

- The beta contributions of the "sequential" process through the intermediate

single excited states:

$$\frac{d^2\beta^l_{f,v_f}(\tau;\epsilon)}{dE_{v_f}dE(\epsilon)} = \sum_m \sum\!\!\!\!\!\!\int_{v_m} \left|b^{m,v_m}_{f,v_f,l}(\epsilon)\right|^2 + \sum_{m,m'>m} \sum\!\!\!\!\!\!\int_{v_m,v'_{m'}>v_m} \left\{\Re\left[\overline{b}^{m',v'_{m'}}_{f,v_f,l}(\epsilon)\, b^{m,v_m}_{f,v_f,l}(\epsilon)\right]\cos\left[\frac{E_{m',v'_{m'}} - E_{m,v_m}}{\hbar}\tau\right] - \right. \\ \left. -\Im\left[\overline{b}^{m',v'_{m'}}_{f,v_f,l}(\epsilon)\, b^{m,v_m}_{f,v_f,l}(\epsilon)\right]\sin\left[\frac{E_{m',v'_{m'}} - E_{m,v_m}}{\hbar}\tau\right]\right\} \tag{7.1.7}$$

- The gamma contribution, which is the crossing term between the "direct" and "sequential" contributions:

$$\frac{d^2\gamma^{l_f}_{f,v_f}(\tau;\epsilon)}{dE_{v_f}dE(\epsilon)} = \sum_m \sum\!\!\!\!\!\!\int_{v_m} \left(\Re\left[\overline{a}_{f,v_f,l_f}(\epsilon)\, b^{m,v_m}_{f,v_f,l_f}(\epsilon)\right]\right. \\ \left\{\cos\left[\frac{E_{f,v_f}(\epsilon) - E_{m,v_m}}{\hbar}\tau\right] + \cos\left[\frac{E_{m,v_m} - E_0}{\hbar}\tau\right]\right\} - \\ -\Im\left[a_{f,v_f,l_f}(\epsilon)\,\overline{b}^{m,v_m}_{f,v_f,l_f}(\epsilon),\epsilon\right] \\ \left.\left\{\sin\left[\frac{E_{f,v_f}(\epsilon) - E_{m,v_m}}{\hbar}\tau\right] - \sin\left[\frac{E_{m,v_m} - E_0}{\hbar}\tau\right]\right\}\right) \tag{7.1.8}$$

As was presented in chapter 4, the ionization probabilities for the α, β, and γ contributions can be obtained from the fully energy-differential probability distributions, integrating or/and summing over both electronic, ϵ, and nuclear, v_f, kinetic energies. Thus, if we sum and integrate over all, only sum over the bound or only integrate over the continuum vibrational states, we obtain the TI, NDI and DI yields, respectively.

The α, β and γ contributions of the TI yield for the pump - probe scheme with 12.25 eV pulses are plotted in the upper panel of figure 7.1.7. As is observed, the slow oscillation, around 30.0 fs, is due to the "sequential" process (β contribution), and the faster oscillation, around 0.35 fs, comes from the cross term (γ contribution). While the "direct" process (α contribution) can be considered time delay independent. The observed beatings can be easily understood assuming that the $a^l_{f,v_f}(\epsilon)$ and $b^{m,v_m}_{f,v_f,l}(\epsilon)$ amplitudes are almost independent of electronic and nuclear energies in the region of interest (which excludes the case of autoionization). Considering these simplifications, the ionization yields obtained from the equations 7.1.6, 7.1.7 and 7.1.8 become:

$$\alpha_{f,l}(\tau) = A_{f,l} \tag{7.1.9}$$

$$\beta_{f,l}(\tau) = B_{f,l} + \\ \sum_{m,m'>m} \sum\!\!\!\!\!\!\int_{v_m,v'_{m'}>v_m} C^{m,v_m}_{f,l}\cos\left[\frac{E_{m',v'_{m'}} - E_{m,v_m}}{\hbar}\tau\right] \tag{7.1.10}$$

$$\gamma_{f,l} = \sum_{m} \sum_{v_m} E_{f,l}^{m,v_m} \cos\left[\frac{E_{m,v_m} - E_0}{\hbar}\tau\right] \tag{7.1.11}$$

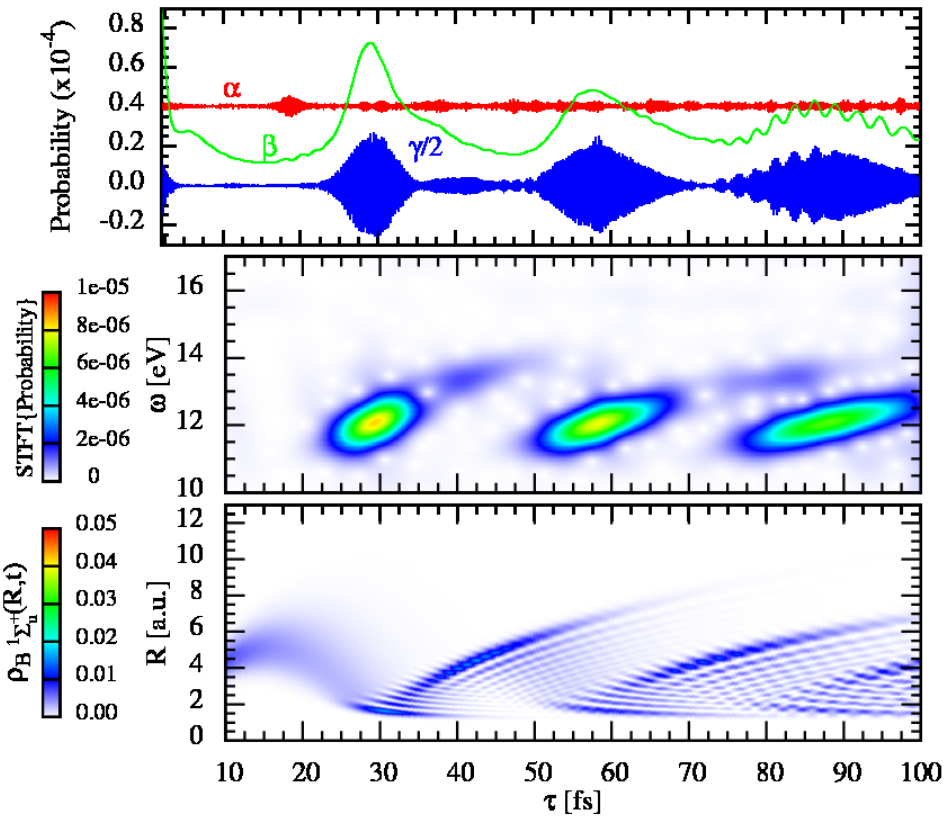

Figure 7.1.7: Upper panel: Contribution of the different paths (α, β and γ) to the total ionization yield for pump - probe scheme with 12.15 eV pulses. Middle panel: STFT of the total ionization yield. Lower panel: Vibrational wavepacket of the unique populated intermediate states ($B\,^1\Sigma_u^+$).

where $A_{f,l}$, $B_{f,l}$, $C_{f,l}^{m,v_m}$ and $E_{f,l}^{m,v_m}$ are constants for each final state f and l. For comparison purposes, it is shown in the middle panel of figure 7.2.1, the STFT using a Gaussian window function with a 2.0 fs width, and in the lower panel, the $B\,^1\Sigma_u^+$ vibrational wavepacket, generated after the pump pulse, as a function of the internuclear distance and time. It is clear that the energy difference between the intermediate vibronic states, $E_{m',v'_{m'}} - E_{m,v_m}$, controls the slow oscillations and the energy difference between the intermediate and ground vibronic states corresponds to the fast oscillations, because a smaller energy difference gives larger periods for the cosine function. Thus, the slow oscillation associated with the β contribution represents the average period, around 30.0 fs, of the $B\,^1\Sigma_u^+$ vibrational wavepacket created by the pump pulse. The maxima in the yields (associated with their STFT maxima) correspond to revivals of the vibrational

wavepacket components in the inner turning point, where the Franck-Condon overlap between the intermediate and final vibrational wavefunctions is maximum. While, the γ component is controlled by the $E_{m,v_m} - E_0$ energy difference between the intermediate and the ground vibronic states. Note that the integration over the nuclear and electronic energies practically washes out the time delay dependence of the α contribution, given by the relative phase $E_{f,v_f}(\epsilon) - E_0$.

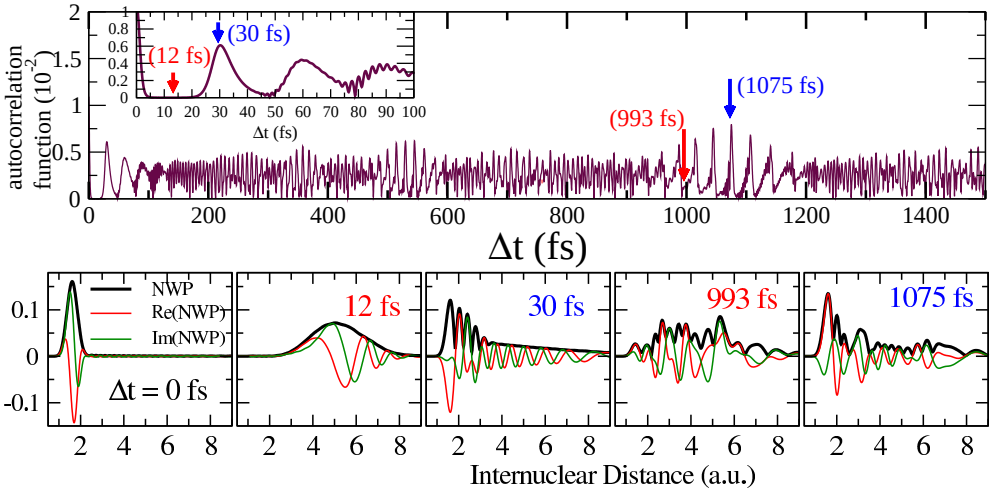

Figure 7.1.8: Upper panel: Autocorrelation function for the vibrational wavepacket associated with the first single excited state, $B\ ^1\Sigma_u^+$, as a function of time delay. Lower row of panels: Vibrational wavepackets at different propagation times, after the absorption of the pump pulse. The real and imaginary components of the vibrational wavepackets are plotted in red and green colors, respectively, and the absolute value in black thick line.

It is now clear that the repetition of the features along the time delay observed in the STFT as well as in β contribution of the ionization yield, are due to the revivals when the vibrational wavepacket comes back in a complete oscillation to the inner turning point. However, as was presented in chapter 4, the anharmonic potential (PEC) in which the nuclei move, produces the spreading of the wavepacket. This spreading can be clearly observed in the lower panel of figure 7.1.7, where after the first complete oscillation, the interferences among the different $B\,^1\Sigma_u^+$ vibrational states prevent the full reconstruction of the wavepacket. In this way, the partial reconstructions, revivals, of the vibrational wavepacket can be analyzed using the autocorrelation function, $R_n(\triangle t)$, introduced in chapter 4 as:

$$R_n(\triangle t) = \sum_{v_n} \int |c_{n,v_n}(T)|^2 \, e^{\left[-i\frac{E_{n,v_n}}{\hbar}\triangle t\right]} dv_n \tag{7.1.12}$$

where $\triangle t$ is $t - t_0$, being t and t_0 the final and initial propagation times. In figure 7.1.8, we plot the autocorrelation function of the vibrational wavepacket, generated by a 12.25 eV pulse in the $B\ ^1\Sigma_u^+$ state, as a function of $\triangle t$ up to 1.5 ps (picoseconds). After 5 fs, the nuclei have already moved apart reaching distances

to 4 a.u.. As we expected, the partial revivals appear at every 30 fs, which is the average period of a complete oscillation for this vibrational wavepacket. These revivals become smaller until 1075 fs, when it is again obtained a large revival. The vibrational wavepacket computed right at the end of the pulse, as well as for the two maxima (largest revivals) and two minima found in the autocorrelation function are plotted in the lower panel of figure 7.1.8. To observe the phases we plot in colors both real and imaginary parts of the vibrational wavepacket, $\phi_n(R,t)$, and its module as a black thick line. For the minimum at $\triangle t = 12$ fs the amplitude is zero in the internuclear distances where the initial vibrational wavepacket is located. Other minimum, such the one plotted at $\triangle t = 933$ fs, has non-zero amplitudes but phases that deconstructively interfere with respect to the initial vibrational wavepacket. For the two maximums, at 30 fs and 1075 fs, the maximum module of the vibrational wavepacket matches that at $\triangle t = 0$ fs, but more importantly the phases add up coherently.

More interesting is the pump - probe scheme for 14.0 eV pulses, whose α, β and γ contributions to the TI yield are plotted in the upper panel of figure 7.1.9. In this case, the pump is capable of populating several single excited electronic states as well as the bound vibrational states of the first ionic threshold, $1s\sigma_g$, by one-photon absorption. In figure 7.1.9, it is plotted the STFT using a Gaussian window function with a 2.0 fs width (upper-middle panel) and the vibrational wavepackets for the $1s\sigma_g$, $B\,^1\Sigma_u^+$ and $B'\,^1\Sigma_u^+$ in this order from middle to lower panels, respectively, as a function of the propagation time after the pump and the internuclear distance. As in the previous case for the pump - probe scheme with 12.25 eV pulses, the slow oscillation corresponds to the β contribution, but for the 14.0 eV pulses, the beatings from the second single excited state cannot be neglected. It is difficult to observe the different slow oscillations for each single excited state in the TI yield, but its STFT spectrum clearly shows the presence of two vibrational wavepackets for different energy regions corresponding to the $B\,^1\Sigma_u^+$ and $B'\,^1\Sigma_u^+$ states. As was explained in the STFT spectrum, these peaks in the TI yield correspond to time delays in which the B and B' wavepackets have a maximum close to the inner turning point, where the Franck-Condon overlap is maximum to the transition between them and the final ionic states, observed in figure 7.1.9. In addition, there are periodic signals in the energy region of the $1s\sigma_g$ bound vibrational states, corresponding to the direct transition from the ground state, which are included in the α contribution. In this case, the direct beating with the ground state, $E(v_f,\epsilon) - E_0$, which contains the dynamical information of the $1s\sigma_g$ bound vibrational states. Therefore, the wavepacket periodicity around 15.0 fs is imprinted in the α contribution to the TI yield.

At this point, it is important to emphasize that short pulses, i.e., pulses with rather large bandwidth, are strictly necessary to make a coherent superposition of vibronic states, therefore to produce a vibronic wavepacket. The requirement is that the bandwidth is larger than the energy separation between the vibronic states that are populated. Although the use of short pulses is in principle at the cost of energy resolution, the use of the present pump - probe scheme (the molecular interferometer), in which the time delay between pulses is varied, allows one to retrieve the relative energies (beatings) of all the states that are efficiently

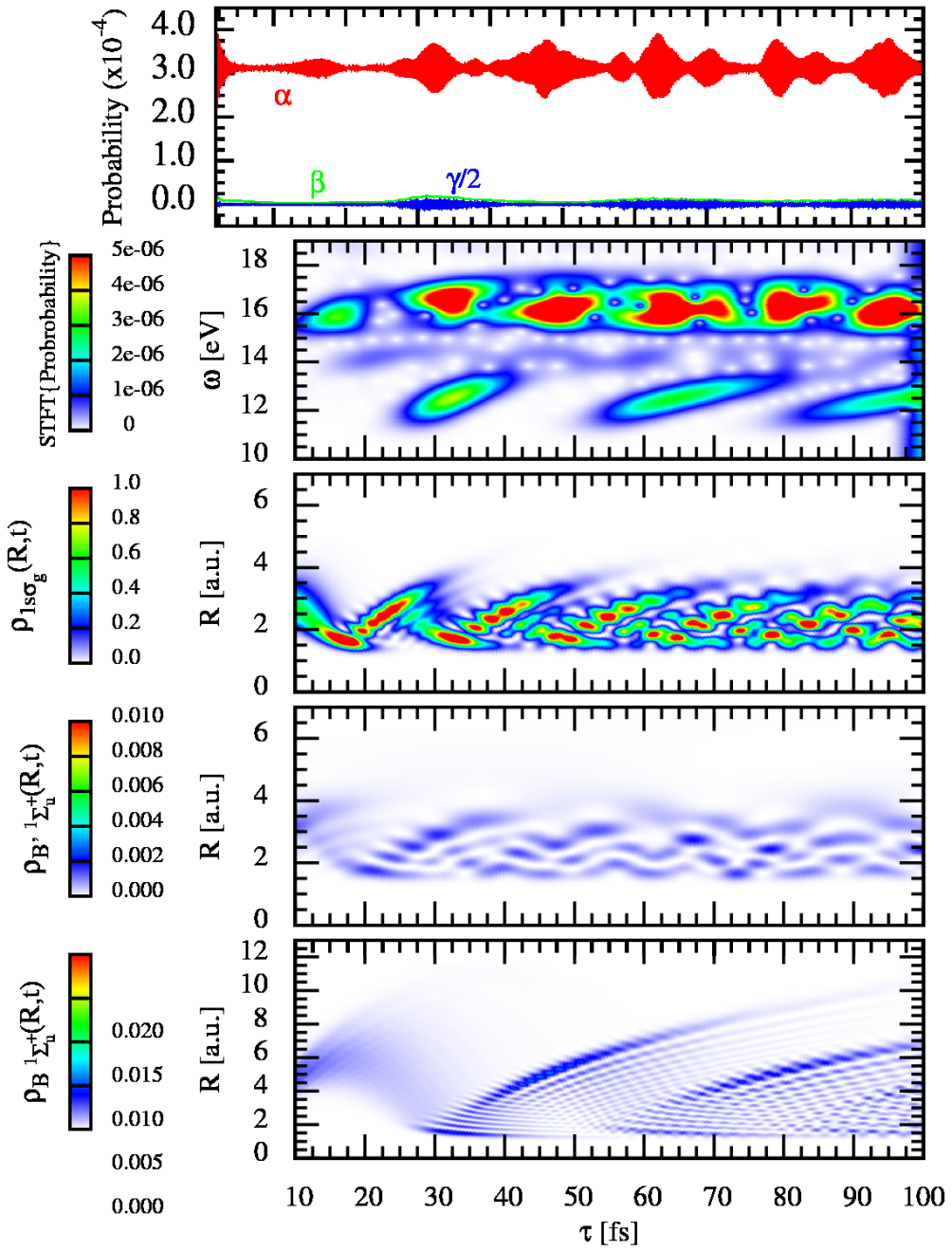

Figure 7.1.9: Upper panel: Contribution from the different paths to the total ionization yield for the 14.0 eVcase. Upper-middle panel: STFT of the total ionization yield. Middle panel: Vibrational wavepacket of the populated $B\,^1\Sigma_u^+$ intermediate state. Loer-middle panel: Vibrational wavepacket of the populated $B'\,^1\Sigma_u^+$ intermediate state. Lower panel: Vibrational wavepacket for the bound states of the first ionic threshold ($1s\sigma_g$).

populated by the pump pulse. These vibronic beatings can be extracted from the FT of the total dissociative ionization yield, performed for both 12.25 eV and 14.0 eV pump-probe schemes in figure 7.1.10. Following common experimental practice, we have removed a constant background from the calculated yields. We have also included a finite energy resolution of 5 meV for better visualization. As can be seen, the observed peaks reveal all the $E_{m,v_m} - E_0$ and $E_{m',v'_{m'}} - E_{m,v_m}$ beatings in the vibronic wavepacket. The $E_{m',v'_{m'}} - E_{m,v_m}$ beatings appear between 0 and 2.5 eV. Since only the $B\,^1\Sigma_u^+$ and $B'\,^1\Sigma_u^+$ electronic states are efficiently populated, one can distinguish three kinds of $E_{m',v'_{m'}} - E_{m,v_m}$ beatings: Those involving two vibrational states in the $B\,^1\Sigma_u^+$ state (denoted as $B - B$), two vibrational states in the $B'\,^1\Sigma_u^+$ state (denoted as $B' - B'$), and one vibrational state in the $B\,^1\Sigma_u^+$ state and one vibrational state in the $B'\,^1\Sigma_u^+$ state (denoted as $B - B'$). A blow up of the low energy region of the FT in which this beating appears are plotted in figure 7.1.11, where the left column is for the 12.25 eV and the right for the 14.0 eV pulses. $B-B$ and $B'-B'$ beatings, plotted in the upper-middle and lower-middle panels of both columns in figure 7.1.11, are associated with the vibrational components of the vibronic wavepacket in the $B\,^1\Sigma_u^+$ and $B'\,^1\Sigma_u^+$ states, respectively. $B - B'$ beatings, plotted in both columns of figure 7.1.11 in the lower panels, are associated with the electronic component of the vibronic wavepacket, corresponding to electron dynamics between both electronic states, $B\,^1\Sigma_u^+$ and $B'\,^1\Sigma_u^+$.

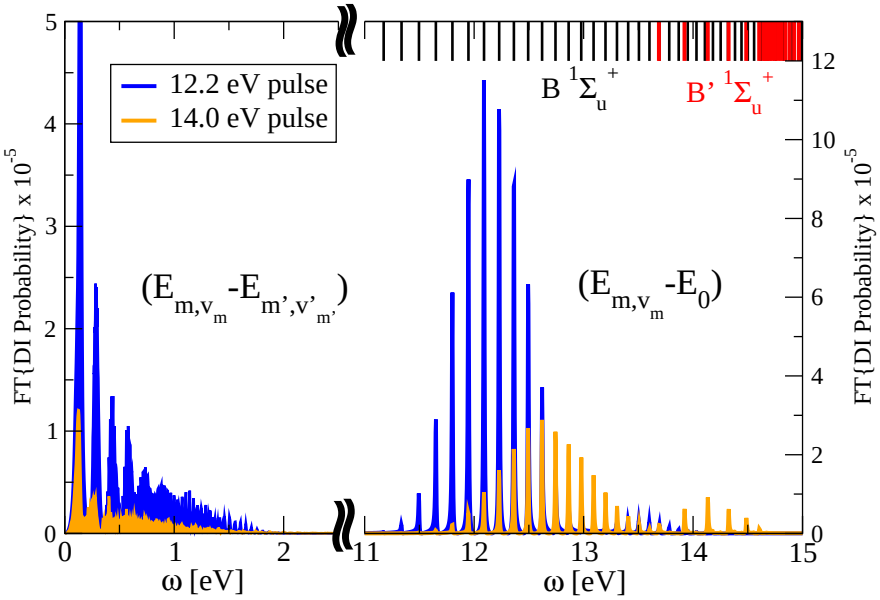

Figure 7.1.10: Fourier transform of the DI probabilities shown in figures 7.1.5 for 12.25 eV and 7.1.6 for 14.0 eV pump-probe schemes. In the upper side of the x-axis there are the energy position of the different vibronic intermediate states: The vibrational states of the $B\,^1\Sigma_u^+$ state in black and the vibrational ones associated with the $B'\,^1\Sigma_u^+$ in red.

It is clear that the $B-B$ beatings, which appear at FT energies from 0 eV to 2 eV, dominate in the standard FT for the pump - probe scheme with 12.25 eV pulses,

because the $B\,^1\Sigma_u^+$ state is the only one significantly populated. However, for the case with 14.0 eV pulses, both $B\,^1\Sigma_u^+$ and $B'\,^1\Sigma_u^+$ states are efficiently populated, and three families of beatings, $B-B$, $B'-B'$ and $B-B'$, are present. As for the 12.25 eV pulses, the $B-B$ and $B'-B'$ beatings appear at FT energies from 0 eV to 2 eV. We can also see that the amplitude of the $B'-B'$ and $B-B'$ beatings is comparable, as soon as the relative populations in both electronic states, $B\,^1\Sigma_u^+$ and $B'\,^1\Sigma_u^+$, are similar. In addition, figure 7.1.11 shows the $B-B$' beatings, which appear from 1.5 to 2.5 eV, with a lower amplitude that the vibrational beatings of the electronic $B\,^1\Sigma_u^+$ or $B'\,^1\Sigma_u^+$ states. Finally, the extraction of the different beating families from the standard FT of the ionization yields proves that the present pump - probe scheme gives access to both electron and nuclear dynamics.

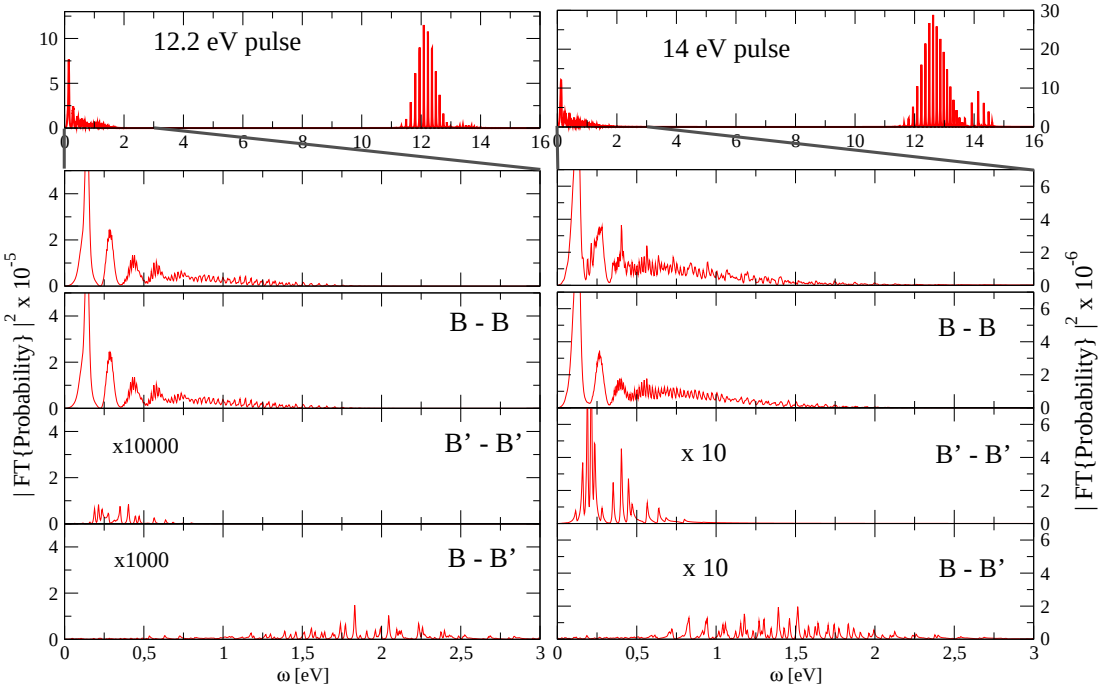

Figure 7.1.11: Upper row: FT of the DI probabilities for 12.25 eV, in the left column, and the 14.0 eV pump - probe schemes, in the right column. Upper-middle row: Blow up of the FT in the region from 0 eV to 1.6 eV, where the $B-B$, $B'-B'$ and $B-B'$ beatings appear. Middle row: Zoom in the low energy region, for a simulation where only the $B\,^1\Sigma_u^+$ (only the $B-B$ beatings) are included. Lower-middle row: The same as the middle row, but only includes the vibronic states associated with the $B'\,^1\Sigma_u^+$ (the $B'-B'$ beatings). Lower row: FT of a simulation in which only $B-B'$ beatings corresponding to vibronic states associated with different electronic, $B\,^1\Sigma_u^+$ and $B'\,^1\Sigma_u^+$, states are included.

7.1.1 Singly energy-differential probability distributions

Now, we focus on the single energy-differential distributions. As was presented in chapter 4, the most straightforward single differential distributions are the

NKE/PKE (and EKE) distributions obtained from the doubly differential distributions, summing and/or integrating over the electron (or nuclear/proton) kinetic energies, respectively. We specially focus on the PKE distributions, where as in the ionization probabilities the interferences between the different quantum paths can be extracted from the spectra using a standard FT analysis. In figure 7.1.12, it is plotted the FT of the PKE distribution for the scheme with 12.25 eV pulses and in figure 7.1.13 for the scheme with 14.0 eV pulses, as a function of the PKE and the FT frequency. The features observed in both figures can be analyzed taking into account the model presented in the above section, where the density of probability is separated in three components, given in equations 7.1.6, 7.1.7 and 7.1.8. To give the PKE distribution, each component is integrated over the electron kinetic energies.

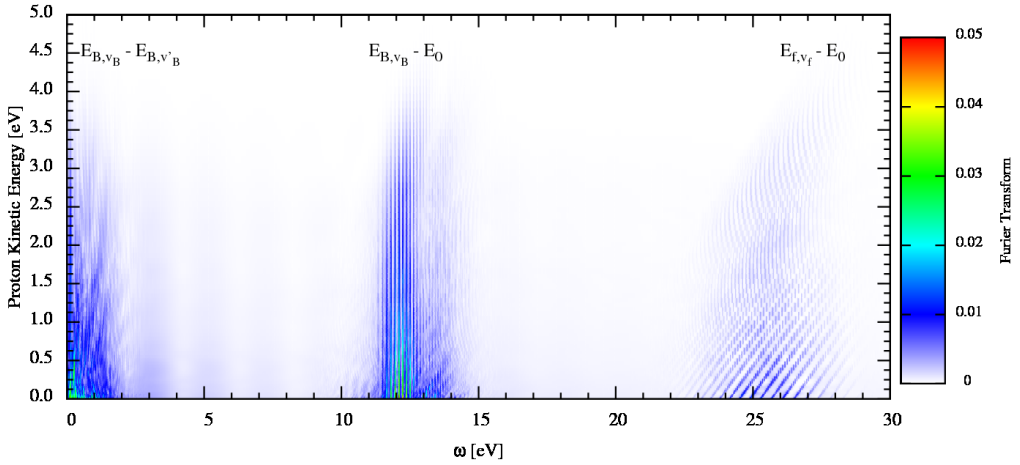

Figure 7.1.12: FT of the PKE distributions as a function of the proton kinetic energy (PKE) and FT frequency, for a pump-probe scheme with 12.25 eV pulses.

On both figures 7.1.15 and 7.1.15, the signal at 25.0 eV and 28.0 eV, respectively, is associated with the two-photon absorption with the α contribution. The linear variation with the FT frequency and the proton kinetic energy, is because the α contribution depends on the energy difference $E_{f,v_f} - E_0$, and therefore, depends on the proton kinetic energy. Similar to these fringes, the spikes observed at 12.25 eV of FT frequency, in both pulse cases, and at 14.0 eV, only for the scheme with 14.0 eV pulses, correspond to the γ contribution. This contribution is given by the $E_{f,v_f} - E_{m,v_m}$ and $E_{m,v_m} - E_0$ energy differences, which directly involve the intermediate states with the ground and final states. These FT frequencies should increase with the final energy because the accumulated phase difference does it. However, these lines are hardly visible in both figures 7.1.12 and 7.1.13, because, by integrating over electron energy, one looses the information about individual frequencies, i.e., one can only visualize a sort of unresolved average value with no information about individual vibronic states. The same occurs for EKE distributions. Finally, the features observed at lower frequency correspond to the β contribution.

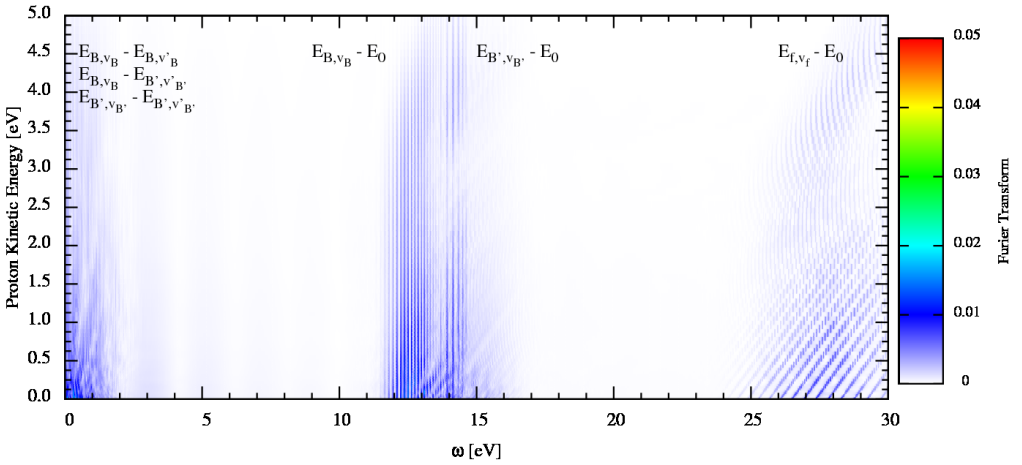

Figure 7.1.13: Same as in figure 7.1.12 for the 14.0 eV pulses

Focusing on the region where the γ contribution takes place, it is clear the $E_{m,v_m} - E_0$ beatings at well-defined energies of the intermediate states. However, as can be seen in figure 7.1.14, these signals contain more information about the intermediate vibronic states. In this figure, we compare the blow up of this region for the FT of the PKE distribution with the bound vibrational distribution as a function of the energetic position of the vibrational states respected to the ground states for the $B\ ^1\Sigma_u^+$ state, populated by 12.25 eV. As can be observed, the shape of both distributions has a similar structure. This structure represents the relative population of the vibronic states and indicates the weight of these states in the vibrational wavepacket. Consequently, the FT analysis of the PKE distribution can give not only the energetic position of the different vibronic states, unless also their relative population.

At a difference with the atomic single ionization, as in He, where the total energy obtained by the system is fully carried by the ejected electron [108, 86], in H_2, the total energy is shared between nuclei and electrons. Therefore, while the total and electron differential-energy distributions are the same in atoms, in molecules this relation does not satisfy. This is the main reason because the PKE and EKE distributions do not give a clear access to the vibronic energy difference of the different paths involved in the pump - probe ionization process. In this way, it is more adequate to study the single energy-differential distributions as a function of the total energy in H_2, which is obtained integrating the doubly energy-differential distributions over the energy sharing, i.e. by fixing the final energy, E_f. As with the PKE distributions, the complex oscillation patterns, observed in the total energy-differential distributions can be analyzed using the standard FT and the second order approximation presented in the above section.

Figure 7.1.15 shows the FT of the energy-differential distribution as a function of both total energy and FT frequency for the pump - probe scheme with 12.25 eV pulses. The fringes observed for frequencies larger than 24.0 eV in figure 7.1.15, correspond to the two-photon absorption region, around 24.5 eV, associated with

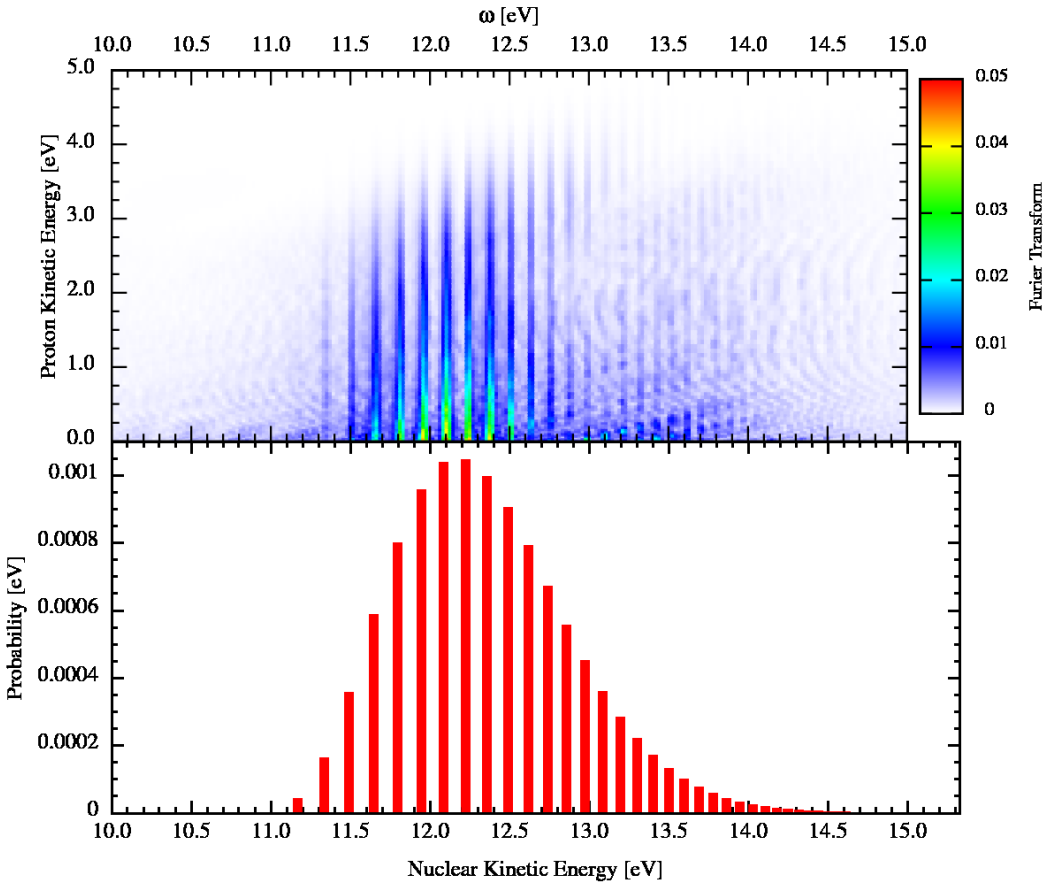

Figure 7.1.14: Upper panel: Blow up of the region around 12 eV of FT frequency from figure 7.1.12, for the 12.25 eV pulse case. Lower panel: Bound vibrational distributions, as a function of the position energy with respected to the electronic ground states, for the $B\ ^1\Sigma_u^+$ state populated by the one-photon absorption with a 12.25 eV pulse.

the α contribution. These fringes present a linear variation between the FT frequency and the total energy, constituted lines with a slope 1, because α contribution depends on the $E_f - E_0$ energy difference. Following with the analysis, it is clear from equation 7.1.7 that the β contribution only depends on the vibronic energy difference between the intermediate states, $E_{m,v'_m} - E_{m,v_m}$, given signals over well-defined FT frequencies, around 1.0 eV or less, similar to those found in atomic interferometry experiments reported in [108, 86]. In addition, for the 12.25 eV pump - probe schemes, only the $B^1\Sigma_u^+$ state gives a non-negligible β contribution. Because the standard FT extracts all the vibronic energy differences, the β contribution signal appears as vertical lines at the FT frequencies associated with all the energy differences among the relevant populated vibrational states of the $B\ ^1\Sigma_u^+$ state. Finally, the signals observed around 12 eV, associated with the one-photon absorption (12.25 eV), come from the γ contribution, which corresponds to the $E_f - E_{m,v_m}$ and $E_{m,v_m} - E_0$ energy differences. Although the $E_{m,v_m} - E_0$ energy differences are independent of the total energy, giving vertical

lines with the same energy of the vibrational $B\,^1\Sigma_u^+$ state with respected to the ground state, the $E_f - E_{m,v_m}$ energy differences vary with the FT frequency. Thus, in figure 7.1.15, the structure associated with the γ contribution has vertical lines which increase with the FT frequency to higher total energies.

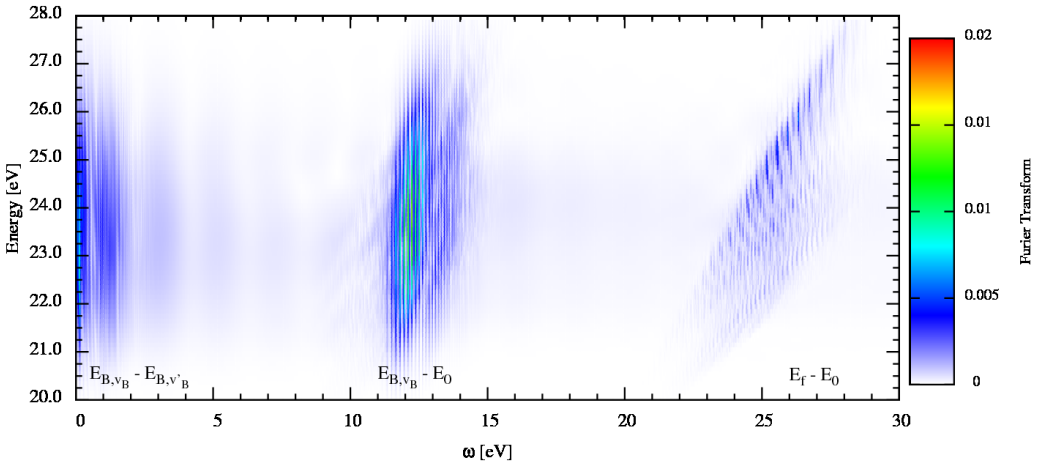

Figure 7.1.15: Fourier transform (FT) of the differential probability integrated over the energy sharing as a function total energy, for the pump - probe scheme with 12.25 eV pulses. In the plot we show the beatings corresponding to the interaction between the vibrational states of the $B\,^1\Sigma_u^+$ ($E_{B,v'_B} - E_{B,v_B}$), between the vibrational states of the $B\,^1\Sigma_u^+$ with the ground state ($E_{B,v_B} - E_0$), and between ionic states with the ground state ($E_f - E_0$).

As for the 12.25 eV pulses, figure 7.1.16 shows the FT spectrum of the differential energy distributions as a function of both total energy and FT frequency for the scheme with 14.0 eV pulses, where we observe similar structures, previously discussed. The α contribution, is clearly appreciable as a bunch of lines tilted 45° with the FT frequency and total energy, but appears over the region upper to 28 eV, corresponding to the two-photon absorption of 14.0 eV energy, instead of the 12.25 eV. The γ contribution appears in the region of the one-photon absorption energy, around 14 eV, where it is clear two groups of signals. The group at 12 eV of FT frequency corresponds to the $E_f - E_{m,v_m}$ and $E_{m,v_m} - E_0$ beatings of the $B\,^1\Sigma_u^+$ state. The other group at higher FT frequencies, which does not appear in the case with 12.25 eV pulses, are due to the same beatings but for the second single excited state, $B'\,^1\Sigma_u^+$, given a vertical lines in the energies corresponding to their vibrational states (higher in energy respected to the ground state than the $B\,^1\Sigma_u^+$ state). Finally, the β contribution not only contains the beatings between two vibrational states of each $B\,^1\Sigma_u^+$ and $B'\,^1\Sigma_u^+$ states, but also they present the beatings between one vibronic state of the $B\,^1\Sigma_u^+$ and one of the $B'\,^1\Sigma_u^+$ electronic state.

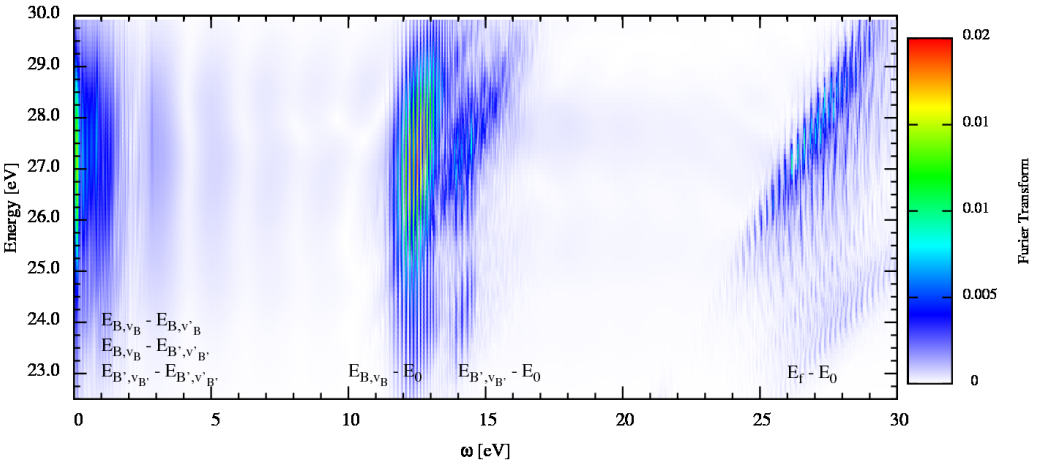

Figure 7.1.16: FT of the differential probability integrated over the energy sharing as a function total energy, for the pump - probe scheme with 14.0 eV pulses. In the plot we show the beatings corresponding to the β contribution ($E_{B,v_B} - E_{B,v'_B}$, $E_{B',v_{B'}} - E_{B',v'_{B'}}$ and $E_{B,v_B} - E_{B',v'_{B'}}$), γ contribution ($E_{B,v_B} - E_0$ and $E_{B',v_{B'}} - E_0$), and α contribution (E_f - E_0).

7.2 Doubly energy-differential probability distributions

We can go further and explore the electronic and nuclear energy-differential probability distributions. The calculated two-dimensional (2D) coincidence spectra for 12.25 eV and 14.0 eV pulses are plotted in figures 7.2.1 and 7.2.2, respectively. Figures 7.2.3 and 7.2.4, show the separated contribution of the $1s\sigma_g$ threshold and figures 7.2.6 and 7.2.7 of the $2p\sigma_u$. The figures only show results for short time delays because, as for the total yield, the main patterns repeat with a periodicity of $28-30$ fs. For analysis purposes, in the first column it is plotted an illustration of the energetics and the position of the vibrational wavepacket for each time delay. As can be observed in figures 7.2.3 and 7.2.6 of the 12.25 eV, for short time delays, ionization can only proceed through the $1s\sigma_g$ threshold, while for larger time delays, ionization through the $2p\sigma_u$ threshold is also possible. However, for the 14.0 eV case, due to the larger photon energy, even for short time delays, the ionization can occur in both threshold, $1s\sigma_g$ and $2p\sigma_u$. In addition, in all figures, we include the fully energy-differential distributions obtained with the analysis tool proposed in section 7.1, where the α contribution is given by the equation 7.1.6 (plotted in the third column), the β contribution is given in the equation 7.1.7 (plotted in the forth column) and the γ contribution is given in the equation 7.1.7 (plotted in the fifth column).

The doubly energy-differential probability distributions exhibit an increasing number of oscillations when the time delay increases. As it can be observed in figures 7.2.1 and 7.2.2, most of these oscillations come from the α contribution,

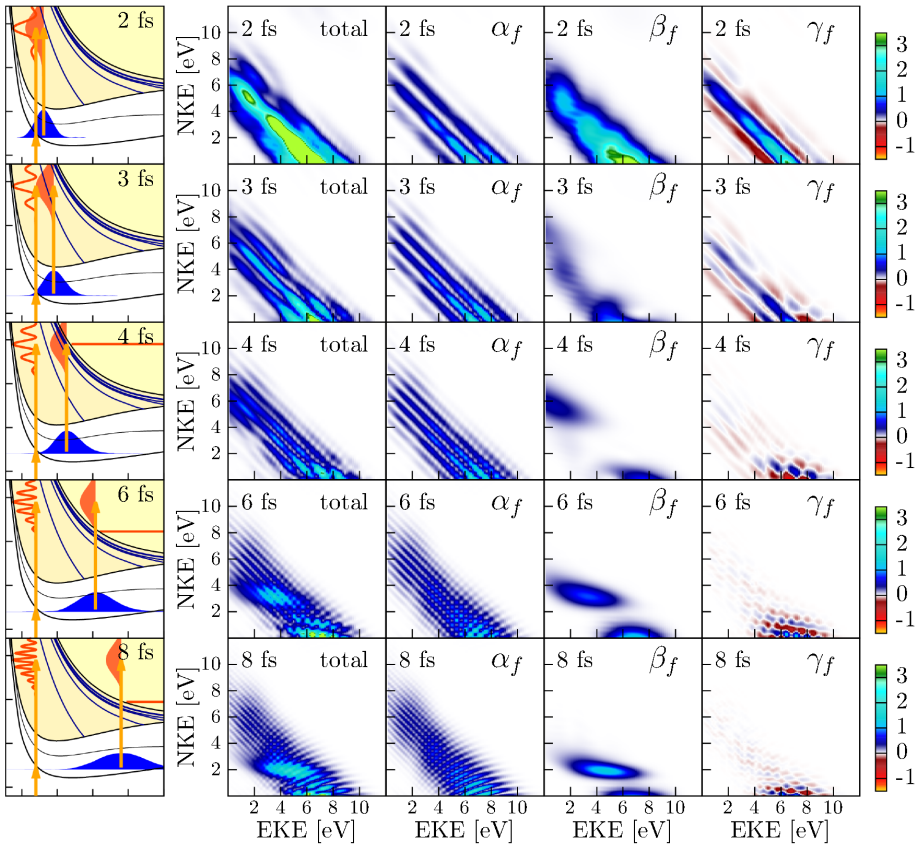

Figure 7.2.1: Column 1: Diagrams showing the relevant potential energy curves, an illustration of the direct and sequential ionization processes and the evolution of the different wavepackets ($B^1\Sigma_u^+$ state as blue shape) at different time delays for the pump - probe scheme with 12.25 eV pulses. Column 2: Dissociative densities of ionization probability as a function of electron (x axis) and nuclear kinetic energy (y axis) in eV. Each row corresponds to a given time delay between the pulses. Columns 3−5: α, (equation 7.1.6), β (equation 7.1.7) and γ contributions (equation 7.1.7).

associated with the direct ionization process. In particular, the oscillations are produced by the interference between the wavepacket generated by the pump pulse and its exact delayed replica generated by the probe pulse in the dissociative ionic continuum. Taking into account the equation 7.1.6, these interferences are described by the expression $1 + \cos\{[E_f(v_f, \epsilon) - E_0]\tau/\hbar\}$, in terms of the final energy, and constitute the molecular analog of the Ramsey interferences in atoms [169, 45, 16, 75, 138, 176]. The oscillatory pattern given in molecules is two dimensional because, as was explained in the previous section, the two-photon absorbed energy, into the ionization thresholds, $DI = 18.15$ eV, is shared between the ejected electron and the remaining molecular ion energies, $E_f(v_f, \epsilon) = E_f(v_f) + E_f(\epsilon) = 2\omega + E_0 - DI$. Thus, the fully energy-differential distributions give a clear picture of the beatings among the final ionic states and, as we well see later, even the $E(v_f, \epsilon) - E_m(v_m)$ beatings among the final and intermediate vibronic states, contrary to the ionization yields, in which these

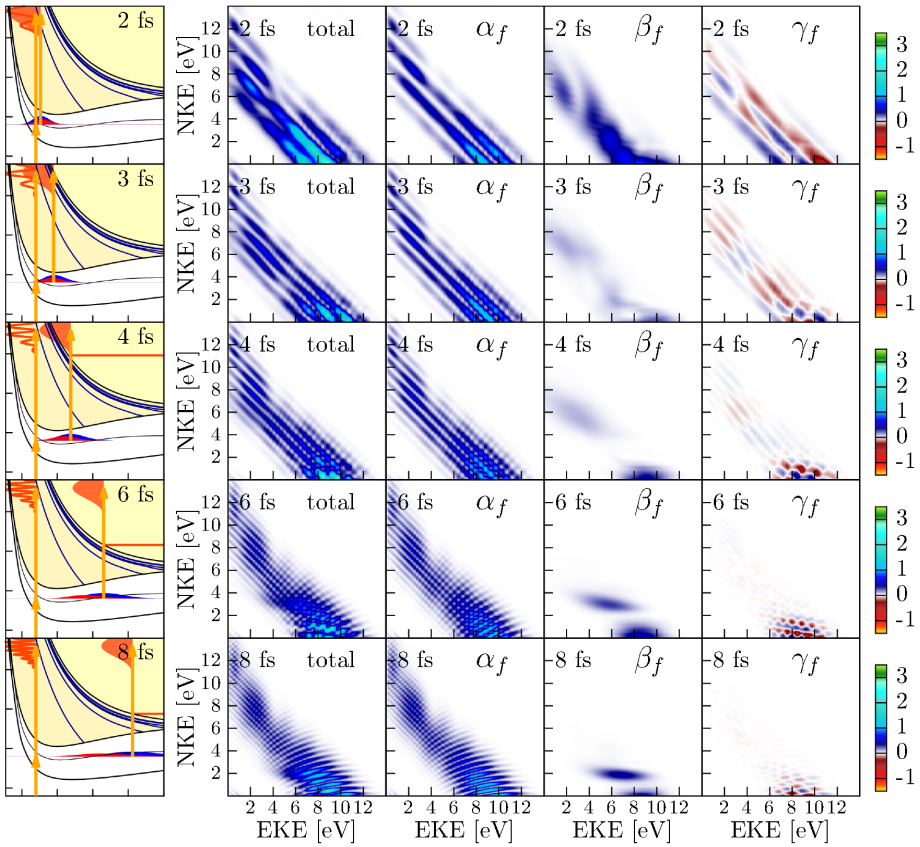

Figure 7.2.2: Column 1: Diagrams showing the relevant potential energy curves, an illustration of the direct and sequential ionization processes and the evolution of the different wavepackets ($B\,^1\Sigma_u^+$ state as blue shape and $B'\,^1\Sigma_u^+$ state as red shape) at different time delays for the pump - probe scheme with 14.0 eV pulses. Column 2: Dissociative densities of ionization probability as a function of electron (x axis) and nuclear kinetic energy (y axis) in eV. Each row corresponds to a given time delay between the pulses. Columns $3-5$: α, (equation 7.1.6), β (equation 7.1.7) and γ contributions (equation 7.1.7).

beatings are wiped out, because the fully energy-differential distributions are integrated over both electronic and nuclear energies. These beatings also do not appear clear in the FT analysis of the PKE and EKE distributions as a function of the time delay, where the integration is performed over either the electronic or nuclear energy, respectively, because the corresponding electronic or nuclear phases are averaged. In addition, note that for the 14.0 eV case, we can observe in figure 7.2.7 for the $2p\sigma_u$ threshold a feature with Ramsey oscillations at low electron and high proton kinetic energies, due to the α contribution, which does not appear in the 12.25 eV case. These features, as in the first ionization threshold, are consequence of the interference between the wavepacket generated by the pump pulse and its exact delayed replica generated by the probe pulse into the second ionic threshold, because the higher photon energy of the 14.0 eV pulse can reach energy regions in which the second threshold is populated by the "direct" ionization process from the ground state.

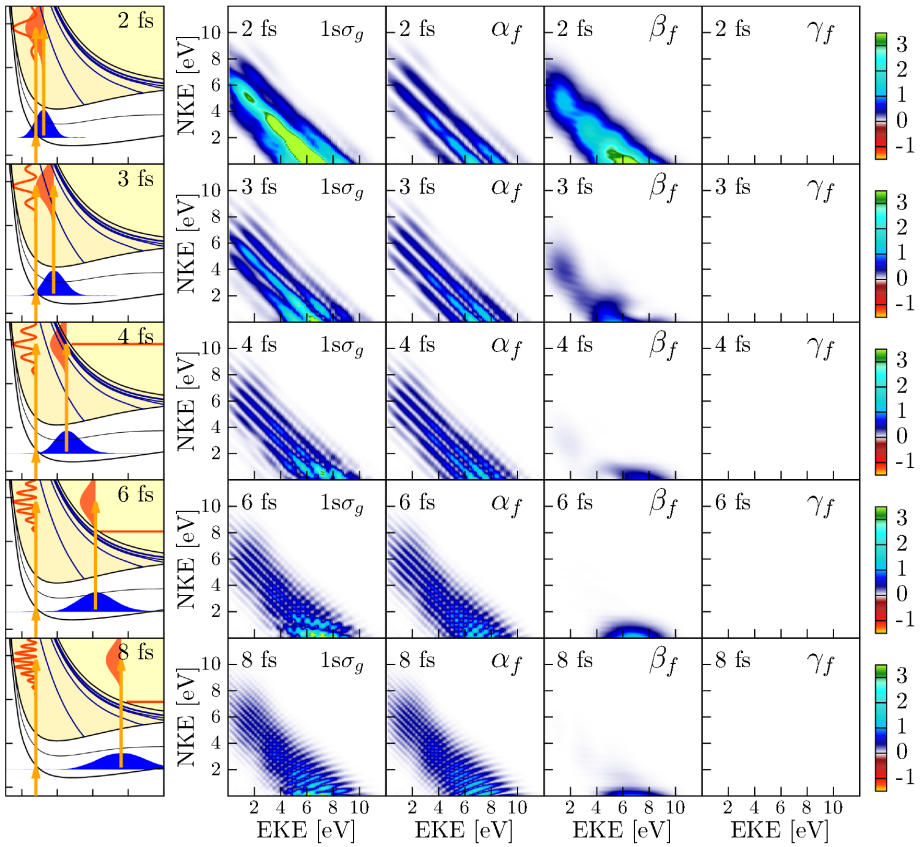

Figure 7.2.3: Same as in figure 7.2.1, for the dissociative densities of ionization probability in the $1s\sigma_g$ channel.

Following with the analysis of the different paths in the fully energy-differential distributions, for larger time delays than 4 fs it is clear the feature, which moves towards low proton and high electron kinetic energies when the time delay increases. This peak, also observed in the forth column, is a signal due to the β contribution associated with the "sequential" ionization process, through the intermediate vibronic states. At time delays equal to 4 fs, the vibrational wavepacket generated by the pump pulse into the $B\ ^1\Sigma_u^+$ state reaches internuclear distances around 2.5 a.u., where the photon absorption of the probe pulse can populate the second ionization channel, the $2p\sigma_u$ threshold. The motion of this vibrational wavepacket to larger internuclear distances, when the time delay increases, allows to reach vibrational states of this pure dissociative $2p\sigma_u$ state of lower energy, given ejected electron with higher kinetic energy due to the sharing of the same total energy, producing the characteristic motion of the feature observed in figures 7.2.1 and 7.2.6. This feature also appears for the 14.0 eV case, where the peak is also due to the vibrational wavepackets of $B\ ^1\Sigma_u^+$ intermediate states populated by the pump.

The purely dissociative form of the $2p\sigma_u$ PEC can be used to directly map the motion of the intermediate vibrational wavepacket as a function of the time delay, projecting the component of this ionic threshold from the fully energy-differential spectrum into the proton energy axis through the $2p\sigma_u$ PEC. This is the well-

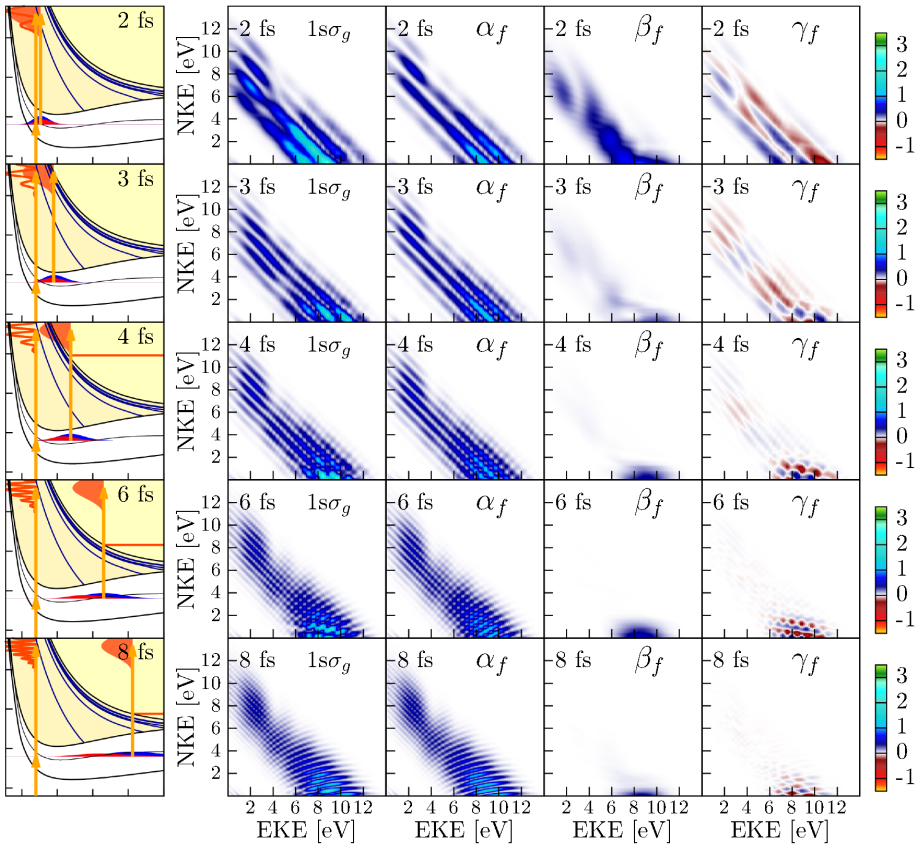

Figure 7.2.4: Same as in figure 7.2.2, for the dissociative densities of ionization probability in the $1s\sigma_g$ channel.

known reflection approximation, exposed in appendix C, where the photoionization transition amplitude, from the localized vibrational wavepacket, $\phi_n(R,t)$, (or in general a bound state) to a dissociative vibrational state of the final electronic continuum, $\chi_{f,v_f}(R)$, can be written as:

$$\int_0^\infty \chi_{f,v_f}(R)\, d(R)\, \psi_n(R,t)\, dR \simeq \int_{R_{inner}}^{R_{outer}} \left|\frac{dV_f(R)}{dR}\right|^{-1/2} \delta(R-R_c)\, d(R)\, \phi_n(R,t)\, dR = \\ = \left|\frac{dV_f(R)}{dR}\right|^{-1/2}_{R=R_c} d(R_c)\, \phi_n(R_c,t) \tag{7.2.1}$$

where R_{inner} and R_{outer} is the region of internuclear distances where $\phi_n(R,t)$ is localized, $d(R)$ is the electronic dipole transition element between the initial and the final states, given its expression in appendix C, and $d(R_c)$ is its value around the classical turning point R_c. Finally, we assume that $\chi_{f,v_f}(R)$ is an energy-normalized continuum vibrational function into an electronic state whose PEC, $V_f(R)$, is a pure dissociative curve. Using this formula, we can obtain by the projection of the probability in terms of the electronic and nuclear energies, the motion of the vibrational wavepacket in the electronic $B\ ^1\Sigma_u^+$ state. This signal generated by the vibrational wavepacket of the intermediate state into the final

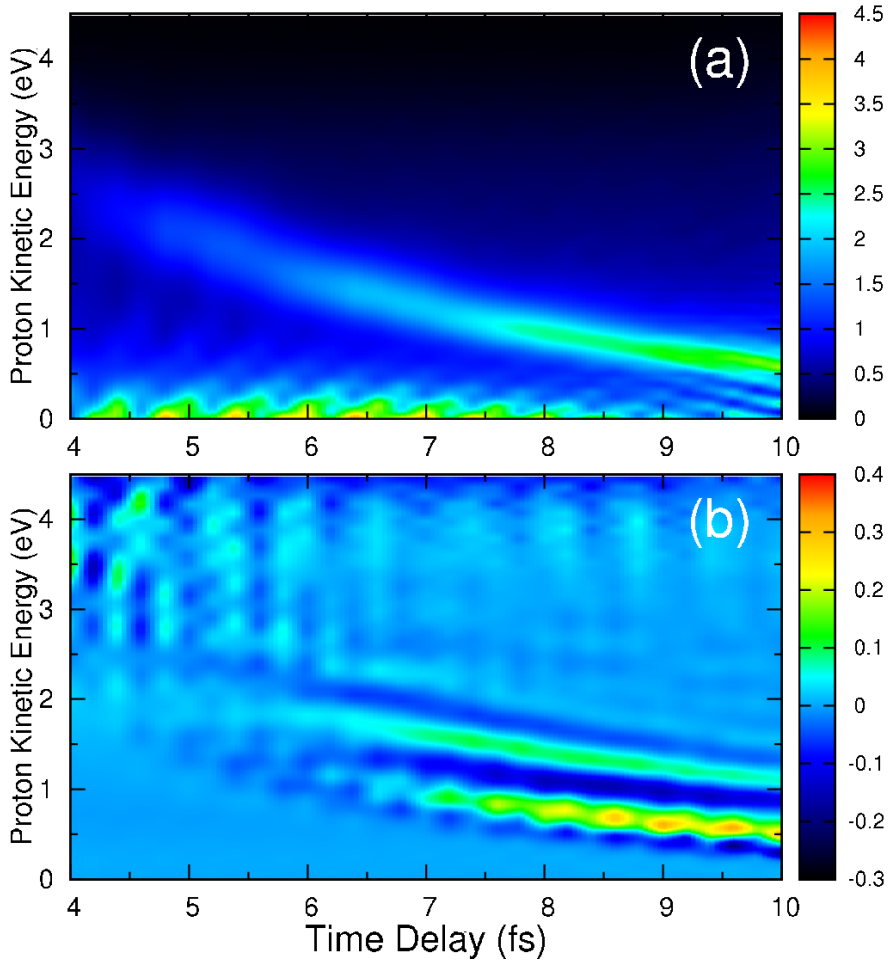

Figure 7.2.5: (a): Proton kinetic energy (PKE) distributions as a function of the time delay between both pulses for XUV pulses with an energy of 12.25 eV. (b): Asymmetry parameter of the ejected electron as a function of the PKE (y axis) and the time delay (x axis).

ionic channels also is appreciated in other observables, as in the PKE distributions as a function of the time delay, given in the upper panel of figure 7.2.5. However, as can be seen in that figure, the signal of the $2p\sigma_u$, presented as curves from high to lower proton energies, is obscured when the time delay increases by the direct ionization into the first ionization threshold, $1s\sigma_g$. This is increased in the experimental measurements, when the sampling used is not enough. In this way, we can use the PKE distribution resolved in space for the ejected electron (the proton energy-differential electron angular distributions), and more concrete its asymmetry parameter. As was explained in section 5.3, the population of the first and second ionization thresholds is produced from the ground state with a two-photon absorption process. Following the dipole selection rules, the final total symmetry, Σ_g, over both thresholds is the same. However, the different symmetry of the wavefunction for the residual ion, Σ_g for $1s\sigma_g$ and Σ_u for $2p\sigma_u$, produces that the partial waves of the ejected electron are even, $l = 0, 2, 4, \ldots$, or odd angular quantum numbers, $l = 1, 3, 5, \ldots$, respectively. The combination of both

threshold in the electron angular distributions produces that the different parity, g and u, of the ejected electron induces the asymmetries in the electron angular distributions. Using this, the lower panel of figure 7.2.5 shows the asymmetry parameter for the pump - probe scheme using 12.25 eV pulses. As it is clear, this asymmetry signal comes from the $2p\sigma_u$ threshold by the probe transition from the vibrational wavepacket of the $B\,^1\Sigma_u^+$ state. With this spectrum and using the equation 7.2.1, where the electronic dipole transition element, $d\,(R_c)$ can be considered constant, we can obtain the motion of the vibrational wavepacket by projection of the asymmetry parameter into the $2p\sigma_u$ PEC.

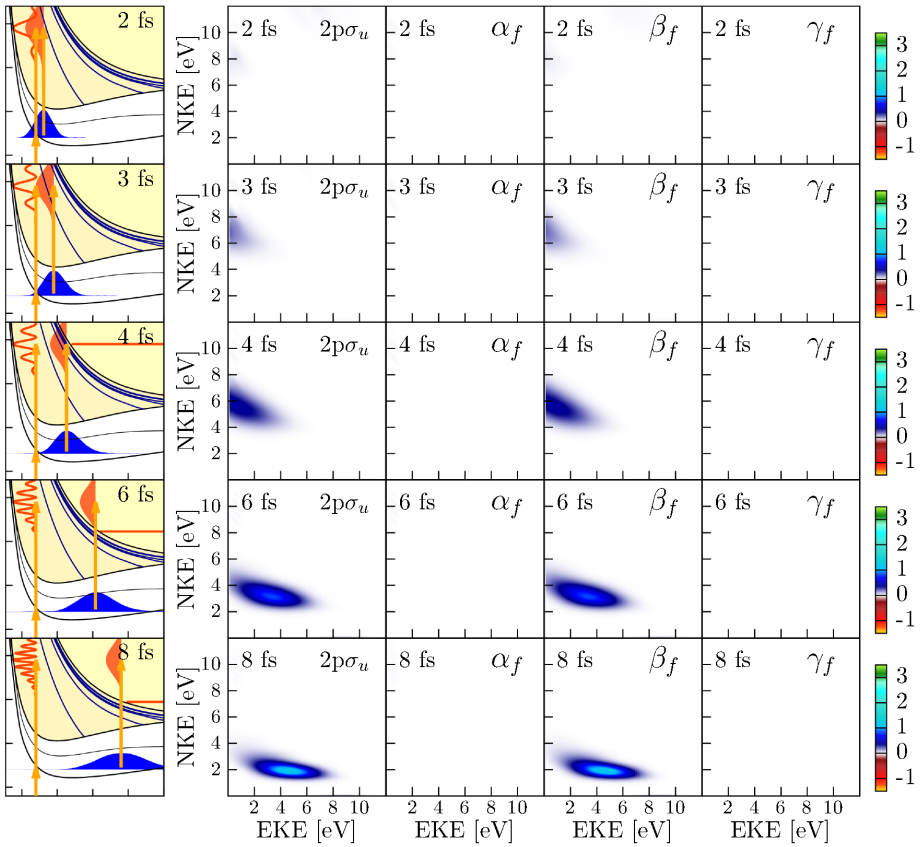

Figure 7.2.6: Same as in figure 7.2.1, for the dissociative densities of ionization probability in the $2p\sigma_u$ channel.

Coming back to the analysis of the β contribution in the electronic and nuclear energy-differential distributions, apart from the signal generated by the direct photoionization to the final ionic states, we can observe for the shortest time delay complex structure over the $1s\sigma_g$ threshold. This feature is a consequence of the autoinization of the Q_1 series of resonant states (doubly excited states) into the first threshold. As we commented in previous chapters, the resonant states are metastable states which decay into the continua as a function of their lifetimes. The typical lifetime for these states is much longer than the typical time for direct ionization and is comparable to the time needed by the nuclei to move significantly, in order of several fs. Because the similar timescales of the decay with the nuclear motion, the decay of the resonant states into the first threshold

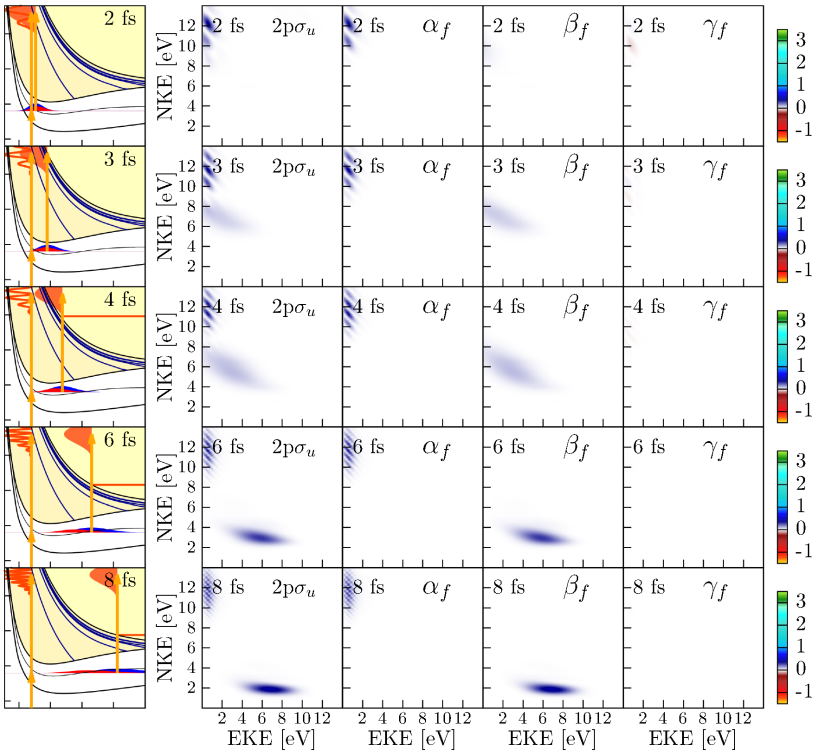

Figure 7.2.7: Same as in figure 7.2.2, for the dissociative densities of ionization probability in the $2p\sigma_u$ channel.

populates a wide range of proton and electron energies [57], given the complex structure observed in figures 7.2.3 and 7.2.4 for both pump - probe schemes with pulses of 12.25 eV and 14.0 eV. The left column of both figures shows the PEC of the six first $Q_1\,{}^1\Sigma_u$ states, which according to the dipole selection rules, are the only ones that can be populated by absorption of two photons. For very short time delay, around 2 fs, only the first $Q_1\,{}^1\Sigma_u$ state is accessible for the two-photon absorption process, being the unique state which contributes in the feature observed at this time delay. When the time delay increases to $4-5$ fs, the two-photon absorption through the intermediate states can be accessed to higher $Q_1\,{}^1\Sigma_u$ states, due to the motion of the intermediate vibrational wavepacket to larger internuclear distances. This makes that the features observed at this time delays are composed of the decay of several $Q_1\,{}^1\Sigma_u$ states. Finally, at larger time delays than 6 fs, the intermediate vibrational wavepacket evolves to internuclear distances where the transition from the intermediate to the $Q_1\,\Sigma_u$ states is not accessible for the probe pulse, until the vibrational wavepacket turns back in its periodic motion and reaches again the region of internuclear distances at which the transition to the $Q_1\,\Sigma_u$ states is possible.

Finally, the γ contribution presents positive and negative values as a function of the proton and electron energies, but these signals are several orders of magnitude smaller than the corresponding to the α and β contributions. The rapid oscillation of the pattern observed in the γ contribution with the time delay corresponds to the large value of the $E_m\,(v_m) - E_0$ phase from equation 7.1.8, giving oscillation

always around a mean value of zero. Consequently, the physical information contained in the γ contribution is not relevant with respect to the autoionization features.

The results obtained in the analysis of the electronic and nuclear energy-differential distributions, for both 12.25 eV and 14.0 eV pulses, suggest that one can extract the signature of autoionization using the model, developed by A. Palacios et al [128], for the decay of the resonant states presented in chapter 5. Although from a theoretical point of view the calculation of the β contribution in the first ionic threshold is direct, the separation on the different contributions of the experimental measure is not so easy. In this case, the Ramsey oscillations can be removed through the fully energy-differential distributions measured for the single pulse interaction with the molecular system, and later, using the simple formula $1 + \cos\left[E_f\left(v_f, \epsilon\right) - E_0\tau/\hbar\right]$ over the previous spectrum. For the β contribution into the second ionization threshold, they can be removed using the reflexion approximation into the vibrational wavepacket of the intermediate states, which can be obtained from the free evolution of the Franck-Condon projection of the initial vibrational state onto the vibrational states contained in the intermediate state PECs. Other way to obtain this wavepacket is through the projection of the asymmetry parameter, plotted in the lower panel of figure 7.2.5, over the $2p\sigma_u$ PEC. Finally, the γ contribution oscillates very rapidly around a mean value of zero. Thus, unless experimental energy resolution is large enough to see these oscillations, its contribution will be barely seen in the spectrum.

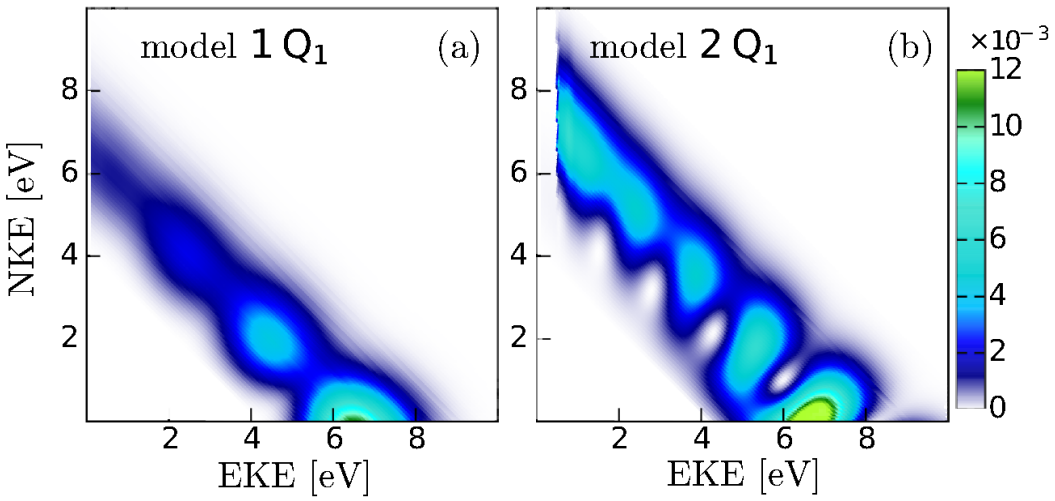

Figure 7.2.8: Densities of dissociative ionization probability as a function of electron (x axis) and nuclear kinetic energies (y axis) resulting from the semiclassical model. Left panel (a): Decay contribution into the first ionic threshold of the lowest $Q_1\ ^1\Sigma_g^+$ doubly excited state. Right panel (b): Same as the left panel for the second lowest $Q_1\ ^1\Sigma_g^+$ doubly excited state.

With the obtained final β contribution into the first ionization threshold, we can extract information about the autoinization dynamics. The model, presented in chapter 5, makes use of the phase difference between the classical paths followed

by the nuclei in the PEC associated with the direct ionization and autoionization. More specifically, the dissociative ionization probability is written [128]:

$$P\left(v_f,\epsilon\right)=\left|c_P\left(v_f,\epsilon\right)e^{\left(-i\theta_P\right)}e^{\left(-i\delta_c\right)}+\sum_k a_Q\left(v_f,\epsilon\right)e^{\left(-i\theta_Q\right)}\right|^2 \tag{7.2.2}$$

where $a_Q\left(v_f,\epsilon\right)$ is the amplitude to populate the k-th resonant state, $c_P\left(v_f,\epsilon\right)$ is the amplitude for direct ionization, θ_Q and θ_P are, respectively, the accumulated WKB phases in the PEC for the k-th resonant state and the $1s\sigma_g$ state of the residual ion and δ_c is an electronic phase. By using the PECs and autoionization widths reported in the literature [144], we have applied the above expression to identify the signature of the different resonances in the β contribution to the 2D ionization spectra. The results for the two lowest doubly excited states are plotted in figure 7.2.8. A comparison with the β contribution resulting from the *ab initio* calculations at zero time delay or the direct two-photon absorption from the ground, as well as any other time delay at which the pump and the probe pulses still overlap (time delay shorter than 2 fs) shows that the observed pattern corresponds to that of the lowest $Q_1\ \Sigma_u$ state. Following the chapter 5, a reasonable approximation to the variation of the lifetime with R could then be obtained by fitting the zero-delay doubly energy-differential distribution to equation 7.2.2, in which Γ_{Q_k} acts now as a parametric function.

The use of such a simple model opens the door to control the electronic and nuclear wavepackets associated with autoionization in the sub-fs time scale, when several doubly excited states contribute to the ionization yields. Indeed, by performing a fine scan of time delays in the interval between 0 fs and 4 fs, one could eventually see the subsequent population of higher resonances as a result of the vibrational wavepacket motion in the singly excited state. As this wavepacket moves towards larger internuclear distances, excitation to the second lowest, then third lowest, etc, resonant states is energetically possible by absorption of a single photon from the probe pulse. Thus, at specific values of the time delay, in the interval between 0 fs and 4 fs, one could a priori see the signature of specific resonance or combinations of them, allowing for control schemes similar to those described for the bound states of the molecule.

Conclusions

We have presented a theoretical study of the laser-molecule interaction in the hydrogen molecule (H_2), using different schemes. The simulations are performed solving the full dimensional TDSE, with all the electronic and nuclear degrees of freedom. In the spectral method used, our time dependent wavefunction is expressed as a linear combination of the eigenstates of the field-free hydrogen molecule. The vibronic (electronic and nuclear) eigenstates are obtained for the bound, resonant and ejected electron continuum states within the Born-Oppenheimer approximation and the Feshbach formalism. The corresponding eigenfunctions are calculated as antisymmetric products of the one-electron wavefunctions, which are expressed as a central expansion on spherical harmonics, using a B-spline basis set for the radial part.

We have explored different pump - probe schemes interacting with the hydrogen molecule. We aim to elucidate the role of the laser parameters (pulse duration, intensity, etc.), as well as the effects of the nuclear motion in the excitation and ionization processes. H_2 is used as a benchmark to unravel the fundamental physics and mechanism governing the different processes.

We have first investigated the autoionization process obtaining a time-resolved image of its decay in time. The analysis of the structure observed in the single (NKE) energy-differential distributions show a strong dependency with the pulse duration, specially in the energy region where appear the fingerprint of the resonant states. However, this variation of the features obtained is a pure numerical effect due to the average over the energy of one of the ejected particles for ultrashort pulses, which wash out part of the dynamical information. The fully energy-differential distributions, where all the fragments are measured in coincidence, show the same structure for different pulse durations. The effect of the pulse duration only reveal a certain energy region associated with the pulse bandwidth around the main diagonal for the total energy of the pulse.

The fingerprint leaved by autoionization does not present the well-known Fano-lineshapes observed in theoretical simulations for atoms and the hydrogen molecule within the FNA. However the features observed in the hydrogen molecule are also generated by a coherent superposition among the direct photoionization and autoionization paths into the same continuum states. To study the autoionization processes and its fingerprint in the final distributions, we compare with a semi-classical model discussed in [128]. This model is based on the well-established models for Penning ionization [91, 112], while also accounting for the presence of direct ionization, which interferes coherently with autoionization. We show that

this interference is responsible for the pronounced structures observed at low nuclear kinetic energies and is well-described by the phase accumulated along two classical paths followed by the nuclei. The observed interferences are thus found to be mainly governed by nuclear effects and fundamentally different from a Fano profile. The temporal build-up of these interferences has also been presented. The time evolution of the energy-differential apparent cross sections is found to be accurately represented within the semiclassical approach as well, as demonstrated by its excellent agreement with the solution of the TDSE. This evolution is again shown to be dominated by nuclear dynamics. The electronic decay rate $\Gamma(R)$ determines the amplitude of the contribution at a given nuclear kinetic energy, but the timing is determined by how long the nuclear wavepacket takes to accelerate to the given energy as it slides down the doubly excited states PEC, $V_Q(R)$.

Autoionization also leaves its fingerprint in the angular-resolved ejected electron photoionization spectrum. We analyzed the energy dependent of the asymmetry in the electron angular distributions as a function of the electron and proton kinetic energies, caused by the interference of both first ionic threshold of the H_2^+, $1s\sigma_g$ and $2p\sigma_u$, in the dissociative process. We found very good agreement between the experimental measurements, performed in Heidelberg laboratory by the group of Prof. J. Ullrich and Prof. Robert Moshammer, the semicalssical model developed by A. Palicios et al [128], and our theoretical simulations that fully accounts for the period of the oscillation and does so with very high accuracy. We found that the period observed in the asymmetry parameter as a function of the nuclear and electron energies are due to the interference between ionic channels with different parity of the ejected electron angular momentum for a given energy, associated to two ionic thresholds with different symmetry.

The characterization and control in the time domain of the autoionization process, can be accounted using a pump - probe scheme. To this purposed, we first presented the most traditional SAP XUV pump - IR probe scheme. At such intensities, most features observed in the NKE and fully energy-differential ionization distributions as a function of the time delay between the pulses can be explained in terms of transitions involving a single XUV photon and up to three IR photons. We have shown that:

- For time delays smaller than around -2 fs, the IR arrives before than the XUV and the distributions obtained are the same than the obtained with an isolated XUV pulse, because autoionization takes place after the IR interacts with the system.

- For time delays longer than before but less than around 4 fs, autoionization is suppressed due to absorption of IR photons from the doubly excited states populated by the XUV pulse. This is possible because the IR photons are absorbed before the doubly excited states autoionize.

- For longer time delays, autoionization occurs before the IR field arrives, and the distributions obtained have the usual pattern observed in the one-photon ionization.

We have also shown that the streaking signal of the photoelectron follows the IR field when electrons ejected in both dissociative ($H + H^+ + e^-$) and non-dissociative ($H_2^+ + e^-$) ionization channels are not resolved. However, this is no longer true for the streaking signal associated to the dissociative ionization channel, since the presence of autoionizing states destroys the simple streaking picture based on the single active electron approximation. This opens the question about how to extract ionization times from the streaking signal when autoionization is present. To answer this question further investigations are required.

Apart of this, a XUV pump - IR probe scheme have been used to follow the nuclear motion into different single excited states of H_2. The simulations obtained in H_2 using an XUV APT with and an IR as the pump and a second IR pulse as the probe were compared with the experimental measurements performed by the group of Prof. M. Murname and H. Kapteyn in JILA (USA). The interference of electronic wavepackets excited by the XUV and IR laser fields can be used to control excitation and ionization on attosecond timescales while maintaining good energy resolution and state selectivity. Selective bond-breaking is achieved by controlling the excitation wavelength as well as the time delay between the pump and probe pulses. We also observe and characterize the periodicity of the nuclear wavepacket generated into the $B\,^1\Sigma_u^+$ and $EF\,^1\Sigma_g^+$ states, especially focusing on the nuclear wavepacket tunneling in the double-well of the $EF\,^1\Sigma_g^+$ PEC.

In contrast with the above pump - probe schemes, where the probe field drives the dynamics of the systems, the XUV pump - XUV probe scheme constitutes the state-of-art techniques to explore the vibronic (vibrational and electronic) dynamics of the system without significant distortions introduced by the IR probe in the PEC. Our analysis is based on an accurate solution of the TDSE for the hydrogen molecule and on the use of a 2^{nd} order approximation that allows one to extract the relevant dynamical information from the theoretical simulations as well as in a real experiment. The key point in this scheme is the use of two identical XUV pulses, which build up a molecular interferometer based on "direct" and "sequential" two-photon ionization processes leading to the same final states. The use of identical pulses also simplifies its experimental implementation. Total (dissociative) ionization yields provide information about the amplitudes and phases (energy beatings) that build up the vibronic wavepacket created by the pump pulse but not about the wavepacket created by the probe pulse. Information about the latter wavepacket can only be retrieved from fully energy-differential distributions, where one needs to measure all ejected charged particles in coincidence. The resulting fully energy-differential distributions provides the necessary energy resolution to analyze all of the final states populated by the probe pulse, and the only limiting factor being the energy resolution of the detectors. Time resolution comes from recording these fully energy-differential distributions as a function of time delay.

The investigated dynamics result from the coherent superposition of vibronic states associated with the various electronic states populated by the XUV pump pulse. Although this coherent superposition evolves in time, thus generating a coupled electronic plus nuclear wavepacket, population of the different states does

not vary with time. Then the use of another XUV pulse to probe the system, in combination with the interpretation scheme as that described in chapter 7, should also allow one to reveal the variations of the intermediate state populations with time. Finally, although this study has been restricted to the H_2 molecule, a similar scheme can be applied to more complex molecules, i.e. to investigate and control the dynamics through conical intersections [153].

Conclusiones

Nosotros hemos presentado un estudio teórico de la interacción láser-molécula en la molécula de hidrógeno (H_2), usando diferentes esquemas láser. Las simulaciones son llevadas a cabo resolviendo la TDSE, incluyendo todos los grados de libertad electrónicos y nucleares. En el método espectral usado, nuestra función de onda dependiente del tiempo es expresada como una combinación lineal de los estados propios de la molécula de hidrógeno sin la interacción con el campo. Los estados propios vibrónicos (electrónicos y nucleares) son obtenidos para estados ligados, resonantes y del continuo del electrón eyectado dentro de la aproximación de Born-Oppenheimer y del formalismo Feshbach. Las correspondientes funciones propias son calculadas como productos antisimétricos de dos funciones de onda para un electrón, las cuales son expresadas como un expansión central en armónicos esféricos, usando un conjunto de funciones de base de B-splines para la parte radial.

Nosotros hemos explorado diferentes esquemas pump - probe interaccionando con la molécula de hidrógeno. Nosotros pretendemos elucidar el rol que juegan los parámetros del láser (duración del pulso, intensidad, etc.) así como los efectos del movimiento nuclear en los procesos de excitación e ionización. El H_2 es usado como estándar de comparación para resolver los mecanismos y los fundamentos físicos que gobiernan los diferentes procesos.

Primero hemos investigado el proceso de autoionización obteniendo la imagen temporal de su decaimiento. El análisis de la estructura observada en la distribuciones diferenciales energéticas de la energía cinética nuclear (NKE) muestran una fuerte dependencia con la duración del pulso, especialmente en la región energética donde aparecen la huella dactilar del decaimiento de los estados resonantes. Sin embargo, esta variación de las señales obtenidas es un efecto puramente numérico debido al promedio sobre la energía de una de la partículas eyectadas por pulsos ultracortos, que difuminan parte de la información dinámica. En este sentido, las distribuciones diferenciales energéticas completas, donde todos los fragmentos son medidos en coincidencia, muestran la misma estructura para diferentes duraciones del pulso. El efecto de la duración del pulso es revelar solo una cierta región energética asociada al ancho de banda del pulso alrededor de la diagonal principal para la energía total asociada a la energía del pulso.

La señal dejada por la autoionización no presenta las bien conocidas estructuras de Fano observadas en las simulaciones teóricas para átomos y la molécula de hidrógeno dentro de la aproximación de núcleos fijos (FNA). Sin embargo, las características observadas en la molécula de hidrógeno son también generadas

por una superposición coherente entre los caminos de fotoionización directa y la autoionización en los mismos estados del continuo. Para estudiar los procesos de autoionización y su señal en las distribuciones finales, nosotros comparamos con un modelo semiclásico presentado en [128]. Este modelo está basado en los bien establecidos modelos para la ionización de Penning [91, 112], teniendo en cuenta también la presencia de la ionización directa, que interfiere coherentemente con la autoionización. Nosotros mostramos que esta interferencia es responsable de las estructuras pronunciadas observadas a bajas energías cinética nuclear y es bien descrita por la fase acumulada a lo largo de los dos caminos clásicos seguidos por el movimiento de los núcleos. De esta manera, las señales encontradas son principalmente gobernadas por los efectos nucleares y son fundamentalmente diferentes al perfil de Fano. Además, la construcción temporal de estas interferencias ha sido también presentada. La evolución temporal de las secciones eficaces aparentes diferenciales en energía son obtenidas de manera precisa con el modelo semiclásico, como demostramos por su excelente acuerdo con la solución de la TDSE. Esta evolución, otra vez muestra la predominancia de la dinámica nuclear. En este sentido, la tasa de decaimiento, $\Gamma(R)$, determina la amplitud de la contribución a una energía cinética nuclear dada, pero el tiempo es determinado por cuanto le toma al paquete de ondas nuclear acelerar hasta la energía dada, deslizándose por la curva de energía potencial de los estados doblemente excitados, $V_Q(R)$.

La autoionización también deja su señal en el espectro de fotoionización del electrón eyectado resuelto angularmente. Nosotros analizamos la dependencia energética de la asimetría en las distriuciones del electrón eyectado en función de las energía del electrón y del protón, causadas por la interferencia de los dos primeros límites iónicos del H_2^+, el $1s\sigma_g$ y el $2p\sigma_u$, en el proceso de disociación. Nosotros encontramos un gran acuerdo entre las mediadas experimentales, realizadas en el Laboratorio de Heidelberg por el grupo de los Profesores J. Ullrich and Robert Moshammer, el modelo semiclásico desarrollado por A. Palacios y colaboradores [128], y nuestras simulaciones teóricas que representan completamente los periodos de la oscilación y lo hacen con una gran exactitud. Finalmente, encontramos que el periodo observado en el parámetro de asimetría en función de las energías nuclear y electrónica es debido a la interferencia entre canales iónicos con diferente paridad del momento angular del electrón eyectado para una energía dada, debido a que proceden de limites iónicos de diferente simetría.

La caracterización y control en el dominio temporal del proceso de autoionización puede se obtenida usando un esquema pump - probe. Para este propósito, primero presentamos el esquema XUV pump - IR probe más tradicional. A esas intensidades, muchas de las características observadas en las distribuciones de NKE y diferenciales en la energía de ambas partículas en función del retraso temporal entre los pulsos pueden ser explicadas en términos de las transiciones que involucran la absorción de un fotón XUV y uno a tres fotones de IR. Nosotros hemos observado que:

- Para separaciones temporales menores a alrededor de $-2\,\mathrm{fs}$, el IR llega antes que el XUV y por lo tanto la distribución obtenida es la misma que la obtenida con un pulso XUV aislado, porque la autoionización tiene lugar

después que el IR interaccione con el sistema.

- Para separaciones temporales mayores que la anterior pero menores a alrededor de 4 fs, la autoionización es suprimida debido a la absorción de fotones de IR desde los estados doblemente excitados poblados por el pulso XUV. Esto es posible porque los fotones de IR son absorbidos antes de la autoionización de los estados doblemente excitados.

- Para separaciones de tiempo mayores, la autoionización ocurre antes que el campo IR llegue, y las distribuciones obtenidas tienen el patrón usual observado en la ionización con un fotón.

Nosotros también hemos mostrado que las señales de streaking del fotoelectrón siguen el campo IR cuando los electrones eyectados en ambos canales de ionización disociativa ($H + H^+ + e^-$) y no disociativa ($H_2^+ + e^-$) no son resueltos angularmente. Sin embargo, esto no se cumple para la señal del streaking asociada al canal de ionización disociativa, debido a que la presencia de los estado autoionizantes destruyen la imagen simple del streaking basada en la aproximación de un solo electrón activo (SAE). Esto genera la pregunta sobre como extraer los tiempos de ionización de la señal de streaking cuando la autoionización está presente. Para responder a esta cuestión, son necesarias futuras investigaciones.

Aparte de esto, el esquema XUV pump - IR probe ha sido usado para seguir el movimiento nuclear in los diferentes estados simplemente excitados del H_2. Las simulaciones obtenidas en el H_2 usando un tren de pulsos de attosegundo de energía XUV con un IR como el pump y un segundo IR como el probe fueron comparadas con las medidas experimentales realizadas por el grupo de los Profesores M. Murname y H. Kapteyn en JILA (USA). Las interferencias de los paquetes de ondas electrónicos excitados por los campos láser XUV e IR pueden ser usados para controlar la excitación e ionización en escalas de tiempo de attosegundos mientras mantenemos una buena resolución energética y una selectividad de los estados poblados. La selectividad en la ruptura de enlaces es alcanzada por el control de la longitud de onda usada en la excitación así como por la separación temporal entre los pulsos pump y probe. Nosotros también observamos y caracterizamos la periodicidad de los paquetes de onda nucleares generados en los estados $B\,^1\Sigma_u^+$ and $EF\,^1\Sigma_g^+$, especialmente centrándonos en el tuneleo del paquete de ondas nuclear en el doble pozo de la curva de energía potencial del estado $EF\,^1\Sigma_g^+$.

En contraste con el anterior esquema pump - probe, donde el campo probe conduce la dinámica del sistema, los esquemas XUV pump - XUV probe constituyen las técnicas más avanzadas para explorar la dinámica vibrónica (electrónica y nuclear) del sistema sin distorsiones significativas en las curvas de energía potencial introducidas por el IR probe. Nuestro análisis está basado en una solución precisa de la TDSE para la molécula de hidrógeno y en el uso de una aproximación de segundo orden que permite a uno extraer la información dinámica relevante tanto desde las simulaciones teóricas como en un experimento real. La clave de este esquema es el uso de dos pulsos XUV idénticos, que construyen un interferómetro

molecular basado en los procesos de ionización de dos fotones "directa" y "secuencial" que dejan en los mismos estados finales. El uso de pulsos idénticos también simplifica su implementación experimental. Los rendimientos de ionización (disociativa) aportan información sobre las amplitudes y fases (beatings electrónicos) que construyen el paquete de ondas vibrónico creado por el pulso pump pero no sobre el paquete de ondas creado por el pulso probe. La información sobre este último paquete de ondas solo puede ser rescatada desde las distribuciones diferenciales en energía para todas partículas, donde uno necesita medir todas todas las partículas eyectadas en coincidencia. Las distribuciones diferenciales en energía para todas las partículas eyectadas resultantes aportan la suficiente resolución energética para analizar todos los estados final poblados por el pulso probe, siendo el único factor limitante la resolución energética del detector. La resolución temporal viene dada desde la captación de estas distribuciones diferenciales en energía para todas las partículas eyectadas en función del retraso temporal entre los pulsos.

La dinámica investigada resulta de la superposición coherente de estados vibracionales asociados con varios estados electrónicos poblados por el pulso pump de energía XUV. Aunque esta superposición coherente evoluciona en el tiempo, generando un paquete de ondas nuclear y electrónico acoplado, la población de los diferentes estados no varia con el tiempo. Por lo tanto, el uso de otro pulso XUV para probar el sistema, en combinación con la interpretación del esquema descrito en el capítulo 7, debería también permitirnos desentrañar la variación de las poblaciones de los estados intermedios con el tiempo. Finalmente, aunque este estudio ha sido realizado en la molécula de H_2, un esquema similar puede ser aplicado a moléculas más complejas, como por ejemplo para investigar y controlar la dinámica a través de las intersecciones cónicas [153].

Appendix A

Maxwell's equations and gauge invariance

The equations whose solutions describe the time and spatial evolution of the electromagnetic fields in classical electrodynamics are the well-known Maxwell's equations:

$$\nabla \cdot \mathbf{B}(\mathbf{r}, t) = 0 \tag{A.0.1}$$

$$\nabla \cdot \mathbf{E}(\mathbf{r}, t) = \frac{\rho(\mathbf{r}, t)}{\varepsilon_0} \tag{A.0.2}$$

$$\nabla \times \mathbf{E}(\mathbf{r}, t) + \frac{\partial \mathbf{B}(\mathbf{r}, t)}{\partial t} = \mathbf{0} \tag{A.0.3}$$

$$\nabla \times \mathbf{B}(\mathbf{r}, t) - \mu_0 \varepsilon_0 \frac{\partial \mathbf{E}(\mathbf{r}, t)}{\partial t} = \mu_0 \mathbf{J}(\mathbf{r}, t) \tag{A.0.4}$$

where $\mathbf{E}(\mathbf{r}, t)$ is the electric field vector, $\mathbf{B}(\mathbf{r}, t)$ is the magnetic field vector, $\rho(\mathbf{r}, t)$ is the charge density and $\mathbf{J}(\mathbf{r}, t)$ is the current density vector. ε_0 is an electric constant, called vacuum permittivity or permittivity of free space, and μ_0 is an magnetic constant, called vacuum permeability or permeability of free space. $\nabla\cdot$ is the divergence of any vector and $\nabla\times$ is the rotational of any vector. To solve the Maxwell's equations, it is useful to introduce two physical magnitudes which are the vector potential, $\mathbf{A}(\mathbf{r}, t)$, and the scalar potential, $\phi(\mathbf{r}, t)$. The definition of the vector potential, $\mathbf{A}(\mathbf{r}, t)$, is that its rotational is equal to the magnetic field vector, $\mathbf{B}(\mathbf{r}, t)$:

$$\mathbf{B}(\mathbf{r}, t) = \nabla \times \mathbf{A}(\mathbf{r}, t) \tag{A.0.5}$$

This definition satisfies the first Maxwell equation A.0.1, because the divergence of the rotational of any vector, $\mathbf{V}(\mathbf{r}, t)$, is equal to zero, $\nabla \cdot [\nabla \times \mathbf{V}(\mathbf{r}, t)] = 0$. On the other hand, the definition of the scalar potential, $\phi(\mathbf{r}, t)$, is that the rotational of its gradient is equal to the zero vector:

$$\nabla \times [\nabla \phi (\mathbf{r}, t)] = \mathbf{0} \tag{A.0.6}$$

To express the electric field vector, $\mathbf{E}(\mathbf{r}, t)$, in terms of the vector potential, $\mathbf{A}(\mathbf{r}, t)$, and the scalar potential, $\phi(\mathbf{r}, t)$, equation A.0.5 is introduced in the equation A.0.3. Knowing that the gradient, ∇, does not depend on the time, it is obtained the equation:

$$\nabla \times \left[\mathbf{E}(\mathbf{r}, t) + \frac{\partial \mathbf{A}(\mathbf{r}, t)}{\partial t} \right] = \mathbf{0} \tag{A.0.7}$$

This equation and equation A.0.6 are equal to the zero vector. Consequently, equation A.0.6, which define the scalar potential, can be introduced in this above equation, obtaining:

$$\nabla \times \left[\mathbf{E}(\mathbf{r}, t) + \nabla \phi (\mathbf{r}, t) + \frac{\partial \mathbf{A}(\mathbf{r}, t)}{\partial t} \right] = \mathbf{0} \tag{A.0.8}$$

To satisfy that the rotational is equal to the zero vector in the above equation, the term inside the brackets has to be equal to the zero vector. Therefore, the electric field vector, $\mathbf{E}(\mathbf{r}, t)$, defined in terms of the vector potential, $\mathbf{A}(\mathbf{r}, t)$, and the scalar potential, $\phi(\mathbf{r}, t)$, is:

$$\mathbf{E}(\mathbf{r}, t) = -\nabla \phi (\mathbf{r}, t) - \frac{\partial \mathbf{A}(\mathbf{r}, t)}{\partial t} \tag{A.0.9}$$

On the other hand, the Maxwell's equations A.0.3 and A.0.4 can be written in terms of the vector potential, $\mathbf{A}(\mathbf{r}, t)$, and the scalar potential, $\phi(\mathbf{r}, t)$, introducing equations A.0.5 and A.0.9 in them:

$$-\nabla \cdot \nabla \phi (\mathbf{r}, t) - \nabla \cdot \frac{\partial \mathbf{A}(\mathbf{r}, t)}{\partial t} = \frac{\rho(\mathbf{r}, t)}{\varepsilon_0} \tag{A.0.10}$$

$$\nabla \times [\nabla \times \mathbf{A}(\mathbf{r}, t)] + \mu_0 \varepsilon_0 \frac{\partial \nabla \phi (\mathbf{r}, t)}{\partial t} + \mu_0 \varepsilon_0 \frac{\partial^2 \mathbf{A}(\mathbf{r}, t)}{\partial t^2} = \mu_0 \mathbf{J}(\mathbf{r}, t) \tag{A.0.11}$$

where the rotational of the rotational of the vector potential, $\nabla \times [\nabla \times \mathbf{A}(\mathbf{r}, t)]$, can be develop as:

$$\nabla \times [\nabla \times \mathbf{A}(\mathbf{r}, t)] = \nabla \cdot [\nabla \cdot \mathbf{A}(\mathbf{r}, t)] - \nabla^2 \mathbf{A}(\mathbf{r}, t) \tag{A.0.12}$$

Using this identity, the Maxwell's equations A.0.3 and A.0.4 in terms of the vector potential, $\mathbf{A}(\mathbf{r}, t)$, and the scalar potential, $\phi(\mathbf{r}, t)$, can be written as:

$$-\nabla^2 \phi (\mathbf{r}, t) - \nabla \cdot \frac{\partial \mathbf{A}(\mathbf{r}, t)}{\partial t} = \frac{\rho(\mathbf{r}, t)}{\varepsilon_0} \tag{A.0.13}$$

$$\nabla \cdot [\nabla \cdot \mathbf{A}(\mathbf{r},t)] - \nabla^2 \mathbf{A}(\mathbf{r},t) + \mu_0 \varepsilon_0 \frac{\partial \nabla \phi(\mathbf{r},t)}{\partial t} + \\ + \mu_0 \varepsilon_0 \frac{\partial^2 \mathbf{A}(\mathbf{r},t)}{\partial t^2} = \mu_0 \mathbf{J}(\mathbf{r},t) \tag{A.0.14}$$

When the Maxwell's equations are defined in terms of the vector potential, $\mathbf{A}(\mathbf{r},t)$, and the scalar potential, $\phi(\mathbf{r},t)$, the solutions of these physical magnitudes contain an indeterminacy. This indeterminacy is introduced because the electric field vector, $\mathbf{E}(\mathbf{r},t)$, and the magnetic field vector, $\mathbf{B}(\mathbf{r},t)$, are associated with vector potential, $\mathbf{A}(\mathbf{r},t)$, and the scalar potential, $\phi(\mathbf{r},t)$, .through their gradients or their time derivatives. However, the indeterminacy does not affect the electric and magnetic field vector, $\mathbf{E}(\mathbf{r},t)$ and $\mathbf{B}(\mathbf{r},t)$, respectively. To probe this property, it is defined two new vector and scalar potentials, $\mathbf{A}'(\mathbf{r},t)$ and $\phi'(\mathbf{r},t)$, which are associated with the original vector and scalar potentials, $\mathbf{A}(\mathbf{r},t)$ and $\phi(\mathbf{r},t)$, through the gauge transformations:

$$\mathbf{A}'(\mathbf{r},t) = \mathbf{A}(\mathbf{r},t) + \nabla \lambda(\mathbf{r},t) \tag{A.0.15}$$

$$\phi'(\mathbf{r},t) = \phi(\mathbf{r},t) - \frac{\partial \lambda(\mathbf{r},t)}{\partial t} \tag{A.0.16}$$

This scalar function, $\lambda(\mathbf{r},t)$, is any arbitrary function. we define a new magnetic field vector, $\mathbf{B}'(\mathbf{r},t)$, which depends on the new vector potential, $\mathbf{A}'(\mathbf{r},t)$, and satisfies the equation A.0.5. Introducing equation A.0.15 in the definition of the new magnetic field vector, $\mathbf{B}'(\mathbf{r},t)$, given in equation A.0.5, it is obtained:

$$\mathbf{B}'(\mathbf{r},t) = \nabla \times \mathbf{A}'(\mathbf{r},t) = \nabla \times \mathbf{A}(\mathbf{r},t) + \nabla \times [\nabla \lambda(\mathbf{r},t)] \tag{A.0.17}$$

As it was explained, the rotational of the gradient of any scalar function is equal to the zero vector. Consequently, the new magnetic field vector, $\mathbf{B}'(\mathbf{r},t)$, satisfies:

$$\mathbf{B}'(\mathbf{r},t) = \nabla \times \mathbf{A}(\mathbf{r},t) = \mathbf{B}(\mathbf{r},t) \tag{A.0.18}$$

This equation demonstrates that the new magnetic field vector, $\mathbf{B}'(\mathbf{r},t)$, is equal to the original magnetic field vector, $\mathbf{B}(\mathbf{r},t)$, and consequently, the indeterminacy does not affect to the magnetic field vector, $\mathbf{B}(\mathbf{r},t)$. Focusing on the electric field vector, $\mathbf{E}(\mathbf{r},t)$, we can define a new electric field vector, $\mathbf{E}'(\mathbf{r},t)$, which satisfies the equation A.0.9. Substituting equations A.0.15 and A.0.16 in equation A.0.9, the new electric field vector, $\mathbf{E}'(\mathbf{r},t)$, with respect to the original vector potential, $\mathbf{A}(\mathbf{r},t)$, and scalar potential, $\phi(\mathbf{r},t)$, is:

$$\mathbf{E}'(\mathbf{r},t) = -\nabla \phi'(\mathbf{r},t) - \frac{\partial \mathbf{A}'(\mathbf{r},t)}{\partial t} = -\nabla \phi(\mathbf{r},t) + \frac{\partial \nabla \lambda(\mathbf{r},t)}{\partial t} - \\ - \frac{\partial \mathbf{A}(\mathbf{r},t)}{\partial t} - \frac{\partial \nabla \lambda(\mathbf{r},t)}{\partial t} = -\nabla \phi(\mathbf{r},t) - \frac{\partial \mathbf{A}(\mathbf{r},t)}{\partial t} = \mathbf{E}(\mathbf{r},t) \tag{A.0.19}$$

As the magnetic field vector, $\mathbf{B}(\mathbf{r},t)$, the above equation demonstrates that the new electric field vector, $\mathbf{E}'(\mathbf{r},t)$, is equal to the original electric field vector,

$\mathbf{E}(\mathbf{r},t)$. We obtained that both electric and magnetic field vectors, $\mathbf{E}(\mathbf{r},t)$ and $\mathbf{B}(\mathbf{r},t)$, do not change with the indeterminacy introduced by the vector and scalar potentials, $\mathbf{A}(\mathbf{r},t)$ and $\phi(\mathbf{r},t)$. Consequently, the electric and magnetic field vectors, $\mathbf{E}(\mathbf{r},t)$ and $\mathbf{B}(\mathbf{r},t)$, are invariant with the gauge transformation. This invariance indicates that we can remove the indeterminacy introduced in the solutions of the Maxwell's for the vector and scalar potentials, $\mathbf{A}(\mathbf{r},t)$ and $\phi(\mathbf{r},t)$, using the boundary conditions, called gauge, without affecting the physical description of the electromagnetic field.

Appendix B

Gauss-Legendre evaluation for randomly oriented molecules

The general expression for the density of probability as a function of the nuclear and electronic kinetic energies averaged over all possible orientations of the electromagnetic field with respect to the molecular axis, is:

$$\frac{dP^{l,m}_{\alpha,v_\alpha}(t;\varepsilon)}{dv_\alpha d\varepsilon} = \frac{1}{4\pi}\int_0^{\pi}\int_0^{2\pi} \left|c^{l,m}_{\alpha,v_\alpha}(t,\theta;\varepsilon)\right|^2 \sin(\theta)\, d\theta d\varphi \tag{B.0.1}$$

where using the variable transformation $x = -\cos(\theta)$, the above equation becomes:

$$\frac{dP^{l,m}_{\alpha,v_\alpha}(t;\varepsilon)}{dv_\alpha d\varepsilon} = \frac{1}{2}\int_{-1}^{1} \left|c^{l,m}_{\alpha,v_\alpha}(t,\arccos(-x);\varepsilon)\right|^2 dx \tag{B.0.2}$$

The above integral can be resolved by any numerical integration method. In this way, the interval of definition of the sine function allows us to use Gaussian quadrature methods, which select the points in the interval $[-1,1]$ for the optimal integration. Specially, the Gaussian-Legendre quadrature [1, 117] is based on express the integrated function as the product of an approximately polynomial, $P_n(x)$, multiplied by a weight function, $\omega(x)$:

$$\int_{-1}^{1} f(x)\, dx = \int_{-1}^{1} \omega(x)\, P_n(x)\, dx \simeq \sum_{i=1}^{n} \omega(x_i)\, P(x_i) \tag{B.0.3}$$

The number of evaluation points, x_i, and weights, $\omega(x_i)$, used in the integration is equal to the number of the order of the Legendre polynomials used. The evaluation points, x_i, are the values in which the Legendre polynomials are zero, and the weights are given by the general expression:

$$\omega(x_i) = \frac{2}{(1-x_i^2)\left|\frac{dP_n(x)}{dx}\right|^2_{x=x_i}} \tag{B.0.4}$$

Using this method, the density of probability as a function of the nuclear and electronic kinetic energies integrated over all possible orientations becomes:

$$\frac{dP^{l,m}_{\alpha,v_\alpha}(t;\varepsilon)}{dv_\alpha d\varepsilon} \simeq \frac{1}{2}\sum_{i=1}^{n}\omega(x_i)\left|c^{l,m}_{\alpha,v_\alpha}(t,\arccos(-x_i);\varepsilon)\right| \tag{B.0.5}$$

As example, we can take a seven order Legendre polynomials, given the weights and evaluation positions:

i	x_i	θ_i [rad]	$\omega(x_i)$
1	-0.9491079123427585	0.32040509	0.1294849661688697
2	-0.7415311855993945	0.735446614	0.2797053914892766
3	-0.4058451513773972	1.152892954	0.3818300505051189
4	0.0	1.570796327	0.4179591836734694
5	0.4058451513773972	1.9886997	0.3818300505051189
6	0.7415311855993945	2.406146039	0.2797053914892766
7	0.9491079123427585	2.821187563	0.1294849661688697

where only with the simulations obtained for this seven values of θ_i and the above weights we can calculate the electronic and nuclear energy-differential probability distributions integrated over all possible orientations. In addition, in the case of the homonuclear diatomic molecules, the symmetry plane perpendicular to the molecular axis and which contains the inversion center, makes that the negative values of x_i give the same time dependent coefficients than their respective positive values, and consequently, it is only necessary calculate to 4 values of x_i, corresponding to the positives or negatives values plus the 0.0.

Appendix C

The WKB and the reflection approximation

The WKB approximation

The WKB approximation is based on the semiclassical solution of the s-wave ($l = 0$) scattering problem by a central potential, $V(r)$ [7, 49]:

$$\hbar^2 \frac{d^2\Phi_0(r)}{dr^2} + 2m\left[E - V(r)\right]\Phi_0(r) = 0 \tag{C.0.1}$$

where E is the energy and $\Phi_0(r)$ is the s-wavefunction of the scattering problem. In the limit of the free particle problem, where the central potential is zero, $V(r) = 0$, the general solution for $\Phi_0(r)$, is the plane wave:

$$\Phi_0(r) = e^{\left(\pm i\sqrt{\frac{2mE}{\hbar}}r\right)} \tag{C.0.2}$$

Consequently, a reasonable solution of the equation C.0.1 is a linear combination of two functions, $\Phi_a(r)$ and $\Phi_b(r)$:

$$\Phi_0(r) = c_a\Phi_a(r) + c_b\Phi_b(r) = c_a e^{\left(i\frac{S_a(r)}{\hbar}\right)} + c_b e^{\left(-i\frac{S_b(r)}{\hbar}\right)} \tag{C.0.3}$$

where $\Phi_a(r)$ and $\Phi_b(r)$ are the imaginary exponential of the $S_a(r)$ and $S_b(r)$ functions, which depend on the radial position, r. Using the above expression of the wavefunction $\Phi_0(r)$, equation C.0.1 can be transformed in a second order differential equation for both $S_a(r)$ and $S_b(r)$ functions:

$$\begin{aligned} &c_a\left\{i\hbar\frac{d^2S_a(r)}{dr^2} - \left[\frac{dS_a(r)}{dr}\right]^2 + 2m\left[E - V(r)\right]\right\}e^{\left(-i\frac{S_b(r)}{\hbar}\right)} + \\ &+c_b\left\{-i\hbar\frac{d^2S_b(r)}{dr^2} - \left[\frac{dS_b(r)}{dr}\right]^2 + 2m\left[E - V(r)\right]\right\}e^{\left(-i\frac{S_b(r)}{\hbar}\right)} = 0 \end{aligned} \tag{C.0.4}$$

where each term in the sum only depends on one of the two different functions, $S_a(r)$ and $S_b(r)$. In this way, the above equation can be separated in two independent differential equations for $S_a(r)$ and $S_b(r)$ functions, respectively:

$$i\hbar\frac{d^2S_a(r)}{dr^2} - \left[\frac{dS_a(r)}{dr}\right]^2 + 2m\left[E - V(r)\right] = 0 \tag{C.0.5}$$

$$-i\hbar\frac{d^2S_b(r)}{dr^2} - \left[\frac{dS_b(r)}{dr}\right]^2 + 2m\left[E - V(r)\right] = 0 \tag{C.0.6}$$

To solve both differential equations, the $S_a(r)$ and $S_b(r)$ functions are expanded in series of power of $\hbar$:

$$S_x(r) = \hbar^0 S_{x,0}(r) + \hbar^1 S_{x,1}(r) + \hbar^2 S_{x,2}(r) + \cdots = \sum_{n=0}^{\infty}\hbar^n S_{x,n}(r) \tag{C.0.7}$$

where x can be a or b. Using these power expansions of $S_a(r)$ and $S_b(r)$, equations C.0.5 and C.0.6, become:

$$i\sum_{n=0}^{\infty}\hbar^{n+1}\frac{d^2S_{a,n}(r)}{dr^2} - \sum_{n=0}^{\infty}\sum_{m=0}^{\infty}\hbar^{n+m}\left[\frac{dS_{a,n}(r)}{dr}\right]\left[\frac{dS_{a,m}(r)}{dr}\right] + 2m\left[E - V(r)\right] = 0 \tag{C.0.8}$$

$$-i\sum_{n=0}^{\infty}\hbar^{n+1}\frac{d^2S_{b,n}(r)}{dr^2} - \sum_{n=0}^{\infty}\sum_{m=0}^{\infty}\hbar^{n+m}\left[\frac{dS_{b,n}(r)}{dr}\right]\left[\frac{dS_{b,m}(r)}{dr}\right] + 2m\left[E - V(r)\right] = 0 \tag{C.0.9}$$

where the terms with the same $\hbar$ power can be assembled. To assure that the series are equal to zero for all powers of $\hbar$, the terms with the same $\hbar$ power, have to be equal to zero. To simplify the problem, we can truncate the series of $\hbar$ powers until determine value, which is the WKB approximation. In the first order of the WKB approximation, all the $\hbar$ powers higher than 1 are neglected, and the differential equations which it necessary to solve, are the zero and first order of $\hbar$ powers:

- The differential equations for the $\hbar^0$ are:

$$\left[\frac{dS_{a,0}(r)}{dr}\right]^2 + 2m\left[E - V(r)\right] = 0 \tag{C.0.10}$$

$$\left[\frac{dS_{b,0}(r)}{dr}\right]^2 + 2m\left[E - V(r)\right] = 0 \tag{C.0.11}$$

  whose solutions of the $S_{a,0}(r)$ and $S_{b,0}(r)$ are:

$$S_{a,0}(r) = \int \left\{2m\left[E - V(r)\right]\right\}^{1/2} dr \tag{C.0.12}$$

$$S_{b,0}(r) = \int \{2m[E - V(r)]\}^{1/2} dr \tag{C.0.13}$$

- The differential equations for the $\hbar^1$ are:

$$-2\left[\frac{dS_{a,0}(r)}{dr}\right]\left[\frac{dS_{a,1}(r)}{dr}\right] + i\frac{d^2 S_{a,0}(r)}{dr^2} = 0 \tag{C.0.14}$$

$$-2\left[\frac{dS_{b,0}(r)}{dr}\right]\left[\frac{dS_{b,1}(r)}{dr}\right] + i\frac{d^2 S_{b0}(r)}{dr^2} = 0 \tag{C.0.15}$$

whose solutions of the $S_{a,1}(r)$ and $S_{b,1}(r)$ are:

$$S_{a,1}(r) = i\frac{1}{2}\ln\left[\frac{dS_{a,0}(r)}{dr}\right] = i\frac{1}{2}\ln\left[\{2m[E - V(r)]\}^{1/2}\right] \tag{C.0.16}$$

$$S_{b,1}(r) = -i\frac{1}{2}\ln\left[\frac{dS_{b,0}(r)}{dr}\right] = -i\frac{1}{2}\ln\left[\{2m[E - V(r)]\}^{1/2}\right] \tag{C.0.17}$$

Introducing the expressions obtained for $S_{a,0}(r)$, $S_{b,0}(r)$, $S_{a,1}(r)$ and $S_{b,1}(r)$ in equation C.0.3, the wavefunction $\Phi_0(r)$ in the case of a s-wave scattering by a central potential, $V(r)$, is written as:

$$\Phi_0(r) = \frac{1}{\{2m[E - V(r)]\}^{1/4}}\left\{c_a e^{\left[\frac{i}{\hbar}\int\{2m[E-V(r)]\}^{1/2}dr\right]} + c_b e^{\left[-\frac{i}{\hbar}\int\{2m[E-V(r)]\}^{1/2}dr\right]}\right\} \tag{C.0.18}$$

The above expression for wavefunction $\Phi_0(r)$ diverges when the r is r_0, because the potential is equal to the energy, $V(r_0) = E$, and consequently, the term $2m[E - V(r_0)]$ goes to zero. To avoid this divergence, the wavefunction $\Phi_0(r)$ can be separated in two regions limited by the classical turning point, r_0:

$$\Phi_0^+(r) = \frac{1}{\{2m[E - V(r)]\}^{1/4}}\left\{c_a e^{\left[\frac{i}{\hbar}\int_{r_0}^{\infty}\{2m[E-V(r)]\}^{1/2}dr\right]} + c_b e^{\left[-\frac{i}{\hbar}\int_{r_0}^{\infty}\{2m[E-V(r)]\}^{1/2}dr\right]}\right\} \tag{C.0.19}$$

$$\Phi_0^-(r) = \frac{i^{1/2}}{i\{2m|E - V(r)|\}^{1/4}}\left\{c_a e^{\left[-\frac{1}{\hbar}\int_0^{r_1}\{2m|E-V(r)|\}^{1/2}dr\right]} + c_b e^{\left[\frac{1}{\hbar}\int_0^{r_1}\{2m|E-V(r)|\}^{1/2}dr\right]}\right\} \tag{C.0.20}$$

where the wavefunction $\Phi_0^+(r)$ is defined for r values from r_0 to ∞ and the wavefunction $\Phi_0^-(r)$ is defined for r values from 0 to r_0. In this separation of the wavefunction $\Phi_0(r)$, the region from r_0 to ∞ gives positive values of $2m[E - V(r_0)]$, and the region from 0 to r_0 gives negative values of $2m[E - V(r_0)]$, which can be transformed in $i\{2m|E - V(r)|\}^{1/2}$. To assure the continuity of the wavefunction $\Phi_0(r)$, both solutions have to be connected for the r_0 value. Thus, an asymptotic analysis can provide this connection and the relative phases of the coefficients c_a and c_b in the long range limit, when r tends to ∞.

The reflection approximation

The reflection approximation is based on the spatial form of the final continuum wavefunctions as a function of the internuclear distance in molecules. This approximation is used to simplify the transition amplitude between the initial ground state, usually a bound state, with any final continuum state. The general expression for the transition amplitude, $c_{0,0\to f,v_f}$, between a vibronic initial ground state, $\psi_0(\mathbf{r},R)\,\chi_{0,0}(R)$, and the vibronic final state, $\psi_f(\mathbf{r},R)\,\chi_{f,v_f}(R)$, is:

$$c_{0,0\to f,v_f} = \int_0^\infty \overline{\chi}_{f,v_f}(R)\, d(R)\, \chi_{0,0}(R)\, dR \tag{C.0.21}$$

where $\chi_{0,0}(R)$ and $\chi_{f,v_f}(R)$ are the vibrational wavefunctions of the ground state and the final state, respectively, and $d(R)$ is the electronic dipole coupling between both initial, $\psi_0(\mathbf{r},R)$, and final, $\psi_f(\mathbf{r},R)$, electronic wavefunctions:

$$d(R) = \langle \psi_f(R)|\, \widehat{D}\, |\psi_0(R)\rangle \tag{C.0.22}$$

In the above equation C.0.22, $\widehat{D}$ is the electronic dipole operator, which can be expressed in any gauge, as the velocity or length gauge presented in chapter 1. In this way, we focus on a molecular system in which the vibrational ground state is well localized around the equilibrium distance and the continuum final state with a vibrational wavefunction energy-normalized, presents a repulsive potential energy curve. Because this potential energy curve decreases with the internuclear distance, it can be assumed that the final vibrational wavefunction presents a maximum, peak, around the inner classical turning point and this vibrational wavefunction can be represented by the Dirac delta function around the classical turning point, R_c, normalized by the inverse of the derivative of the potential energy curve. Considering this approximation valid, which is the reflection approximation, equation C.0.21 can be written as:

$$\begin{aligned} c_{0,0\to f,v_f} &\simeq \int_0^\infty \left|\frac{dV_f(R)}{dR}\right|^{-1/2} \delta(R-R_c)\, d(R)\, \chi_{0,0}(R)\, dR = \\ &= \left|\frac{dV_f(R)}{dR}\right|^{-1/2}_{R=R_c} d(R_c)\, \chi_{0,0}(R_c) \end{aligned} \tag{C.0.23}$$

where V_f is the electronic PEC of the final states as a function of the internuclear distance. Finally the transition amplitude in the reflection approximation is evaluated considering only the square root inverse of the potential energy curve derive, the dipole operator and the vibrational ground state wavefunction in the classical turning point, R_c.

We can go further and apply the reflexion approximation to the Franck-Condon factor, which is the overlap between two vibrational wavefunction of two different electronic states. The transition amplitude can be considered proportional to the Franck-Condon factor, when the dipole operator does not change too much with the internuclear distance. In this case, the Franck-Condon factor in the reflection approximation is:

$$\int_0^\infty \overline{\chi}_{f,v_f}(R)\,\chi_{0,0}(R)\,dR \simeq \int_0^\infty \left|\frac{dV_f(R)}{dR}\right|^{-1/2} \delta(R-R_c)\,\chi_{0,0}(R)\,dR = \\ = \left|\frac{dV_f(R)}{dR}\right|^{-1/2}_{R=R_c} \chi_{0,0}(R_c) \tag{C.0.24}$$

Appendix D

Time evolution operator method

The Time Dependent Schrödinger Equation (TDSE) for our hydrogen molecular system, $H_2/H_2^+ + e^-$, is:

$$i\hbar\frac{\partial}{\partial t}\left|\Psi\left(t\right)\right\rangle = \widehat{H}\left|\Psi\left(t\right)\right\rangle \tag{D.0.1}$$

where $\widehat{H}\left(t\right)$ is the Hamiltonian operator of the system and $\left|\Psi\left(t\right)\right\rangle$ is the time dependent wavefunction as a vector in the Hilbert space. As we presented in chapter 1, the $\widehat{H}\left(t\right)$ can be expressed as a combination of the field-free Hamiltonian operator of the system without the interaction with the electromagnetic field, $\widehat{H}_0$, and the time-dependent external potential operator, $\widehat{V}\left(t\right)$:

$$\widehat{H}\left(t\right) = \widehat{H}_0 + \widehat{V}\left(t\right) \tag{D.0.2}$$

The field-free Hamiltonian operator, which does not dependent on time, satisfies the time independent Schrödinger equation (TISE). As was proposed in chapter 3, the bound, continuum and resonant states of the hydrogen molecular system, can be treated separately, given three TISE:

$$\begin{aligned}
\widehat{H}_0\left|\Phi_{n,v_n}\right\rangle &= E_{n,v_n}\left|\Phi_{n,v_n}\right\rangle \\
\widehat{P}\widehat{H}_0\widehat{P}\left|\Phi^{l,m}_{\alpha,v_\alpha}\left(\varepsilon\right)\right\rangle &= E_{\alpha,v_\alpha}\left(\varepsilon\right)\left|\Phi^{l,m}_{\alpha,v_\alpha}\left(\varepsilon\right)\right\rangle \\
\widehat{Q}\widehat{H}_0\widehat{Q}\left|\Phi_{r,v_r}\right\rangle &= E_{r,v_r}\left|\Phi_{r,v_r}\right\rangle
\end{aligned} \tag{D.0.3}$$

where $\left|\Phi_{\mu_n}\right\rangle$, $\left|\Phi^{l,m}_{\alpha,v_\alpha}\left(\varepsilon\right)\right\rangle$ and $\left|\Phi_{r,v_r}\right\rangle$ are the bound, continuum and resonant vibronic wavefunctions (eigenfunctions) and E_{n,v_n}, $E_{\alpha,v_\alpha}\left(\varepsilon\right)$ and E_{r,v_r} are their respective energies (eigenvalues). For convenience, we simplify the notation of the quantum number of each state joint them in $\mu_n = n, v_n$, $\mu_\alpha = \alpha, v_\alpha, \epsilon, l, m$ and $\mu_r = r, v_r$. $\widehat{P}$ and $\widehat{Q}$ are the projectors into the scattering and resonant subspaces, within the Feshbach formalism, which satisfy the relation:

$$\widehat{P} + \widehat{Q} = \widehat{I} \tag{D.0.4}$$

On the other hand, the time dependent wavefunction, $\left|\Psi\left(t\right)\right\rangle$, can be expressed in terms of the time evolution operator, $\hat{U}\left(t - t_0\right)$:

$$|\Psi(t)\rangle = \widehat{U}(t-t_0)\,|\Psi(t_0)\rangle \tag{D.0.5}$$

In the abose expression, the time evolution operator, $\widehat{U}(t-t_0)$, applies over the time dependent wavefunction at the initial time, $|\Psi(t_0)\rangle$, to give the wavefunction at any time t. This time evolution operator satisfies the properties given in [142]. We focus our study on the XUV pump - XUV probe schemes and only consider the cases when both XUV pulses are not overlapped. Within this assumptions, the time evolution operator, $\widehat{U}(t-t_0)$, can be separated in the product of three time evolution operators:

$$\widehat{U}(t-t_0) = \widehat{U}^{(2)}(t-t_2)\,\widehat{U}^{(i)}(t_2-t_1)\,\widehat{U}^{(1)}(t_1-t_0) \tag{D.0.6}$$

where each of these time evolution operators is associated with:

- $\widehat{U}^{(1)}(t_1-t_0)$ is the time evolution operator during the first pulse, the pump.
- $\widehat{U}^{(i)}(t_2-t_1)$ is the time evolution operator between the first and the second pulse. As in this time region, the external potential, $\widehat{V}(t)$, is zero, the Hamiltonian operator of the system, $\hat{H}(t)$, becomes to the field-free Hamiltonian operator of system, $\widehat{H}_0$. Consequently, this time evolution operator, $\widehat{U}^{(i)}(t_2-t_1)$, becomes equal to the field-free stationary phase:

$$\widehat{U}^{(i)}(t_2-t_1) = e^{\left[-i\frac{\widehat{H}_0}{\hbar}(t_2-t_1)\right]} \tag{D.0.7}$$

- $\widehat{U}^{(2)}(t-t_2)$ is the time evolution operator from the beginning of the second pulse, the probe, until the final propagation time of the system.

Considering that the system is in the ground state, $|\Phi_0\rangle$, at the initial time, the time dependent wavefunction becomes:

$$|\Psi(t)\rangle = \widehat{U}^{(2)}(t-t_2)\,e^{\left[-i\frac{\widehat{H}_0}{\hbar}(t_2-t_1)\right]}\widehat{U}^{(1)}(t_1-t_0)\,|\Phi_0\rangle \tag{D.0.8}$$

On the other hand, as we discussed in chapter 1, the wavefunctions, $|\Phi_{\mu_n}\rangle$, $|\Phi_{\mu_\alpha}\rangle$ and $|\Phi_{\mu_r}\rangle$ are eigenfunctions of hermitician operators, and therefore, they constitute a complete set of orthonormal functions, which satisfies the closure relation:

$$\sum\!\!\!\!\!\!\int_{\mu_n} |\Phi_{\mu_n}\rangle\langle\Phi_{\mu_n}|\,d\mu_n + \sum\!\!\!\!\!\!\int_{\mu_\alpha} |\Phi_{\mu_\alpha}\rangle\langle\Phi_{\mu_\alpha}|\,d\mu_\alpha + \sum\!\!\!\!\!\!\int_{\mu_r} |\Phi_{\mu_r}\rangle\langle\Phi_{\mu_r}|\,d\mu_r = \widehat{I} \tag{D.0.9}$$

Substituting the above closure relation in equation D.0.8, the time dependent wavefunction becomes:

$$|\Psi(t)\rangle = |A(t)\rangle + |B(t)\rangle + |C(t)\rangle \tag{D.0.10}$$

where the three different components are:

- For the component $|A(t)\rangle$:

$$|A(t)\rangle = \sum\!\!\!\!\!\!\int_{\mu_n} \left\{ \hat{U}^{(2)}(t-t_2)\,|\Phi_{\mu_n}\rangle\langle\Phi_{\mu_n}|\, e^{\left[-i\frac{\hat{H}_0}{\hbar}(t_2-t_1)\right]} \left[\sum\!\!\!\!\!\!\int_{\mu'_n} |\Phi_{\mu'_n}\rangle\langle\Phi_{\mu'_n}|\, d\mu'_n + \right.\right.$$
$$\left.\left. + \sum\!\!\!\!\!\!\int_{\mu'_\alpha} |\Phi_{\mu'_\alpha}\rangle\langle\Phi_{\mu'_\alpha}|\, d\mu'_\alpha + \sum\!\!\!\!\!\!\int_{\mu'_r} |\Phi_{\mu'_r}\rangle\langle\Phi_{\mu'_r}|\, d\mu'_r \right] \hat{U}^{(1)}(t_1-t_0)\,|\Phi_0\rangle\, d\mu_n \right\} \tag{D.0.11}$$

- For the component $|B(t)\rangle$:

$$|B(t)\rangle = \sum\!\!\!\!\!\!\int_{\mu_\alpha} \left\{ \hat{U}^{(2)}(t-t_2)\,|\Phi_{\mu_\alpha}\rangle\langle\Phi_{\mu_\alpha}|\, e^{\left[-i\frac{\hat{H}_0}{\hbar}(t_2-t_1)\right]} \left[\sum\!\!\!\!\!\!\int_{\mu'_n} |\Phi_{\mu'_n}\rangle\langle\Phi_{\mu'_n}|\, d\mu'_n + \right.\right.$$
$$\vdots$$
$$\left.\left. + \sum\!\!\!\!\!\!\int_{\mu'_\alpha} |\Phi_{\mu'_\alpha}\rangle\langle\Phi_{\mu'_\alpha}|\, d\mu'_\alpha + \sum\!\!\!\!\!\!\int_{\mu'_r} |\Phi_{\mu'_r}\rangle\langle\Phi_{\mu'_r}|\, d\mu'_r \right] \hat{U}^{(1)}(t_1-t_0)\,|\Phi_{0,0}\rangle\, d\mu_\alpha \right\} \tag{D.0.12}$$

- For the component $|C(t)\rangle$:

$$|C(t)\rangle = \sum\!\!\!\!\!\!\int_{\mu_r} \left\{ \hat{U}^{(2)}(t-t_2)\,|\Phi_{\mu_r}\rangle\langle\Phi_{\mu_r}|\, e^{\left[-i\frac{\hat{H}_0}{\hbar}(t_2-t_1)\right]} \left[\sum\!\!\!\!\!\!\int_{\mu'_n} |\Phi_{\mu'_n}\rangle\langle\Phi_{\mu'_n}|\, d\mu'_n + \right.\right.$$
$$\vdots$$
$$\left.\left. + \sum\!\!\!\!\!\!\int_{\mu'_\alpha} |\Phi_{\mu'_\alpha}\rangle\langle\Phi_{\mu'_\alpha}|\, d\mu'_\alpha + \sum\!\!\!\!\!\!\int_{\mu'_r} |\Phi_{\mu'_r}\rangle\langle\Phi_{\mu'_r}|\, d\mu'_r \right] \hat{U}^{(1)}(t_1-t_0)\,|\Phi_{0,0}\rangle\, d\mu_\alpha \right\} \tag{D.0.13}$$

As we commented, the bound state wavefunctions, $|\Phi_{\mu_n}\rangle$, are orthonormal between them and with the $|\Phi_{\mu_\alpha}\rangle$ and $|\Phi_{\mu_r}\rangle$, satisfying the relations:

$$\begin{aligned}
\langle\Phi_{\mu_n}|\, e^{\left[-i\frac{\hat{H}_0}{\hbar}(t_2-t_1)\right]} \left|\Phi_{\mu'_n}\right\rangle &= e^{\left[-i\frac{E_{\mu_n}}{\hbar}(t_2-t_1)\right]} \delta(\mu_n-\mu_n) \\
\langle\Phi_{\mu_\alpha}|\, e^{\left[-i\frac{\hat{H}_0}{\hbar}(t_2-t_1)\right]} |\Phi_{\mu'n}\rangle &= \langle\Phi_{\mu_n}|\, e^{\left[-i\frac{\hat{H}_0}{\hbar}(t_2-t_1)\right]} |\Phi_{\mu'\alpha}\rangle = 0 \\
\langle\Phi_{\mu_r}|\, e^{\left[-i\frac{\hat{H}_0}{\hbar}(t_2-t_1)\right]} |\Phi_{\mu'n}\rangle &= \langle\Phi_{\mu_n}|\, e^{\left[-i\frac{\hat{H}_0}{\hbar}(t_2-t_1)\right]} \left|\Phi_{\mu'_r}\right\rangle = 0
\end{aligned} \tag{D.0.14}$$

where $\delta(\mu_n-\mu_n)$ is a Dirac delta when the quantum number is continuous and a Kronecker delta when is discrete. However, the continuum and resonant state are not eigenfunctions of the field-free Hamiltonian operator, $\widehat{H}_0$, unless they are

eigenfunctions of the associated subspaces of this Hamiltonian operator. We can transform the stationary time phase between both pump and probe pulses in:

$$\begin{aligned} e^{\left[-i\frac{\hat{H}_0}{\hbar}(t_2-t_1)\right]} &= e^{\left[-i\frac{(\hat{P}+\hat{Q})\hat{H}_0(\hat{P}+\hat{Q})}{\hbar}(t_2-t_1)\right]} = \\ = e^{\left[-i\frac{\hat{P}\hat{H}_0\hat{P}}{\hbar}(t_2-t_1)\right]} e^{\left[-i\frac{\hat{Q}\hat{H}_0\hat{Q}}{\hbar}(t_2-t_1)\right]} e^{\left[-i\frac{\hat{P}\hat{H}_0\hat{Q}}{\hbar}(t_2-t_1)\right]} e^{\left[-i\frac{\hat{Q}\hat{H}_0\hat{P}}{\hbar}(t_2-t_1)\right]} \end{aligned} \tag{D.0.15}$$

And the projections of the above expression into the $|\Phi_{\mu_\alpha}\rangle$ and $|\Phi_{\mu_r}\rangle$ wavefunctions are:

$$\begin{aligned} \langle\Phi_{\mu_\alpha}| e^{\left[-i\frac{\hat{H}_0}{\hbar}(t_2-t_1)\right]} |\Phi_{\mu'_\alpha}\rangle &= e^{\left[-i\frac{E_{\mu_\alpha}}{\hbar}(t_2-t_1)\right]}\delta\left(\mu_\alpha-\mu'_\alpha\right) \\ \langle\Phi_{\mu_r}| e^{\left[-i\frac{\hat{H}_0}{\hbar}(t_2-t_1)\right]} |\Phi_{\mu'_r}\rangle &= e^{\left[-i\frac{E_{\mu_r}}{\hbar}(t_2-t_1)\right]}\delta\left(\mu_r-\mu'_r\right) \\ \langle\Phi_{\mu_\alpha}| e^{\left[-i\frac{\hat{H}_0}{\hbar}(t_2-t_1)\right]} |\Phi_{\mu'_r}\rangle &= \langle\Phi_{\mu_\alpha}| e^{\left[-i\frac{\hat{P}\hat{H}_0\hat{Q}}{\hbar}(t_2-t_1)\right]} |\Phi_{\mu'_r}\rangle \\ \langle\Phi_{\mu_r}| e^{\left[-i\frac{\hat{H}_0}{\hbar}(t_2-t_1)\right]} |\Phi_{\mu'_\alpha}\rangle &= \langle\Phi_{\mu_r}| e^{\left[-i\frac{\hat{Q}\hat{H}_0\hat{P}}{\hbar}(t_2-t_1)\right]} |\Phi_{\mu'_\alpha}\rangle \end{aligned} \tag{D.0.16}$$

Introducing all above expressions in equation D.0.10, and projecting the $|A(t)\rangle$, $|B(t)\rangle$ and $|C(t)\rangle$ components into the final scattering state, $\langle\Phi_{\mu_\alpha}|$, the density of probability as a function of the electronic and nuclear kinetic energy, $d^2P^{l,m}_{\alpha,v_\alpha}(t;\varepsilon)/dE_{v_\alpha}dE_\epsilon$, is:

$$\frac{d^2P^{l,m}_{\alpha,v_\alpha}(t;\varepsilon)}{dE_{v_\alpha}dE(\varepsilon)} = \left|\langle\Phi_{\mu_\alpha}|A(t)\rangle + \langle\Phi_{\mu_\alpha}|B(t)\rangle + \langle\Phi_{\mu_\alpha}|C(t)\rangle\right|^2 \tag{D.0.17}$$

We can make the assumption that the $\hat{Q}\hat{H}_0\hat{P}$ coupling is several orders of magnitude less than the $\hat{P}\hat{H}_0\hat{Q}$ coupling, so it can be removed from the $\langle\Phi_{\mu_\alpha}|C(t)\rangle$ component. Consequently, the components are:

- For the component $\langle\Phi_{\mu_\alpha}|A(t)\rangle$:

$$\langle\Phi_{\mu_\alpha}|A(t)\rangle = \sum\!\!\!\!\!\!\int_{\mu_n} \langle\Phi_{\mu_\alpha}|\hat{U}^{(2)}(t-t_2)|\Phi_{\mu_n}\rangle e^{\left[-\frac{E_{\mu_n}}{\hbar}(t_2-t_1)\right]} \langle\Phi_{\mu_n}|\hat{U}^{(1)}(t_1-t_0)|\Phi_0\rangle d\mu_n \tag{D.0.18}$$

- For the component $\langle\Phi_{\mu_\alpha}|B(t)\rangle$:

$$\begin{aligned} \langle\Phi_{\mu_\alpha}|B(t)\rangle = &\sum\!\!\!\!\!\!\int_{\mu'_\alpha} \langle\Phi_{\mu_\alpha}|\hat{U}^{(2)}(t-t_2)|\Phi_{\mu'_\alpha}\rangle e^{\left[-i\frac{E_{\mu'_\alpha}}{\hbar}(t_2-t_1)\right]} \langle\Phi_{\mu'_\alpha}|\hat{U}^{(1)}(t_1-t_0)|\Phi_0\rangle d\mu'_\alpha + \\ &\sum\!\!\!\!\!\!\int_{\mu_r}\sum\!\!\!\!\!\!\int_{\mu'_\alpha} \langle\Phi_{\mu_\alpha}|\hat{U}^{(2)}(t-t_2)|\Phi_{\mu'_\alpha}\rangle \langle\Phi_{\mu'_\alpha}| e^{\left[-i\frac{\hat{P}\hat{H}_0\hat{Q}}{\hbar}(\tau-T)\right]} |\Phi_{\mu_r}\rangle \langle\Phi_{\mu_r}|\hat{U}^{(1)}(t_1-t_0)|\Phi_0\rangle d\mu_r \end{aligned} \tag{D.0.19}$$

- For the component $\langle \Phi_{\mu_\alpha} | C(t) \rangle$:

$$\langle \Phi_{\mu_\alpha} | C(t) \rangle = \sum\!\!\!\!\!\!\int_{\mu_r} \langle \Phi_{\mu_\alpha} | \hat{U}^{(2)}(t - t_2) | \Phi_{\mu_r} \rangle e^{\left[-i\frac{E_{\mu_r}}{\hbar}(t_2 - t_1)\right]} \langle \Phi_{\mu_r} | \hat{U}^{(1)}(t_1 - t_0) | \Phi_0 \rangle \, d\mu'_\alpha \tag{D.0.20}$$

We are focused on the ionization processes induced by two identical XUV pulses, whose graphical representation of the vector potential, $A(t)$, as a function of time, t, is plotted in figure D.0.1.

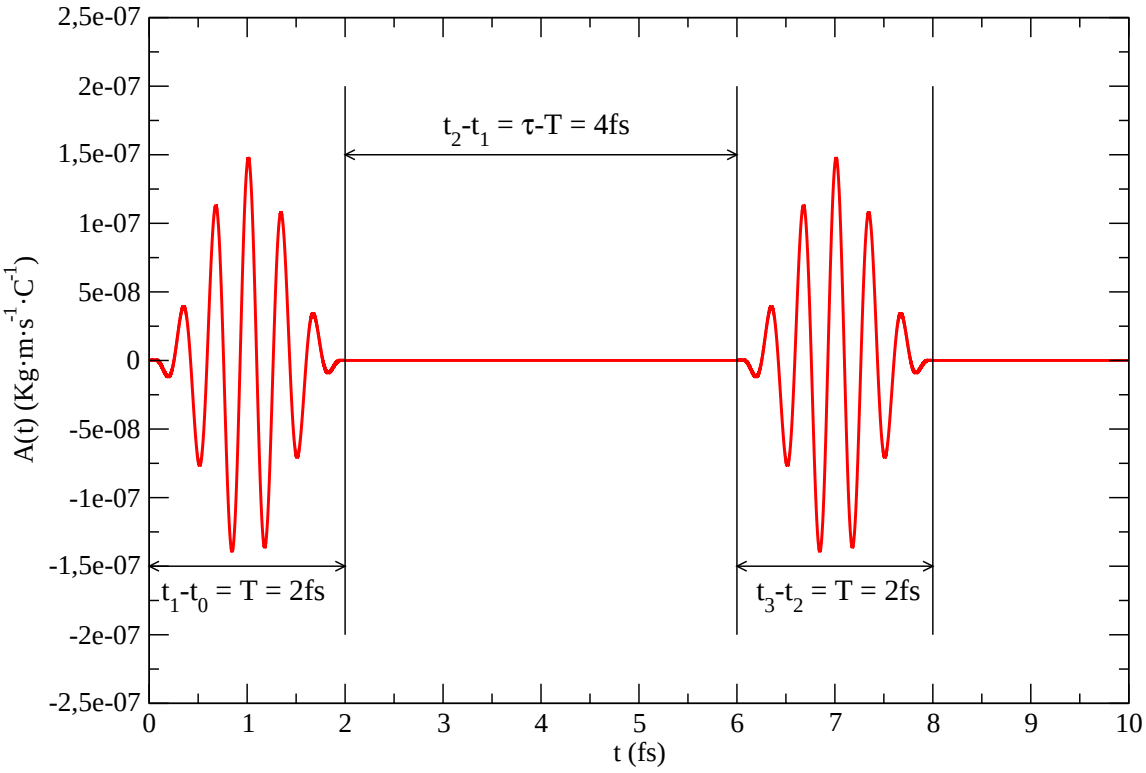

Figure D.0.1: Representation of the vector potentials, $A(t)$, as a function of time, t, for our problem. Both pulses are identical with the parameters: $T = 2\,\text{fs}$, $E = 12.28\,\text{eV}$, $I = 10^{12}\,\text{W} \cdot \text{cm}^{-2}$.

Therefore, in our system, the pump - probe scheme produces:

- The one-photon absorption due to the pump pulse leads the system in a bound excited state, H_2^*, and a second-photon absorption brings the system to the final ionization state, $H_2^+ + e^-$, and resonant state, H_2^{**}.
- The one and second-photon absorption due to the probe produces the same transitions than the pump pulse, but delayed in time. In addition, from the bound excited state, H_2^*, populated by the pump, the probe populates to the final ionization state, $H_2^+ + e^-$, and resonant state, H_2^{**}.

Considering the different processes that our pump - probe scheme induced in the system, we can apply several approximation:

- We can extract from the first term of the $\langle \Phi_{\mu_\alpha} | A(t) \rangle$ component, the two-photon absorption transition from the ground state to the final continuum by the probe pulse:

$$\langle \Phi_{\mu_\alpha} | A(t) \rangle = \langle \Phi_{\mu_\alpha} | \hat{U}^{(2)}(t - t_2) | \Phi_0 \rangle e^{\left[-\frac{E_0}{\hbar}(t_2 - t_0)\right]} + \\ + \sum\!\!\!\!\!\!\int_{\mu_n \neq 0} \langle \Phi_{\mu_\alpha} | \hat{U}^{(2)}(t - t_2) | \Phi_{\mu_n} \rangle e^{\left[-\frac{E_{\mu_n}}{\hbar}(t_2 - t_1)\right]} \langle \Phi_{\mu_n} | \hat{U}^{(1)}(t_1 - t_0) | \Phi_0 \rangle d\mu \tag{D.0.21}$$

- We focus on an energy region where the XUV energy photon used cannot produce transitions between both ionization thresholds, $1s\sigma_g$ and $2p\sigma_u$, and between one of them with the resonant states. Therefore, $\langle \Phi_{\mu_\alpha} | B(t) \rangle$ and $\langle \Phi_{\mu_\alpha} | C(t) \rangle$ are:

$$\langle \Phi_{\mu_\alpha} | C(t) \rangle = 0 \tag{D.0.22}$$

and:

$$\langle \Phi_{\mu_\alpha} | B(t) \rangle = e^{\left[-i\frac{E_{\mu_\alpha}}{\hbar}(t - t_1)\right]} \langle \Phi_{\mu_\alpha} | \hat{U}^{(1)}(t_1 - t_0) | \Phi_0 \rangle + \\ + e^{\left[-i\frac{E_{\mu_\alpha}}{\hbar}(t-\tau)\right]} \sum\!\!\!\!\!\!\int_{\mu_r} \langle \Phi_{\mu'_\alpha} | e^{\left[-i\frac{\hat{P}\hat{H}_0\hat{Q}}{\hbar}(\tau - T)\right]} | \Phi_{\mu_r} \rangle \langle \Phi_{\mu_r} | \hat{U}^{(1)}(t_1 - t_0) | \Phi_0 \rangle d\mu_r \tag{D.0.23}$$

It's satisfied the relation $t'_1 < t_2$ and $t'_1 - T$ is the time which the $\hat{P}\hat{H}_0\hat{Q}$ coupling becomes to zero (The lifetime of the resonance). In addition, we can combinate the two last terms in only one:

$$\langle \Phi_{\mu_\alpha} | B(t) \rangle = e^{\left[-i\frac{E_{\mu_\alpha}}{\hbar}\left(t - t'_1\right)\right]} \langle \Phi_{\mu_\alpha} | \hat{U}'^{(1)}(t'_1 - t_0) | \Phi_0 \rangle \tag{D.0.24}$$

where:

$$\left\{ e^{\left[-i\frac{E_{\mu_\alpha}}{\hbar}\left(t'_1 - T\right)\right]} + e^{\left[-i\frac{\hat{P}\hat{H}_0\hat{Q}}{\hbar}\left(t'_1 - T\right)\right]} | \Phi_{r,v_r} \rangle \langle \Phi_{r,v_r} | \right\} \hat{U}^{(1)}(T) = \hat{U}'^{(1)}(t'_1) \tag{D.0.25}$$

- The terms from $\langle \Phi_{\mu_\alpha} | A(t) \rangle$ for the transition from the ground state to the final states due to the probe pulse, can be written as:

$$\begin{aligned} &\langle \Phi_{\mu_\alpha} | \hat{U}^{(2)}(t - t_2) | \Phi_0 \rangle e^{\left[-\frac{E_0}{\hbar}(t_2 - t_0)\right]} = \\ &= e^{\left[-i\frac{E_{\mu_\alpha}}{\hbar}\left(t - t'_1 - \tau\right)\right]} \langle \Phi_{\mu_\alpha} | \hat{U}^{(2)}(t'_1) | \Phi_0 \rangle e^{\left[-i\frac{E_0}{\hbar}\tau\right]} \simeq \\ &\simeq e^{\left[-i\frac{E_{\mu_\alpha}}{\hbar}\left(t - t'_1\right)\right]} \langle \Phi_{\mu_\alpha} | \hat{U}'^{(1)}(t'_1) | \Phi_0 \rangle e^{\left[i\frac{E_{\mu_\alpha} - E_0}{\hbar}\tau\right]} \end{aligned} \tag{D.0.26}$$

Using the above approximations, equation D.0.17 becomes:

$$\frac{d^2P^{l,m}_{\alpha,v_\alpha}(t;\varepsilon)}{dE_{v_\alpha}dE_\epsilon} = \left| e^{\left[-i\frac{E_{\mu_\alpha}}{\hbar}(t-T-t')\right]} \langle\Phi_{\mu_\alpha}|\hat{U}'^{(1)}(T+t')|\Phi_0\rangle \left\{1+e^{\left[i\frac{\left(E_{\alpha,v_\alpha}(\varepsilon)-E_{0,0}\right)}{\hbar}\tau\right]}\right\} + \right.$$
$$\left. + \sum\!\!\!\!\!\!\int_{\mu_n\neq 0} \langle\Phi_{\mu_\alpha}|\hat{U}^{(2)}(t-\tau)|\Phi_{\mu_n}\rangle e^{\left[-i\frac{E_{\mu_n}}{\hbar}(\tau-T)\right]} \langle\Phi_{\mu_n}|\hat{U}^{(1)}(T)|\Phi_0\rangle d\mu_n \right|^2 \tag{D.0.27}$$

where we can change the time variable, doing $t'_1 = T + t'$ and combine the two terms in which the transition is from the ground state to the final state

We can make the connection between time evolution operator and our spectral method. For the conection, each term in the density of probability definition is expressed as:

- The first term in equation D.0.27 is associated with:

$$\begin{aligned}\langle\Phi_{\mu_\alpha}|\hat{U}'^{(1)}(T+t')|\Phi_0\rangle &= \left\langle\Phi^{l,m}_{\alpha,v_\alpha}(\varepsilon)\right|\hat{U}'^{(1)}(T+t')|\Phi_{0,0}\rangle = \\ &= c^{l,m}_{\alpha,v_\alpha}(T+t';\varepsilon)\, e^{\left[-i\frac{E_{\alpha,v_\alpha}(\varepsilon)}{\hbar}(T+t')\right]}\end{aligned} \tag{D.0.28}$$

- In the second term of equation D.0.27 we have two transition terms, which can be associated with the coefficients as:

$$\langle\Phi_{\mu_n}|\hat{U}^{(1)}(T)|\Phi_0\rangle = \langle\Phi_{n,v_n}|\hat{U}^{(1)}(T)|\Phi_{0,0}\rangle = c_{n,v_n}(T)e^{\left[-i\frac{E_{n,v_n}}{\hbar}T\right]} \tag{D.0.29}$$

$$\begin{aligned}\langle\Phi_{\mu_\alpha}|\hat{U}^{(2)}(t-\tau)|\Phi_{\mu_n}\rangle &= \left\langle\Phi^{l,m}_{\alpha,v_\alpha}(\varepsilon)\right|\hat{U}^{(2)}(t-\tau)|\Phi_{n,v_n}\rangle = \\ &= c^{n,v_n}_{\alpha,v_\alpha,l,m}(t-\tau;\varepsilon)\, e^{\left[-i\frac{E_{\alpha,v_\alpha}(\varepsilon)}{\hbar}(t-\tau)\right]}\end{aligned} \tag{D.0.30}$$

Substituting and operating in equation D.0.27, the density of probability to find the system in a final state $\alpha, v_\alpha, \epsilon, l, m$, $d\left[P^{l,m}_{\alpha,v_\alpha}(t;\varepsilon)\right]^2/dE_{v_\alpha}dE_\epsilon$, is:

$$\frac{d^2P^{l,m}_{\alpha,v_\alpha}(t;\varepsilon)}{dE_{v_\alpha}dE_\epsilon} = \left| c^{l,m}_{\alpha,v_\alpha}(T+t';\varepsilon)\left\{1+e^{\left[i\frac{\left(E_{\alpha,v_\alpha}(\varepsilon)-E_{0,0}\right)}{\hbar}\tau\right]}\right\} + \right.$$
$$\left. + \sum_{n\neq 0}\sum\!\!\!\!\!\!\int_{v_n} c^{n,v_n}_{\alpha,v_\alpha,l,m}(t-\tau;\varepsilon)\, e^{\left[i\frac{\left(E_{\alpha,v_\alpha}(\varepsilon)-E_{n,v_n}\right)}{\hbar}\tau\right]} c_{n,v_n}(T+t')\, dv_n \right|^2 \tag{D.0.31}$$

where, as after the pulse, the population in the bound states do not change, their amplitudes (coefficients) do not vary:

$$c_{n,v_n}(T+t') = c_{n,v_n}(T) \tag{D.0.32}$$

Publications

1. Alicia Palacios, Alberto González-Castrillo and Fernando Martín. Molecular interferometer to decode attosecond electron-nuclear dynamics. *Proceedings of the National Academy of Sciences* **111** (11), 3973-3978 (2014)

2. Alicia Palacios, Alberto González-Castrillo and Fernando Martín. Electron streaking and dissociation in laser-assisted photoionization of molecular hydrogen. Journal of Physics B: Atomic, Molecular and Optical Physics **47**, 124013 (2014)

3. Alicia Palacios, Alberto González-Castrillo, Henri Bachau and Fernando Martín. Wave packet dynamics in molecular excited electronic states. *Journal of Physics: Conference Series* **488**, 012017 (2014)

4. Alicia Palacios, Paula Rivière, Alberto González-Castrillo and Fernando Martín. XUV Lasers for Ultrafast Electronic Control in H2, (Ultrafast phenomena in molecular sciences) Springer International Publishing (2014)

5. Predrag Ranitovic , Craig W. Hogle, Paula Rivière, Alicia Palacios, Xiao-Ming Tong, Nobuyuki Toshima, Alberto González-Castrillo, Leigh Martin, Fernando Martín, Margaret M. Murnane and Henry Kapteyn. Attosecond vacuum UV coherent control of molecular dynamics. *Proceedings of the National Academy of Sciences* **111** (3), 912 (2013)

6. Andreas Fischer, Alexander Sperl, Philipp Cörlin, Michael Schönwald, Helga Rietz, Alicia Palacios, Alberto González-Castrillo, Fernando Martín, Thomas Pfeifer, Joachim Ullrich, Arne Senftleben, and Robert Moshammer. Electron localization involving doubly excited states in broadband extreme ultraviolet ionization of H2. *Physical Review Letters* **110**, 213002 (2013)

7. Alicia Palacios, Johannes Feist, Alberto González-Castrillo, Jose Luis Sanz-Vicario and Fernando Martín. Autoionization of molecular hydrogen: where do the Fano lineshapes go?. *ChemPhysChem* **14**, 1456 (2013)

8. Alberto González-Castrillo, Alicia Palacios, Henri Bachau and Fernando Martín. Clocking ultrafast wave packet dynamics in molecules through UV-induced symmetry. *Physical Review Letters* **108**, 063009 (2012)

9. Alberto González-Castrillo, Alicia Palacios, Fabrice Catoire, Henri Bachau and Fernando Martín. Reproducibility of observables and coherent control

in molecular photionization: From continuous wave to ultrashort pulsed radiation. *Journal of Physical Chemistry A* **116** (11), 2704-2712 (2011)

10. Alberto González-Castrillo, Jhon Fredy Pérez-Torres, Alicia Palacios and Fernando Martín. Probing vibrational wave packets in molecular excited states. *Theoretical Chemistry Accounts* **128**, 735-742 (2010)

11. Alberto González-Castrillo, Marcela Hurtado, Otilia Mó, Manuel Yañéz and Jean-Claude Guillemin. The role of hyperconjugate π-aromacity on the enhanced acidity of methil-, silyl- and germylcyclopentadienes. *Molecular Physics* **108**, 2467-2476 (2010)

Bibliography

[1] Milton Abramowitz and Irene A. Stegun. *Handbook of mathematical functions*. New York: Dover, 1965.

[2] Leslie Allen and Joseph H. Eberly. *Optical Resonance and Two-level Atoms*. Wiley-Interscience Publication, 1987.

[3] Maxim V. Ammosov, Nikolai B. Delone, and Vladimir P. Krainov. Tunnel ionization of complex atoms and atomic ions in electromagnetic field. *Proc. SPIE*, 0664:138–141, 1986.

[4] Amalia Apalategui and Alejandro Saenz. Multiphoton ionization of the hydrogen molecule h 2. *Journal of Physics B: Atomic, Molecular and Optical Physics*, 35(8):1909, 2002.

[5] Tom M. Apostol. *Calculus*. Wesley, 2nd edition, 1975.

[6] S. Arai, T. Kamosaki, M. Ukai, K. Shinsaka, Y. Hatano, Y. Ito, H. Koizumi, A. Yagishita, K. Ito, and K. Tanaka. Lyman-α coincidence detection in the photodissociation of doubly excited molecular hydrogen into two $h(2p)$ atoms. *The Journal of Chemical Physics*, 88(5):3016–3021, 1988.

[7] Peter W. Atkins. *Molecular Quantum Mechanics*. Oxford University Press, 4th edition, 2005.

[8] Manohar Awasthi, Yulian V Vanne, and Alejandro Saenz. Non-perturbative solution of the time-dependent schrÃ¶dinger equation describing h 2 in intense short laser pulses. *Journal of Physics B: Atomic, Molecular and Optical Physics*, 38(22):3973, 2005.

[9] V. Ayvazyan, N. Baboi, I. Bohnet, R. Brinkmann, M. Castellano, P. Castro, L. Catani, S. Choroba, A. Cianchi, M. Dohlus, H. T. Edwards, B. Faatz, A. A. Fateev, J. Feldhaus, K. Flöttmann, A. Gamp, T. Garvey, H. Genz, Ch. Gerth, V. Gretchko, B. Grigoryan, U. Hahn, C. Hessler, K. Honkavaara, M. Hüning, R. Ischebeck, M. Jablonka, T. Kamps, M. Körfer, M. Krassilnikov, J. Krzywinski, M. Liepe, A. Liero, T. Limberg, H. Loos, M. Luong, C. Magne, J. Menzel, P. Michelato, M. Minty, U.-C. Müller, D. Nölle, A. Novokhatski, C. Pagani, F. Peters, J. Pflüger, P. Piot, L. Plucinski, K. Rehlich, I. Reyzl, A. Richter, J. Rossbach, E. L. Saldin, W. Sandner, H. Schlarb, G. Schmidt, P. Schmüser, J. R. Schneider, E. A. Schneidmiller,

H.-J. Schreiber, S. Schreiber, D. Sertore, S. Setzer, S. Simrock, R. Sobierajski, B. Sonntag, B. Steeg, F. Stephan, K. P. Sytchev, K. Tiedtke, M. Tonutti, R. Treusch, D. Trines, D. Türke, V. Verzilov, R. Wanzenberg, T. Weiland, H. Weise, M. Wendt, I. Will, S. Wolff, K. Wittenburg, M. V. Yurkov, and K. Zapfe. Generation of gw radiation pulses from a vuv free-electron laser operating in the femtosecond regime. *Phys. Rev. Lett.*, 88:104802, Feb 2002.

[10] H. Bachau, E. Cormier, P. Decleva, J. E. Hansen, and F. Martín. Applications of b-splines in atomic and molecular. *Rep. Prog. Phys.*, 64:1815–1942, 2001.

[11] Anton Barty. Time-resolved imaging using x-ray free electron lasers. *Journal of Physics B: Atomic, Molecular and Optical Physics*, 43(19):194014, 2010.

[12] W J Bates. A wavefront shearing interferometer. *Proceedings of the Physical Society*, 59(6):940, 1947.

[13] G. Berden, W. A. Gillespie, S. P. Jamison, E.-A. Knabbe, A. M. MacLeod, A. F. G. van der Meer, P. J. Phillips, H. Schlarb, B. Schmidt, P. Schmüser, and B. Steffen. Benchmarking of electro-optic monitors for femtosecond electron bunches. *Phys. Rev. Lett.*, 99:164801, Oct 2007.

[14] Hans A. Bethe and Edwin E. Salpeter. *Quantum Theory.* Springer-Verlag OHG, 1957.

[15] V. Blanchet, Mohamed Aziz Bouchène, and Bertrand Girard. Temporal coherent control in the photoionization of cs[sub 2]: Theory and experiment. *The Journal of Chemical Physics*, 108(12):4862, 1998.

[16] Valérie Blanchet, Céline Nicole, Mohamed-Aziz Bouchene, and Bertrand Girard. Temporal coherent control in two-photon transitions: From optical interferences to quantum interferences. *Physical Review Letters*, 78(14):2716–2719, Apr 1997.

[17] David Bohm. *Quantum Theory.* Courier Dover Publications, 1989.

[18] Paul Brumer and Moshe Shapiro. Control of unimolecular reactions using coherent light. *Chemical Physics Letters*, 126(6):541–546, 1986.

[19] Paul Brumer and Moshe Shapiro. Laser control of molecular processes. *Annual Review of Physical Chemistry*, 43(1):257–282, 1992. PMID: 18397166.

[20] P. H. Bucksbaum, A. Zavriyev, H. G. Muller, and D. W. Schumacher. Softening of the h_2^+ molecular bond in intense laser fields. *Phys. Rev. Lett.*, 64:1883–1886, Apr 1990.

[21] K. S. Budil, P. Salières, Anne L'Huillier, T. Ditmire, and M. D. Perry. Influence of ellipticity on harmonic generation. *Phys. Rev. A*, 48:R3437–R3440, Nov 1993.

[22] John C. Butcher. *The Numerical Analysis of Ordinary Differential Equations: Runge-Kutta and General Linear Methods*. John Wiley & Sons Publications, 1987.

[23] P. A. Carpeggiani, P. Tzallas, A. Palacios, D. Gray, F. Martín, and D. Charalambidis. Tracing molecular dynamics at the femto-/atto-second boundary through extreme-ultraviolet pump-probe spectroscopy. *ArXiv e-prints*, apr 2013.

[24] F. Catoire, R. E. F. Silva, P. Rivière, H. Bachau, and F. Martín. Molecular resolvent-operator method: Electronic and nuclear dynamics in strong-field ionization. *Phys. Rev. A*, 89:023415, Feb 2014.

[25] Zenghu Chang. *Fundamentals of Attosecond Optics*. John Wiley & Sons Publications, 2011.

[26] Zhidang Chen, Paul Brumer, and Moshe Shapiro. Coherent radiative control of molecular photodissociation via resonant two-photon versus two-photon interference. *Chemical Physics Letters*, 198(5):498 – 504, 1992.

[27] Wei-Chun Chu, Song-Feng Zhao, and C. D. Lin. Laser-assisted-autoionization dynamics of helium resonances with single attosecond pulses. *Phys. Rev. A*, 84:033426, Sep 2011.

[28] Bernard Diu Claude Cohen-Tannoudji and Frank Lalo. *Quantum Mechanics*, volume 2. John Wiley & Sons Publications, 1977.

[29] Bernard Diu Claude Cohen-Tannoudji and Frank Lalo. *Quantum Mechanics*, volume 1. John Wiley & Sons Publications, 1977.

[30] Stanley Cohen, John R. Hiskes, and Robert J. Riddell. Vibrational states of the hydrogen molecular ion. *Phys. Rev.*, 119(3):1025–1027, Aug 1960.

[31] J Colgan, D H Glass, K Higgins, and P G Burke. R -matrix floquet theory of molecular multiphoton processes: Ii. multiphoton ionization of h 2. *Journal of Physics B: Atomic, Molecular and Optical Physics*, 34(11):2089, 2001.

[32] P. B. Corkum. Plasma perspective on strong field multiphoton ionization. *Phys. Rev. Lett.*, 71:1994–1997, Sep 1993.

[33] P. B. Corkum and Ferenc Krausz. Attosecond science. *Nature Physics*, 3(6):381–387, June 2007.

[34] Eric Cormier, Ian A. Walmsley, Ellen M. Kosik, Adam S. Wyatt, Laura Corner, and Louis F. DiMauro. Self-referencing, spectrally, or spatially encoded spectral interferometry for the complete characterization of attosecond electromagnetic pulses. *Phys. Rev. Lett.*, 94:033905, Jan 2005.

[35] M. Cortés and F. Martín. Multichannel close-coupling method with l^2 integrable bases. *J. Phys. B: At. Mol. Opt. Phys.*, 27(23):5741–5760, Jun 1994.

[36] J M Dahlström, A L'Huillier, and A Maquet. Introduction to attosecond delays in photoionization. *Journal of Physics B: Atomic, Molecular and Optical Physics*, 45(18):183001, 2012.

[37] Carl de Boor. *A Practical Guide to Splines*. Applied Mathematical Sciences. Springer, 1978.

[38] P. Dietrich, N. H. Burnett, M. Ivanov, and P. B. Corkum. High-harmonic generation and correlated two-electron multiphoton ionization with elliptically polarized light. *Phys. Rev. A*, 50:R3585–R3588, Nov 1994.

[39] Dan Dill. Fixedmolecule photoelectron angular distributions. *The Journal of Chemical Physics*, 65(3):1130–1133, 1976.

[40] S.N. Dixit and V. McKoy. Ionic rotational selection rules for (n + 1) resonant enhanced multiphoton ionization. *Chemical Physics Letters*, 128(1):49 – 54, 1986.

[41] R. Dörner, J. M. Feagin, C. L. Cocke, H. Bräuning, O. Jagutzki, M. Jung, E. P. Kanter, H. Khemliche, S. Kravis, V. Mergel, M. H. Prior, H. Schmidt-Böcking, L. Spielberger, J. Ullrich, M. Unversagt, and T. Vogt. Fully differential cross sections for double photoionization of he measured by recoil ion momentum spectroscopy. *Phys. Rev. Lett.*, 77(6):1024–1027, Aug 1996.

[42] D. Dowek, J. F. Pérez-Torres, Y. J. Picard, P. Billaud, C. Elkharrat, J. C. Houver, J. L. Sanz-Vicario, and F. Martín. Circular dichroism in photoionization of *h_2*. *Phys. Rev. Lett.*, 104:233003, Jun 2010.

[43] V. Engel and H. Metiu. Two-photon wave-packet interferometry. *The Journal of Chemical Physics*, 100(8):5448–5458, 1994.

[44] U. Fano. Effects of configuration interaction on intensities and phase shifts. *Phys. Rev.*, 124:1866–1878, Dec 1961.

[45] J. Feist, S. Nagele, C. Ticknor, B. I. Schneider, L. A. Collins, and J. Burgdörfer. Attosecond two-photon interferometry for doubly excited states of helium. *Physical Review Letters*, 107(9):093005, Aug 2011.

[46] H. Feshbach. A unified theory of nuclear reactions, {II}. *Ann. Phys.*, 19(287-313):519 – 546, 1962.

[47] Herman Feshbach. Unified theory of nuclear reactions. *Ann. Phys.*, 5(4):357 – 390, 1958.

[48] Andreas Fischer, Alexander Sperl, Philipp Cörlin, Michael Schönwald, Helga Rietz, Alicia Palacios, Alberto González-Castrillo, Fernando Martín, Thomas Pfeifer, Joachim Ullrich, Arne Senftleben, and Robert Moshammer. Electron localization involving doubly excited states in broadband extreme ultraviolet ionization of $\mathbf{H}_2$. *Phys. Rev. Lett.*, 110:213002, May 2013.

[49] Harald Siegfried Friedrich. *Theoretical Atomic Physics*. Springer, 2006.

[50] Hideki Fujiwara, Hidehisa Takasaki, Jun-ichi Hotta, and Keiji Sasaki. Observation of the discrete transition of optically trapped particle position in the vicinity of an interface. *Applied Physics Letters*, 84(1):13–15, 2004.

[51] F. Kelkensberg J. F. Pérez-Torres F. Morales M. F. Kling W. Siu O. Ghafur P. Johnsson M. Swoboda E. Benedetti F. Ferrari F. Lépine J. L. Sanz-Vicario S. Zherebtsov I. Znakovskaya A. L'Huillier M. Yu. Ivanov M. Nisoli F. Martín G. Sansone and M. J. J. Vrakking. Electron localization following attosecond molecular photoionization. *Nature*, 465:763–766, 2010.

[52] Steve Gilbertson, Michael Chini, Ximao Feng, Sabih Khan, Yi Wu, and Zenghu Chang. Monitoring and controlling the electron dynamics in helium with isolated attosecond pulses. *Phys. Rev. Lett.*, 105:263003, Dec 2010.

[53] M. Glass-Maujean. Photodissociation of doubly excited states of h_2, hd, and d_2. *The Journal of Chemical Physics*, 85(9):4830–4834, 1986.

[54] M. Glass-Maujean. Photodissociation of doubly excited states of h_2: Emission of balmer lines. *The Journal of Chemical Physics*, 89(5):2839–2843, 1988.

[55] M Glass-Maujean and H Schmoranzer. Dissociation dynamics of doubly excited states of molecular hydrogen. *Journal of Physics B: Atomic, Molecular and Optical Physics*, 38(8):1093, 2005.

[56] Roy J. Glauber. The quantum theory of optical coherence. *Phys. Rev.*, 130:2529–2539, Jun 1963.

[57] A. González-Castrillo, A. Palacios, F. Catoire, H. Bachau, and F. Martín. Reproducibility of observables and coherent control in molecular photoionization: From continuous wave to ultrashort pulsed radiation. *The Journal of Physical Chemistry A*, 116(11):2704–2712, 2012.

[58] Alberto González-Castrillo, Alicia Palacios, Henri Bachau, and Fernando Martín. Clocking ultrafast wave packet dynamics in molecules through uv-induced symmetry breaking. *Phys. Rev. Lett.*, 108:063009, Feb 2012.

[59] Alberto González-Castrillo, JhonFredy Pérez-Torres, Alicia Palacios, and Fernando Martín. Probing vibrational wave packets in molecular excited states. *Theoretical Chemistry Accounts*, 128(4-6):735–742, 2011.

[60] E. Goulielmakis, M. Schultze, M. Hofstetter, V. S. Yakovlev, J. Gagnon, M. Uiberacker, A. L. Aquila, E. M. Gullikson, D. T. Attwood, R. Kienberger, F. Krausz, and U. Kleineberg. Single-cycle nonlinear optics. *Science*, 320(5883):1614–1617, 2008.

[61] E. Goulielmakis, M. Uiberacker, R. Kienberger, A. Baltuska, V. Yakovlev, A. Scrinzi, Th. Westerwalbesloh, U. Kleineberg, U. Heinzmann,

M. Drescher, and F. Krausz. Direct measurement of light waves. *Science*, 305(5688):1267–1269, 2004.

[62] Eleftherios Goulielmakis, Zhi-Heng Loh, Adrian Wirth, Robin Santra, Nina Rohringer, Vladislav S Yakovlev, Sergey Zherebtsov, Thomas Pfeifer, Abdallah M Azzeer, Matthias F Kling, Stephen R Leone, and Ferenc Krausz. Real-time observation of valence electron motion. *Nature*, 466(7307):739–43, August 2010.

[63] Chris H. Greene and Byungduk Yoo. Doubly-excited states in the spectrum of molecular hydrogen. *The Journal of Physical Chemistry*, 99(6):1711–1718, 1995.

[64] David Jeffrey Griffiths. *Introduction to Electrodynamics*. Prentice Hall, 3rd edition, 1999.

[65] Steven L. Guberman S. L. The doubly excited autoionizing states of h_2. *The Journal of Chemical Physics*, 78(3):1404–1413, 1983.

[66] M Hentschel, R Kienberger, C Spielmann, G A Reider, N Milosevic, T Brabec, P Corkum, U Heinzmann, M Drescher, and F Krausz. Attosecond metrology. *Nature*, 414(6863):509–13, November 2001.

[67] Jorge Fernández Hernández. *Dissociative and non dissociative ionization of H_2^+, HeH^+ and H_2 molecules by photons and fast particles*. PhD thesis, Universidad Autónoma de Madrid (UAM), 2006.

[68] C. Iaconis and I.A. Walmsley. Spectral phase interferometry for direct electric-field reconstruction of ultrashort optical pulses. *Opt. Lett.*, 23(10):792–794, May 1998.

[69] J. Itatani, F. Quéré, G. L. Yudin, M. Yu. Ivanov, F. Krausz, and P. B. Corkum. Attosecond streak camera. *Phys. Rev. Lett.*, 88:173903, Apr 2002.

[70] Kenji Ito, Richard I. Hall, and Masatoshi Ukai. Dissociative photoionization of h2 and d2 in the energy region of 25–45 ev. *The Journal of Chemical Physics*, 104(21):8449–8457, 1996.

[71] John David Jackson. *Classical Electrodynamics*. John Wiley & Sons Publications, 3rd edition, 1998.

[72] J. Javanainen, J. H. Eberly, and Qichang Su. Numerical simulations of multiphoton ionization and above-threshold electron spectra. *Phys. Rev. A*, 38:3430–3446, Oct 1988.

[73] Charles J. Joachin. *Quantum Collision Theory*. Elsevier Science Publishers Company Inc., 3rd edition, 1983.

[74] P. Johnsson, J. Mauritsson, T. Remetter, A. L'Huillier, and K. J. Schafer. Attosecond control of ionization by wave-packet interference. *Phys. Rev. Lett.*, 99:233001, Dec 2007.

[75] R. Jones, C. Raman, D. Schumacher, and P. Bucksbaum. Ramsey interference in strongly driven rydberg systems. *Physical Review Letters*, 71(16):2575–2578, oct 1993.

[76] Itamar Borges Jr and Carlos E Bielschowsky. Doubly excited states of molecular hydrogen: theoretical absorption and photodissociation cross sections. *Journal of Physics B: Atomic, Molecular and Optical Physics*, 33(9):1713, 2000.

[77] Itamar Borges Jr. and Carlos E. Bielschowsky. On the semiclassical dissociation yields of the doubly excited states of h_2. *Chemical Physics Letters*, 342(3–4):411–416, 2001.

[78] Daniel J. Kane. Principal components generalized projections. *J. Opt. Soc. Am. B*, 25(6):A120–A132, Jun 2008.

[79] D.J. Kane. Recent progress toward real-time measurement of ultrashort laser pulses. *Quantum Electronics, IEEE Journal of*, 35(4):421–431, Apr 1999.

[80] Henry Kapteyn, Oren Cohen, Ivan Christov, and Margaret Murnane. Harnessing attosecond science in the quest for coherent x-rays. *Science*, 317(5839):775–778, 2007.

[81] L. V. Keldysh. Ionization in the field of a strong electromagnetic wave. *Sov. Phys. JETP*, 20(5):1307–1314, 1965.

[82] F. Kelkensberg, C. Lefebvre, W. Siu, O. Ghafur, T. T. Nguyen-Dang, O. Atabek, A. Keller, V. Serov, P. Johnsson, M. Swoboda, T. Remetter, A. L'Huillier, S. Zherebtsov, G. Sansone, E. Benedetti, F. Ferrari, M. Nisoli, F. Lépine, M. F. Kling, and M. J. J. Vrakking. Molecular dissociative ionization and wave-packet dynamics studied using two-color xuv and ir pump-probe spectroscopy. *Phys. Rev. Lett.*, 103:123005, Sep 2009.

[83] R Kienberger, E Goulielmakis, M Uiberacker, A Baltuska, V Yakovlev, F Bammer, A Scrinzi, Th Westerwalbesloh, U Kleineberg, U Heinzmann, M Drescher, and F Krausz. Atomic transient recorder. *Nature*, 427(6977):817–21, Feb 2004.

[84] Kyung Taec Kim, Chunmei Zhang, Andrew D. Shiner, Sean E. Kirkwood, Eugene Frumker, Genevieve Gariepy, Andrei Naumov, D. M. Villeneuve, and P. B. Corkum. Manipulation of quantum paths for space-time characterization of attosecond pulses. *Nature Physics*, 9(3):159–163, Jan 2013.

[85] M. F. Kling, Ch. Siedschlag, A. J. Verhoef, J. I. Khan, M. Schultze, Th. Uphues, Y. Ni, M. Uiberacker, M. Drescher, F. Krausz, and M. J. J. Vrakking. Control of electron localization in molecular dissociation. *Science*, 312(5771):246–248, 2006.

[86] K. Klünder, P. Johnsson, M. Swoboda, A. L'Huillier, G. Sansone, M. Nisoli, M. J. J. Vrakking, K. J. Schafer, and J. Mauritsson. Reconstruction of attosecond electron wave packets using quantum state holography. *Phys. Rev. A*, 88:033404, Sep 2013.

[87] Ferenc Krausz and Misha Ivanov. Attosecond physics. *Reviews of Modern Physics*, 81(1):163–234, February 2009.

[88] Manuel Kremer, Bettina Fischer, Bernold Feuerstein, Vitor L. B. de Jesus, Vandana Sharma, Christian Hofrichter, Artem Rudenko, Uwe Thumm, Claus Dieter Schröter, Robert Moshammer, and Joachim Ullrich. Electron localization in molecular fragmentation of $\mathbf{h}_2$ by carrier-envelope phase stabilized laser pulses. *Phys. Rev. Lett.*, 103:213003, Nov 2009.

[89] A Lafosse, M Lebech, J C Brenot, P M Guyon, L Spielberger, O Jagutzki, J C Houver, and D Dowek. Molecular frame photoelectron angular distributions in dissociative photoionization of h 2 in the region of the q 1 and q 2 doubly excited states. *Journal of Physics B: Atomic, Molecular and Optical Physics*, 36(23):4683, 2003.

[90] C J Latimer, K F Dunn, N Kouchi, M A McDonald, V Srigengan, and J Geddes. A dissociative photoionization study of the autoionization lifetime of the lowest 1 sigma u superexcited state in hydrogen and deuterium. *Journal of Physics B: Atomic, Molecular and Optical Physics*, 26(18):L595, 1993.

[91] C J Latimer, A D Irvine, M A McDonald, and O G Savage. The dissociative photoionization of hydrogen via two-electron excitation at 27.5 ev and 30.5 ev. *Journal of Physics B: Atomic, Molecular and Optical Physics*, 25(8):L211, 1992.

[92] C. Lefebvre, T. T. Nguyen-Dang, F. Dion, M. J. J. Vrakking, V. N. Serov, and O. Atabek. Attosecond pump-probe transition-state spectroscopy of laser-induced molecular dissociative ionization: Adiabatic versus nonadiabatic dressed-state dynamics. *Phys. Rev. A*, 88:053416, Nov 2013.

[93] Steve Taylor Leonard F. Bjeldanes and Takayuki Shibamoto. *Introduction to Electrodynamics*. Benjamin Cummings, 1999.

[94] M. Leventhal, R. T. Robiscoe, and K. R. Lea. Velocity distribution of metastable h atoms produced by dissociative excitation of h2. *Phys. Rev.*, 158:49–56, Jun 1967.

[95] Ira N. Levine. *Química Cuántica*. Prentice Hall, 5th edition, 2001.

[96] Robert J. Levis, Getahun M. Menkir, and Herschel Rabitz. Selective bond dissociation and rearrangement with optimally tailored, strong-field laser pulses. *Science*, 292(5517):709–713, 2001.

[97] M. Hentschel R. Kienberger M. Uiberacker V. Yakovlev A. Scrinzi Th. Westerwalbesloh U. Kleineberg U. Heinzmann F. Krausz M. Drescher. Time-resolved atomic inner-shell spectroscopy. *Nature*, 419:803–807, 2002.

[98] Th. Uphues M. Schultze A. J. Verhoef V. Yakovlev M. F. Kling J. Rauschenberger N. M. Kabachnik H. Schröder M. Lezius K. L. Kompa H.-G. Muller M. J. J. Vrakking S. Hendel U. Kleineberg U. Heinzmann M. Drescher & F. Krausz M. Uiberacker. Attosecond real-time observation of electron tunnelling in atoms. *Nature*, 446:0028–0836, May 2007.

[99] J R Machacek, V M Andrianarijaona, J E Furst, A L D Kilcoyne, A L Landers, E T Litaker, K W McLaughlin, and T J Gay. Production of excited atomic hydrogen and deuterium from h_2, hd and d_2 photodissociation. *Journal of Physics B: Atomic, Molecular and Optical Physics*, 44(4):045201, 2011.

[100] John M. J. Madey. Stimulated emission of bremsstrahlung in a periodic magnetic field. *Journal of Applied Physics*, 42(5):1906–1913, 1971.

[101] Maia Magrakvelidze, Feng He, Thomas Niederhausen, Igor V. Litvinyuk, and Uwe Thumm. Quantum-beat imaging of the nuclear dynamics in D_2^+: Dependence of bond softening and bond hardening on laser intensity, wavelength, and pulse duration. *Phys. Rev. A*, 79:033410, Mar 2009.

[102] Y. Mairesse and F. Quéré. Frequency-resolved optical gating for complete reconstruction of attosecond bursts. *Phys. Rev. A*, 71:011401, Jan 2005.

[103] F. Martín. Completely l^2 integrable method for strong-coupling multichannel photoionization: Photoelectron emission of he between the n=3 and 4 thresholds. *Phys. Rev. A*, 48(1):331–337, Jul 1993.

[104] F Martín, J Fernández, T Havermeier, L Foucar, Th Weber, K Kreidi, M Schöffler, L Schmidt, T Jahnke, O Jagutzki, a Czasch, E P Benis, T Osipov, a L Landers, a Belkacem, M H Prior, H Schmidt-Böcking, C L Cocke, and R Dörner. Single photon-induced symmetry breaking of h_2 dissociation. *Science (New York, N.Y.)*, 315(5812):629–33, feb 2007.

[105] F. Martín, O. Mó, A. Riera, and M. Yá nez. Feshbach resonant energies and widths in a pseudopotential approach. *EPL (Europhysics Letters)*, 4(7):799, 1987.

[106] Fernando Martín. Ionization and dissociation using b-splines: photoionization of the hydrogen molecule. *Journal of Physics B: Atomic, Molecular and Optical Physics*, 32(16):R197, 1999.

[107] J. Mauritsson, P. Johnsson, E. Mansten, M. Swoboda, T. Ruchon, A. L'Huillier, and K. J. Schafer. Coherent electron scattering captured by an attosecond quantum stroboscope. *Phys. Rev. Lett.*, 100:073003, Feb 2008.

[108] J. Mauritsson, T. Remetter, M. Swoboda, K. Klünder, A. L'Huillier, K. J. Schafer, O. Ghafur, F. Kelkensberg, W. Siu, P. Johnsson, M. J. J. Vrakking, I. Znakovskaya, T. Uphues, S. Zherebtsov, M. F. Kling, F. Lépine, E. Benedetti, F. Ferrari, G. Sansone, and M. Nisoli. Attosecond electron spectroscopy using a novel interferometric pump-probe technique. *Phys. Rev. Lett.*, 105:053001, Jul 2010.

[109] A. McPherson, G. Gibson, H. Jara, U. Johann, T. S. Luk, I. A. McIntyre, K. Boyer, and C. K. Rhodes. Studies of multiphoton production of vacuum-ultraviolet radiation in the rare gases. *J. Opt. Soc. Am. B*, 4(4):595–601, Apr 1987.

[110] Christoph Meier and Volker Engel. Interference structure in the photoelectron spectra obtained from multiphoton ionization of na_2 with a strong femtosecond laser pulse. *Phys. Rev. Lett.*, 73:3207–3210, Dec 1994.

[111] V. Mergel, M. Achler, R. Dörner, Kh. Khayyat, T. Kambara, Y. Awaya, V. Zoran, B. Nyström, L. Spielberger, J. H. McGuire, J. Feagin, J. Berakdar, Y. Azuma, and H. Schmidt-Böcking. Helicity dependence of the photon-induced three-body coulomb fragmentation of helium investigated by cold target recoil ion momentum spectroscopy. *Phys. Rev. Lett.*, 80(24):5301–5304, Jun 1998.

[112] William H. Miller. Theory of penning ionization. i. atoms. *The Journal of Chemical Physics*, 52(7):3563–3572, 1970.

[113] R. Mitzner, A. A. Sorokin, B. Siemer, S. Roling, M. Rutkowski, H. Zacharias, M. Neeb, T. Noll, F. Siewert, W. Eberhardt, M. Richter, P. Juranic, K. Tiedtke, and J. Feldhaus. Direct autocorrelation of soft-x-ray free-electron-laser pulses by time-resolved two-photon double ionization of he. *Phys. Rev. A*, 80(2):025402, Aug 2009.

[114] Felipe Morales, Jhon Fredy Pérez-Torres, José Luis Sanz-Vicario, and Fernando Martín. Probing h_2 quantum autoionization dynamics with xuv atto and femtosecond laser pulses. *Chemical Physics*, 366(1-3):58 – 63, 2009. Attosecond Molecular Dynamics.

[115] R Moshammer, J Ullrich, M Unverzagt, W Schmidt, P Jardin, R E Olson, R Mann, R Dorner, V Mergel, and U Buck. ow-energy electrons and their dynamical correlation with recoil ions for single ionization of helium by fast, heavy-ion impact. *Physical Review Letters*, 73(25):3371–3374, 1994.

[116] H.G. Muller. Reconstruction of attosecond harmonic beating by interference of two-photon transitions. *Applied Physics B*, 74(1):s17–s21, 2002.

[117] Seymour Lipschutz Murray Spiegel and John Liu. *Schaum's Outline of Mathematical Handbook of Formulas and Tables*. McGraw Hill Professional, 3rd edition, 2008.

[118] Alicia Palacios Ca nas. *Ionización y disociación de H_2^+ y H_2 por pulsos láser ultracortos en la región XUV*. PhD thesis, Universidad Autónoma de Madrid (UAM), 2006.

[119] Roger G. Newton. *Scattering theory of waves and particles*. Springer, 1982.

[120] Hiromichi Niikura, F Légaré, R Hasbani, Misha Yu Ivanov, DM Villeneuve, and PB Corkum. Probing molecular dynamics with attosecond resolution using correlated wave packet pairs. *Nature*, 421(6925):826–829, 2003.

[121] M. Nisoli and G. Sansone. New frontiers in attosecond science. *Progress in Quantum Electronics*, 33(1):17–59, Jan 2009.

[122] Mauro Nisoli, S Stagira, S De Silvestri, O Svelto, S Sartania, Z Cheng, M Lenzner, Ch Spielmann, and F Krausz. A novel-high energy pulse compression system: generation of multigigawatt sub-5-fs pulses. *Applied Physics B: Lasers and Optics*, 65(2):189–196, 1997.

[123] Christian Ott, Andreas Kaldun, Philipp Raith, Kristina Meyer, Martin Laux, Jörg Evers, Christoph H. Keitel, Chris H. Greene, and Thomas Pfeifer. Lorentz meets fano in spectral line shapes: A universal phase and its laser control. *Science*, 340(6133):716–720, 2013.

[124] Kurt E. Oughstun. *Electromagnetic and Optical Pulse Propagation 1*, volume 125 of *Springer Series in Optical Sciences*. Springer International Publishing, 200.

[125] Kurt E. Oughstun. *Electromagnetic and Optical Pulse Propagation 2*, volume 144 of *Springer Series in Optical Sciences*. Springer International Publishing, 2009.

[126] A. Palacios, T. N. Rescigno, and C. W. McCurdy. Cross sections for short-pulse single and double ionization of helium. *Phys. Rev. A*, 77:032716, Mar 2008.

[127] A. Palacios, T. N. Rescigno, and C. W. McCurdy. Time-dependent treatment of two-photon resonant single and double ionization of helium by ultrashort laser pulses. *Phys. Rev. A*, 79:033402, Mar 2009.

[128] Alicia Palacios, Johannes Feist, Alberto González-Castrillo, José Luis Sanz-Vicario, and Fernando Martín. Autoionization of molecular hydrogen: Where do the fano lineshapes go? *ChemPhysChem*, 14(7):1456–1463, 2013.

[129] Alicia Palacios, Paula Rivière, Alberto González-Castrillo, and Fernando Martín. *XUV Lasers for Ultrafast Electronic Control in H2*, volume 107 of *Springer Series in Chemical Physics*. Springer International Publishing, 2014.

[130] Seung Min Park, Shao-Ping Lu, and Robert J. Gordon. Coherent laser control of the resonance-enhanced multiphoton ionization of hcl. *The Journal of Chemical Physics*, 94(12):8622–8624, 1991.

[131] A. Paul, E.A. Gibson, X. Zhang, A. Lytle, T. Popmintchev, Xibin Zhou, M.M. Murnane, I.P. Christov, and H.C. Kapteyn. Phase-matching techniques for coherent soft x-ray generation. *IEEE Journal of Quantum Electronics*, 42(1):14–26, Jan 2006.

[132] P. M. Paul, E. S. Toma, P. Breger, G. Mullot, F. AugÃ©, Ph. Balcou, H. G. Muller, and P. Agostini. Observation of a train of attosecond pulses from high harmonic generation. *Science*, 292(5522):1689–1692, 2001.

[133] J. F. Pérez-Torres, J. L. Sanz-Vicario, H. Bachau, and F. Martín. The role of autoionizing states in two-photon dissociative ionization of h_2 by xuv ultrashort laser pulses. *Journal of Physics B: Atomic, Molecular and Optical Physics*, 43(1):015–204, 2010.

[134] Adrian N. Pfeiffer and Stephen R. Leone. Transmission of an isolated attosecond pulse in a strong-field dressed atom. *Phys. Rev. A*, 85:053422, May 2012.

[135] Frank L. Pilar. *Elementary quantum chemistry*. Courier Dover Publications, 2001.

[136] F. Quéré, J. Itatani, G. L. Yudin, and P. B. Corkum. Attosecond spectral shearing interferometry. *Phys. Rev. Lett.*, 90:073902, Feb 2003.

[137] F. Quéré, Y. Mairesse, and J. Itatani. Temporal characterization of attosecond xuv fields. *Journal of Modern Optics*, 52(2-3):339–360, 2005.

[138] N. F. Ramsey. Experiments with separated oscillatory fields and hydrogen masers. *Science (New York, N.Y.)*, 248(4963):1612–9, Jun 1990.

[139] P Ranitovic, X M Tong, B Gramkow, S De, B DePaola, K P Singh, W Cao, M Magrakvelidze, D Ray, I Bocharova, H Mashiko, A Sandhu, E Gagnon, M M Murnane, HC Kapteyn, I Litvinyuk, and C L Cocke. Ir-assisted ionization of helium by attosecond extreme ultraviolet radiation. *New Journal of Physics*, 12(1):013008, 2010.

[140] T. J. Reddish, A. Padmanabhan, M. A. MacDonald, L. Zuin, J. Fernández, A. Palacios, and F. Martín. Observation of interference between two distinct autoionizing states in dissociative photoionization of h2. *Phys. Rev. Lett.*, 108:023004, Jan 2012.

[141] Javier Núñez Delgado; Joan Bertrán Rusca. *Química física (Volumen I)*, volume 1. Ariel Ciencia, 2002.

[142] Jun J. Sakurai and Jim J. Napolitano. *Modern Quantum Mechanics*. Addison-Wesley, 2nd edition, 2010.

[143] El Saldin, W Sandner, Z Sanok, H Schlarb, G Schmidt, P Schmuser, Jr Schneider, Ea Schneidmiller, H Schreiber, S Schreiber, P Schutt, J Sekutowicz, L Serafini, D Sertore, S Setzer, S Simrock, B Sonntag, B Sparr,

F Stephan, Va Sytchev, S Tazzari, F Tazzioli, M Tigner, M Timm, M Tonutti, and E Trakhtenberg. First observation of self-amplified spontaneous emission in a free-electron laser at 109 nm wavelength. *Physical Review Letters*, 85(18):3825–3829, Oct 2000.

[144] I. Sánchez and F. Martín. The doubly excited states of the h_2 molecule. *The Journal of Chemical Physics*, 106(18):7720–7730, 1997.

[145] I. Sánchez and F. Martín. Origin of unidentified structures in resonant dissociative photoionization of h2. *Phys. Rev. Lett.*, 79:1654–1657, Sep 1997.

[146] I. Sánchez and F Martín. Representation of the electronic continuum of h_2 with b-spline basis. *Journal of Physics B: Atomic, Molecular and Optical Physics*, 30(3):679, 1997.

[147] I. Sánchez and F. Martín. Resonant dissociative photoionization of h_2 and d_2. *Phys. Rev. A*, 57:1006–1017, Feb 1998.

[148] I. Sánchez and F. Martín. Doubly excited autoionizing states of h_2 above the second ionization threshold: the q2 resonance series. *The Journal of Chemical Physics*, 110(14):6702–6713, 1999.

[149] G. Sansone, E. Benedetti, F. Calegari, C. Vozzi, L. Avaldi, R. Flammini, L. Poletto, P. Villoresi, C. Altucci, R. Velotta, S. Stagira, S. De Silvestri, and M. Nisoli. Isolated single-cycle attosecond pulses. *Science*, 314(5798):443–446, 2006.

[150] G. Sansone, F. Calegari, and M. Nisoli. Attosecond technology and science. *Selected Topics in Quantum Electronics, IEEE Journal of*, 18(1):507–519, Jan 2012.

[151] José Luis Sanz-Vicario, Henri Bachau, and Fernando Martín. Time-dependent theoretical description of molecular autoionization produced by femtosecond xuv laser pulses. *Phys. Rev. A*, 73:033410, Mar 2006.

[152] Matthias Schnürer, Z Cheng, S Sartania, M Hentschel, Gabriel Tempea, Thomas Brabec, and Ferenc Krausz. Guiding and high-harmonic generation of sub-10-fs pulses in hollow-core fibers at 1015 w/cm2. *Applied Physics B*, 67(2):263–266, 1998.

[153] Michael S. Schuurman and Albert Stolow. *Conical Intersections: Theory, Computation and Experiment*, volume 17 of *Advanced Series in Physical Chemistry*. World Scientific, 2011.

[154] Marlan O. Scully and M. Suhail Zubairy. *Quantum Optics*. Cambridge University Press, 1997.

[155] Tamar Seideman, Moshe Shapiro, and Paul Brumer. Coherent radiative control of unimolecular reactions: Selective bond breaking with picosecond pulses. *The Journal of Chemical Physics*, 90(12):7132–7136, 1989.

[156] Moshe Shapiro and Paul Brumer. Controlled photon induced symmetry breaking: Chiral molecular products from achiral precursors. *The Journal of Chemical Physics*, 95(11):8658–8661, 1991.

[157] Moshe Shapiro, Einat Frishman, and Paul Brumer. Coherently controlled asymmetric synthesis with achiral light. *Phys. Rev. Lett.*, 84:1669–1672, Feb 2000.

[158] B. W. Shore. Use of the rayleigh-ritz-galerkin method with cubic splines for constructing single-particle bound-state radial wavefunctions: The hydrogen atom and its spectrum. *J. Phys. B: Atom. Molec. Phys.*, 6:1923–1932, 1973.

[159] Bruce W Shore. Use of boundary-condition wavefunctions for bound states, continuum states, and resonances. *J. Phys. B: Atom. Molec. Phys.*, 7(18):2502–2517, 1974.

[160] L D A Siebbeles and C Le Sech. A simple method to calculate potential curves of two-electron molecules at intermediate nuclear distances. *Journal of Physics B: Atomic, Molecular and Optical Physics*, 27(19):4443, 1994.

[161] Olga Smirnova, Michael Spanner, and Misha Yu Ivanov. Coulomb and polarization effects in laser-assisted xuv ionization. *Journal of Physics B: Atomic, Molecular and Optical Physics*, 39(13):S323, 2006.

[162] Zhigang Sun and Nanquan Lou. Autler-townes splitting in the multiphoton resonance ionization spectrum of molecules produced by ultrashort laser pulses. *Phys. Rev. Lett.*, 91:023002, Jul 2003.

[163] Attila Szabo and Neil S. Ostlund. *Modern quantum chemistry*. Courier Dover Publications, 1996.

[164] P. Johnsson J. Mauritsson K. Varjú Y. Ni F. Lépine E. Gustafsson M. Kling J. Khan R. López-Martens K. J. Schafer M. J. J. Vrakking & A. L'Huillier T. Remetter. Attosecond electron wave packet interferometry. *Nature*, 2:1745–2473, 2006.

[165] David J. Tannor, Ronnie Kosloff, and Stuart A. Rice. Coherent pulse sequence induced control of selectivity of reactions: Exact quantum mechanical calculations. *The Journal of Chemical Physics*, 85(10):5805–5820, 1986.

[166] David J. Tannor and Stuart A. Rice. Control of selectivity of chemical reaction via control of wave packet evolution. *The Journal of Chemical Physics*, 83(10):5013–5018, 1985.

[167] Michal Tarana and Chris H. Greene. Femtosecond transparency in the extreme-ultraviolet region. *Phys. Rev. A*, 85:013411, Jan 2012.

[168] P Tzallas, D Charalambidis, N A Papadogiannis, K Witte, and G D Tsakiris. Direct observation of attosecond light bunching. *Nature*, 426(6964):267–71, Nov 2003.

[169] P. Tzallas, E. Skantzakis, L. A. A. Nikolopoulos, G. D. Tsakiris, and D. Charalambidis. Extreme-ultraviolet pump-probe studies of one-femtosecond-scale electron dynamics. *Nature Physics*, 7(10):781–784, Jul 2011.

[170] J. Ullrich, R. Moshammer, R. Diörner, O. Jagutzki, V. Mergel, H. Schmidt-Böcking, and L. Spielberger. Recoil-ion momentum spectroscopy. *Journal of Physics B: Atomic, Molecular and Optical Physics*, 30:2917–2974, 1997.

[171] J. Ullrich, R. Moshammer, A. Dorn, R. Dörner, L. Ph H. Schmidt, and H. Schmidt-Böcking. Recoil-ion and electron momentum spectroscopy: reaction-microscopes. *Reports on Progress in Physics*, 66(9):1463, Sep 2003.

[172] W. Vanroose, D. A. Horner, F. Martín, T. N. Rescigno, and C. W. McCurdy. Double photoionization of aligned molecular hydrogen. *Phys. Rev. A*, 74:052702, Nov 2006.

[173] Wim Vanroose, Fernando Martín, Thomas N. Rescigno, and C. William McCurdy. Complete photo-induced breakup of the h2 molecule as a probe of molecular electron correlation. *Science*, 310(5755):1787–1789, 2005.

[174] Valérie Véniard, Richard Taïeb, and Alfred Maquet. Phase dependence of $(n+1)$-color (n) ir-uv photoionization of atoms with higher harmonics. *Phys. Rev. A*, 54:721–728, Jul 1996.

[175] H Wabnitz, L Bittner, A R B de Castro, R Döhrmann, P Gürtler, T Laarmann, W Laasch, J Schulz, A Swiderski, K von Haeften, T Möller, B Faatz, A Fateev, J Feldhaus, C Gerth, U Hahn, E Saldin, E Schneidmiller, K Sytchev, K Tiedtke, R Treusch, and M Yurkov. Multiple ionization of atom clusters by intense soft x-rays from a free-electron laser. *Nature*, 420(6915):482–5, dec 2002.

[176] Qiaoling Wang and Anthony F. Starace. Coherent control of h^- photodetachment in parallel static electric and magnetic fields. *Phys. Rev. A*, 51:1260–1276, Feb 1995.

[177] L. Wolniewicz. Relativistic energies of the ground state of the hydrogen molecule. *The Journal of Chemical Physics*, 99(3):1851–1868, 1993.

[178] L. Wolniewicz and K. Dressler. The ef, gk, and hh $^1\Sigma_g^+$ states of hydrogen. improved ab initio calculation of vibrational states in the adiabatic approximation. *The Journal of Chemical Physics*, 82(7):3292–3299, 1985.

[179] Jinchun Xie and Richard N. Zare. Selection rules for the photoionization of diatomic molecules. *The Journal of Chemical Physics*, 93(5):3033–3038, 1990.

[180] Alberto Requena y José Zúniga. *Espectroscopía*. Prentice Hall, 2004.

[181] Vladislav S. Yakovlev, Ferdinand Bammer, and Armin Scrinzi. Attosecond streaking measurements. *Journal of Modern Optics*, 52(2-3):395–410, 2005.

[182] C. W. Yip, F. L. andMcCurdy and T. N. Rescigno. Hybrid orbital and numerical grid representation for electronic continuum processes: Double photoionization of atomic beryllium. *Phys. Rev. A*, 81:053407, May 2010.

[183] L. H. Yu. High-gain harmonic-generation free-electron laser. *Science*, 289(5481):932–934, aug 2000.

[184] Richard N. Zare. Dissociation of h2+ by electron impact: Calculated angular distribution. *The Journal of Chemical Physics*, 47(1):204–215, 1967.

[185] A. Zavriyev, P. H. Bucksbaum, H. G. Muller, and D. W. Schumacher. Ionization and dissociation of h2 in intense laser fields at 1.064 μm, 532 nm, and 355 nm. *Phys. Rev. A*, 42:5500–5513, Nov 1990.

[186] M. Zepf, B. Dromey, M. Landreman, P. Foster, and S. M. Hooker. Bright quasi-phase-matched soft-x-ray harmonic radiation from argon ions. *Phys. Rev. Lett.*, 99:143901, Oct 2007.

[187] Ahmed H. Zewail. 4d ultrafast electron diffraction, crystallography, and microscopy. *Annual Review of Physical Chemistry*, 57(1):65–103, 2006. PMID: 16599805.

[188] X. Zhang, A. R. Libertun, A. Paul, E. Gagnon, S. Backus, I. P. Christov, M. M. Murnane, H. C. Kapteyn, R. A. Bartels, Y. Liu, and D. T. Attwood. Highly coherent light at 13 nm generated by use of quasi-phase-matchedhigh-harmonic generation. *Opt. Lett.*, 29(12):1357–1359, Jun 2004.

[189] Xiaoshi Zhang, Amy Lytle, Tenio Popmintchev, Ariel Paul, Nick Wagner, Margaret Murnane, Henry Kapteyn, and Ivan P. Christov. Phase matching, quasi-phase matching, and pulse compression in a single waveguide for enhanced high-harmonic generation. *Opt. Lett.*, 30(15):1971–1973, Aug 2005.

[190] Kun Zhao, Qi Zhang, Michael Chini, Yi Wu, Xiaowei Wang, and Zenghu Chang. Tailoring a 67 attosecond pulse through advantageous phase-mismatch. *Opt. Lett.*, 37(18):3891–3893, Sep 2012.

[191] X. Zhou, P. Ranitovic, C. W. Hogle, J. H. D. Eland, H. C. Kapteyn, and M. M. Murnane. Probing and controlling non-born-oppenheimer dynamics in highly excited molecular ions. *Nature Physics*, 8(3):232–237, Jan 2012.

[192] Langchi Zhu, Valeria Kleiman, Xiaonong Li, Shao Ping Lu, Karen Trentelman, and Robert J. Gordon. Coherent laser control of the product distribution obtained in the photoexcitation of hi. *Science*, 270(5233):77–80, 1995.